

14

Single Electron Charging and Quantum Effects in Semiconductor Nanostructures

by

Ethan Bradley Foxman

B.S., Massachusetts Institute of Physics (1988)

Submitted to the Department of Physics
in partial fulfillment of the requirements for the degree of
Doctor in Philosophy

at the

MASSACHUSETTS INSTITUTE OF TECHNOLOGY

August 1993

© Massachusetts Institute of Technology 1993. All rights reserved.

Author
Department of Physics
August 6, 1993

Certified by
Marc A. Kastner
Donner Professor of Science
Thesis Supervisor

Accepted by
George F. Koster
Chairman, Departmental Committee on Graduate Students

MASSACHUSETTS INSTITUTE
OF TECHNOLOGY

NOV 02 1993

ARCHIVES

Single Electron Charging and Quantum Effects in Semiconductor Nanostructures

by

Ethan Bradley Foxman

Submitted to the Department of Physics
on August 6, 1993, in partial fulfillment of the
requirements for the degree of
Doctor in Philosophy

Abstract

We present an experimental study of a small region ($\sim 0.3 \times 0.3 \mu\text{m}^2$) of two-dimensional electron gas in a GaAs/Al_xGa_{1-x}As heterostructure. The small electron gas is coupled to electrical leads through tunnel barriers formed by negatively biased Schottky gates on the surface of the heterostructure. Electron transport is studied as a function of gate voltage, magnetic field, temperature, bias voltage and tunneling barrier height.

We observe a rich interplay between single electron charging and quantum effects. The conductance of such systems was known to consist of a series of nearly periodic conductance peaks.^{1,2} We further investigate this behavior and show that our observations are consistent with a model that synthesizes classical single electron charging and a discrete tunneling density of states.^{3,4}

We investigate the nature and origin of this tunneling density of states. The spectrum of states is determined through current-voltage measurements and low-bias conductance measurements. The tunneling density of states is mapped as a function of gate voltage and magnetic field. In the latter case, we show that our observations can be understood through a self-consistent model of single electron charging in the quantum Hall regime.⁵

Lastly, we report conductance measurements in the regime where the conductance across the tunnel barriers separating the small electron gas from its leads becomes

¹J.H.F. Scott-Thomas, S.B. Field, M.A. Kastner, H.I. Smith, and D.A. Antoniadis, *Phys. Rev. Lett.* **62**, 583 (1989).

²U. Meirav, M.A. Kastner, and S.J. Wind, *Phys. Rev. Lett.* **65**, 771 (1990).

³Yigal Meir, Ned S. Wingreen, P.A. Lee, *Phys. Rev. Lett.* **66**, 3048 (1991).

⁴C.W.J. Beenakker, *Phys. Rev. B* **44**, 1646 (1991).

⁵P.L. McEuen, E.B. Foxman, Jari Kinaret, U. Meirav, M.A. Kastner, Ned S. Wingreen, and S. J. Wind, *Phys. Rev. B* **45**, 11419 (1992).

of order e^2/h . We observe that in this regime single electron charging effects are quenched. This effect is shown to arise from an increased capacitance across one of the barriers and from the increased lifetime broadening of states in the small electron gas.⁶

Thesis Supervisor: Marc A. Kastner

Title: Donner Professor of Science

⁶E.B. Foxman, P. L. McEuen, U . Meirav, Ned S. Wingreen, Yigal Meir, Paul A. Belk, N.R. Belk, M.A. Kastner and S.J. Wind, *Phys. Rev. B* **47**, 10020 (1993).

For W.T.

Acknowledgements

If the clock were turned back four years and I began graduate school once again, knowing what I do today, I would join the same research group, work on the same project, and hope to work with the same people. As such, it is genuinely a pleasure to be able to acknowledge some of the people who have made the past four years a fruitful, enriching and enjoyable period of my life.

I must start with my advisor, Marc Kastner, who has been for me a teacher in the highest sense of the word. He teaches not so much by presentation as by example. His style and approach to thinking about physical problems is one of the most valuable assets I have received from graduate school. His enthusiasm and unshakable optimism for his students' work is something I have respected and appreciated throughout my time in his group. Finally, I must express my gratitude for his genuine support and encouragement of my career decisions.

I inherited the project that became my thesis research from a previous student in our group, Udi Meirav. I thank him not only for a vital introduction to this research and for providing us with the devices that we later studied, but also for conversation, ideas and wit that are uniquely his.

After Udi graduated, I worked with Paul McEuen while he was a postdoc in our group. In essence, Paul was my second advisor. Being able to work closely with him through the course of a very exciting project taught me more about science and the way to approach research than any other single experience. I am grateful for this and for the many hours we spent chewing over ideas about science and beyond. I am still

struck by how deeply Paul thinks about physics, and by how much fun he had doing so.

After Paul McEuen left our group, I worked most closely with Paul Belk. I am glad to be able to thank Paul for the numerous times that he unconditionally offered his help in life inside and outside the lab. This includes his reading and rereading of multiple drafts of this thesis. Most importantly though, I thank him for his friendship.

Along the way, I have enjoyed the company of my fellow students in Marc's group. It has been said that adversity forges a special bond between comrades in arms; it is the same between comrades in lab coats. Jens Petter Falck, who was my office mate from day one, has become a good friend, and I am glad to be able to thank him for this. Nathan Belk brought to bear his unparalleled technical expertise to much improve our experiment, making possible many of the results contained in this thesis. I happily acknowledge him for this, for teaching me all sorts of odds and ends in the lab, and for the unique character that he has brought to the group.

I appreciate the truly unselfish way in which Ady Levy helped me and many others in the group during the trials and tribulations of exams and life in the lab, not to mention the times I stayed in his home while I was working at IBM. David Abusch is the newest student in the project. He has reconfirmed for me that to be a student and to be able to look for wonder in how the world works is a luxury. I thank him for this. I also wish to thank Pamela Blakeslee for the times that she has helped me in the lab and the measure of serenity which she has contributed to our group. Olivier Klein is the newest member of our group and I regret that I will not be able to work with him further since it has been a pleasure to do so over the past few weeks.

I thank Ned Wingreen and Yigal Meir, who were our collaborators on the theory side of things, for making the research all the more interesting. The same goes for Arvind Kumar and Mitya Chklovskii, both of whom gave me the benefit of their clear thinking about many of the issues relevant to our work.

I am also indebted to the former students in Marc's group who were able to find

time to help me as a new student starting out in the lab. This includes Chih-Yung Chen, Norris Preyer, Tineke Thio, Sam Park, and John Scott-Thomas. Now that I am graduating I hope to be able at least in some small measure to do the same for the newest members of the lab for whom I wish the best, Erika Chuang and Danielle Kleinberg.

The samples that I have studied were fabricated at IBM's Research Laboratory in Yorktown Heights, New York. I gratefully acknowledge the help and resources that were made available to me by IBM. In particular, I wish to thank Shalom Wind who is our collaborator at IBM, and who facilitated life for me, both scientific and otherwise, when I was at IBM. Also, I would like to acknowledge Michael Melloch who provided us with material that was the starting point in the fabrication of our most recent samples.

I have always felt that my graduate education began the year before I came to M.I.T. when I began working at the Nippon Electric Company (NEC) Fundamental Research Center in Kawasaki, Japan. So many people genuinely went out of their way to make my year at NEC an entirely worthwhile experience. This includes U. Tsuda, A. Normura, K. Nishi, T. Noguchi, M. Baba, M. Miyada, Uchiro Takeda, Astsushi Oshiyama, and in particular, Kazeyuki Hirose, who in addition to all else, I thank for his friendship. I also feel indebted to members of the M.I.T.-Japan Program who made it possible for me to contact NEC and who put me in touch with a number of people after returning from Japan: Patricia Gercik, Susan Bergman, Kathleen Schaefer and Richard Samuels.

I thank those at the Harvard Medical school who helped introduce me to the world of medicine and the possibilities of working in the field: Ichiro Uchioda, Michael Wiedman, Herman Strauss, Craig Wu, and Herman Weiss.

Finally, I thank my family for their constant love and support.

Contents

Acknowledgements	7
List of Figures	15
List of Tables	20
Preface	23
 1 Introduction	 27
 2 The Zero-Dimensional Electron Gas System	 33
2.1 Device Fabrication	33
2.1.1 GaAs/AlGaAs Heterostructures	34
2.1.2 Electron-beam Lithography	38
2.1.3 Layout and Ohmic Contacts	42
2.1.4 Final Remarks	46
2.2 A Quantitative View of a Typical Device	46
2.2.1 Electronic Properties of the 2-DEG	47
2.2.2 Theoretical Modeling of the Device	53
2.3 Energy Scales and Probing a Device	53
2.3.1 Electronic Excitations of a Small Electron Gas	53
2.3.2 Experimental Requirements for Probing the Small Electron Gas	56
 3 Classical Single Electron Charging	 57
3.1 Conductances Measurements of a Small Electron Gas	58

3.2	Conductance versus Gate-voltage Data	61
3.3	Introduction to the Classical Coulomb Blockade Model	62
3.3.1	Single-electron charging and the Origin of Periodic Conductance Peaks	67
3.3.2	Recasting the Single Electron Charging model in the Single Particle Tunneling Framework	70
3.3.3	Thermally Broadened Conductance Peak Lineshapes in the Model of Classical Single Electron Charging	74
3.4	Large-Bias I-V Characteristic	78
3.4.1	Current-Voltage (I - V_{ds}) Measurements	79
3.4.2	I - V_{ds} Data	79
3.4.3	Single-Electron Charging I - V_{ds} Characteristics	80
3.4.4	Computer Modeling of Single Electron Charging at Zero Temperature	85
3.5	Capacitance in Multiple Gate Geometries	88
4	Single Electron Charging and a Quantized Energy Spectrum	95
4.1	Introduction	95
4.2	The Discrete Energy Spectrum of a Small Electron Gas	96
4.2.1	The Level Spectrum as a Function of V_g	104
4.2.2	Discrete Energy Levels and Gate Voltage Sweeps at Fixed V_{ds}	106
4.3	The Temperature Behavior of Conductance Peaks	113
4.3.1	Conductance Peak Temperature Data	113
4.3.2	The Theory of Coulomb-blockade oscillations in the Presence of a Discrete level spectrum	124
4.3.3	Back to the Data	130
5	Single Electron Charging in the Quantum Hall Regime	133
5.1	Introduction	133

5.2	Transport Measurements in the Quantum Hall Regime	134
5.3	The Self-consistent Model of Single Electron Charging in then Quan- tum Hall Regime	142
5.4	Comparison of the Self-consistent Model with Experiment	149
6	Electron Transport in Weakly Blockaded Regime	155
6.1	Introduction	155
6.2	Conductance Measurements in the Weakly Blockaded Regime	156
6.3	Thermally broadened Lorentzian lineshapes at high V_g	158
6.4	Lorentzian Fits over a range of Conductance Peaks	160
6.5	Quantum Mechanical Cheating in the Coulomb Blockade	162
6.5.1	Thouless' Criteria for Single-electron Charging	163
6.5.2	Macroscopic Quantum Tunneling	165
6.5.3	The Kondo Transmission Resonance	166
7	Conclusion	169
7.1	Summary	169
7.2	Odds and Ends	170
A	Additional Gate Geometries	175
B	Heterostructure Wafers	181
C	Notes on the Fabrication Process	185
D	Notes on the Operation of the Dilution Refrigerator	187
E	The Low-Noise Current-to-Voltage Amplifier	195
F	Computer Code to calculate I versus V_{ds} in the classical Coulomb blockade model	197

G	Computer Code to calculate I versus V_g at finite V_{ds} in the classical Coulomb blockade model	201
H	Electrons in a Magnetic Field	207
I	Reprints	215
	Bibliography	229
	Biographical Sketch of the Author	245

List of Figures

2-1	GaAs/AlGaAs Heterostructure Schematic	34
2-2	MBE Schematic	35
2-3	GaAs/Al _x Ga _{1-x} As heterostructure band diagram	36
2-4	GaAs/AlGaAs heterostructure schematic with metal electrodes	38
2-5	PMMA Bilayer for <i>e</i> -beam Lithography	39
2-6	Gate Level SEM	40
2-7	Gate level sem micrograph for an independent barrier control device .	41
2-8	Chiplet layout design	44
2-9	Hall bar layout design	45
2-10	The inverted-semiconductor-insulator-semiconductor (ISIS) structure of Meirav <i>et al.</i>	47
2-11	Shubnikov-DeHaas Oscillations	48
2-12	Shubnikov-DeHaas Oscillations Periodic in $\Delta(1/B)$	49
2-13	The tunneling conductance through a single barrier	52
2-14	Equipotentials in a zero-dimensional electron gas structure.	54
3-1	The small electron gas system as conceptualized in the classical single electron charging model	59
3-2	The method of measuring the conductance of a small electron gas as a function of gate voltage	60
3-3	Conductance versus gate-voltage of a small electron gas	63

3-4	Periodic peaks in the conductance of a small electron gas as a function of gate voltage	64
3-5	The gate-voltage of consecutive conductance peaks as a function of peak number	65
3-6	Conductance versus gate-voltage of a small electron gas on a semi-logarithmic scale	66
3-7	Charge as a function of gate-voltage in a small electron gas system . .	68
3-8	Current flow through a small electron gas in term of single electron tunneling	69
3-9	Single electron charging and the origin of periodic conductance peaks	71
3-10	Tunneling diagram representation of single electron charging	72
3-11	Figure 1 of 3 showing the charge state of a small electron gas as V_g is cycled through one period of the conductance oscillations	75
3-12	Figure 2 of 3 showing the charge state of a small electron gas as V_g is Cycled through one period of the conductance oscillations	76
3-13	Figure 3 of 3 showing the charge state of a small electron gas as V_g is cycled through one period of the conductance oscillation	77
3-14	The measurement configuration for large-bias current-voltage measurements at fixed V_g	80
3-15	Coulomb blockade staircase	81
3-16	$I-V_{ds}$ Data showing the coulomb blockade suppression of current about zero-bias.	82
3-17	Figure 1 of 2 showing the mechanism that gives rise to the Coulomb-blockade staircase	83
3-18	Figure 2 of 2 showing the the mechanism that gives rise to the Coulomb-blockade staircase	84
3-19	Calculated $I-V_{ds}$ showing the coulomb blockade staircase	88

3-20	Calculated I - V_{ds} showing the coulomb suppression of current in the neighborhood of $V_{ds} = 0$ for asymmetric barriers.	89
3-21	Calculated I - V_{ds} showing the coulomb suppression of current in the neighborhood of $V_{ds} = 0$ for symmetric barriers.	90
3-22	A representation of a device showing its relevant capacitances	91
4-1	Introduction to the discrete level spectrum in a small electron gas . .	98
4-2	Current-voltage characteristics in the presence of a discrete level spectrum	99
4-3	I versus V_{ds}	100
4-4	$\log(I)$ versus V_{ds}	101
4-5	dI/dV_{ds} as a function of V_{ds} for $B = 3.35$ T	102
4-6	The level spectrum of a small electron gas as a function of V_g	103
4-7	The level spectrum determined from dI/dV_{ds} versus V_{ds} plotted in Figure 4-5	105
4-8	I versus V_g for finite V_{ds} calculated in the classical model for the case of symmetric barriers	107
4-9	I versus V_g for finite V_{ds} calculated in the classical model for nonsymmetric barriers, case I	108
4-10	I versus V_g for finite V_{ds} calculated in the classical model for nonsymmetric barriers, case II	109
4-11	The current, I as a function of gate voltage, V_g for drain-source biases, V_{ds} , ranging from $50 \mu\text{V}$ to $500 \mu\text{V}$ in increments of $25 \mu\text{V}$	110
4-12	I versus V_g for $V_{ds} = 0.5 \text{ mV}$ and $B = 2.53 \text{ T}$	111
4-13	I versus V_g at finite V_{ds} calculated in the discrete level model	112
4-14	The temperature evolution of conductance peaks	115
4-15	The temperature behavior of the conductance peak at $V_g = -0.6593 \text{ mV}$ in Figure 4-14	116

4-16	The temperature behavior of the conductance peak at $V_g = -0.6548$ mV in Figure 4-14	117
4-17	The temperature behavior of the conductance peak at $V_g = -0.6503$ mV in Figure 4-14	118
4-18	The temperature behavior of the conductance peak at $V_g = -0.6457$ mV in Figure 4-14	119
4-19	The temperature behavior of the conductance peak at $V_g = -0.6413$ mV in Figure 4-14	120
4-20	The Temperature behavior of the conductance peak at $V_g = -0.6367$ mV in Figure 4-14	121
4-21	Peak amplitude at 1 K versus peak position	122
4-22	The full-width at half-maximum of the conductance peak at $V_g \approx$ -0.6453 mV from Figure 4-14 as a function of T	123
4-23	An expanded view of a single conductance peak on a semilogarithmic scale	124
4-24	A representation of the single level case considered in the text	126
4-25	A representation of the classical case considered in the text	128
4-26	A conductance peak fit to the resonant tunneling lineshape	132
5-1	The evolution of conductance peaks in low magnetic fields	135
5-2	Peak gate-voltage and amplitude as a function of B	136
5-3	Peak position and amplitude as a function of B in the quantum Hall regime	138
5-4	Conductance peak temperature dependence as a function of B	139
5-5	Peak position as a function of B for consecutive conductance peaks .	140
5-6	G as a function of gate-voltage in zero and finite B	141
5-7	Electrons in a harmonic confinement potential	144
5-8	The self-consistent model in the quantum Hall regime	146

5-9	Comparison of the self-consistent model with experiment	150
5-10	Peak position versus B for successive peaks calculated in the self-consistent model	153
5-11	Peak position versus B over a wide range in B	154
6-1	G versus V_g showing the quenching of the Coulomb Blockade	157
6-2	Mechanism of the Quenching of the Coulomb Blockade	161
7-1	A Composite View of the Hall resistance and the longitudinal resistance of a 2-DEG	172
A-1	A Metallization Geometry with a Longitudinal Accumulation Gate	176
A-2	A Metallization Geometry with a Transverse Accumulation Gate	177
A-3	A Metallization Geometry for Coupling Between Adjacent Electron Gases Using a Floating Gate	178
A-4	A Metallization Geometry for Small Electron Gases in Series	179
A-5	A Metallization Geometry for Small Electron Gases in Parallel	180
B-1	Heterostructure #111488C	182
B-2	Heterostructure #113088B	182
B-3	Heterostructure #010389B	183
B-4	Heterostructure #010588	183
E-1	The Low-Noise Current-to-Voltage Amplifier	196
H-1	The Longitudinal and Hall Resistance of a GaAs 2-DEG	210
H-2	The Noninteracting Level Spectrum in a 2-D harmonic oscillator as a function of B	212
H-3	The Noninteracting Level Spectrum in a 2-D harmonic oscillator as a function of B at low fields	213

List of Tables

2.1	The Electronic Properties of GaAs(100) 2-DEG	51
3.1	The measured values of the capacitances in Figure 3-22	92

Preface:

Electrons are Green

Once a year a special day is set aside at the Boston Museum of Science for what is known as “Science is Fun Day”. Two years ago, I was one of a dozen or so graduate students recruited for the occasion. We were to present five minute explanations of our research to a group of “enthusiastic and interested young scientists” from elementary schools around the Boston area. When I arrived at the museum, the director of the day’s activities informed me that my talk had been canceled. It was deemed too technical (too far removed from daily life), probably because its title contained the word “transistor.” I was told that I had been rescheduled to give another talk called “The History of the Steam Engine.” The talk was to include a demonstration of the museum’s fully operational steam engine. I think the assumption was made that as an M.I.T. student I would be familiar with the operation of a seven ton, turn-of-the-century steam engine. Fortunately, before going into the limelight I was able to buttonhole a member of the museum cleaning staff. Though we did not speak a common language, I communicated to him my dilemma and he directed me towards some valves near the engine.

About two hundred kids were assembled. I was introduced as a scientist from M.I.T.. I walked up to the engine and knowingly turned two valves, and the engine’s fifteen foot fly wheel began to turn. The audience applauded, the director looked

happy, and the M.I.T. aura was impressed on another generation.

Four minutes and thirty seconds to go. I proceeded to give an talk on the history of the steam engine, based extensively on the placard found in front of the exhibit. I then opened the floor for questions. The audience showed a level of enthusiasm commensurate with what is to be expected from children who have been transported to a museum on a Saturday morning. After answering one question (and realizing that no more would be forthcoming), I turned to the director and asked if we had time for any more questions. She missed her cue: “Oh, don’t worry about time, Ethan. You still have twenty-five minutes left.” At that point, I had no recourse but to talk about my research.

For a long time, I have had a sense that, no more than one need be a musician to enjoy music, does one need to be a scientist to be intrigued by science: Perhaps if the beauty of science is lost to those outside the field, it is not because the tune is bad, but because scientists often play it a little off key. It seems to me that if you cannot explain your research to the non-specialist so as to make it interesting, then this is probably because the explanation is uninteresting, the research is uninteresting, or the researcher is uninteresting. Well, for me, theory confronted reality in front of two hundred elementary school children. Here is a condensed version of the explanation of my thesis work, first heard on “Science is Fun Day.”

“Imagine water flowing through a straw. Now imagine water flowing through a large pipe. In both cases, you probably imagined the same picture except for the size of the tube carrying the water, and that’s correct. Water running through a tiny straw behaves about the same as water running through a large pipe. If you can picture one, then all you have to do is to scale up or down to picture the other. This scaling idea is the same thing that engineers do when they build a small model of an airplane and then test it in a wind tunnel. They do not have to build a full size airplane before the design can be tested; they just scale the behavior of the model in the wind tunnel.

“Now let’s think about electricity. When you turn on a light switch, it’s like opening a valve which lets electrons flow through the wires. When electrons reach the filament in a light bulb they make the filament heat up and glow, which is why the lights come on.

“Now picture a really big wire, like the kind that carries power from a power plant to a city. Electrons travel through it just like they travel through the smaller wires in your home. Like with water, the picture of electrons flowing through a large wire is the same as for electrons flowing through a small wire. This is how people understand electrons flowing through a wire.

“Here’s where things get a little different. Imagine making the wire smaller and smaller. You might think that you can keep on scaling the picture in your mind to imagine this smaller and smaller wire. But there’s one thing we haven’t thought about yet — you can change the size of a wire, but you can’t change the size of the electrons. Sooner or later, if you make the wire small enough, the size of a single electron will be pretty big compared with the size of the wire. At that point, our ideas about scaling aren’t going to work anymore.

“Actually making a wire this small is pretty hard, but in the past couple of years people have figured out how to do it. This has happened mostly because, as people have tried to make computers faster and smaller, the wires they use have gotten smaller and smaller. So finally people started making wires that really are small compared to the size of a single electron. In fact, just a few years ago, people started making wires so small that electrons had to line up in single file to get through them.

“At M. I. T., I’ve been part of an experiment using these small wires. What we do is take a really small wire and pinch it off at two nearby places along the wire. What you’re left with is a section of wire with electrons in it that is isolated from the other parts of the wire. [At this point in the talk, I used a marker board to get the idea across.] In our experiments this little section of wire is so small that it only holds about 50 electrons. Remember, just a single atom of gold has more electrons

than that.

“We can change the size of this small, pinched-off section of wire so that we can isolate any number of electrons that we want. In other words, if there are fifty electrons trapped in this section of wire, we can make it just a little bigger so that there are fifty-one electrons in it. So we can add or subtract electrons from this tiny region one at a time.

“Another way you can think about this is to imagine that we are making a very small box into which we put a small number of electrons. (The box is just the pinched off section of wire.) [Again I used the marker board.] So the system that we are studying can be described as a small box of electrons, and what we do is look at how the electrons bounce off each other and off the walls of the box. Then we can look, for example, at what happens when we change the temperature inside the box, or place the box near a magnet.

“Let’s think about this: Up until now, the only system that could hold such a small number of electrons in such a small space was an atom. Now, with our tiny box of electrons, we can do something that, until now, could only be done by mother nature.”

At that point, I thought that, even if they were not interested in my work, I could at least say that some kids now understood something about what I did in the lab.

Several weeks later, I learned from one of the teachers who had been present that the students in her class had written essays about the talks they had heard on “Science is Fun Day.” Apparently my talk was remembered by a number of the kids. When I had used the marker board to draw a picture of a box with electrons in it, I drew the electrons with a green pen. The teacher informed that my talk made one lasting impression on her class: Electrons are green.

Chapter 1

Introduction

Much of solid state physics is an effort to understand the behavior of electrons in the potential of a large array of atomic nuclei. This field, in a sense, is a natural outgrowth of atomic physics, which considers electrons in the potential of a single atom. In both cases it can be said somewhat metaphorically that nature has decided upon a particular potential in which to place electrons and that we are left to observe how these systems behave. It is possible, however, to ask how electrons might behave if placed in a different potential, one that can not be found in nature. In actuality, for most people who approach these sorts of questions the line of inquiry is reversed. Almost universally, an introduction to quantum mechanics first considers particles confined to physically unrealizable, though mathematically tractable potentials. Only later are Hamiltonians more representative of actual physical systems considered. In short, on paper we are used to prescribing the potential in which particles operate while understanding that in practice a similar freedom does not exist. That is, not until very recently.

In recent years the confluence of many disparate technologies has made it possible to build structures that confine electrons in what are largely man-made, or artificial potentials[1, 2]. Semiconducting nanostructures have, to date, been the most exper-

imentally fruitful systems for creating artificial confining potentials[3, 4, 5, 6, 7, 8, 9, 10]. Among these structures, GaAs/AlGaAs heterostructures have emerged as a model system for creating artificial potentials[11]. In these structures electrons are confined at the interface between GaAs and AlGaAs. Normally in three dimensions, electronic states can be labeled with three continuous spatial quantum numbers, k_x , k_y , and k_z . The electrons confined in suitably constructed GaAs/AlGaAs heterostructures are confined strongly enough in the direction perpendicular to the interface plane (usually denoted by z) that k_z for all electrons present corresponds to occupation of only the lowest subband mode in the z direction ($k_z = \pi/L_z$, $\hbar^2 k_z^2/2m^* \sim 0.1\text{ eV}$). Consequently, motion in the z direction is frozen out and electrons accumulated at the heterointerface are dynamically two-dimensional. As such, these electrons compose what is referred to as a two-dimensional electron gas (2-DEG).

In addition to reduced dimensionality, GaAs 2-DEG systems present a number of other interesting properties. They have low electron densities that can readily be varied by moderate electric fields. These low densities result in a Fermi wavelength ($\lambda_F \sim 40\text{ nm}$) that is much larger than that in metals, and in fact is comparable with the dimensions of features that can be fabricated with standard semiconductor processing techniques. The electron mean free path in high mobility samples can exceed $10\mu\text{m}$. The 2-D Fermi surface is nearly circular which simplifies analysis and the effective in-plane electron mass is $m^* = 0.067 m_o$ which generally increase the magnitude of quantum effects in the 2-DEG.

GaAs 2-DEGs have been the focus of intensive research over the past dozen years or so. Excellent reviews of the field can be found in Refs. [3, 4, 12]. A partial list of just some of the phenomena seen in these systems includes the integer quantum hall effect [13], the fractional quantum hall effect[14], weak localization[15, 16, 17, 18, 19], universal conductance fluctuations [20, 21, 22], the Aharonov-Bohm effect in connected geometries[23, 24, 25, 26, 27], 2-DEG lateral superlattice effects[28, 29, 30, 31, 32], guiding-center drift resonances[33, 34], and edge state equilibration and

non-local resistances[35, 36, 37].

A one-dimensional electron gas is realizable from a 2-DEG by constricting the lateral extent of a 2-DEG to form a channel of width of order λ_F . In 1988 the first measurements of such systems revealed that the conductance of a 1-DEG is exactly e^2/h ($1/(25813 \Omega)$)[38, 39]. This striking result is well described by the Landauer-Buttiker formalism[40, 41] which relates conductance and quantum mechanical transmission probabilities[40, 42]. Current injected from a 1-DEG into a 2-DEG has also proven to be an interesting system in which to study ballistic transport phenomena such as coherent electron focusing[43, 44], junction scattering[45, 46], and electrostatic[47, 48] and magnetic[43, 49] focusing.

The above attempts to touch on some of the most interesting results from the investigation of two-dimensional and one-dimensional electron systems. The next question is clear: Is it possible to fabricate and study a zero-dimensional electron gas. In other words, is it possible to fabricate an artificial potential that confines electrons strongly enough so that excitations (in all three dimensions) are not continuous but rather discrete, and is it then possible to probe this system? The answer is yes, and in fact this thesis reports our most recent measurements of a zero-dimensional electron gas[50, 51, 52].

This work was motivated by some of the first successful attempts to study zero-dimensional electron gases. Several approaches were taken towards the fabrication of such systems but in each case the starting point was a semiconductor 2-DEG. The trick was limiting the in-plane extent of the 2-DEG on a sub-micron scale. One method involves etching away all except a small portion of the macroscopic 2-DEG[53, 54]. The remaining section of 2-DEG forms a post and electrical contact is made to the top and bottom of the post. Electron transport is measured as electrons move between the contacts via tunneling to and from the remaining small area of 2-DEG which is so small that it is now a 0-DEG. Such structures are referred to as vertical structures because because the plane of the original 2-DEG is by convention taken to

be horizontal. The most successful structures built along these lines have employed a shallow-mesa etch which removes only a thin layer of heterostructure[55, 56]. The electron gas is depleted under the etch regions, and since the etch does not penetrate the 2-DEG heterointerface, no surface states are created[57].

A second approach to confining electrons entails not etching away peripheral 2-DEG as in vertical devices but rather depleting electrons by means of a gate electrode[58, 59]. (In silicon devices, the reverse is true and gates are usually used to accumulate electrons.) A negatively biased electrode ($\sim -0.6\text{ V}$) patterned on the surface of a GaAs heterostructure will fully deplete the 2-DEG underneath it. So by patterning electrodes a small region of zero-dimensional electron gas can be isolated from macroscopic regions of 2-DEG. Electrical contact is made to the resulting small electron gas by patterning the electrodes to create tunnel barriers from the 0-DEG to macroscopic 2-DEG on opposite sides of the 0-DEG.

The first observation of a 0-DEG in planar devices was made serendipitously by J. H. F. Scott-Thomas, *et al.* in the course of investigating disordered narrow channels in narrow-gate silicon MOSFETs[60]. Most likely, either individual impurities or fluctuations in the impurity potential along the narrow channel created tunnel barriers that isolated a small section of electron gas. The conductance of the narrow channel was then studied as a function of electron density in the gas. A completely unexpected result was seen: The conductance of the channel exhibited a series of nearly periodic peaks as a function of electron density. Similar behavior was later seen in disordered GaAs heterostructures[61, 62].

In order to further examine this behavior, U. Meirav, *et al.* constructed a similar device in a GaAs heterostructure with the important difference that a section of electron gas was isolated by lithographically patterned barriers rather than by disorder[63]. The period of the conductance oscillations was shown to increase as the size of the isolated electron gas was decreased. H. van Houten and C. W. J. Beenakker[64] pointed out that this behavior was consistent with a semi-classical model of single

electron charging[65]. Roughly speaking, in this model, sometimes referred to as the Coulomb blockade model[66], conductance peaks are observed when the amount of charge on the isolated electron gas that is electrostatically most favorable is a half-integer multiple of electron charges, *i.e.* $e(N + \frac{1}{2})$. Under these conditions the charge state of the electron gas is energetically free to fluctuate between N and $N + 1$ electrons. In other words, there is no electrostatic barrier to electrons tunneling on and off of the isolated electron gas, and therefore a large conductance is measured.

While the Coulomb blockade model successfully explained much of the observed behavior, several shortcomings of the simple charging model were clear from the outset[63]. In particular, the Coulomb blockade model could not account for the observed temperature behavior of the conductance peaks, nor for the slight deviations from exact periodicity seen in the peak position. In order to resolve these and other shortcomings the Coulomb blockade model was extended to incorporate a discrete set of quantum mechanical levels in the isolated electron gas[67, 68]. This was done by assuming that electrons on the isolated electron gas behaved as noninteracting Fermions and as such occupied a set of discrete energy levels, while electron-electron interactions were still described in terms of classical electrostatic charging. With a few reasonable assumptions made about the non-interacting level spectrum of the isolated electron gas, these models accurately described the temperature behavior and deviations from periodicity of the peaks. Consequently, a terminology describing conductance in these systems arose that distinguished between charging effects and quantum effects. It is understood now that this is a somewhat artificial distinction and that electron-electron interactions play a much more subtle role than what can be described by single electron charging[51]. However, this nomenclature persists in the field and is employed in the title of this thesis.

A number of research efforts have been made towards understanding the interplay of single-electron charging and quantum effects in 0-DEG systems. Among the experimental techniques employed are transport measurements[69, 52, 70], as dis-

cussed above, optical spectroscopy[71, 72], and capacitance measurements[73, 74]. Recent reviews of the field can be found in References [75, 76]. The work in this field has also attracted the attention of the popular press, in part because of the novelty of creating structures that manipulate single electrons and in part because of the prospect that this work may lead to the development of innovative devices for use in the semiconductor industry. A sampling of these releases includes reports in *The New York Times*[77], *The Economist*[78], *Science*[79], *Scientific American*[80], *The World & I*[81], *The Cleveland Plain Dealer*[82], *Encyclopedia Britannica*[83], *Byte Magazine*[84] and *Time*[85]. As for the prospect for future device technologies, some have cautioned against extrapolating too far afield[86], whereas optimistic scenarios envision entire computer architectures based on arrays of artificial structures[87].

The goal in writing this thesis is two-fold. First, we aim to give a self-contained overview of the research that we have complete over the past four years. Second, it is hoped that in the process of writing, old ideas might be recast in new terms that may stimulate future insights. Chapter 2 describes the zero-dimensional electron gas system that we have studied and gives a description of our experimental techniques. In Chapter 3, we present conductance measurements of the small electron gas system and show how a very simple model of single electron charging accounts for many of our observations. In Chapter 4 we present additional observations that reveal the interplay of single electron charging and quantum effects. In Chapter 5, we discuss magnetic field measurements which extend the ideas presented in Chapter 4, and finally, in Chapter 6 we discuss our preliminary studies of what will be referred to as the quenching of the Coulomb blockade.

Chapter 2

The Zero-Dimensional Electron Gas System

The aim of this chapter is to describe the zero-dimensional electron gas systems that we have studied. In Section 2.1 the fabrication of these systems is discussed. Section 2.2 covers the preliminary characterization of these structures and continues the discussion of Section 2.1 in more quantitative terms. Finally, in Section 2.3 the energy scales relevant to the electron gas are considered and the experimental apparatus required to probe the gas at these energies is discussed.

2.1 Device Fabrication

Conceptually, the fabrication of the devices that we studied proceeded as follows: First, a heterostructure of GaAs and AlGaAs was grown by molecular beam epitaxy (MBE) on a GaAs substrate such that a two-dimensional electron gas (2-DEG) was established at the interface between heterolayers. Next, metal gates were patterned on the surface of the structure such that the 2-DEG could be patterned by applying voltages to the gates. The geometry of the gates allowed us to pattern a small region of

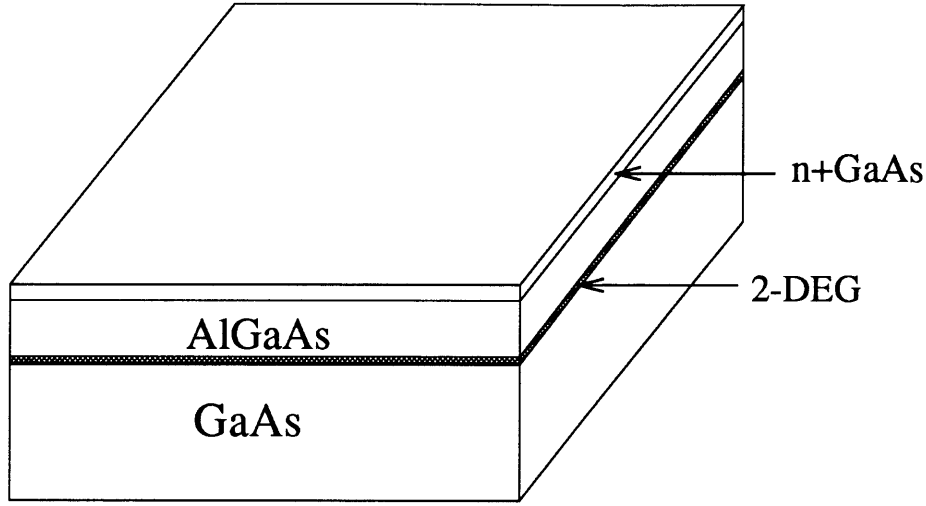


Fig. 2-1. A conventional GaAs/ $\text{Al}_x\text{Ga}_{1-x}\text{As}$ heterostructure. A 2-DEG inversion layer accumulates at the interface between the AlGaAs and undoped GaAs layers.

2-DEG, roughly $0.3 \times 0.3 \mu\text{m}^2$ in area, that is separated from two macroscopic regions of 2-DEG. The separation distance is roughly $\sim 0.1 \mu\text{m}$ which is small enough to allow electrons to tunnel between the macroscopic 2-DEGs and the small electron gas. In this way, the macroscopic 2-DEGs are used as electrical leads to probe the small electron gas. Finally, electrical contact is made from the large-area 2-DEGs to the measurement instrumentation.

2.1.1 GaAs/AlGaAs Heterostructures

A typical GaAs/AlGaAs heterostructure is shown schematically in Fig. 2-1. This structure consists of an undoped (100) GaAs substrate on top of which is deposited a doped layer of AlGaAs followed by a cap layer of n -type GaAs. Such structures are referred to as heterostructures because they are built from two types of semiconducting material, in this case GaAs and $\text{Al}_x\text{Ga}_{1-x}\text{As}$ ($x \approx 0.35$). The lattice constants of GaAs (5.65 \AA) and of AlGaAs (5.66 \AA) are nearly the same which makes it possible to construct a strain-free, lattice-matched interface between GaAs and AlGaAs with good electrical properties[88].

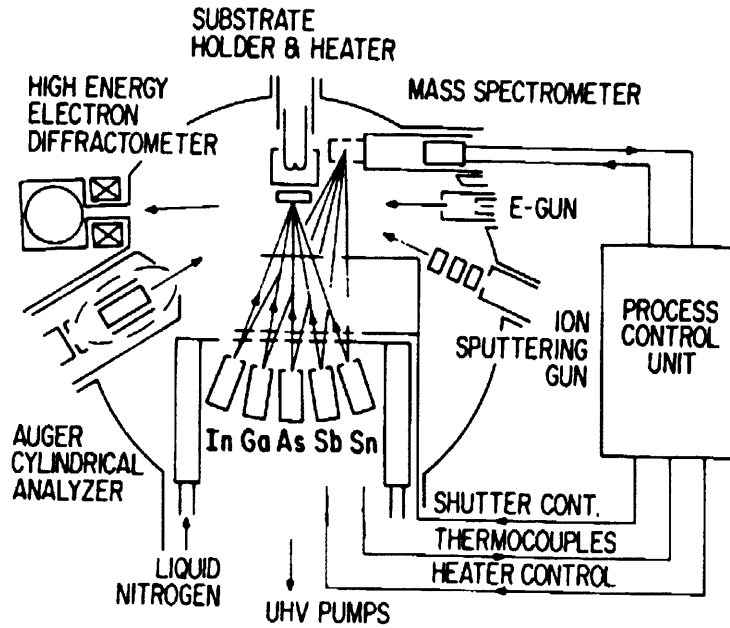


Fig. 2-2. MBE Schematic from Reference [90]. Molecular beam epitaxy is used to fabricate $\text{GaAs}/\text{Al}_x\text{Ga}_{1-x}\text{As}$ heterostructures such as the one represented in 2-1.

The technique for fabricating such structures is referred to as molecular beam epitaxy (MBE)[89]. This is a process in which several atomic (or molecular) beams impinge on a heated substrate, in this case GaAs heated to $\sim 600^\circ\text{C}$, under ultrahigh vacuum conditions ($P \approx 10^{-9}$ torr). Figure 2-2 shows a schematic of a typical MBE system[90]. Atomic beams emanate at thermal velocities from effusion cells which contain ultrahigh purity sources. Under typical conditions, As is heated to $\sim 450^\circ\text{C}$, Ga to $\sim 970^\circ\text{C}$ and Al to $\sim 1100^\circ\text{C}$. The impinging atoms adsorb on the substrate surface and form crystalline monolayers in registry with the substrate lattice (epitaxial growth). Growth rates are typically between 1 to 5 Å/sec and are monitored by reflection high energy electron diffraction (RHEED).

In order to accumulate a 2-DEG, Si donors are incorporated into the AlGaAs layer during growth. The band gap of $\text{Al}_x\text{Ga}_{1-x}\text{As}$ (1.75 eV @ $x \approx 0.3$) is larger than the band gap of GaAs (1.41 eV). At equilibrium, electrons from the ionized donors in $\text{Al}_x\text{Ga}_{1-x}\text{As}$ reside in the smaller band gap GaAs in an inversion layer at the

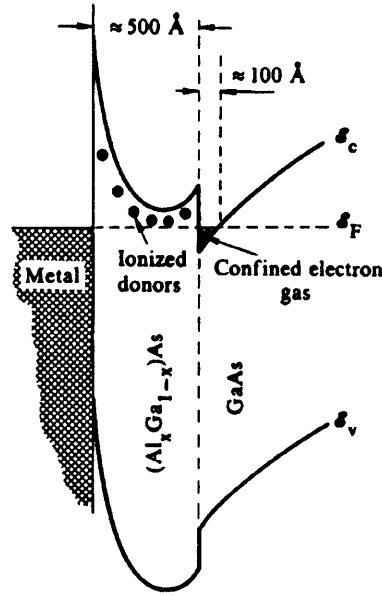


Fig. 2-3. The band diagram of a GaAs/ $\text{Al}_x\text{Ga}_{1-x}\text{As}$ heterostructure from Reference [92]. The energy and distance scales are approximate for $x = 0.35$. Notice that the $\text{Al}_x\text{Ga}_{1-x}\text{As}$ bands bend upward at the GaAs/ $\text{Al}_x\text{Ga}_{1-x}\text{As}$ interface since the last ~ 10 nm of $\text{Al}_x\text{Ga}_{1-x}\text{As}$ adjacent to the interface is not doped[93].

GaAs/ $\text{Al}_x\text{Ga}_{1-x}\text{As}$ interface as indicated in the band diagram in Fig. 2-3. A typical sheet density of carriers in the inversion layer is $\sim 3 \times 10^{15} \text{cm}^{-2}$. The self-consistent confining potential in the inversion layer confines carriers strongly enough in the direction perpendicular to the interface that in this direction all carriers are in the ground state[91]. The first excited state in this direction is $\sim 150 \text{meV}$ above the ground state. Since this energy is significantly larger than both the typical two-dimensional Fermi energy (15 meV) and kT at measurement temperatures ($\leq 100 \mu\text{eV}$) the probability for excitations of the electron gas in the direction perpendicular to the interface can be vanishingly small. Therefore, the inversion layer electron gas is dynamically two-dimensional. Magnetoresistance measurements confirm that the Fermi surface in a (100) GaAs/ $\text{Al}_x\text{Ga}_{1-x}\text{As}$ 2-DEG is nearly circular with no spin-orbital splitting[91].

The 2-DEG electron mobility at low temperatures is limited largely by ionized impurity scattering. One source of such impurities is contaminants in the MBE vac-

uum chamber, which is generally due to impurities in the effusion sources. These problems are minimized by paying extreme care to cleanliness when sealing the MBE chamber and when loading the chamber with growth substrates. Also, impurities in the effusion sources tend to effuse with the greatest flux when initially heated. Therefore, the longer a source has been in use the cleaner it is and generally the highest mobility samples are usually grown when an MBE system has been in operation for several months when the effusion sources are almost exhausted. Another source of electrically active impurities are defect states in the heterolattice. During growth such defects tend to migrate towards the growth surface and strained layers, *e. g.* layers doped with rare-earth impurities[94]. Several schemes have been employed to capitalize on these effects to move defects away from the inversion layer. A good review of some of these effects and in particular the nature a ubiquitous defect in GaAs heterostructures, DX centers, can be found in Reference [95][96][97].

Another source of ionized scattering centers is the dopants in the GaAs/ $\text{Al}_x\text{Ga}_{1-x}\text{As}$ layer. In order to minimize their negative effects on the inversion layer mobility usually $\text{Al}_x\text{Ga}_{1-x}\text{As}$ within the first $\sim 100 \text{ \AA}$ near the the heterointerface is not doped. (This accounts for the upward bend in the $\text{Al}_x\text{Ga}_{1-x}\text{As}$ bands near the heterointerface. See Figure 2-3.) This technique of varying the doping level in the GaAs/ $\text{Al}_x\text{Ga}_{1-x}\text{As}$ layer has by now been highly developed and is referred to as modulation doping. One other consideration, the mobility of a 2-DEG is generally larger at higher sheet density since ionized scattering centers are more strongly screened at higher densities. Inversion layers with electron mobilities of $\geq 10^6 \text{ cm}^2/\text{V} \cdot \text{sec}$ are now routinely prepared.

Lastly, it should be pointed out that the kind of GaAs/ $\text{Al}_x\text{Ga}_{1-x}\text{As}$ heterostructure discussed above is referred to by several names. These include high electron mobility transistor (HEMT), modulation doped field effect transistor (MODFET), selectively doped field effect transistor (SELFET) and transferred electron gas field effect transistor (TEGFET).

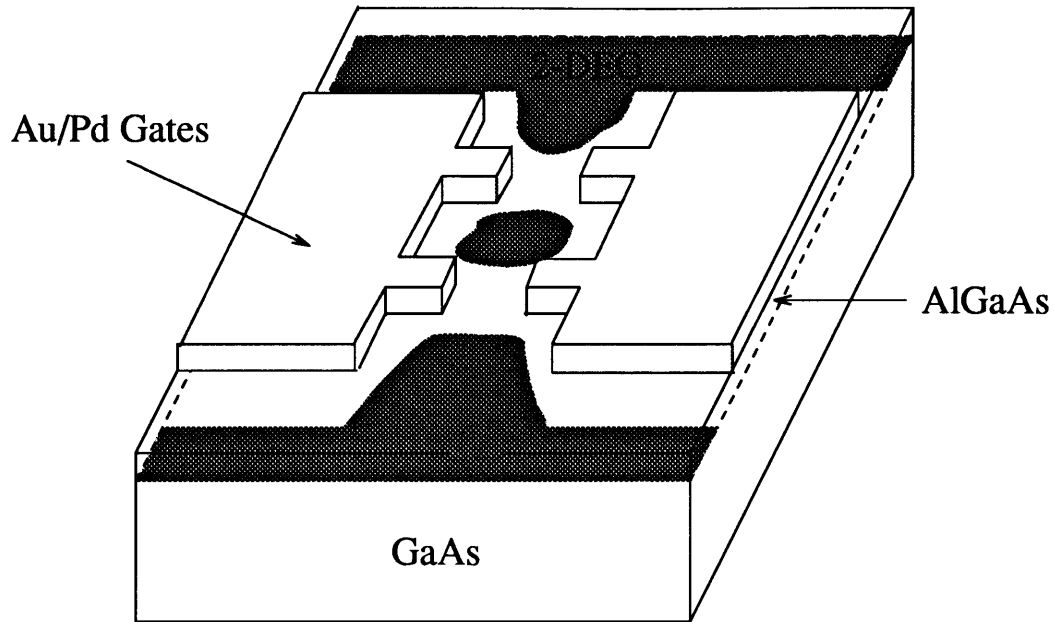


Fig. 2-4. A conventional GaAs/ $\text{Al}_x\text{Ga}_{1-x}\text{As}$ heterostructure with e -beam patterned electrodes. A negative bias applied to the electrodes depletes the 2-DEG and forms a small region of isolated electron gas.

2.1.2 Electron-beam Lithography

Figure 2-4 shows the same schematic of our device as in Fig. 2-1 except at a later processing stage once metal electrodes have been patterned on the surface of the heterostructure wafer. The electrodes, also referred to as gates, are patterned by first applying a layer of Plexiglas (polymethylmethacrylate, PMMA) on the surface of the wafer. In this state the PMMA polymer is highly cross-linked and resistant to chemical solvents. An electron-beam lithography machine exposes selected areas of the PMMA layer typically with a 25 keV, ~ 5 nA electron beam for a dosage of $100 \mu\text{C}/\text{cm}^2$. The exposure breaks the polymer crosslinks. Areas that have been exposed are therefore more susceptible to chemical etching and can be selectively removed. This process is referred to as the development etch. After development, metal is evaporated onto the wafer. The wafer is then placed in a stronger etch which removes all the remaining PMMA, leaving only the metal that was evaporated onto the uncovered areas of the wafer. This process is referred to as lift-off.

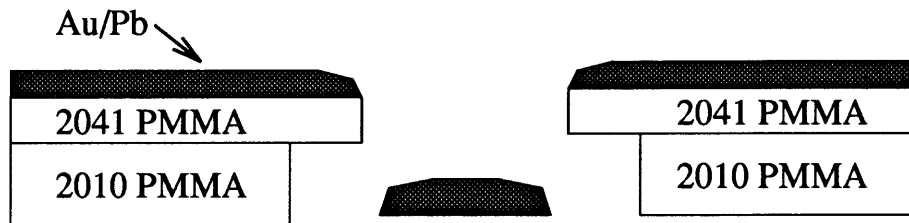


Fig. 2-5. The PMMA Bilayer used for e-beam lithography. The lower weight PMMA layer is more susceptible to the development etch. The resulting undercut facilitates lift-off.

The e-beam writer that was employed in our work is located at the IBM T. J. Watson Research Laboratory in Yorktown Heights, New York. The system was developed at IBM and includes a highly refined proximity correction algorithm that adjusts exposure levels to take into account electron scattering in the PMMA and GaAs layers. The most successful PMMA layer used was a bilayer of 700 Å of 2010 molecular weight PMMA followed by a second 350 Å layer of 2041 molecular weight PMMA. Lower molecular weight PMMA etches faster than higher molecular weight PMMA. So the development etch undercuts the unexposed PMMA layer facilitating lift-off. This is illustrated in Fig. 2-5. Notice that the metal layer can be at most roughly half as thick as the PMMA bilayer, otherwise the lift-off process will not work. When patterning 0.1 μm features PMMA material constraints limit the bilayer thickness to no more than ~ 1000 Å, which in turn limits the metal layer thickness to ≤ 500 Å. The metal layer that lifted-off with the best results was a bilayer of 200 Å of gold on 75 Å of palladium. Palladium acts as a sticking layer between GaAs and Au. Figures 2-6 and 2-7 show SEM micrographs of two different metallization patterns. Additional metallization schemes that have been fabricated but not yet studied are shown in Appendix A.

For reasons that will be made clear in Chapter 3 it is desirable that the isolated region of 2-DEG be as small as possible. In devices such as those shown in Figures 2-6 and 2-7 the limit on the device size is set not by the minimum feature size that is lithographically attainable (the IBM machine is capable of 0.02 μm feature sizes), but

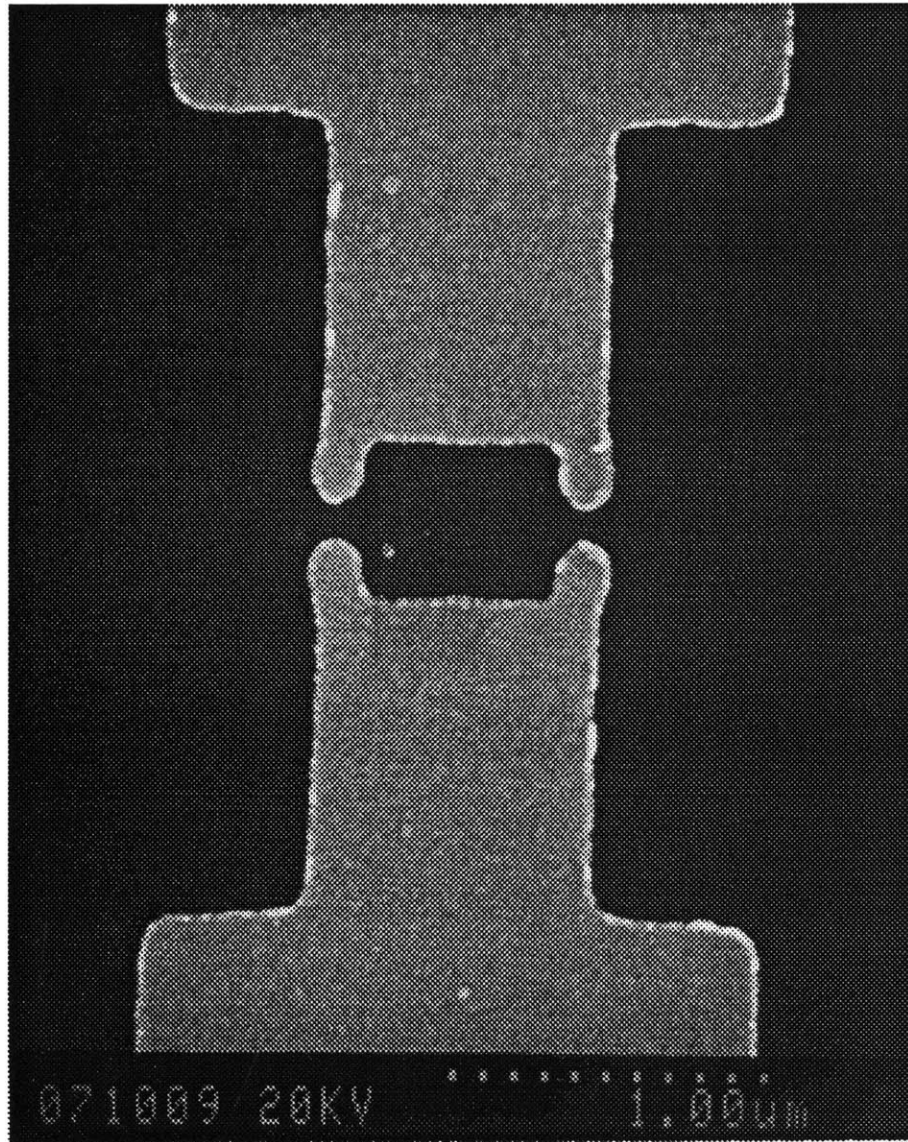


Fig. 2-6. An SEM micrograph of the e-beam patterned gate metallization in a typical device. The light regions are gold metallization. The dark regions are uncovered areas of heterostructure wafer. When the gates are biased negatively the 2-DEG is fully depleted underneath the gates and also in adjacent areas within $\sim 0.1\mu\text{m}$ of the gates. The 2-DEG between opposing tabs is depleted under typical biasing conditions ($\sim -0.5\text{ V}$). This creates an isolated region of 2-DEG in the center of the device between the two pairs of tabs. The regions of depleted 2-DEG between opposing tabs are sufficiently small that electrons can tunnel between the small, isolated region of 2-DEG and the macroscopic areas of 2-DEG.

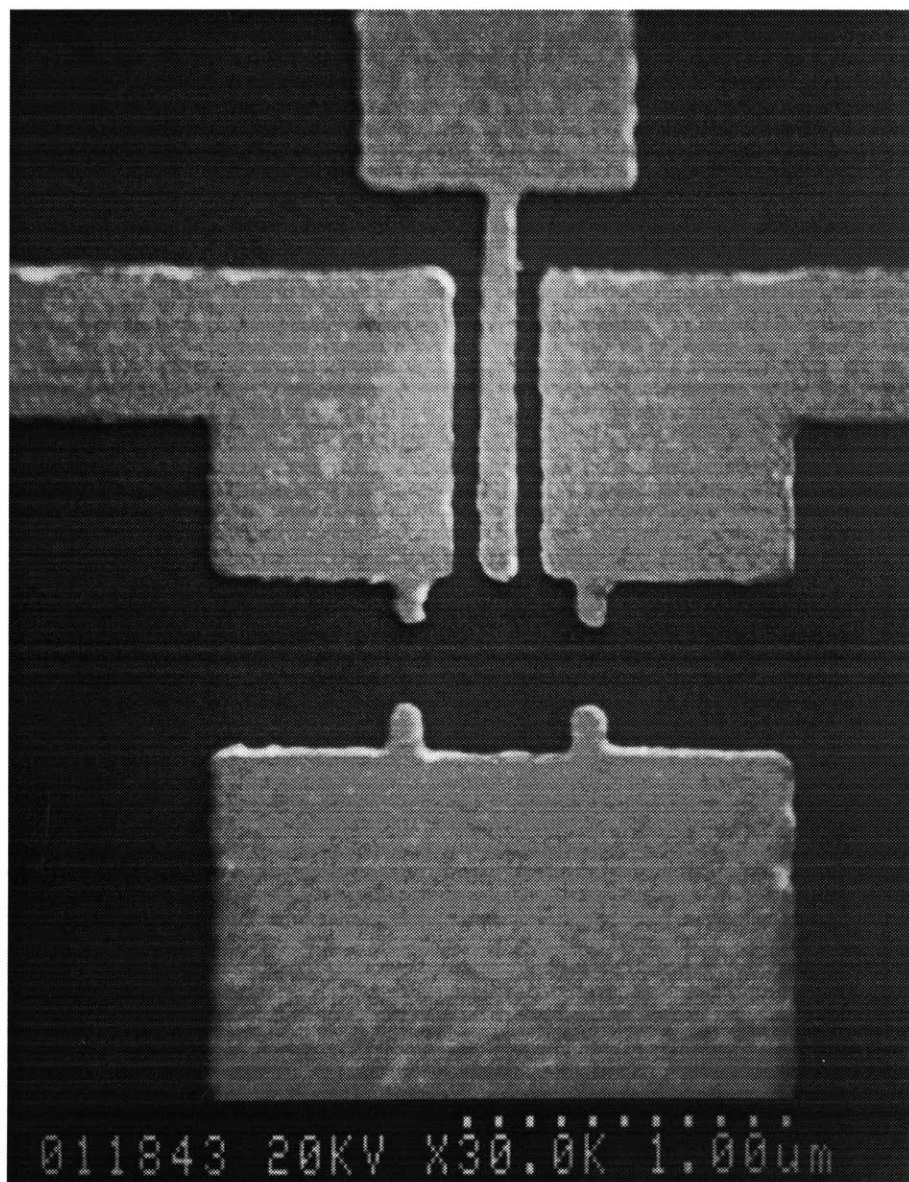


Fig. 2-7. An SEM micrograph similar to Fig. 2-6. This gate geometry allows for independent control of the tunnel barriers that isolate the small region of 2-DEG.

rather by the thickness of layers between the heterostructure 2-DEG and the wafer surface, which in our devices is $\sim 0.1 \mu\text{m}$. See Fig. 2-1 and Appendix B. This is because the potential induced in the plane of the 2-DEG by the gates can not vary on a length scale shorter than the spacer layer thickness. Related to this is the fact that under typical biasing conditions ($\sim -0.5 \text{ V}$) the depletion region extends roughly one spacer layer distance away from the edge of a gate as projected into the plane of the 2-DEG. This is illustrated in Fig. 2-14 on page 54 and has been confirmed by experiment, simulations and semi-analytic calculations.

Therefore the four tabs that define the small region of 2-DEG were patterned to extend out from the large gates by slightly more than one spacer layer distance, $0.15 \mu\text{m}$, and the spacing between opposing tabs was set at two times the spacer layer thickness. The combination of these two parameters fixed the length of the small 2-DEG to be 5 spacer layer thicknesses ($0.5 \mu\text{m}$). For similar reasons the width of the small 2-DEG needed to be roughly the same size, since if it were much smaller then the area between the tabs, it would be fully depleted and there would be no small region of 2-DEG.

GaAs heterostructures can be made with smaller spacer layers than those employed here. However, it is doubtful that this dimension can be reduced to much less than 500 nm [93]. In silicon devices analogous to GaAs MODFETs, a SiO_2 layer serves an equivalent role as the spacer layer in GaAs heterostructures. SiO_2 layers can be fabricated as small as 2 nm which holds the promise that significantly smaller devices may be fabricated using Si structures.

2.1.3 Layout and Ohmic Contacts

The two subsections above, which discuss the GaAs heterostructure and the e -beam metallization in a typical device, describe the essential elements that go into the fabrication of a zero-dimensional electron gas device. What remains to be discussed are how electrical contact is made to the macroscopic areas of 2-DEG adjacent to the

small, isolated region of electron gas, and the methods for laying out large numbers of devices on a single wafer of heterostructure. Figure 2-8 shows the layout of a typical “chiplet”. The chiplet covers an area of wafer $800 \times 800 \mu\text{m}^2$ and contains two devices. The devices are too small to see on the scale in Fig. 2-8 but it is clear that the devices are located in the two regions where the large-size metallizations converge. Figure 2-8 also shows ohmic contact metallizations. These are areas of metal that have been heat to diffuse into the heterostructure and make electrical contact with the 2-DEG which resides $\sim 1000 \text{ \AA}$ below the wafer surface. In Figure 2-8 the $10 \mu\text{m}$ wide trench that has been etched around the perimeter of the metallizations is also shown. The trench is roughly 2000 \AA deep and electrically isolates the 2-DEGs on each chiplet.

The metal used for the ohmic contacts was an alloy of germanium and gold. The ratio of constituents in the alloy is chosen to minimize the melting point of the alloy (a eutectic mixture). Au acts as a conductor and Ge degenerately dopes the underlying heterostructure. In addition, a small amount of nickel was included in the ohmic contact metallization since nickel acts as a diffusion enhancer in GaAs. The microscopic mechanism of this phenomena is not understood[98]. In practice, a multilayer metallization was evaporated on to the wafer and annealed into the wafer generally at 440°C for 20 seconds¹. A typical multilayer was composed of Ni (80 \AA), Ge (300 \AA), Au (600 \AA), Ni (120 \AA) and Au (1000 \AA)[99]. One additional point: care was taken to make sure that the ohmic contacts overlapped the isolation trench. If this were not the done, the ohmic contacts would be surrounded by 2-DEG (a condition referred to as a Corbinno geometry) and in high magnetic fields (the quantum Hall regime) electrical contact would be lost between the ohmic contacts and the 2-DEG.

¹ Making ohmic contacts is a tricky business. The optimal times and temperatures for annealing vary between annealing stations and heterostructure materials. Good contacts usually have room temperatures impedances of $\leq 25,000 \Omega$ and as the device is cooled the contact conductance should increase. At 4 K the contact resistance should drop to $\leq 10,000 \Omega$. Good contacts have resistances in the neighborhood of $\sim 1000 \Omega$. Sometimes contacts that seem fine at room temperature will have unacceptably large impedances at low temperature. This is sometimes a sign that the contacts have been over annealed.

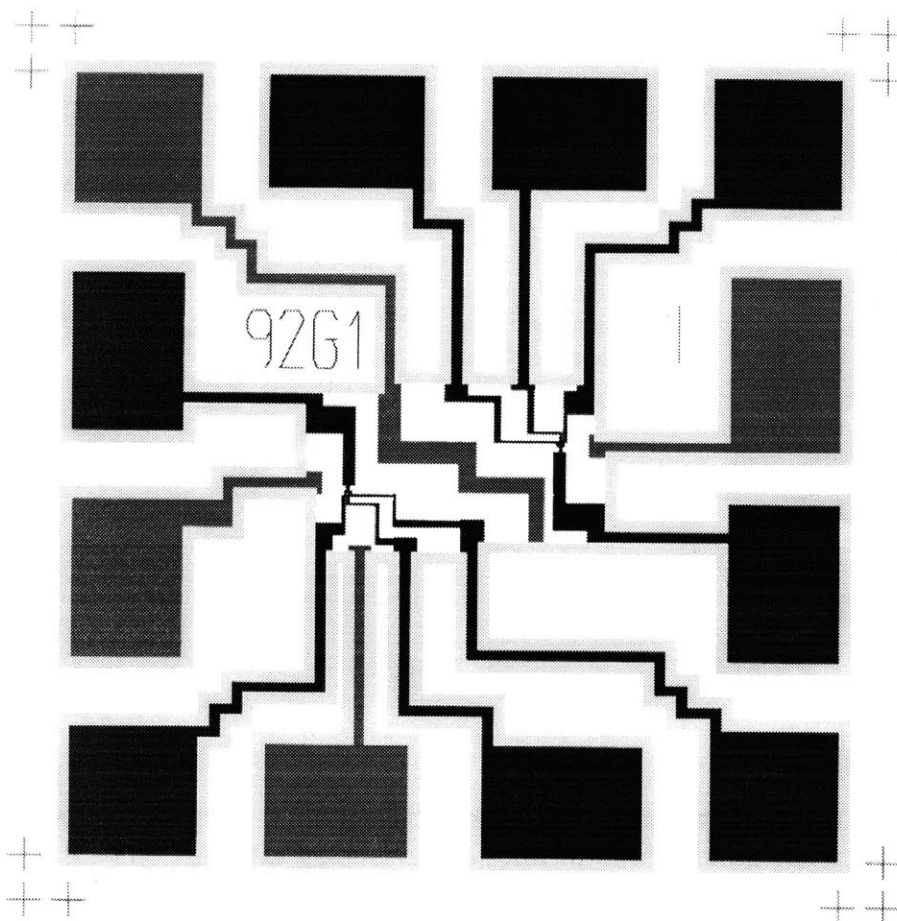


Fig. 2-8. A chiplet layout design. The chiplet covers an area of wafer $800 \times 800 \mu\text{m}^2$ and contains two devices. The darkest areas represent gate metallization. The next darkest areas represent ohmic contacts and the lightest features are the $10 \mu\text{m}$ wide isolation trench. (The ohmic contact pads are, beginning with the upper left pad and counting clock-wise, pads #1, #5, #9 and #11.) The devices are located at the region where the gates converge. Notice that the ohmic contacts overlap the isolation trench. The significance of this is discussed in the text. The cross-hairs in the corners of the chiplet are alignment marks for the IBM e-beam writer.

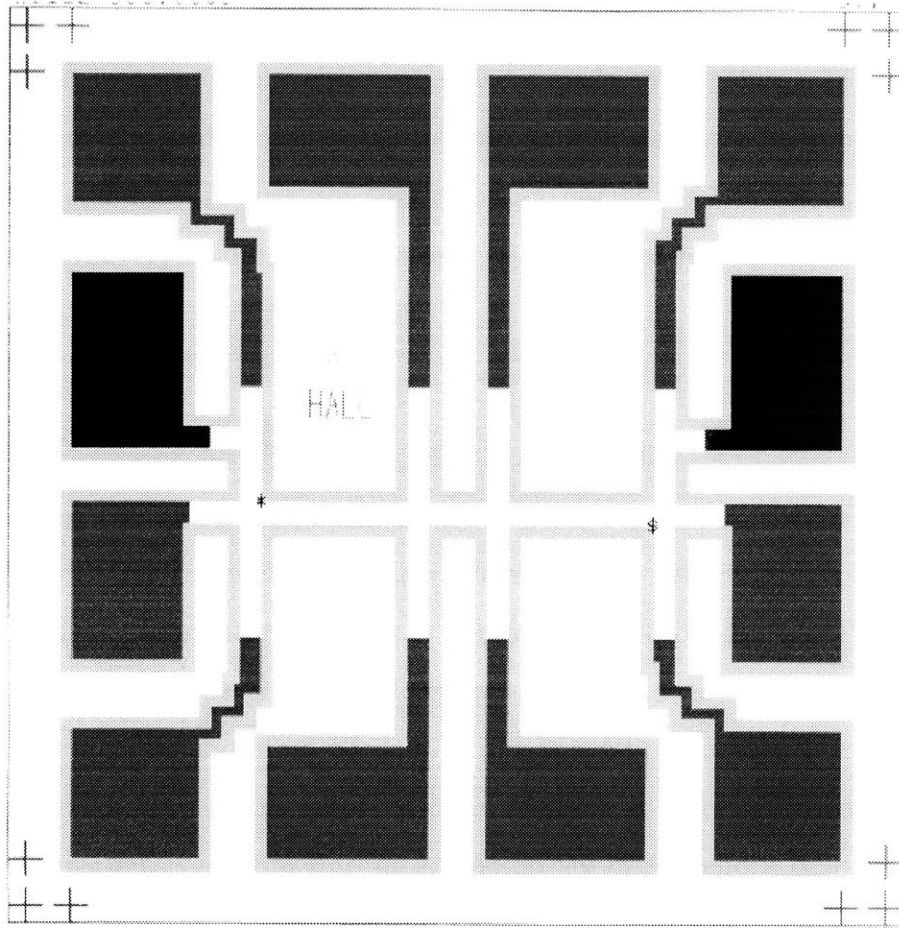


Fig. 2-9. Hall bar layout. This Hall bar is 21.5 squares long. The color key is the same as in 2-8. The Hall bar geometry is useful in determining the conductivity of the heterostructure 2-DEG.

For a discussion of this effect see Reference [100].

Multiple chiplets were patterned on a single wafer. A typical array of chiplets was in the neighborhood of 25 by 30 chiplets. In addition to chiplets as in Fig. 2-8 every fabrication run included Hall bars such the one represented in Fig. 2-9. Measuring the conductance between different probes on the on Hall bar geometry is useful in determining the conductivity of the 2-DEG. This is an important parameter when characterizing the devices. This point will be discussed in greater detail in Section 2.2.

After processing, wafers were diced and individual chiplets or pairs of chiplets were mounted on 24 pin, non-magnetic chip carriers. Chiplets were bonded with

silver paint to the chip carriers. Wire bonds from the chiplet bond pads (roughly $150 \times 120 \mu\text{m}^2$ in area) to the chip carrier were made with either gold or aluminum wires. In principle gold is preferable to aluminum because of its superior thermal conductivity and since it does not superconduct (Al: $T_c = 1.17 \text{ K}$, $H_c = 0.1 \text{ Tesla}$). In practice, however, no difference has been observed between using either Au or Al wire bonds.

2.1.4 Final Remarks

The preceding discussion aimed to convey a sense of some of the larger issues involved in fabricating small electron gas devices in GaAs heterostructures. A detailed description of the fabrication process is contained in Appendix C. This work was carried out at IBM Research lab in Yorktown Heights and in particular was greatly facilitated by our collaborators Shalom Wind and Udi Meirav. The MBE wafers were grown by another collaborator, Michael Melloch at Purdue University. Various heterostructures received from Purdue are described in Appendix B.

Finally, many of the results that will be discussed in the upcoming chapters are measurements conducted on a structure built by Udi Meirav. This structure is shown schematically in Fig. 2-10. Conceptually, it is very similar to the conventional device structure that was discussed above except that Meirav's device has a conducting back gate. (See Fig. 2-10.) The voltage on this back gate tunes the carrier density in the entire 2-DEG. A thorough discussion of this device is found in Udi Meirav's thesis and in his related publications[101, 102]. Unless indicated otherwise, the data presented in this thesis comes from such devices.

2.2 A Quantitative View of a Typical Device

In the above section, a typical device was described in largely qualitative terms. What follows is a discussion of a typical device in quantitative terms. In particular,

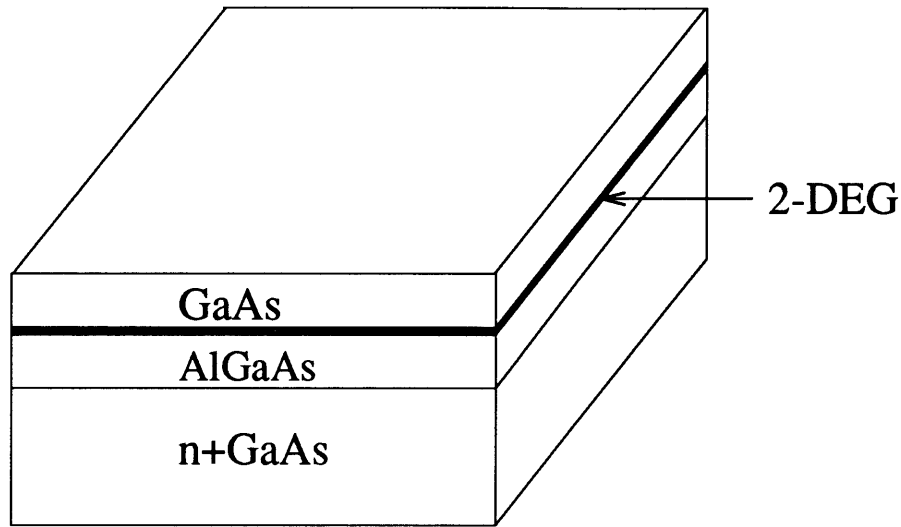


Fig. 2-10. The ISIS Structure of Meirav et al.[101]. This device was used for many of the measurements that will be discussed in upcoming chapters. Conceptually, it is similar to the conventional devices discussed in Sections 2.1.1 - 2.1.3 except for its semiconducting n +GaAs back gate. The voltage on the back gate tunes the carrier density in the entire 2-DEG[102].

Section 2.2.1 considers measurements of the conductivity and carrier density of the heterostructure 2-DEG and information relating to these parameters. In Section 2.2.2 the results of numerical simulations of related devices are discussed. From these authors' work we focus on several key results that are particularly useful in gaining an understanding of the structures that we have fabricated.

2.2.1 Electronic Properties of the 2-DEG

The conductivity of the bulk 2-DEG, σ , is determined from a four terminal measurement of the conductance along a Hall bar geometry such as that pictured in Fig. 2-9. Values of σ^{-1} generally fall in the neighborhood $5\text{ k}\Omega$. The 2-DEG sheet density, n_s , is determined by measuring the conductance along a Hall bar as a function of magnetic field. Figure 2-11 shows the results of such a measurement. Figure 2-12 shows the same data where conductance has been plotted versus the reciprocal of the magnetic field. It is seen here that the conductance is periodic in $1/B$. This is referred to as the

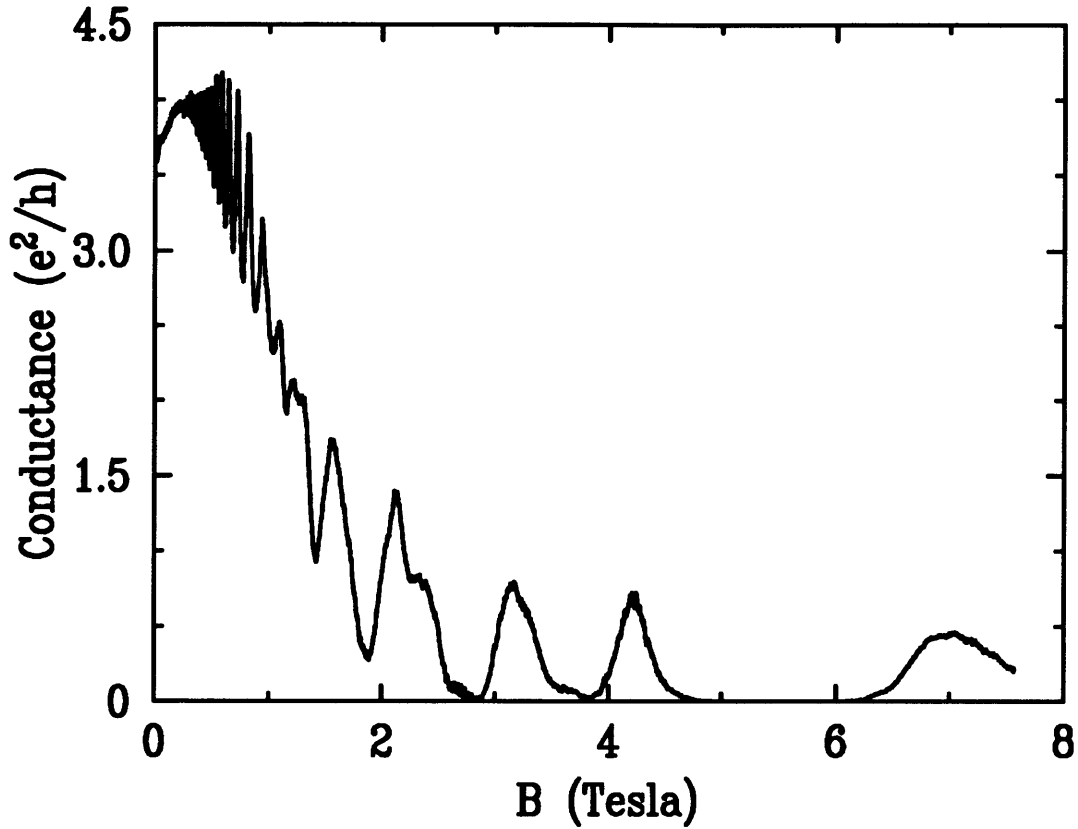


Fig. 2-11. Shubnikov-DeHaas Oscillations in the Conductance of a Hall bar as in 2-9. This data comes from a measurement on a conventional heterostructure device such as that discussed in Section 2.1.1.

Shubnikov-DeHaas effect which arises from the varying number of states at the Fermi level as successive Landau levels are depopulated with increasing magnetic field[103]. The period in $\Delta(1/B)$ is given by

$$\Delta\left(\frac{1}{B}\right) = \frac{e}{\hbar} \frac{g_s g_v}{n_s} \quad (2.1)$$

where g_v is the GaAs(100) valley degeneracy, $g_v = 1$, and where g_s is the spin degeneracy which is 2 at low fields and 1 at high fields ($g_L \mu_B B \geq kT$, $g_L \approx 0.4$).

Elsewhere, cyclotron resonance measurements have determined that the effective mass in GaAs(100) inversion layers is $0.067 m_e$ and that the D.C. dielectric constant in

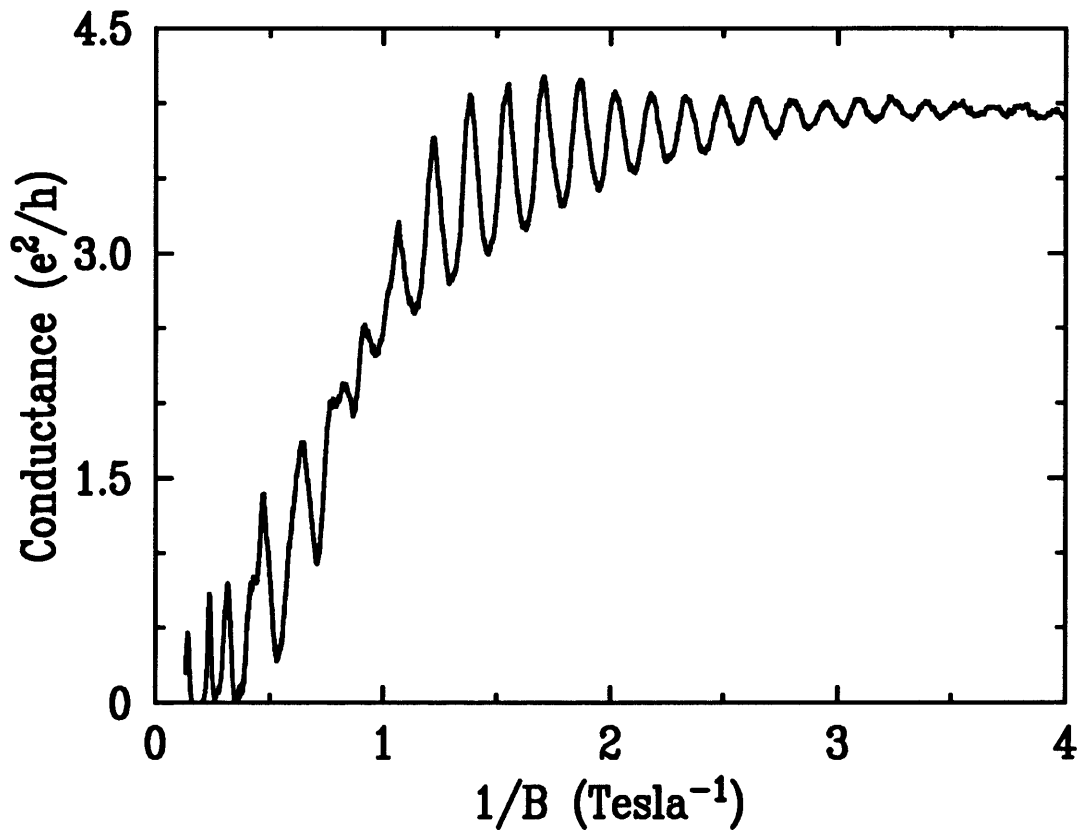


Fig. 2-12. Shubnikov-DeHaas Oscillations Periodic in $\Delta(1/B)$. The density of the 2-DEG is given from the periodicity of conductance in $\Delta(1/B)$ through Equ. 2.1. Notice that the Landau level spin degeneracy is resolved at higher fields.

GaAs is 13.1. With these two values and our measurements of n_s and σ it is possible to infer a number of parameters relating to the electronic properties of the GaAs 2-DEG. From Drudé theory, the 2-DEG mobility, μ_e , scattering time, τ , diffusion constant, D and mean free path, l are determined from n_s and σ through the relations

$$\sigma = n_s e \mu_e = \frac{n_s e^2 \tau}{m^*} = \frac{n_s e^2 l}{m^* v_F} = \frac{2 n_s e^2 D}{m^* v_F^2} \quad (\text{cgs}) \quad (2.2)$$

where v_F is the electron gas Fermi velocity which is given by

$$v_F = \frac{\hbar}{m^*} \sqrt{\frac{4\pi n_s}{g_s g_v}} \quad (2.3)$$

Table 2.1 summarizes these results and other parameters which characterize the 2-DEG. The numerical values cited in Table 2.1 correspond to $n_s = 4 \times 10^{11} \text{ cm}^{-2}$ and $\mu_e = 1 \times 10^6 \text{ cm}^2/\text{V}\cdot\text{sec}$.

Several points from Table 2.1 deserve mention. The effective mass in GaAs(100) is small which implies that quantum kinetic energies scales in GaAs 2-DEGs are enhanced by a factor of $m_e/m^* = 14.9$ over that of a free electron gas and by a factor of $m_{\text{Si}}^*/m_{\text{GaAs}}^* = 2.8$ over that of similar 2-DEGs in Si inversion layers. The spin degeneracy of GaAs is 2 which means that $L \cdot S$ coupling can be ignored when considering the GaAs 2-DEG. (However, recent experiments indicate that under certain conditions $L \cdot S$ splitting can be observed[104].) The effective Landé factor, $g_L^* = 0.4$, can be greatly enhanced in the spin-split Landau level closest to the Fermi level. Values of g_L^* as high as 15 have been reported[105]. The Fermi Wavelength is of the same order of size as the features that were e -beam patterned. The mean free path is much larger than the small region of electron gas in a typical device. (Also, though for high-mobility GaAs(100) inversion layers the phase coherence length is not well characterized, it is presumably comparable to the (elastic) mean free path[106].) The cyclotron radius at $B = 1 \text{ Tesla}$ is $\sim 0.1 \mu\text{m}$ which is comparable to the length of tunnel barriers isolating the small 2-DEG. Consequently, well below

Property	Symbol	Value	Units
Effective Mass	m^*	0.067	$m_e = 9.1 \times 10^{-31} \text{ kg}$
Spin Degeneracy	g_s	2	
Valley Degeneracy	g_v	1	
Dielectric Constant	ϵ	13.1	$\epsilon_o = 8.9 \times 10^{-12} \text{ F m}^{-1}$
Effective Landé Factor	g_L^*	0.4	
Density of States	$\rho(E) = g_s g_v (m^*/2\pi\hbar^2)$	2.8×10^{10}	$\text{cm}^{-2} \text{meV}^{-1}$
Level Spacing	$1/\rho(E)$	3.57	$\mu\text{eV} \cdot \mu\text{m}^2$
		41	$\text{mK} \cdot \mu\text{m}^2$
		0.15	$\text{B} \cdot \mu\text{m}^2$
		0.86	$\text{GHz} \cdot \mu\text{m}^2$
Fermi Wave Vector	$k_F = (4\pi n_s / g_s g_v)^{1/2}$	1.58×10^6	cm^{-1}
Fermi Velocity	$v_F = \hbar k_F / m^*$	2.7×10^7	cm/s
Fermi Energy	$E_F = (\hbar k_F)^2 / 2m^*$	14	meV
		162	K
Fermi Wavelength	$\lambda_F = 2\pi / k_F$	40	nm
Scattering Time	$\tau = m^* \mu_e / e$	38	ps
		26	GHz
Diffusion Constant	$D = v_F^2 \tau / 2$	14,000	cm^2 / sec
Resistivity	$\rho = \sigma^{-1} = (n_s e \mu_e)^{-1}$	16	Ω / \square
Mean Free Path	$l = v_F \tau$	10^4	nm
Thermal Diffusion Length	$l_T = (\hbar D / kT)^{1/2}$	3300	$\text{nm}(\text{T})^{-1/2}$
Cyclotron Radius	$l_c = \hbar k_F / eB$	100	$\text{nm}(\text{B})^{-1}$
Cyclotron Frequency	$\omega_c = eB / m^*$	2.62×10^{12}	s^{-1}
Cyclotron Energy	$\hbar \omega_c$	1.73	meV/B
		19.9	T/B
		418	GHz/B
Zeeman Energy	$g_L^* \mu_B B$	23.2	$\mu\text{eV/B}$
		269	mK/B
		5.6	GHz/B
Magnetic Length	$l_m = (\hbar / eB)^{1/2}$	26	$\text{nm}(\text{B})^{-1/2}$

Table 2.1. The Electronic Properties of GaAs(100) 2-DEG. When appropriate, the numerical values correspond to $n_s = 4 \times 10^{11} \text{ cm}^{-2}$ and $\mu_e = 1 \times 10^6 \text{ cm}^2/\text{V} \cdot \text{sec}$. The units for B are Tesla and for T are degrees Kelvin. Also, for reference the following conversion are presented: $e_{\text{cgs}} = 4.803 \times 10^{-10} \text{ esu}$ and $e_{\text{SI}} = 1.603 \times 10^{-19} \text{ C}$; $1 \text{ K} = 86.2 \mu\text{V}$; $1 \mu\text{V} = 242 \text{ MHz} = 1.24 \text{ m}$.

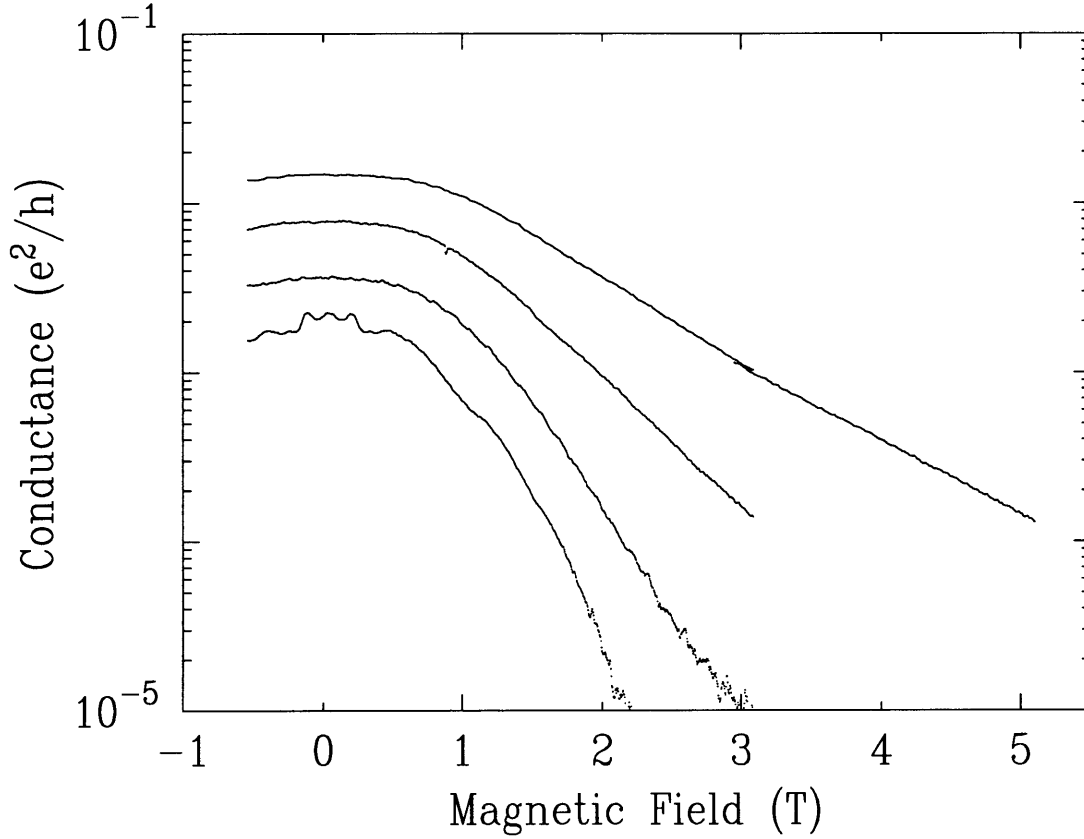


Fig. 2-13. The tunneling conductance through a single barrier at $T = 1$ K, $T = 2$ K, $T = 3$ K and $T = 4.2$ K. The conductance is larger at higher temperatures.

1 Tesla the conductance through a single barrier can be expected to decrease as $\exp(-B/B_o)^2$, and at fields larger than 1 T as $\exp(-B/B')$ [107]. This is in agreement with our measurements as in Figure 2-13. The quantum Hall regime is entered into when roughly $\omega_c\tau \geq 10$ and $\hbar\omega_c \geq 10kT$. This corresponds to ~ 0.1 Tesla at low temperatures. Lastly, $2\pi l_m^2 = A$ where A is the area spanned by one magnetic flux quanta. Setting $A = (0.3 \times 0.3 \mu\text{m}^2)$, the approximate area of the small 2-DEG region, implies that a flux quantum is added to the small 2-DEG when B is increased by ~ 470 gauss. (l_m is sometimes denoted l_b .)

2.2.2 Theoretical Modeling of the Device

A. Kumar, *et al.* carried out elaborate calculations of the charge density in various structures by solving the Poisson and Schrodinger equations self-consistently in three-dimensional device geometries[108][109]. For the purposes of our investigation, we focus on only a small portion of the results of Refs. [108][109]. Figure 2-14 is taken from their results[109]. First, as seen in Fig. 2-14 the 2-DEG is depleted out to $\sim 0.1 \mu\text{m}$ from the projected edge of the gates onto the 2-DEG. (This value is also consistent with analytic calculation by Chklovskii *et al.*[110].) Secondly, the results of A. Kumar, *et al.* results indicate that the self-consistent confining potential of the small region of 2-DEG is roughly parabolic with $\hbar\omega_y = 3.5 \text{ meV}$, and $\hbar\omega_x = 0.8 \text{ meV}$. These values will be employed in a model that will be introduced in Chapter 4. Thirdly, the self-consistent potential of the tunnel barriers can be approximated by a saddle point potential with $\hbar\omega_x = 5 \text{ meV}$ where under typical conditions (ie., in which well-isolated single-electron charging peaks are observed, cf. Chap. 3) the maxima of the barriers lie $\sim 30 \text{ meV}$ above the 2-DEG Fermi level. This implies that the width of the tunnel barriers is $\sim 0.1 \text{ nm}$ [107].

2.3 Energy Scales and Probing a Device

The first part of this section continues the discussion of a typical device in quantitative terms, paying particular attention to the energy scales associated with the small region of 2-DEG. The second part of this section considers the experimental requirements for probing devices on these energy scales.

2.3.1 Electronic Excitations of a Small Electron Gas

Two sorts of excitations of a small electron gas are imaginable. The first is an excitation above the ground state that keeps the number of particles in the gas fixed. This

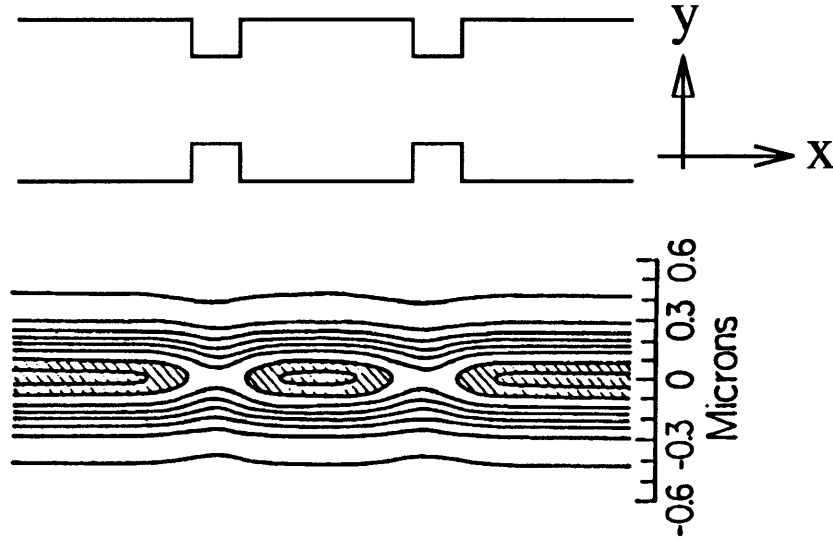


Fig. 2-14. Equipotentials in the plane of the 2-DEG in structures such as Fig. 2-10. (Borrowed from Reference [109].) The shaded areas contain electron gas. Notice that an area of isolated 2-DEG is formed in the center of the channel.

is analogous to exciting the electrons of an atom to higher orbitals states. A second kind of excitation is one that changes the number of electrons in the small electron gas which is analogous to ionizing an atom either positively or negatively.

Consider the energy required to excite the electron gas in the first case. When a single particle excitation is made with a fixed number of particles it is reasonable to imagine that the total spatial distribution of charge changes very little. Consequently, electron-electron interactions contribute very little the energy of this excitation. Rather, the change in kinetic energy of the excited particle is the dominate contribution to the total excitation energy. Perhaps a more familiar situation that might help illustrate this point a system of electrons in a magnetic field viewed in the Hartree approximation[111]. If the spin of one of these electrons is flipped the energy of the system changes by exactly $g\mu_B B$. The electron-electron contribution to the total energy does not need to be considered because flipping a spin does not change the spatial distribution of charge.

Returning to our original point, exciting the electron gas with a fixed number of

particles is assumed to change the spatial distribution of charge by a negligibly small amount. Consequently, if correlations are ignored, excitations can be approximated as single-particle excitations of a noninteracting system of particles. In this case, the energy scale of excitations is given by the single particle level spacing, $\Delta\epsilon$, which in an electron gas of area, A , is given by

$$\Delta\epsilon \approx \frac{1}{A\rho(E)} = \frac{1}{(0.3 \times 0.3 \mu\text{m}^2)(2.8 \times 10^{10} \text{ cm}^{-2}\text{meV}^{-1})} = 0.04 \text{ meV} \quad (2.4)$$

where A has been set equal to the approximate area of the isolated 2-DEG, $0.3 \times 0.3 \mu\text{m}$.

Next, consider excitations that add or subtract an electron from the small 2-DEG. As a first attempt at estimating this energy, consider the system in classical terms. The electron gas has some capacitance, C , and its capacitive charging energy is $Q^2/2C$. The energy scale to change the charge in the gas by a single electron, U , is therefore set by e^2/C . U is widely referred to as the Coulomb charging energy². A. Kumar *et al.* calculated C in several device geometries. In the geometry of a typical device, their calculations gave $C \approx 2 \times 10^{-16} \text{ F}$. C can also be roughly estimated by modeling the gas as a parallel plate capacitor with an area A and a spacing between plates equal to the spacer layer of the heterostructure, $\sim 0.085 \mu\text{m}$, giving $C = 125 \text{ aF}$ which is consistent with the result of A. Kumar *et al.*. Using $2 \times 10^{-16} \text{ F}$ for C gives

$$U \equiv \frac{e^2}{C} = 0.8 \text{ meV} \quad (2.5)$$

²Exactly why U is defined to be e^2/C will be explained in detail in Section 3.3.2 on page 70 in the discussion of the theory of the Coulomb blockade.

2.3.2 Experimental Requirements for Probing the Small Electron Gas

In the above, two energies, U and $\Delta\epsilon$ were considered and their approximate values were shown to be $\sim 0.8 \text{ meV}$ and 0.04 meV respectively. More will be said about these values in the upcoming chapters. For now consider only that, because of the magnitudes of U and $\Delta\epsilon$, measuring these systems requires probing the small 2-DEG on energy scales of order 0.01 meV . In order to resolve effects at these energy scales kT must be less than $\sim 0.01 \text{ meV}$. This corresponds to temperatures of less than 100 mK . To reach these temperatures, devices were cooled to $\sim 50 \text{ mK}$ in an Oxford Instruments $75 \mu\text{Watt}$ dilution refrigerator³. The principles of operation of a dilution refrigerator can be found in Refs. [112]. Appendix D contains a detailed description of the operation of our dilution refrigerator. The conductance of the small 2-DEG is measured by establishing a potential difference between the macroscopic 2-DEGs on opposing sides of the small 2-DEG. The magnitude of this bias must also be limited to of order 0.01 meV . In practice, the bias voltages used were between $2.5 \mu\text{V}$ and $10 \mu\text{V}$. Currents were measured at 8.5 Hz using standard lock-in amplifier techniques. The current-to-voltage amplifier stage was custom built for low-noise operation and is described in Appendix E.

³The nominal base temperature of the dilution refrigerator was 12 mK . At low temperature, however, the thermodynamic coupling between the lattice and electrons is sufficiently weak that their temperature need not be the same. The 50 mK value cited refers to the actual temperature of the electron gas, which was determined from the voltage width of single-electron charging peaks. A detail discussion is contained in Section 3.3.3.

Chapter 3

Classical Single Electron Charging

This chapter is written to stand alone as an introduction to classical single electron charging effects in small electron gas structures. We discuss our measurements of the conductance of the small electron gas system described in Chapter 2. We show that the conductance of this system as a function of gate voltage consists of a series of nearly periodic peaks. In Section 3.3 this striking behavior is explained through a very simple model of classical single electron charging: a model widely referred to as the Coulomb blockade model. Section 3.4 presents additional transport measurements of the device, specifically current-voltage characteristics at fixed gate voltages. We show that these results are also explained by the single electron charging picture. Section 3.5 expands our presentation of the Coulomb blockade model to include multiple gates.

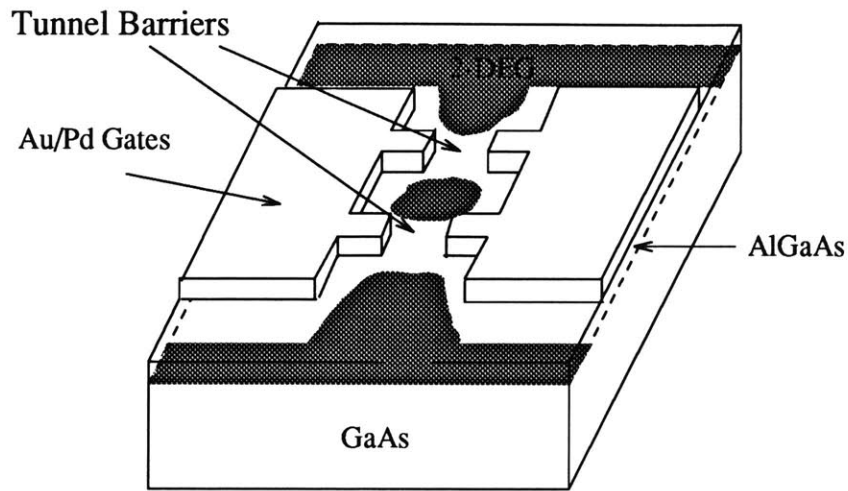
3.1 Conductances Measurements of a Small Electron Gas

This section describes measurements of the conductance of the small electron gas system introduced in Chapter 2. This is not conceptually a complicated measurement, however, we will explain it in some detail since it is important from the outset of this chapter to understand exactly what is being measured as a function of what. Figure 3-1 shows two views of our small electron gas system. The first is the same illustration of the structure that was presented in Chapter 2 on page 34. The second view in Figure. 3-1 is an abstracted schematic structure showing just the conceptually essential components of the small electron gas system, specifically the small electron gas itself, two leads approaching the small electron gas from its left and right sides and a metallic gate in close proximity to the small electron gas.

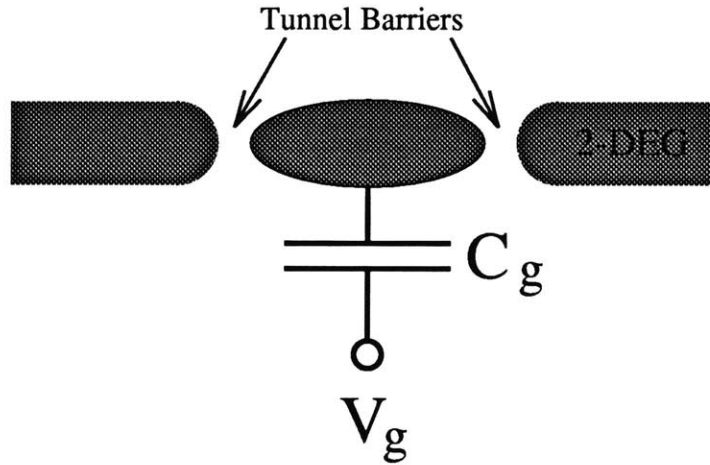
The metallic gate, which represents the metallic electrodes collectively, is shown in Figure 3-1(b) as being capacitively coupled to the small electron gas¹. This reflects the fact that changing the bias on the electrodes changes the equilibrium number of electrons in the small electron gas just as changing the bias on one plate of a capacitor changes the number of charges on the other plate of the capacitor. As the bias on the gates is made more positive, more charge accumulates in the small electron gas. Calculations by A. Kumar *et al.* show that over a small enough range in V_g , the change in charge, ΔQ , is linear with the change in gate voltage, ΔV_g , which expresses the fact that the relationship between ΔQ and ΔV_g can be described in terms of a capacitive coupling, $C = \Delta Q / \Delta V_g$ [113].

Figure 3-2 demonstrates how the conductance through the small electron gas, G , is measured as a function of gate voltage, V_g . The ohm meter in Figure. 3-2 (which in

¹Section 3.5 will expand this model to incorporate multiple gates each with their own capacitances to the small electron gas in addition to included the effects of the capacitance between the electron gas and the leads



(a)



(b)

Fig. 3-1. The small electron gas system as conceptualized in the classical single electron charging model. Figure (a) shows a schematic of a typical small small electron gas system fabricated using a GaAs heterostructure and depletion gates. Notice a small electron gas is isolated between two tunnel barriers. Figure (b) show an abstracted schematic of the system. The interaction between the gates and the small electron gas is represented as a capacitive coupling.

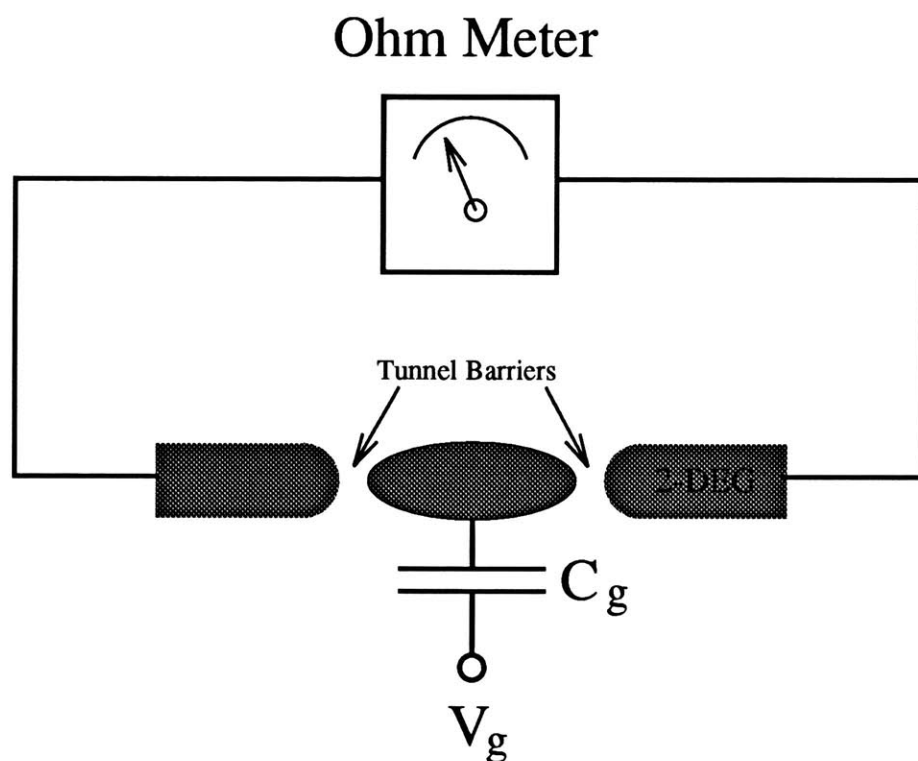


Fig. 3-2. The method of measuring the conductance of a small electron gas as a function of gate voltage. The Ohm meter represents the lock-in amplifier and low-noise current amplifier arrangement described in Section 2.3.2. Electrons tunnel between “the leads of the Ohm meter” and the small electron gas. Conductance is measured as a function of gate-voltage, V_g .

practice is the lock-in measurement apparatus described in Section 2.3.2) measures the current which travels through the small electron gas in response to a small voltage applied between the leads. The magnitude of this current, I , divided by the applied voltage, V_{ds} , is simply the conductance of the electron gas, $G = I/V_{ds}$. (Do not confuse V_{ds} and V_g .) Next, the gate voltage, V_g is changed by a small amount and G is measured again. Repeating this process allows for G to be measured as a function of V_g . In the upcoming section we will present experimental results of G versus V_g .

However, first a few words about all this: To start, it should be reemphasized that there are tunnel barriers between the small electron gas and its leads. (This point was made in the discussion of Figure 2-6 on page 40.) Consequently current flow entails electrons tunneling from one lead onto the electron gas and then tunneling off the the electron gas onto the other lead. Secondly, the current, I , which flows through the electron gas in response to an arbitrary V can be given by a Taylor expansion in the form,

$$I = 0 + \left. \frac{dI}{dV} \right|_{V=0} V + \frac{1}{2} \left. \frac{d^2 I}{dV^2} \right|_{V=0} V^2 + \dots \text{higher order terms} \quad (3.1)$$

In our measurements, the magnitude of V is chosen to be small enough that I is linear for small changes in V so that I/V is a measure of $(dI/dV)_{V=0}$. So our conductance measurements determine the linear conductance of the system about zero-bias. The literature refers to these sorts of measurements in several ways: low-bias measurements, small-bias measurement, zero-bias measurements, conductance measurements, linear-conductance measurements, vanishing conductance measurements and non-perturbative conductance measurements.

3.2 Conductance versus Gate-voltage Data

Figure 3-3 shows the measured linear conductance of a small electron gas, G , as a function of gate voltage, V_g . At low V_g the electron gas is sufficiently small, or equivalently, the tunnel barriers between the gas and the leads are sufficiently large

that no current flow is measurable. At higher V_g , current begins to flow and, generally speaking, G increase with larger V_g . Notice G is plotted in units of e^2/h , the quantum of conductance, which is equal to $3.98 \times 10^{-5} \Omega^{-1}$ or $1/(25813 \Omega)$. Furthermore, superimposed on the rise in G is a periodic oscillation in G which persists over a wide range in V_g . Figure 3-4 shows this behavior on a more magnified scale at low V_g . We see here that the conductance of the small electron gas as a function of gate-voltage consists of a series of nearly periodic peaks roughly 0.82 mV apart. In Figure 3-5 we plot peak position versus peak number, illustrating the near periodicity of the peak spacings. In Figure 3-6 we plot the same data on a semi-log scale. We see that the conductance peaks have peak to valley ratios well over 10^3 and that the tails of the peaks fall off exponentially. For the remainder of this chapter we focus on the electron transport properties of small electron gas in this regime. Later, in Chapter 6 we will reconsider behavior at higher gate-voltages.

3.3 Introduction to the Classical Coulomb Blockade Model

Periodic conductance peaks, such as those present in the previous Section, were experimentally first observed in disordered narrow channel Si 2-DEGs by J.H.F. Scott-Thomas *et al.* in 1989[60]. Other early work includes the observation of periodic conductance peaks in disordered GaAs 2-DEG[62, 61] and in GaAs structures by U. Meirav[63] after which the structures that we have fabricated have been modeled (*e. g.* Figures 2-6 and Figures 2-7). H. van Houten and C.W.J. Beenakker proposed an explanation for these results[64] based on the theory of the Coulomb Blockade which was introduced in 1973 by Kulik and Shekhter[65][114]. This work in turn was motivated in part by single electron charging phenomena first reported by Gorter in 1951[115].

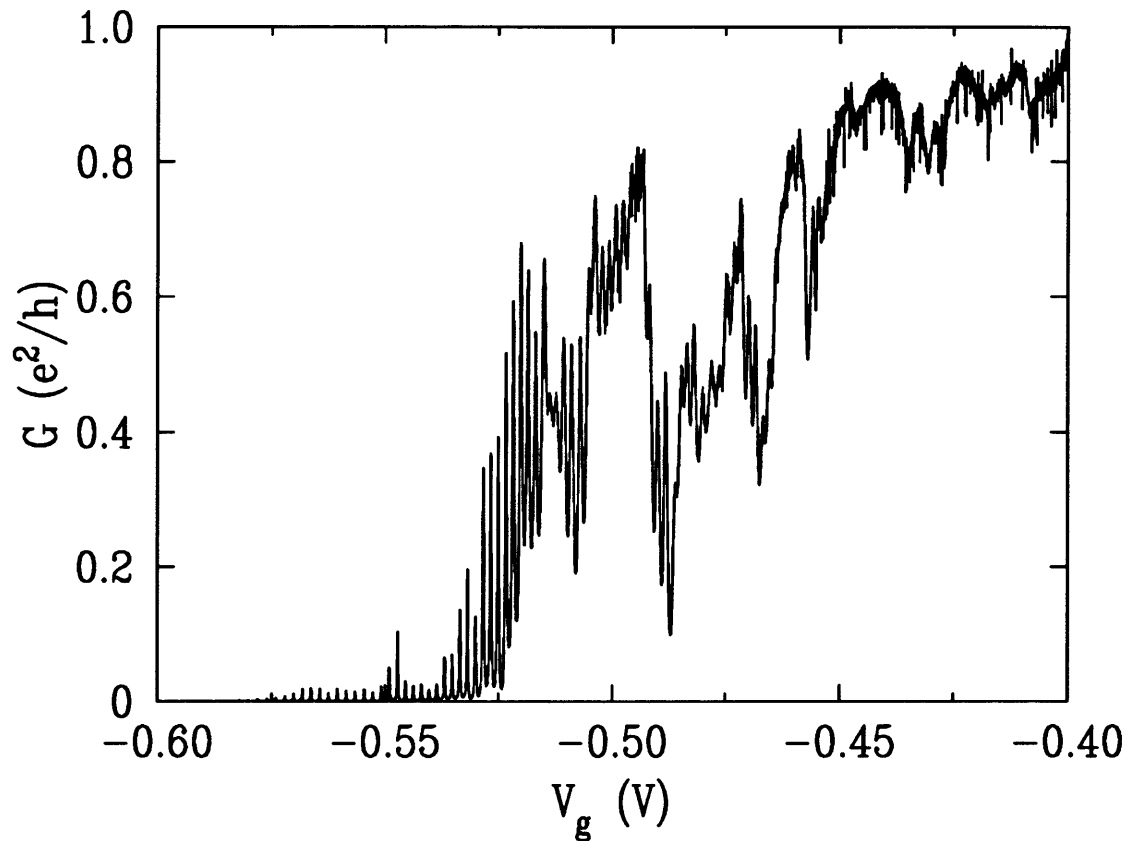


Fig. 3-3. The conductance versus gate-voltage of a small electron gas. These data are from measurements on a structure as shown in Fig. 2-7 on page 41. G is plotted in units of e^2/h , the quantum of conductance, which is equal to $3.98 \times 10^{-5} \Omega^{-1}$ or $1/(25813 \Omega)$. $T \approx 60 \text{ mK}$ and $B = 0 \text{ T}$. Notice the periodic peaks in G at low V_g . This is data from a conventional heterostructure device such as that discussed in Section 2.1.1.

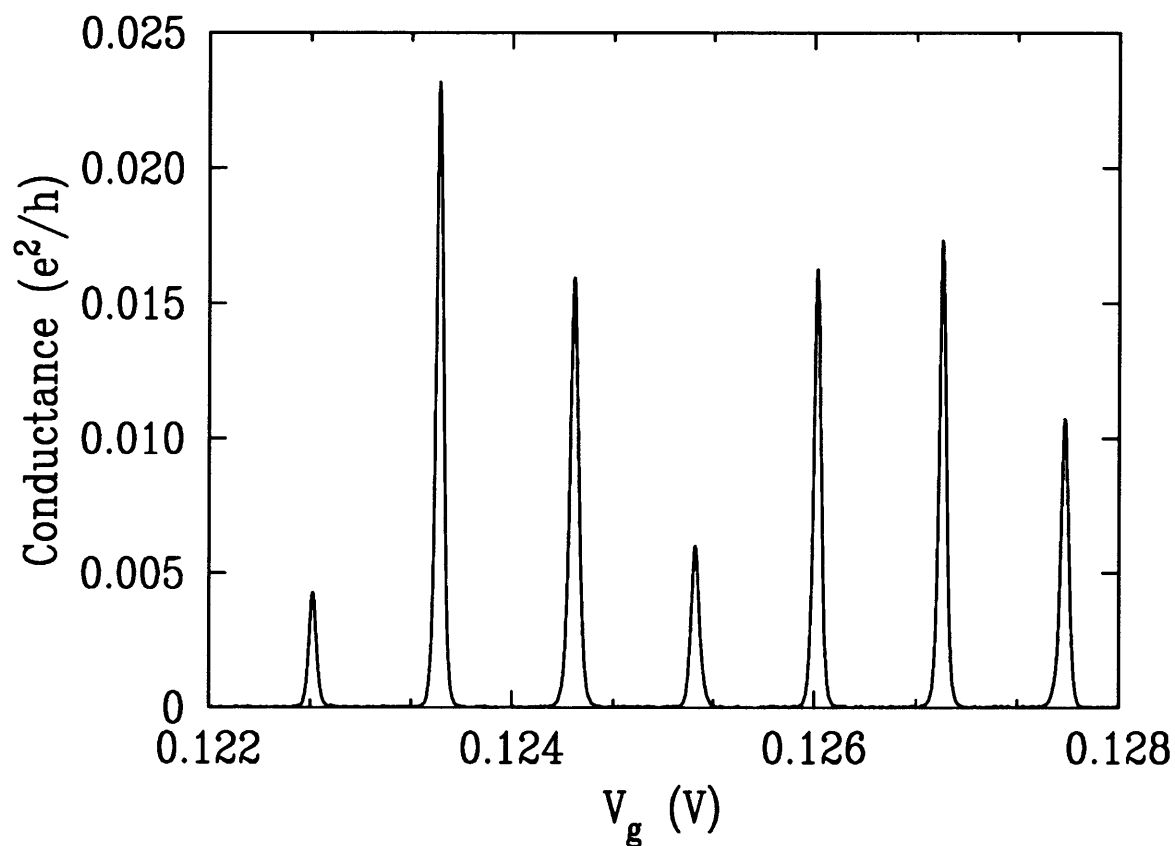


Fig. 3-4. Periodic peaks in the conductance of a small electron gas as a function of gate voltage. These data are from measurements on a structure similar to that shown in Fig. 41 on page 41. V_g represents the voltage simultaneously applied to the large gate and smallest gate. The remaining two gates were both held at a fixed bias of ~ -0.7 V. $T \approx 80$ mK and $B = 0$ Tesla.

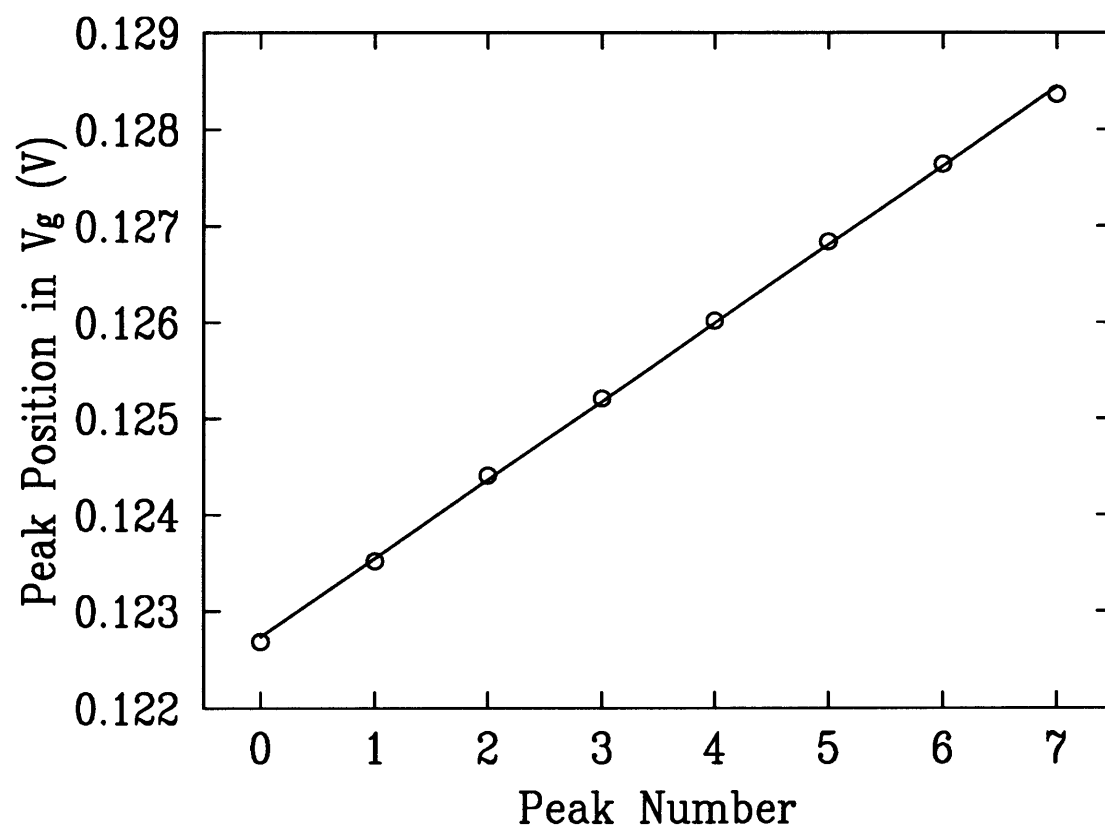


Fig. 3-5. The Gate-voltage of consecutive conductance peaks as function of peak number. These data are based on the data of Fig. 3-4. The periodicity of the conductance peaks is evident from the linearity of the plot. The spacing between conductance peaks is 0.82 mV.

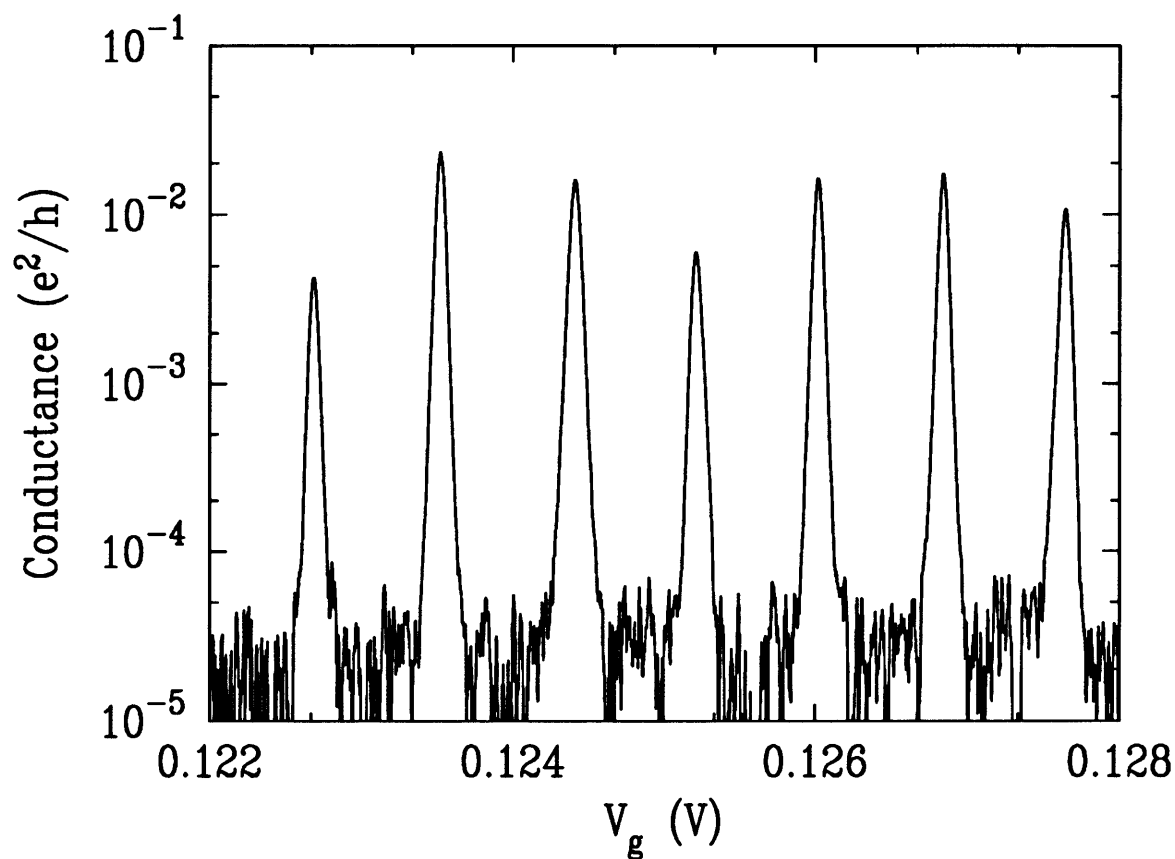


Fig. 3-6. The conductance versus gate-voltage of a small electron gas on a semi-logarithmic scale. These data are the same data as in Fig. 3-4. Plotted on a semi-logarithmic scale it is seen that the peak to valley ratio of a conductance peaks approaches 10^3 and that the tails of the peaks fall off exponentially.

3.3.1 Single-electron charging and the Origin of Periodic Conductance Peaks

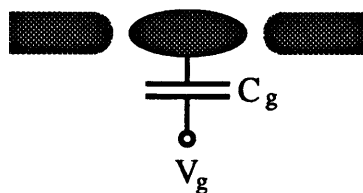
In this section we will describe a very simple model of single electron charging which can account for the periodic conductance oscillations presented in the previous section. This model is in fact a simple case of the more general Coulomb blockade theory which addresses single electron charging under a variety of conditions. However, the simplified model that we will discuss in this section contains nearly all the essential elements of the Coulomb blockade theory. The goal of this section is two fold: to explain the periodic conductance data of the previous section, and to elucidate the fundamental aspects of the Coulomb blockade theory.

Consider the abstracted view of the small 2DEG shown in Figure 3-7a. Since the gate and the 2DEG are coupled capacitively (Section 3.1), we may consider them to be two plates of a conventional parallel plate capacitor. If we assume that charge in the 2DEG, Q , varies continuously, then Q will be a linear function of V : $Q = CV$, where C is the capacitance between the gate and the 2DEG.

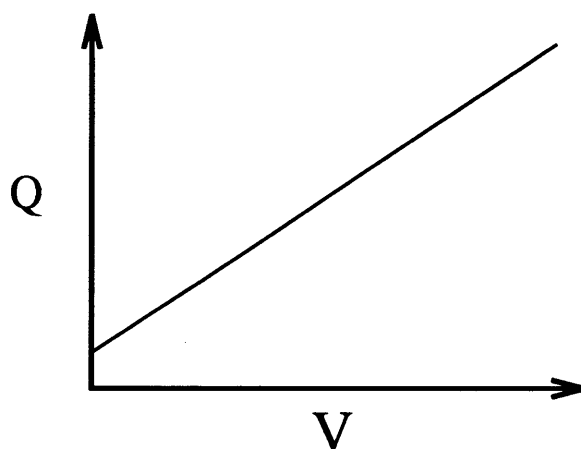
When the charge, Q is very large compared to the charge of an electron, e , it is reasonable to assume that charge is continuous. For our devices, however, $Q \approx 100e$, and this assumption does not apply. In this case, we must take the number of electrons on the 2DEG to be integer multiple of e that is closest to the equilibrium charge, CV , as shown in Figure 3-7c). From The Figure, it is clear that Q increases by e whenever V_g increases by e/C . As we saw in Section 2.3.1 on page 53, C is of the order 2×10^{-16} F, from which, $e/C = 0.8$ mV.

Now we examine how this will effect the measured conductance through the 2DEG. Figure 3-8 shows the lowest order tunneling process by which current can flow through the 2DEG. Here current flow is a repeated process where an electron first tunnels on the 2DEG from one of the leads, the off through the other lead. Thus, the charge in the 2DEG first increases to $(N + 1)e$, as the electron tunnels on, and then returns to

(a)



(b)



(c)

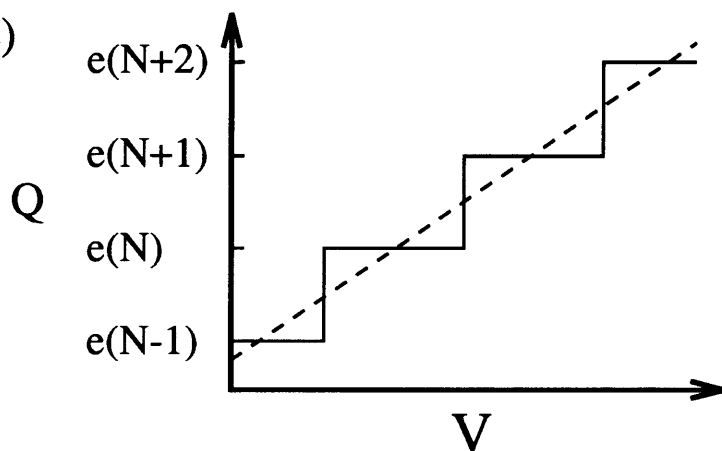


Fig. 3-7. Charge as a function of gate-voltage in a small electron gas system. Varying V_g in (a) changes the equilibrium charge state of the small electron gas due to the capacitive coupling between the gate and the gas. Generally, this implies a charge versus gate voltage relationship that is linear and continuous as in (b). However, for sufficiently small systems, the quantization of charge must be taken into account (c). In this case the number of electrons which reside in the gas is equal to the integer multiple of e that is closest to the equilibrium quantity of charge that would reside on the electron gas if charge were continuous (dashed line in (c)).

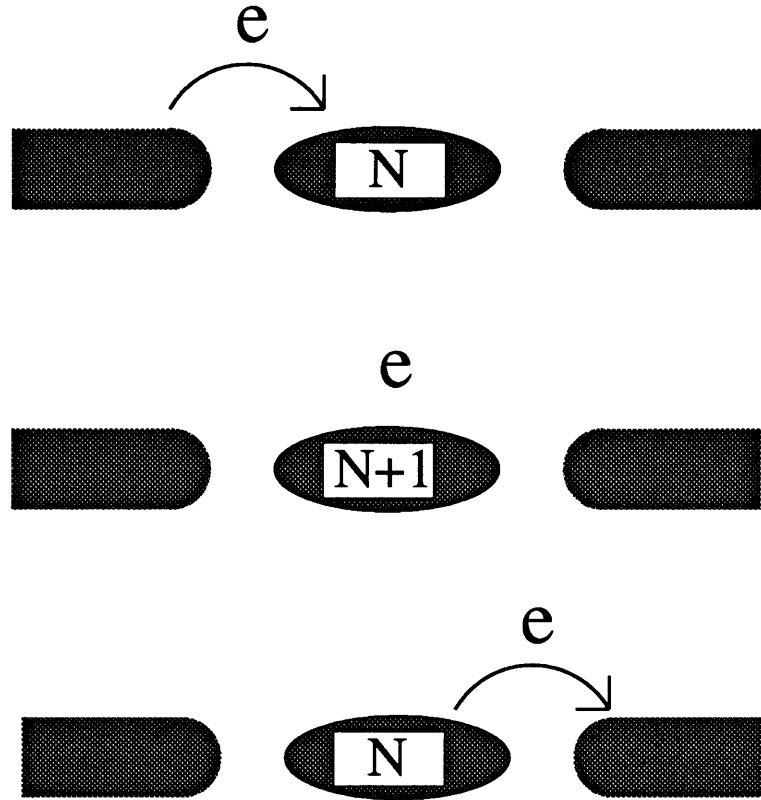


Fig. 3-8. Current flow through a small electron gas in term of single electron tunneling. The lowest order tunneling process by which current flows entails an electron tunneling into the gas, which raises it charge state from eN to $e(N + 1)$, and then an electron tunneling out of the gas which returns its charge state to eN . In short, current flow requires that the charge state of the small electron gas is free to fluctuate by e .

Ne , as it tunnels back off through the other lead. Other processes that can result in current flow are imaginable such as an electron tunneling directly from one lead to the the other lead, or two electrons simultaneously tunneling, one onto the electron gas and one off of it. However, these sorts of mechanisms are higher order processes and their contribution to the total current flow can is much less than the single, uncorrelated tunneling process depicted in Figure 3-8².

Given that conductance occurs through the mechanism in Figure 3-8 and that the

²Higher order tunneling processes have been theoretically[116, 117, 118, 119, 120] and experimentally[121, 122] investigated. Such effects have been referred to in these systems as macroscopic quantum tunneling (MQT). This will be discussed in Section 6.5.2.

equilibrium charge on the island as a function of V_g follows the staircase relationship in Figure 3-7(c) the origin of the periodic conductance oscillation of a small electron gas is clear. Referring to Figure 3-9, when V_g is biased so that the equilibrium charge in the electron gas is an integer number of electrons, eN , current flow is blocked. This is because if an additional electron were to tunnel onto the electron gas it would move the electron gas away from its equilibrium charge by e and this requires a capacitive charging energy of $e^2/2C$. If however, V_g is biased so that the equilibrium charge on the island is a half integer multiple of e , $e(N + \frac{1}{2})$, then the lowest realizable energy charge-state of the electron gas is degenerate at eN or $e(N + 1)$. In other words when the equilibrium charge-state is $e(N + \frac{1}{2})$ then the actual charge in the small electron gas is energetically free to fluctuate between two states, eN and $e(N + \frac{1}{2})$, and current is free to pass through the electron gas by the mechanism described above. Figure 3-8 illustrates this point showing that conductance peaks occur at values of V_g where the equilibrium charge state of the electron gas is doubly degenerate. In Figure 3-8 the finite width of the conductance peaks arises from thermal broadening. At zero temperature, conductance peaks in this model have finite amplitude and zero width. A more detailed description of thermal broadened lineshapes will be given in Section 3.3.3.

3.3.2 Recasting the Single Electron Charging model in the Single Particle Tunneling Framework

In the previous section a simple model of single electron charging was presented. In this Section, the same physical model is presented but in a slightly different way. First, we will present this new formalism, then we will demonstrate its utility.

Figure 3-10 introduces this new formalism. Part (a) of this Figure shows the same abstracted schematic that was discussed above. At zero temperature, when V_g is biased so that the equilibrium charge in the small electron gas is an integral number

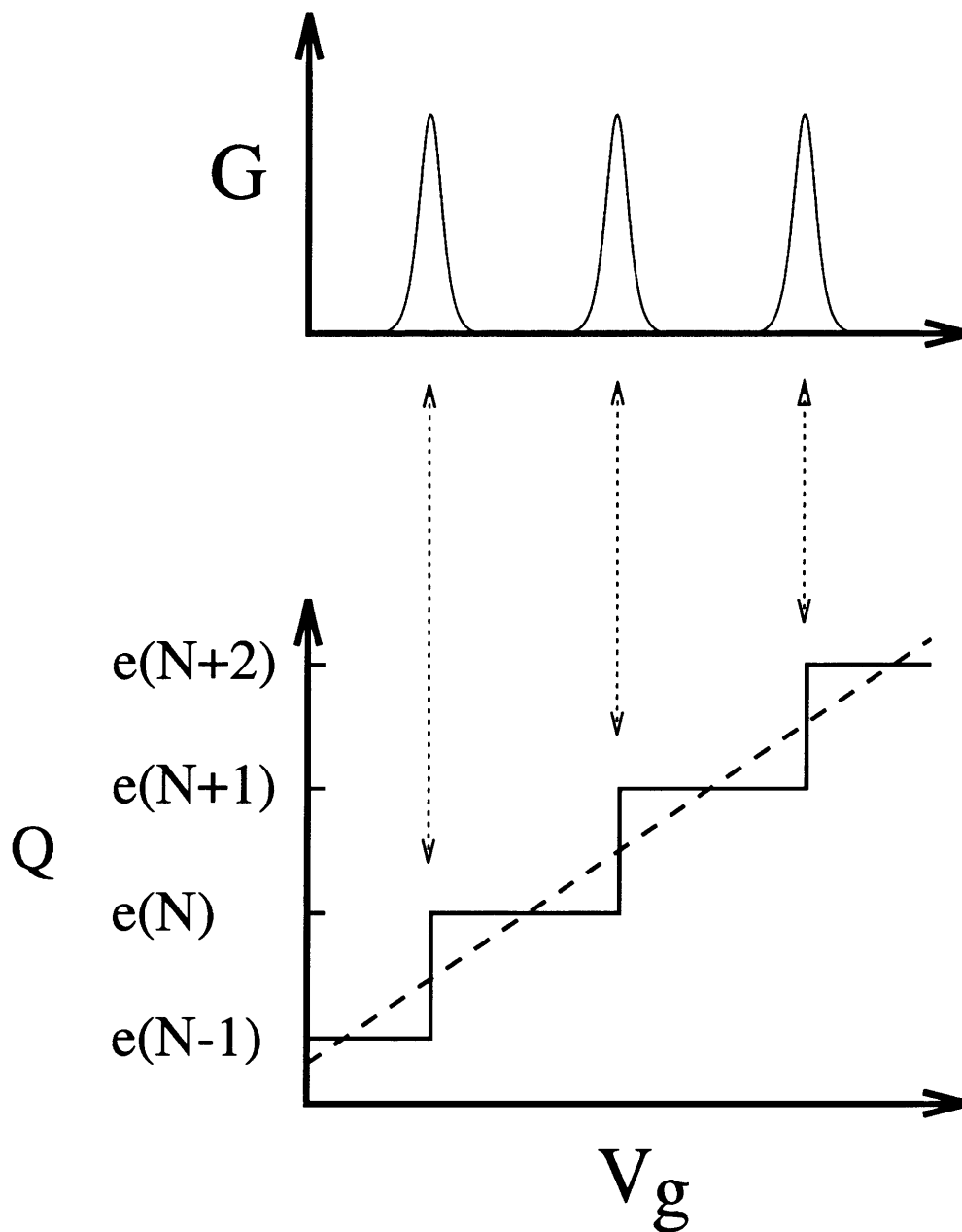


Fig. 3-9. Single electron charging and the origin of periodic conductance peaks. This Figure contains a synthesis of the ideas presented in Figs. 3-7 and 3-8. Conductance peaks occur at gate voltages at which the charge state of the gas is free to fluctuate by an electron. This corresponds to risers in the plot of Q versus V_g .

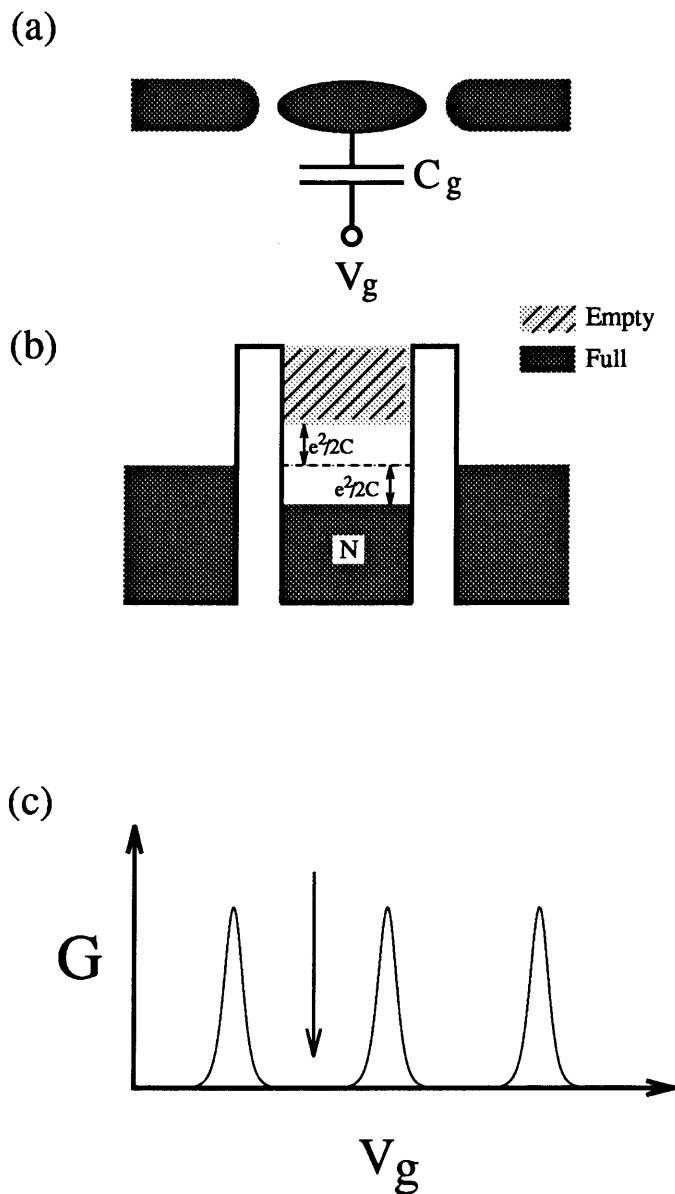


Fig. 3-10. Tunneling diagram representation of single electron charging. The schematic in (a) can be recast in (b) in a manner familiar from single particle tunneling in a double barrier system. When V_g is biased so that the charge in the gas is an integral number of electrons eN , then adding a charge from the gas requires an energy of $\geq e^2/2C$. The empty band of states in (b) denotes this condition. Likewise for an electron tunneling out of the gas, when the initial charge state of the gas is e , requires an energy of $\geq e^2/2C$. This condition is represented by the filled band of states between the barriers. This biasing condition corresponds to V_g between conductance peaks. See(c).

of electrons, eN , then adding or removing an electron from the gas requires a charging energy of $e^2/2C$. This idea is represented in Part (b) of Figure 3-10 as follows: If one additional electron is to be added to the small electron gas then it must have an energy that falls within the band of empty states in the gas. The diagram makes clear that adding one additional electron to the gas requires an energy of $\geq e^2/2C$. Likewise, removing a single electron from the gas requires an energy that corresponds to the difference between the chemical potential in the leads and an energy in the filled band of states. The diagram indicates that this too requires an energy of $\geq e^2/2C$.

In brief, when the Fermi level of the leads is defined to be the zero of energy scale and there are N electrons initially in the small electron gas, then an empty state in diagram represents the energy for a single electron to tunnel into the gas, and full states represent the negative of the energy required for a single electron to tunnel out of the small electron gas. Only these two pieces of information are contained in this diagram: It should not be over interpreted. For example, once an electron has tunneled onto the gas and there are $N + 1$ electrons in it, and it is not correct to say that for an electron to tunnel out of the gas still requires an energy of $\geq e^2/2C$ or that a second electron can tunnel into the gas provided its energy is $\geq e^2/2C$. In short, this diagram looks very similar to other diagrams that depict the non-interacting tunneling density of states in a double barrier system, but it should not be confused with these pictures. In our diagram only one question is answered, how much energy is required to add or subtract one electron when there are N electrons on the gas and V_g is biased so that its equilibrium charge is eN .

In Figure 3-9 we showed how conductance peaks correlate with the staircase relationship between V_g and Q and thus how single electron charging gives rise to periodic conductance peaks. The same behavior is explained in Figures 3-11–3-13 using tunneling diagrams such as those introduced in Figure 3-10. Notice in the sequence of Figures 3-11–3-13 that increasing V_g pulls down the energy levels in the electron gas. Finally when V_g is increased to the point where the equilibrium charge of the gas is

$e(N + \frac{1}{2})$ then the charge state of the gas is electrostatically free to fluctuate between two charge states, eN and $e(N + 1)$. Compare the sequence in Figure 3-9 with that of Figures 3-11–3-13. The same information is depicted in both representations. Also, notice that regardless of V_g the sum of the energy to add an electron to the gas and the energy to subtract one is always e^2/C . In other words, the gap between the full and empty states in the tunneling diagrams is e^2/C regardless of V_g . This gap is referred to as the Coulomb blockade gap, and its magnitude is referred to as the Coulomb blockade energy.

One point needs to be clarified in Figure 3-12. At the charge degeneracy point, there are two tunnel diagrams associated with the small electron gas, indicating that the charge state of the gas fluctuates freely between two states.³ At finite temperatures, however, electrons can be thermally activated over a portion of the Coulomb blockade gap. For example, in Case:2 in Figure 3-11 adding the $N + 1$ electron to the gas requires an energy equal to only $e^2/4C$. This accounts for the finite width of a conductance peak at non-zero temperatures. The form the the conductance peak lineshape will be discussed in the next section.

3.3.3 Thermally Broadened Conductance Peak Lineshapes in the Model of Classical Single Electron Charging

The problem of calculating the lineshape of a thermally broadened conductance peak in the single electron charging model that can be formulated entirely from the discussion above. Its solution requires calculating the occupation probabilities of the small electron gas under the non-equilibrium conditions that occur when a small bias is established between the leads. The non-equilibrium statistics are then linearized with respect to the applied bias and the conductance of the system, $G(V_g)$, follows

³Strictly speaking there can only be one single-particle density of states even for an interacting system such as ours. What we have constructed is a function, conditional density of states when the number of electrons is restricted to be either N or $N + 1$.

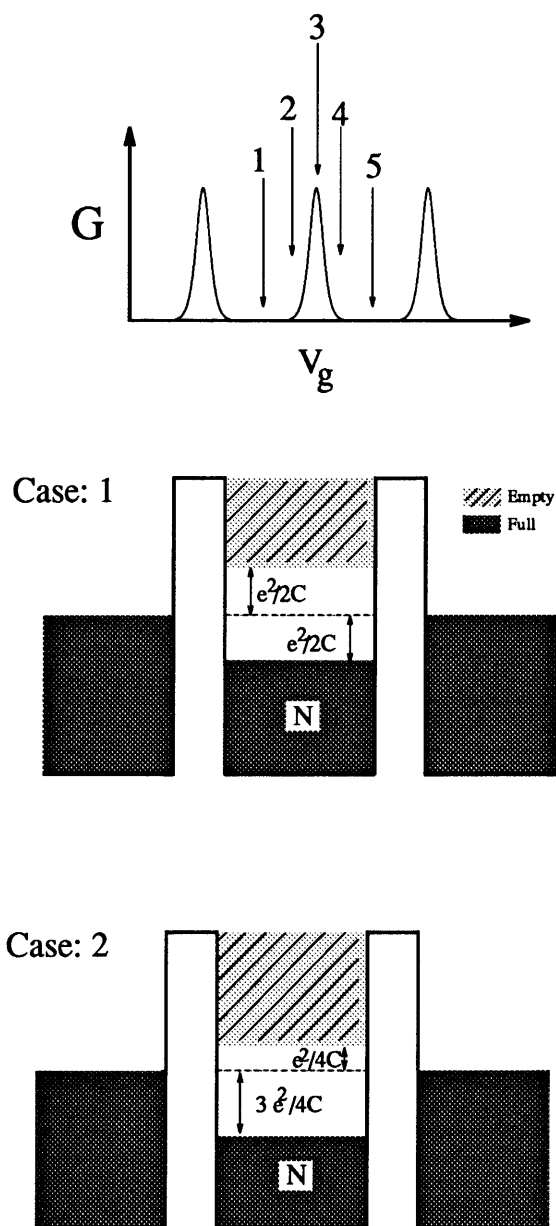


Fig. 3-11. Figure 1 of 3 showing the charge state of a small electron gas as V_g is cycled through one period of the conductance oscillations. Case:1 shows the charge state of the the electron gas when V_g is biased between conductance peaks. There are N electrons in the gas and adding or subtracting an electron from the gas requires and energy of at least $e^2/2C$. Case:2 two corresponds to a slightly higher V_g . If charge were continuous the equilibrium charge of the gas would be $e(N + 1/4)$. However, since the charge on the gas must be an integral multiple of e the equilibrium state of the gas still contains N electrons. Notice that in this case adding an electron to the gas requires and energy of only $e^2/4C$ where as removing one requires $3e^2/4C$. Compare this Figure with Figure 3-9.

Case: 3

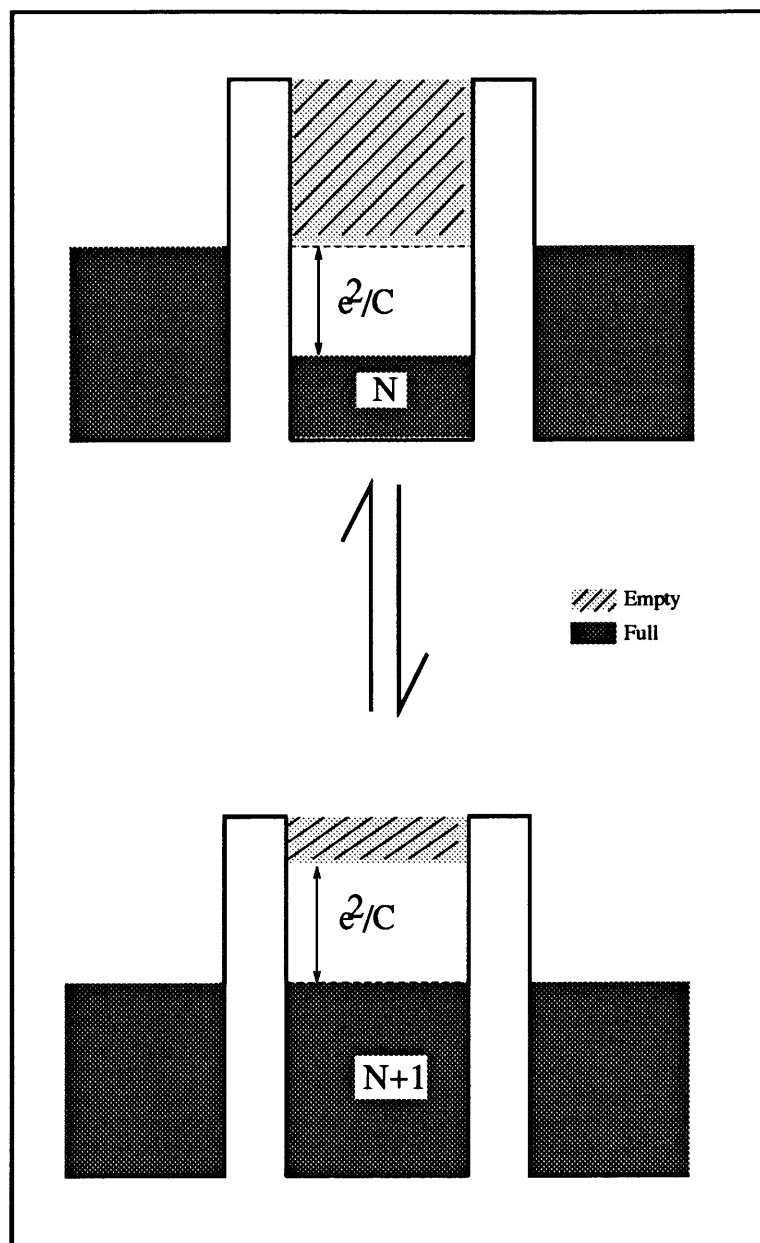


Fig. 3-12. Figure 2 of 3 showing the charge state of a small electron gas as V_g is cycled through one period of the conductance oscillations. Case:3 represents the small electron gas at a conductance peak. V_g has been biased so that the charge on the electron gas is free to fluctuate between eN and $e(N+1)$. As explained in Fig. 3-8 this is the condition that gives rise to a conductance peak. The top diagram indicates that it costs no energy to add the $N+1$ electron. Having done this the system is represented by the lower diagram, which indicates that it costs no energy to remove the $N+1$ electron. At a charge degeneracy point, the system fluctuates between these two states resulting in current flow.

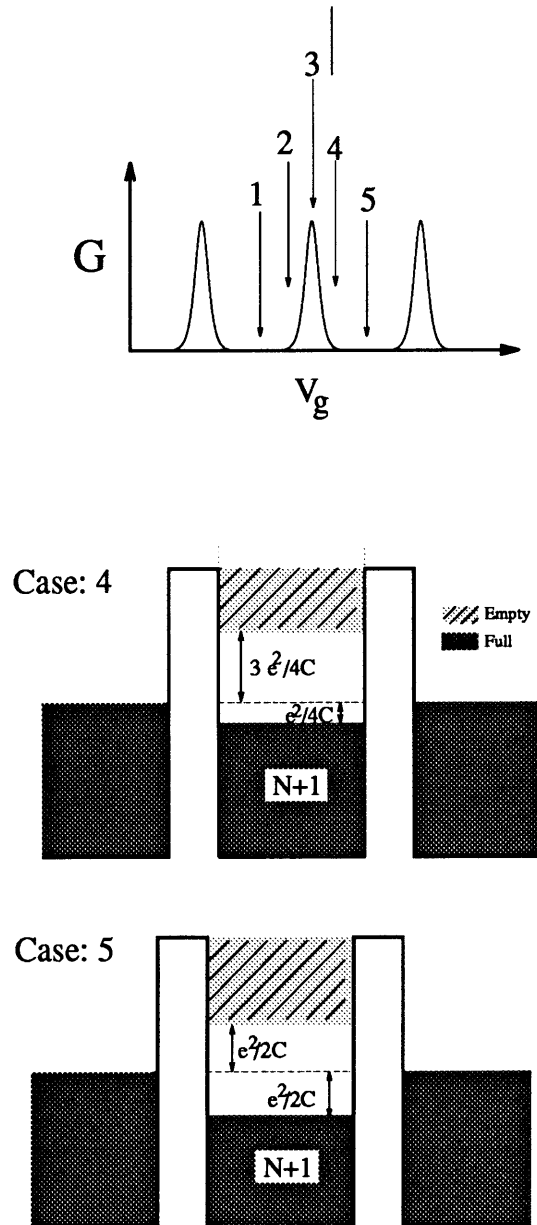


Fig. 3-13. Figure 3 of 3 showing the charge state of a small electron gas as V_g is cycled through one period of the conductance oscillations. The sequence from Case:4 to Case:5 completes the cycle begin in Fig. 3-11. The diagram for Case:5 is the same as that for Case:1 except that an additional electron has been added to the gas. Notice that through the entire course of this cycle the Coulomb Blockade gap is always equal to e^2/C even at a conductance peak (Case:3).

in a straight forward manner. This calculation has been carried out by I.O. Kulik and R.I. Shekhter[114] and more recently in a concise form by L.I. Glazman and R.I. Shekhter[123]. In Chapter 4 we will discuss a lineshape theory that extends the theory of Kulik and Shekhter to a regime where the band of filled and empty states in the model we have been discussing is replaced by a set of discrete levels[67][68]. A limiting case of this model reproduces the lineshape of Kulik and Shekhter. Here we simply state their results. From Kulik and Shekhter, at sufficiently low temperatures when $U \gg kT$,

$$G(V_g, T) = G_0 \frac{e|V_g|/kT}{\sinh(eV_g/kT)} \quad (3.2)$$

where G_0 is the the series conductance of the two tunnel barriers and where $V_g = 0$ corresponds to the center of a conductance peak. Equation 3.2 describes a lineshape that is symmetric, with tails that fall off as $\exp(-eV_g/kT)$, and with an amplitude that is temperature independent, $G(0, T) = G(0)$ and a FWHM $\approx 4.35 kT/e$ which implies that the integrated area under a conductance peak increases in proportion to T .

Our lineshape data such as that in Figure 3-4 can be fit very well with the expression of Kulik and Shekhter. However, the temperature behavior of our data does not agree with this expression. For example, with increasing temperature the amplitude of some peaks increase while others decrease. Furthermore, Equation 3.2 predicts a linear relationship between the FWHM of a peak and kT . However, the observed relationship is more complicated. In Section 4.3, the temperature behavior of conductance peaks will be reexamined in the context of the expanded theory mentioned above.

3.4 Large-Bias I-V Characteristic

In the previous Section, the linear conductance of a small electron gas system was discussed. In this Section, a second kind of measurement is considered, specifically a

measurement of the current that passes through the system as a function of voltage between the leads at fixed V_g . The data will be interpreted in terms of the single-electron charging model explained above. Finally, computer simulations of the single-electron charging model will be discussed.

3.4.1 Current-Voltage (I - V_{ds}) Measurements

Figure 3-14 illustrates a current-voltage (I - V_{ds}) measurement at fixed gate-voltage, V_g . The gate-voltage (or in a multi-gate structure, the voltage of all the gates) is held fixed relative to one of the leads (the source). The voltage on the other lead (the drain) is then swept and the current that passes through the device is measured. The voltage between the source and drain, V_{ds} , is referred to as the drain-source voltage, in analogy to a conventional FET⁴.

3.4.2 I - V_{ds} Data

Figure 3-15 shows I versus V_{ds} measured on a device with a gate geometry such as that shown in Figure 2-6 on page 40 where V_g has been referenced to the right lead of the device. The current increases roughly exponentially, which is consistent with WKB tunneling through a barrier. Additionally, I versus V_{ds} displays a stair step relationship. This I - V_{ds} profile is referred to as the Coulomb Blockade staircase[66]. The voltage length of each stair step is ~ 0.45 mV. Figure 3-16 shows the I - V_{ds} characteristic of the same structure when V_g has been referenced relative to the right lead⁵. In this arrangement I versus V_{ds} exhibits a gap of ~ 0.75 mV about $V_{ds} = 0$

⁴In Appendix E the low-noise current amplifier used in the linear-conductance measurements is shown. For linear-conductance measurements where $V_{ds} \approx 10 \mu\text{V}$ a.c. a capacitor was placed between the current amplifier input and the signal line. This was done to block d.c. offset currents originating in the amplifier from reaching the device. In large-bias measurements this capacitor needs to be removed from the current amplifier circuit. Actual measurements were conducted by riding a $10 \mu\text{V}$ a.c. signal at 8.5 Hz on top of V_{ds} and measuring the dynamic conductance of device. The dynamic conductance which was later integrated to give I versus V_{ds} .

⁵It is understood that “right” and “left” in this case is an arbitrary designation

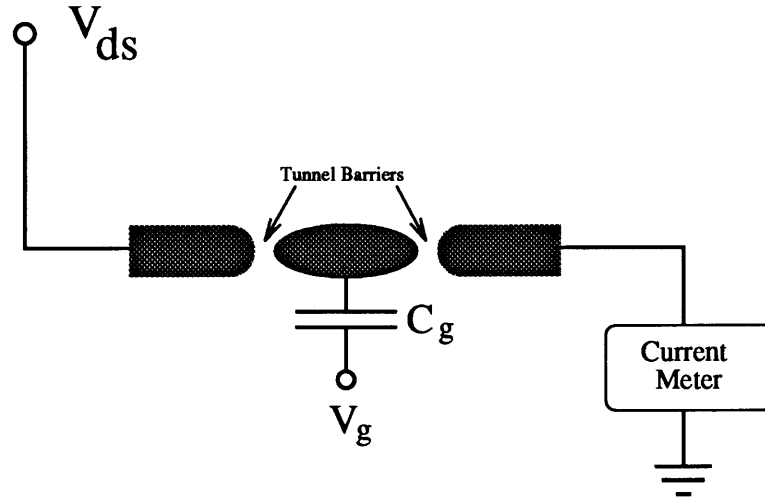


Fig. 3-14. The measurement configuration for large-bias current-voltage measurements at fixed V_g . Actual measurements were conducted by riding a $10\ \mu\text{V}$ a.c. signal at 8.5 Hz on top of V_{ds} and measuring the dynamic conductance of device. The dynamic conductance which was later integrated to give I versus V_{ds} .

after which I increases roughly exponentially with V_{ds} . However in this case, unlike the data in Figure 3-15, the staircase pattern is absent. In the next Section, our I - V_{ds} data will be explained in terms of single-electron charging and the tunneling diagrams introduced in Section 3.3. This explanation lends itself readily to computer simulation which will be covered in Section 3.4.4.

3.4.3 Single-Electron Charging I - V_{ds} Characteristics

We now extend the diagram in Figures 3-11–3-13 to the case of asymmetric barriers. Figure 3-17(a) shows the case where the right barrier is much less transmitting than the left barrier; in fact, consider the limit that where the right barrier is so large that electrons can not tunnel through it. As the chemical potential on the left lead, μ_L is raised beyond $e^2/2C$ an electron tunnels onto the small electron gas⁶. Now the small electron gas has $N + 1$ electrons on it. The diagram is then redrawn to reflect the fact that the empty band must now indicate how much energy is required to add

⁶Raising μ_L corresponds to lowering the voltage on the left lead

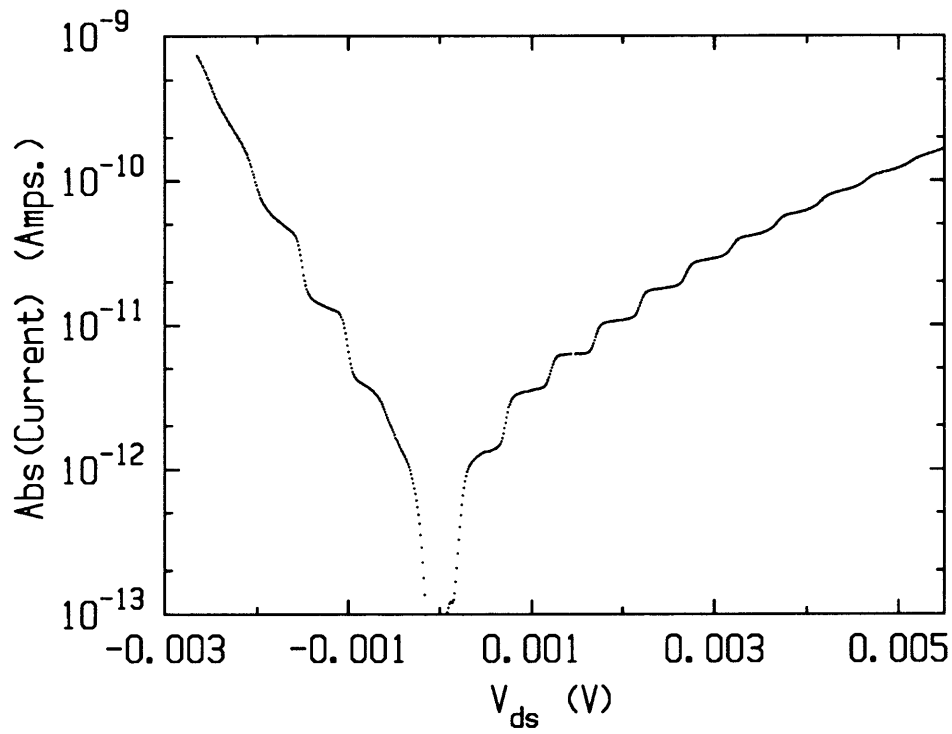


Fig. 3-15. Coulomb blockade staircase. This I - V_{ds} profile is referred to as the Coulomb Blockade staircase[66]. The voltage length of each stair step is ~ 0.45 mV.

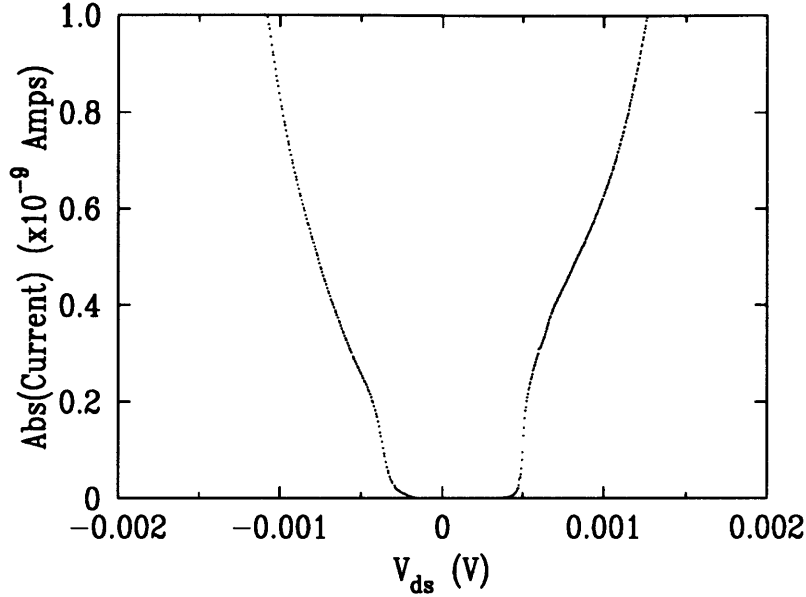


Fig. 3-16. I - V_{ds} Data showing the Colombo Blockade Suppression of Current about Zero-Bias. In this bias configuration (see discussion in text) while the Coulomb blockade as in Fig. 3-15 is absent, single-electron charging is still manifest as the suppression of current in the neighborhood of $V_{ds} = 0$.

the next $N + 2$ electron to the small electron gas. This is shown in Figure 3-17(c). In Figures 3-18(d)–(e) this process is continued until the $N + 2$ electron has been added to the gas which occurs when the chemical potential, μ_L is raised to $3e^2/2C$. In general, after the first electron has been added, each addition electron is added whenever μ_L is increased by e^2/C .

Now imagine that the right barrier instead of being completely opaque is infinitely transmitting. When μ_L is raised beyond $\frac{1}{2}U$ the $N + 1$ electron tunnels onto the gas through the left barrier. The process happens very quickly since the left barrier is very transmitting. Next, over a much longer time period, this electron eventually tunnels through the right barrier, onto the right lead. Quickly following this process, an electron tunnels from the left lead into the gas restoring the charge state of the gas to $N + 1$ electrons. This process occurs even faster if μ_L is further increased, but still kept below $3e^2/2C$ so that the $N + 2$ electron can not yet tunnel

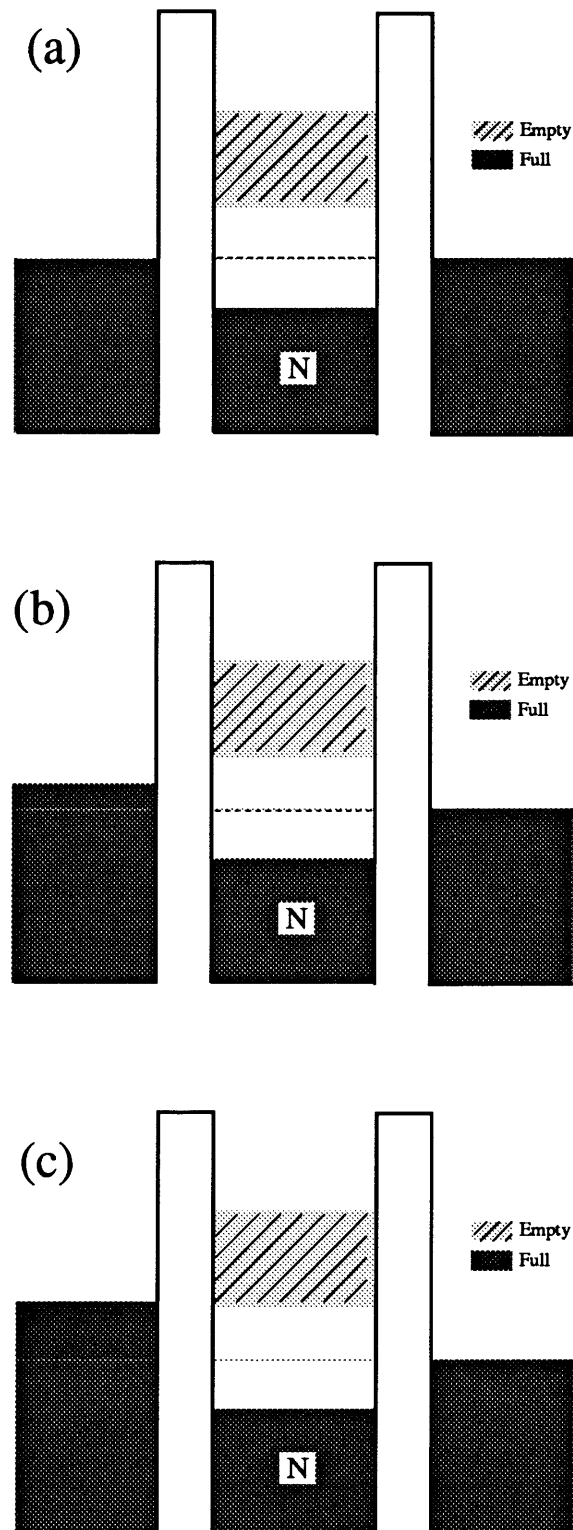


Fig. 3-17. Figure 1 of 2 showing the mechanism that gives rise to the Coulomb-blockade staircase. The diagrams are explained in the text.

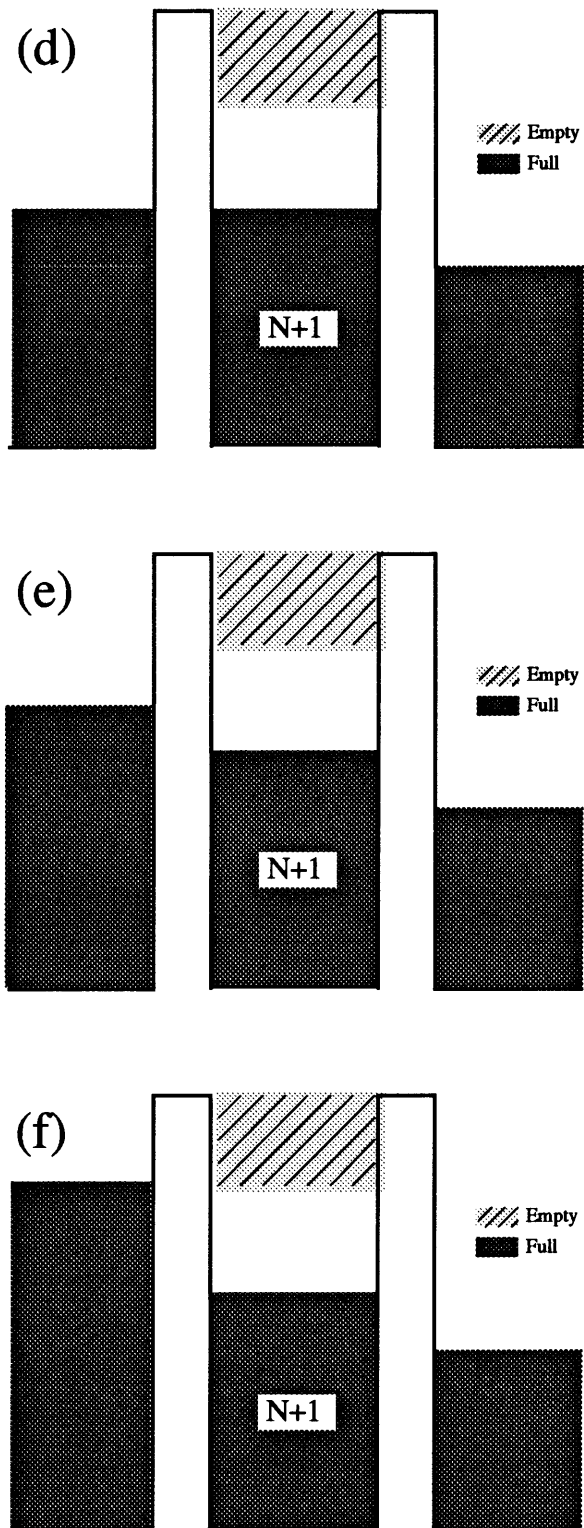


Fig. 3-18. Figure 2 of 2 showing the the mechanism that gives rise to the Coulomb-blockade staircase. The diagrams are explained in the text.

onto the gas⁷. However, even though this step occurs faster, the rate limiting step for transport between the leads is still the second tunneling step across the weakly transmitting right barrier. Consequently, increasing μ_L does not change the rate of current flow, and I has a plateau in V_{ds} . Finally, when μ_L is increased beyond $\frac{3}{2}U$ the $N + 2$ electron can tunnel into the small electron gas. At this point the current jumps to a second plateau. So in simple terms, this is the effect that gives rise to the Coulomb blockade staircase seen in the data of Figure 3-15.

A similar argument explains the I - V_{ds} data of Figure 3-16 which exhibits a Coulomb gap following by a relatively featureless rise in I with increasing V_{ds} . In this case the chemical potential is being raised on the side of the large barrier. As soon as V_{ds} passes $\frac{1}{2}U/e$ an electron can tunnel into the small electron gas. Then it rapidly tunnels out through the other barrier which is much more transmitting. This returns the charge state of the gas to N electrons, and therefore the gas never contains more than $N + 1$ electrons. Therefore, increasing V_{ds} will only increase the rate at which the $N + 1$ electron tunnels into the gas but will never result in the gas being occupied by more than $N + 1$ electrons. Consequently, the I - V_{ds} characteristic is relatively featureless past the initial Coulomb blockade gap.

The further V_{ds} is increased the faster the $N + 1$ electron tunnels into the gas, and even if V_{ds} is increased by several multiples of U/e the tunneling rate is still limited by the $N + 1$ electron tunneling into the gas.

3.4.4 Computer Modeling of Single Electron Charging at Zero Temperature

The process of single electron charging under large-bias conditions at zero temperature readily lends itself to computer modeling. In fact, if the barriers are assumed to be ohmic conductors, meaning that the tunneling rate across a barrier is linearly

⁷This process occurs faster because there are more empty states available to tunnel into as μ_L is increased

proportional the voltage drop experienced by the tunneling electron, then at zero temperature this is an exactly solvable model. The solution proceeds as follows: The barriers are ohmic which means that a resistance can be assigned to the left and right barriers respectively, R_L and R_R . Next, for simplicity assume that at $V_{ds} = 0$, and that the gate voltage is tuned so that the equilibrium charge in the small electron gas is equal to a integer number of electrons. This is the condition shown in Figure 3-17(a). Now if n electrons are added to the small electron gas above its equilibrium charge state of eN the potential of the small electron gas increases to $\frac{e}{C}(n - \frac{1}{2})$. (If this point is confusing refer back to Figure 3-17.)

Next, consider the current which flows across the left barrier. (For the remainder of this discussion assume that the right lead is grounded and V_{ds} is the potential on the left lead.) When there are initially n electrons in the gas the current associated with an electron tunneling from the left lead into the gas and raising its charge state to $n + 1$ is

$$\begin{aligned}
 I_L(n|n+1) &= \frac{1}{R_L} \left[V_{ds} - \frac{e}{C} \left((n+1) - \frac{1}{2} \right) \right] \quad \text{when } V_{ds} \geq \frac{e}{C} \left((n+1) - \frac{1}{2} \right) \\
 &= 0 \quad \text{when } V_{ds} < \frac{e}{C} \left((n+1) - \frac{1}{2} \right)
 \end{aligned} \tag{3.3}$$

Similarly the current associated with an electron tunneling from the gas onto the right lead when the initial charge state of the gas is n is

$$\begin{aligned}
 I_R(n|n-1) &= \frac{1}{R_R} \left[V_{ds} - \frac{e}{C} \left(n - \frac{1}{2} \right) \right] \quad \text{when } V_{ds} \geq \frac{e}{C} \left(n - \frac{1}{2} \right) \\
 &= 0 \quad \text{when } V_{ds} < \frac{e}{C} \left(n - \frac{1}{2} \right)
 \end{aligned} \tag{3.4}$$

In steady-state there exists a probability, $\mathcal{P}(n)$, that there will be n electrons in the small electron gas. Note that $\mathcal{P}(n)$ is not given by Fermi-Dirac statistics since this is

a non-equilibrium configuration. We will calculate $\mathcal{P}(n)$ below. Given $\mathcal{P}(n)$ the total current that flows across the left barrier is given by

$$I_{L,total} = \sum_{n=0}^{n=\infty} \mathcal{P}(n) I_L(n|n+1) \quad (3.5)$$

Furthermore, in steady-state $I_L = I_R$. This in turn means that $I = I_{L,total}$. So the only step remaining to solve for I is to calculate $\mathcal{P}(n)$. This is accomplished by solving the following rate equation which in steady-state must be equal to zero:

$$\begin{aligned} \frac{d}{dt}(\mathcal{P}(n)) = 0 = & \mathcal{P}(n+1)I_R(n+1|n) + \mathcal{P}(n-1)I_L(n-1|n) \\ & - \mathcal{P}(n)I_R(n|n-1) - \mathcal{P}(n)I_L(n|n+1) \end{aligned} \quad (3.6)$$

This set of equations can be solved exactly. Begin by assigning $\mathcal{P}(0)$ any value, which is conveniently chosen to be $\mathcal{P}(0) = 1$. Next, set n equal to 0 in Equation 3.6. Equation 3.6 then reduces to

$$0 = \mathcal{P}(1)I_R(1|0) - I_L(0|1) \quad (3.7)$$

yielding a value for $\mathcal{P}(1)$. We now have values for $\mathcal{P}(0)$ and $\mathcal{P}(1)$. The next step is to set $n = 1$ in Equation 3.6, which with values for $\mathcal{P}(0)$ and $\mathcal{P}(1)$ will give a value for $\mathcal{P}(2)$. This process is iterated until values for $\mathcal{P}(n)$ for all n have been determined. Finally these values are normalized so that $\sum_n \mathcal{P}(n) = 1$. $\mathcal{P}(n)$ into Equation 3.5 solves for I exactly.

The method of solution outlined above is referred to as the method of detailed-balance for the steady-state condition of a kinetic equation. It assumes implicitly that tunneling processes are uncorrelated and stochastic[68]. (A more sophisticated model of the electron gas will be discussed in Chapter 4 whose solution proceeds a similar manner.) A computer program used to solve for I as a function of V_g , given R_L , R_R , and C , is contained in Appendix F. For reference, calculated plots of I versus

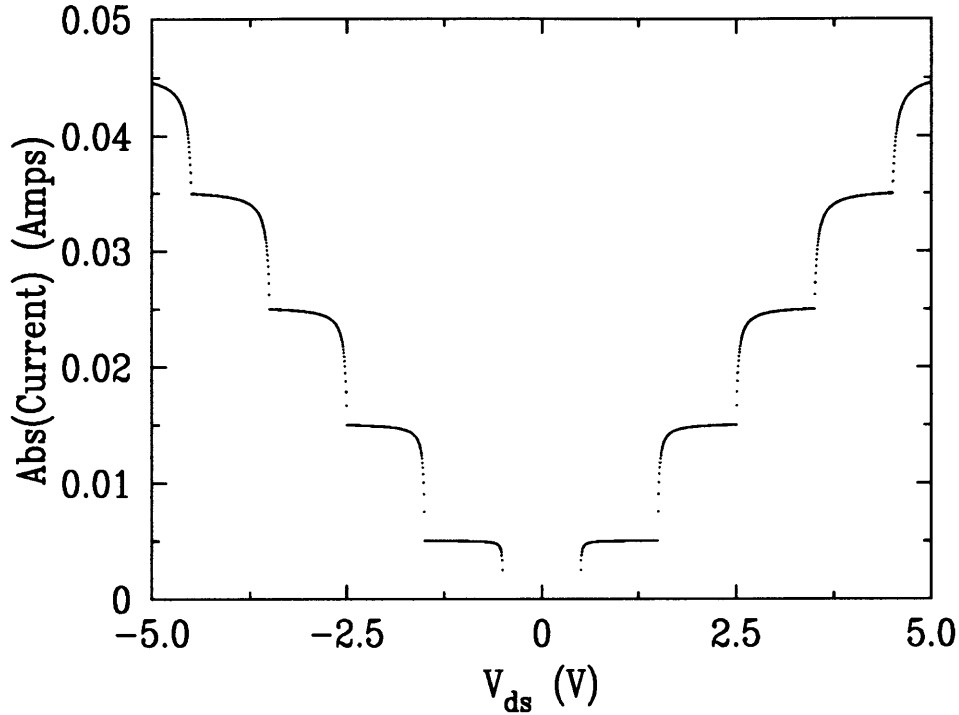


Fig. 3-19. Calculated I - V_{ds} showing the coulomb blockade staircase. The resistance of the barrier on the biased side of the device was set equal to $1\ \Omega$ and the resistance on the grounded side was set equal to $99\ \Omega$. C was set equal to $e/C = 1\ \text{V}$. (Note that the resistances in this calculation are chosen to scale I to V_{ds} . In Section 6.5 we will discuss why R must be greater than h/e^2 .)

V_{ds} for symmetric barriers and asymmetric barriers are shown in Figures 3-19–3-21.

3.5 Capacitance in Multiple Gate Geometries

The abstracted schematic of our small electron gas system introduced at the beginning of this Chapter in Figure 3-1 on page 59 contains only one gate, and our discussion of the electron gas system up until this point has been formulated as if there was only one gate acting on the small electron gas. Actual structures, however, contain several independently controllable gates. See for example Figure 2-7 on page 41. Expanding our discussion to incorporate structures with multiple capacitors requires only a brief elaboration on the ideas already presented.

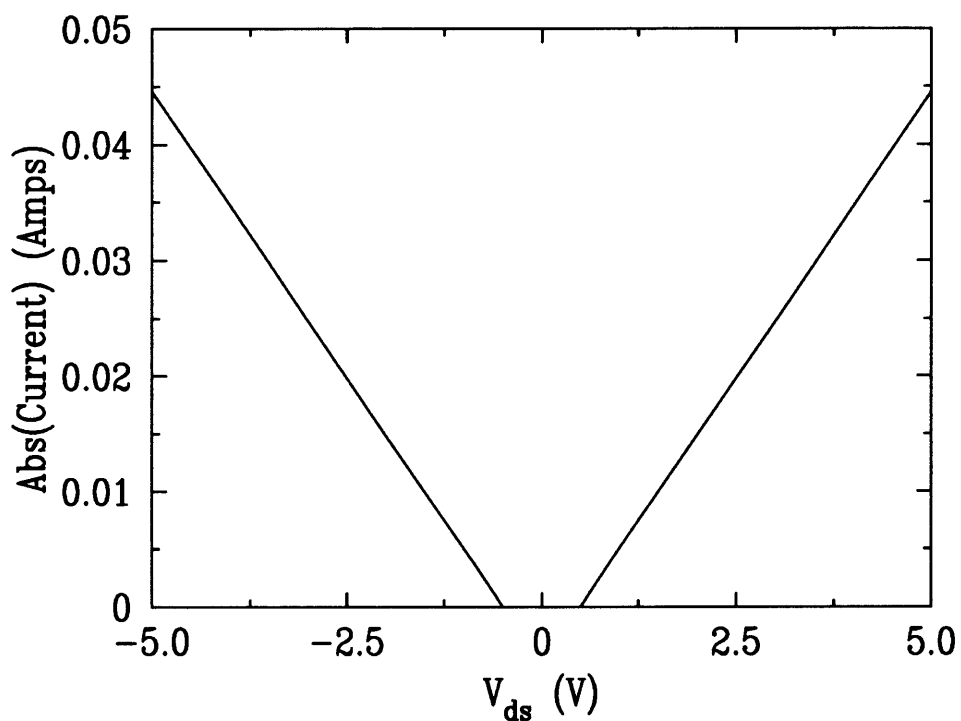


Fig. 3-20. Calculated I - V_{ds} showing the coulomb suppression of current in the neighborhood of $V_{ds} = 0$ for asymmetric barriers. The resistance of the barrier on the biased side of the device was set equal to $99\ \Omega$ and the resistance on the grounded side was set equal to $1\ \Omega$. C was set equal to $e/C = 1\ \text{V}$.

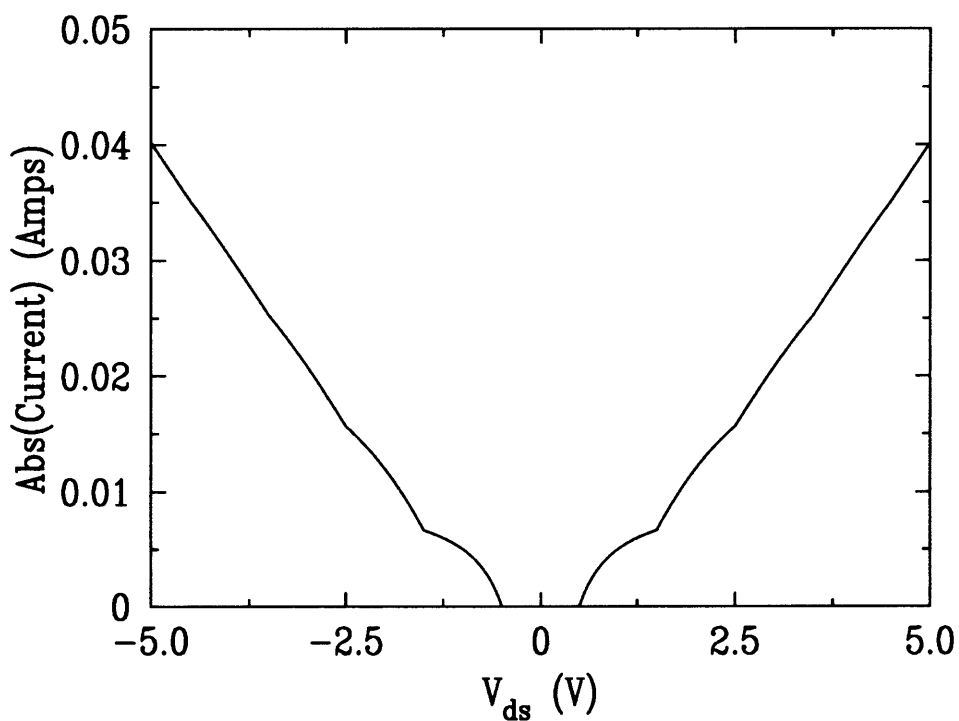


Fig. 3-21. Calculated I - V_{ds} showing the coulomb suppression of current in the neighborhood of $V_{ds} = 0$ for symmetric barriers. The resistance of the barrier on the biased side of the device was set equal to 50Ω and the resistance on the grounded side was set equal to 50Ω . C was set equal to $e/C = 1$ V.

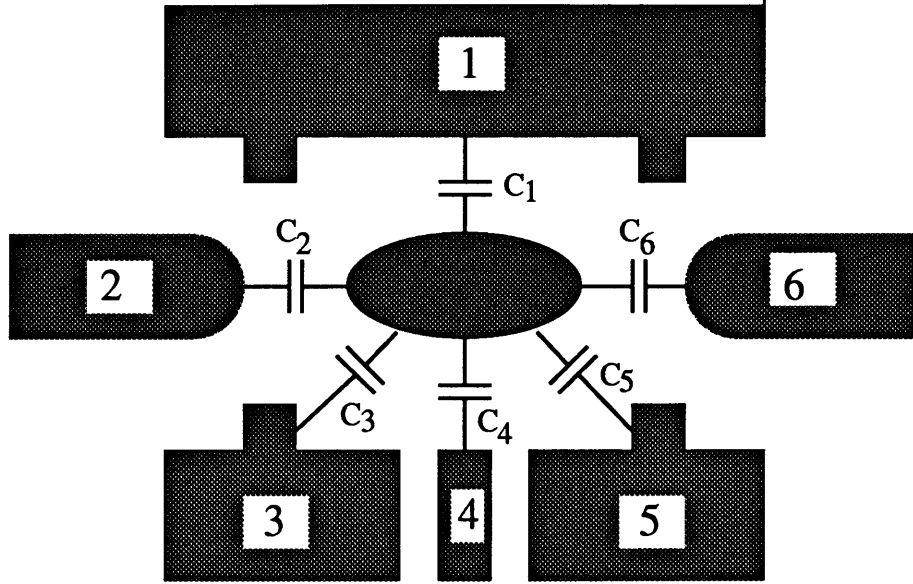


Fig. 3-22. A representation of a device showing its relevant capacitances. This view is based on the structure shown in Figure 2-7.

Figure 3-22 is a representation of the structure shown in Figure 2-7. Figure 3-22 shows the small electron gas capacitively coupled to four different gates in addition to both its left and right leads. (Since the leads are composed of a free electron gas they are metallic and for the purposes of this discussion they can be treated in the same manner as the gates.) The treatment of capacitance in a multiconductor system, such as that in Figure 3-22, can be found in many references on classical electrostatics[124]. We recall from classical electrostatics that given the capacitive coupling expressed in Figure 3-22, the change in the total charge of the small electron gas, ΔQ , is given by

$$\Delta Q = \sum_i \Delta V_i C_i \quad (3.8)$$

where C_i is the capacitance between the i^{th} gate and the small electron gas and where

$$\Delta V_i = V_i - V_{gas} \quad (3.9)$$

where V_i is the voltage of the i^{th} conductor and V_{gas} is the potential of the small

Capacitor	Value
C_1	69 aF
C_2	66 aF
C_3	35 aF
C_4	12 aF
C_5	26 aF
C_6	76 aF
$C \equiv \sum_i C_i$	284 aF

Table 3.1. The measured values of the capacitances in Figure 3-22. $C \equiv \sum_i C_i$. Note 1 aF = 10^{-18} F

electron gas. Actually, though we have called C_i a capacitance it has been pointed out that C_i is more properly referred to as a capacity[125] or as a diagonal member of the heterostatic, multiterminal capacitance matrix[123]. We will, however, continue to referred to them as capacitances.

In Section 3.3, we said that the spacing between peaks, ΔV_g was equal to e/C . This is the case when there is only one independent gate capacitively coupled to the small electron gas. We can generalize to the case of multiple independent gates. When gate i is swept, holding all other gates at a fixed bias, the spacing between peaks is e/C_i , where C_i is the capacitance between the gas and the gate being swept. We can see this by setting ΔQ in Equation 3.8 equal to e . Similarly, the same equation gives the width of the Coulomb blockade gap seen in a plot of $I-V_{ds}$ is equal to $e/(C - C_{bias})$ when changing the chemical potential on one of the leads, where $C \equiv \sum_i C_i$ and C_{bias} is the capacitance between the gas and the biased lead. So by measuring the periodicity of conductance peaks for individual gates and by measuring the Coulomb blockade gap when biasing on different leads, it is possible to determine the values of each of the capacitances expressed in Figure 3-22 for the device shown in Figure 2-7 on page 41. The results of such a measurement are shown in Table 3.1.

The same procedure for determining C was carried out on a second structure which was very similar to the structure above except that this second structure had a conducting back gate. (See Figure 2-10 for a schematic of this structure fabricated

by U. Meirav *et al.*) Initially, it was thought that bringing an additional back gate in close proximity to the small electron gas would result in a significant addition to the total capacitance of the system. However, the total capacitance of the structure in the previous case was measured to be 284 aF. This result is very close to the value of C in the case that there was no back gate (239 aF in Reference [52]). Furthermore, the capacitance of this back gate to the small electron gas was determined to be 124 aF, and the capacitance of all the gates patterned on the surface of the wafer in the second device was determined to be 115 aF. In other words, while bring a back gate in close proximity to the small electron gas was observed to change the capacitance between individual electrodes and the small electron gas, the total capacitance of the small electron gas was not significantly altered.

The apparent mystery of these results is resolved by recalling that capacitances in a multiconductor system need to be calculated self-consistently. When a conductor is added or subtracted from the system the capacitance must be recalculated. For a discussion of this refer to Reference [126]. One question raised by this discussion is what if it were possible to remove away all the conductors illustrated in Figure 3-22. Then what would be the total capacitance of the small electron gas, C . This is the same trying to determine the capacitance between the small electron gas and a conductor infinitely far away. This capacitance is referred to as the self-capacitance of the small electron gas, C_{self} . When there are no conductors in the vicinity of the small electron gas, $C = C_{self}$. Bringing additional conductor in the vicinity of the small electron gas can only increase the magnitude of C . So e^2/C_{self} is the theoretical maximum value of the Coulomb charging energy for a given small electron gas.

An estimate of C_{self} can be made by approximating a particular small electron gas as a conducting sphere of radius a . The self capacitance of a sphere is $4\pi\epsilon_0 a$. From our data, we know that $kT \leq 10e^2/C$ in order to observe single electron charging effects. Using the self capacitance of the sphere or radius a for C gives $T[\text{K}] = 1,700/a[\text{nm}]$. So if only the self-capacitance of a system need be

considered, then to see single electron charging effects at room temperature a needs to be $\sim 6\text{nm}$.⁸ What is less clear, however, is the following: Electrically coupling to a small electron gas requires bringing probes close enough to it that electrons can tunnel on and off of the gas. The capacitance between the probes and the gas may be the dominant contribution to C in actual systems. For a discussion of single-electron charging effects at high temperatures using metal particles see Reference [127].

One last consideration: When the voltage on a particular gate, V_i is varied while the voltage on all the other gates is held fixed, the potential of the small electron gas, V_{gas} varies by an amount proportional to V_i . This “lever arm” is given by setting $\Delta Q = 0$ in Equation 3.8 yielding

$$V_{gas} = \frac{C_i}{C} V_i \equiv \alpha V_i \quad (3.10)$$

One implication of this is that in Equation 3.2 which predicts the lineshape of a thermally broadened conductance peak in the charging model, V_g should be replaced by αV_g .

⁸An estimate of the self-capacitance in our devices can be made by setting $a = 300\text{nm}$, which yields $U = 0.49\text{meV}$ (5.7 K).

Chapter 4

Single Electron Charging and a Quantized Energy Spectrum

4.1 Introduction

In the previous Chapter we discussed the electronic transport properties of a small electron gas in terms of an entirely classical model of single electron charging. The energy scale in this model was set by the capacitive energy to required to add one electron to the gas, $U = e^2/C$, the Coulomb charging energy. We found this energy to be $\sim 0.7\text{ meV}$ in a typical structure.

Now we consider a second relevant energy scale. At this point, we refer back to the discussion of Section 2.3 on page 53. In that discussion it was pointed out that in addition to the energy scale set by single electron charging, a second energy scale is relevant to a small electron gas. This is its single-particle energy level spacing, $\Delta\epsilon$. In Section 2.3 $\Delta\epsilon$ was estimated to be $\sim 0.04\text{ meV}$ or roughly an order of magnitude smaller than U . The fact that $\Delta\epsilon$ is smaller than U accounts for the fact that a classical model of electron charging explains much of the behavior of the

small electron gas system discussed in the previous chapter. However, this model does not fully account for all the behavior of these systems. It was pointed out in Section 3.3.3 on page 74 that the temperature behavior of conductance peaks does not agree with the predictions of the classical charging model. This and other observations along with the fact that estimates of U and $\Delta\epsilon$ differ by only an order of magnitude are compelling reason to reexamine the classical charging model in the context of a nonnegligible quantum energy scale.

The remaining Chapters in this thesis discuss our observations of the interplay between single electron charging and what will be referred to as quantum effects. This chapter proceeds by first discussing a straightforward extension of the classical charging model that incorporates the discrete energy spectrum of a small electron gas. Next, we show that our measurements are in fact very sensitive to this spectrum and that it is possible to map this spectrum as a function of gate-voltage. The remainder of this Chapter compares the observed temperature behavior of conductance peaks with the prediction of this extended charging model.

4.2 The Discrete Energy Spectrum of a Small Electron Gas

In Figure 3-10 on page 72 the classical charging model was described through the diagram reproduced in Figure 4-1(a). In this diagram, the empty and filled states of the small electron gas are represented by a continuous band of states. In light of the discussion above, it is desirable to somehow expand this picture to include the discrete nature of the energy spectrum of the small electron gas. A simple way of doing so is to replace the continuous bands in Figure 4-1(a) with discrete energy levels. This representation is shown in Figure 4-1(b). Just as before in the case of continuous bands, the empty states indicate the allowable energies for adding a single electron to the small gas, and the difference between the Fermi level in the leads and energy of

a filled state indicates how much energy is required to remove a single electron from the small gas.

Figure 4-2 demonstrates how the discrete level spectrum represented in Figure 4-1(b) may be expected to be manifest in an I versus V_{ds} measurement such as those discussed previously in Section 3.4.2. At $T = 0$, each time the quasi-Fermi level in the biased lead passes an additional level I changes by discrete amount. The change in I can be positive or negative, and depends on how easily electrons tunnel into the new level. In general, if the new level is well coupled to the leads (tunneling is easy) the change in I will be positive. However, if the level is very poorly coupled the change in I can be negative (giving negative differential conductance). This is because once an electron tunnels into this level, a relatively long time is required for the electron to tunnel out through the second barrier, and consequently, I decreases.

The implication of Figure 4-2 is that by measuring I as a function of V_{ds} , the discrete level spectrum of a small electron gas can be ascertained. Figure 4-3 shows I versus V_{ds} in a structure similar to the one seen in Figure 2-6 on page 40. For comparison with I - V_{ds} data shown in Chapter 3 the same data is also plotted on a semi-logarithmic scale in Figure 4-4. In these traces, the Coulomb gap of ~ 0.75 mV is evident in the neighborhood of $V_{ds} = 0$. Also, in the direction of positive V_{ds} , the second step of a Coulomb blockade staircase is seen at $V_{ds} \approx 1.1$ mV.

In order to more clearly identify small changes in I with V_{ds} the derivative of I with respect to V_{ds} is plotted in Figure 4-5¹. The trace in Figure 4-5 exhibits a number of peaks in dI/dV_{ds} in addition to a smaller number of valleys below $dI/dV_{ds} = 0$ which correspond to point of negative differential conductance for example at $V_{ds} \approx 0.6$ mV. Referring back to Figure 4-2, peaks in dI/dV_{ds} and minima in valleys of negative dI/dV_{ds} correspond to V_{ds} voltages at which the quasi-Fermi level in the biased lead is aligned with a discrete level in the electron gas. From the plot of

¹In actuality, dI/dV_{ds} as a function of V_{ds} is what our measurement apparatus records and these measurement are integrated to yield I versus V_{ds} . Refer to the discussion in Section 3.4.1.

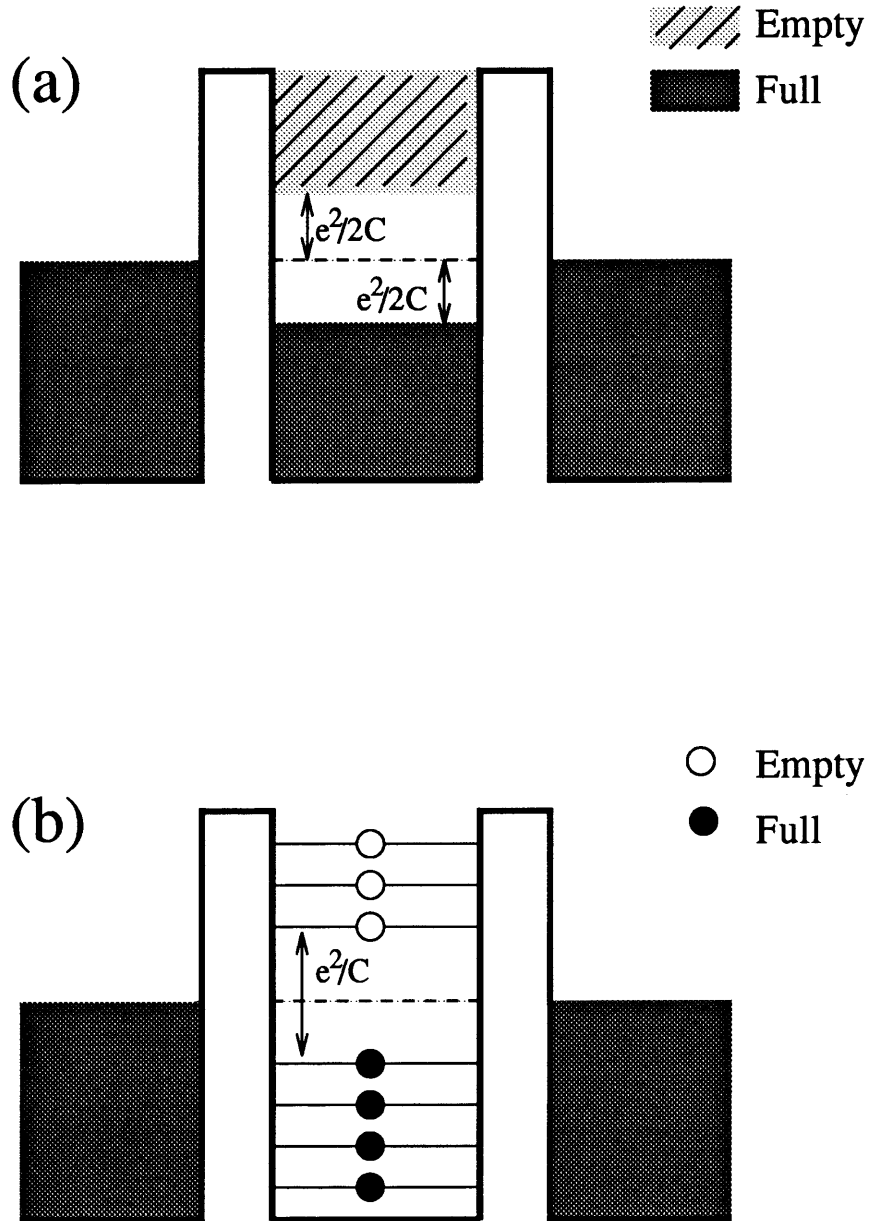
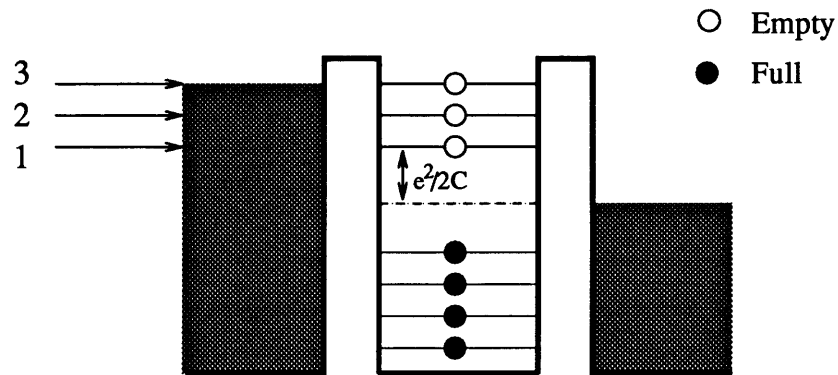
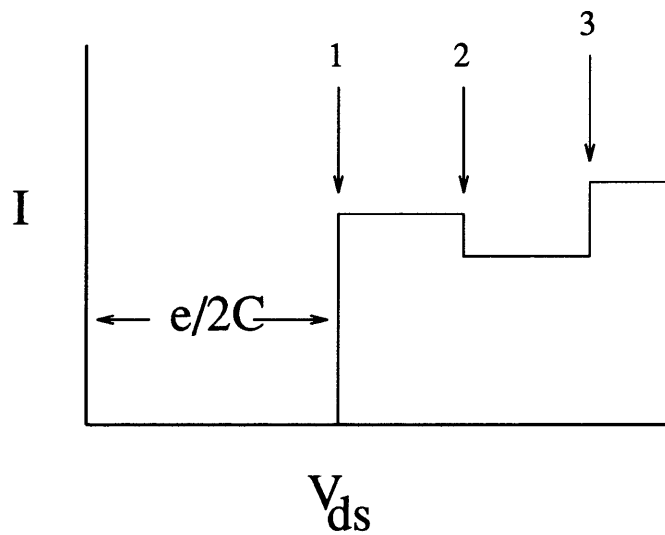


Fig. 4-1. Introduction to the discrete level spectrum in a small electron gas. Figure (a) is a reproduction of the schematic introduced in the previous chapter in relation to classical single-electron charging. Figure (b) shows a second schematic of the small electron gas where the continuous bands of states in (a) have been redrawn as sets of discrete levels.



(a)



(b)

Fig. 4-2. Current-voltage characteristics in the presence of a discrete level spectrum. At $T = 0$, as the quasi-Fermi level in the bias lead passes a discrete level, the current changes by a discrete amount. The shift in I depends on the rate at which electron can tunnel into and out of individual levels.

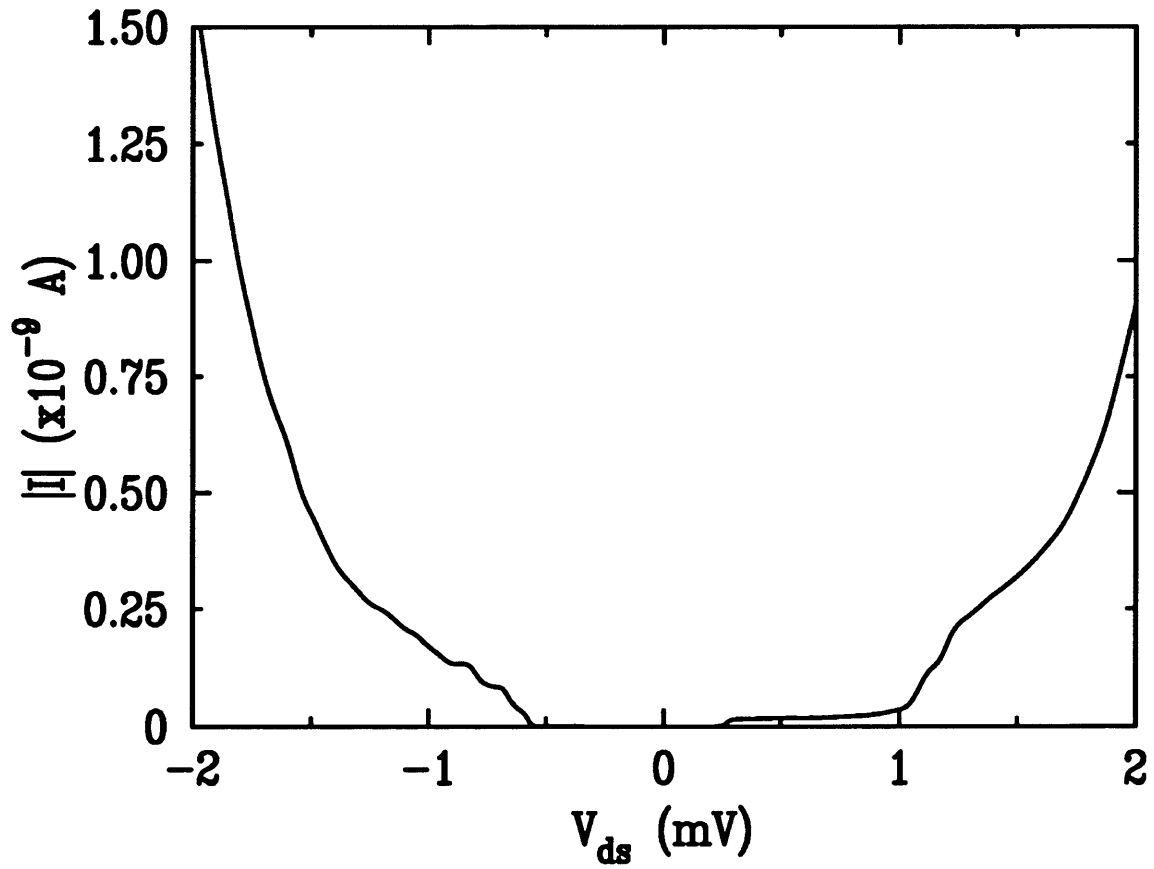


Fig. 4-3. I versus V_{ds} . This data is taken in a magnetic field, $B = 3.35 \text{ T}$ using a structure similar to the one seen in Figure 2-6 on page 40.

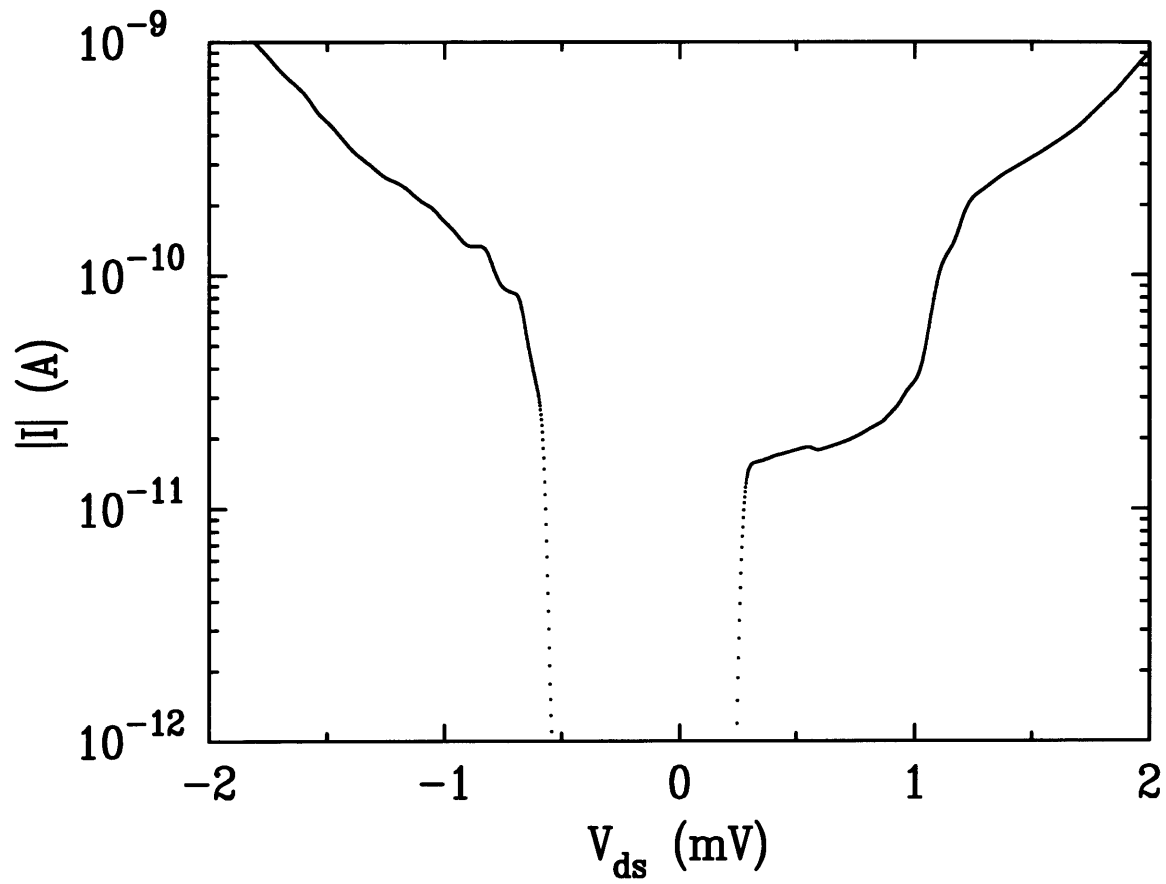


Fig. 4-4. $\log(I)$ versus V_{ds} . This is the same data as plotted in Figure 4-3.

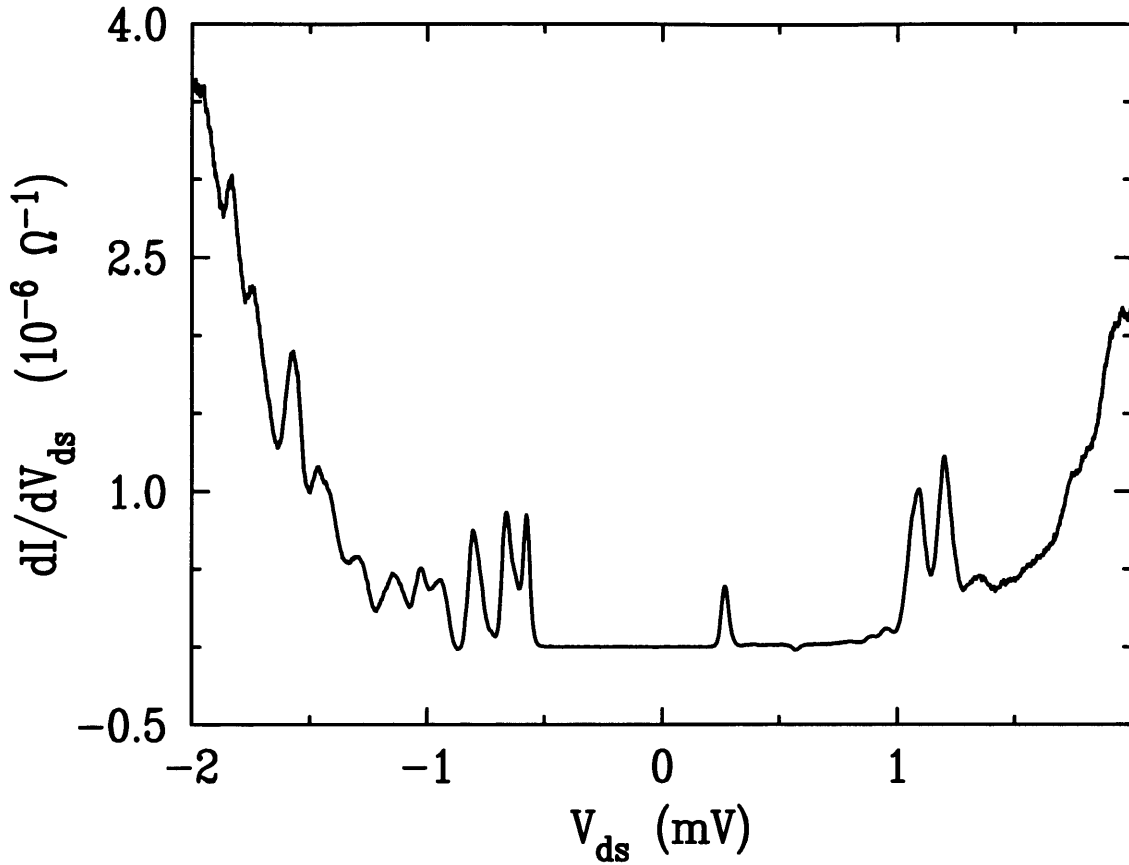


Fig. 4-5. dI/dV_{ds} as a function of V_{ds} for $B = 3.35$ T. Peaks in dI/dV_{ds} and minima in valleys of negative dI/dV_{ds} correspond to V_{ds} voltages at which the quasi-Fermi level in the biased lead is aligned with a discrete level in the electron gas.

dI/dV_{ds} versus V_{ds} in Figure 4-5 the level spectrum of the small electron gas can be determined[128, 129, 130]. This spectrum is plotted in Figure 4-7. A Coulomb-blockade gap in the tunnel density of states is clearly seen in addition to levels with a typical spacing of $\Delta\epsilon \approx 0.1$ meV.

A few words need to be said about this plot. First, keep in mind that the quasi-Fermi level of the biased lead is raised when V_{ds} is lowered. So going between a plot of dI/dV_{ds} versus V_{ds} and a plot of the level spectrum as in Figure 4-7 requires inverting an axis. Furthermore, the relationship between ΔV_{ds} and the Fermi level in the lead depends on C_{bias} as explained in Section 3.5. This dependence is found to

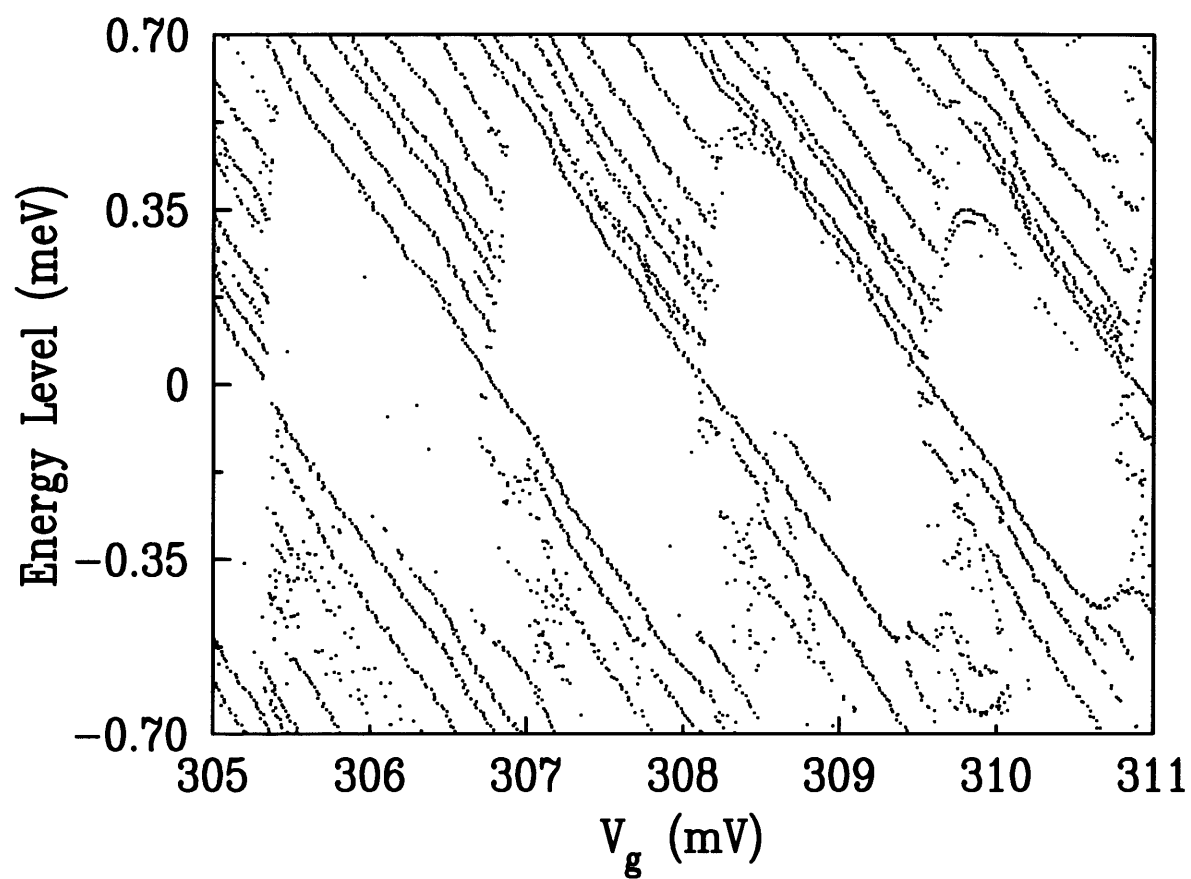


Fig. 4-6. The level spectrum of a small electron gas as a function of V_g .

be $e\Delta V_{ds}(1 - C_{bias}/C)$ where C is the total capacitance of the small electron gas. In this case, $\Delta V_{ds}(1 - C_{bias}/C) = 0.80$.

4.2.1 The Level Spectrum as a Function of V_g

The above procedure maps the discrete level spectrum of a small electron gas at a fixed gate-voltage, V_g . By repeating this procedure at successively incremented gate-voltages it is possible to map the level spectrum of a small electron gas as a function of gate-voltage. Figure 4-6 shows the results of such a measurement. As V_g is increased the levels shift downward in energy. The Coulomb-blockade gap also shifts downward until the top of the gap is aligned with the Fermi-level in the leads at which point the gap realigns and so that the bottom of the gap is commensurate with the Fermi level in the leads. This process of realignment which occurs periodically in V_g is due to single electron charging. Compare this behavior with the discussion of Figures (3-11)-(3-13).

It is tempting to imagine that the level-spectrum mapped in Figures 4-7 and 4-6 might find a simple explanation in terms of non-interacting, single-particle levels. This in fact was the basis of several early interpretations of this and similar data[50]. Despite the initial success of such interpretations, upon closer analysis it becomes clear that the origin of the discrete level spectrum in a small electron gas can not be explained in such simple terms. For example, consider that the data in Figure 4-6 was taken in a magnetic field, $B = 3.35$ T. At this field, single particle levels should be spin split by a Zeeman energy of $g\mu_B B = 0.076$ meV. There is no such level splitting seen in the spectrums of either Figures 4-7 or 4-6.

Chapter 5 is dedicated to interpreting our observations of the discrete level spectrum in a small electron gas. What emerges from that discussion is that electron-electron interactions not only give rise the Coulomb-gap in the tunneling density of states but also are critically importance in determining the discrete level spectrum of the gas. Chapter 5 will also present additional level spectrum data in zero magnetic

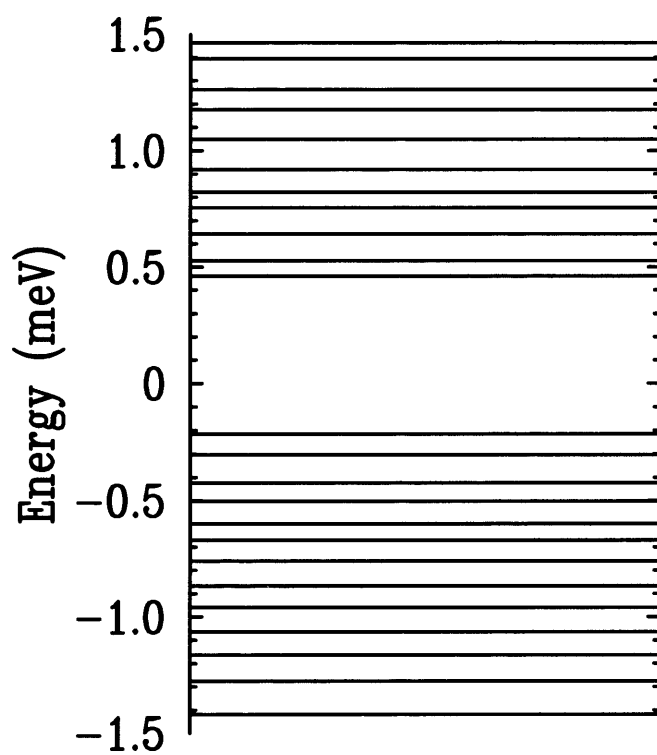


Fig. 4-7. The level spectrum determined from dI/dV_{ds} versus V_{ds} plotted in Figure 4-5. Levels are spaced by $\sim 100 \mu\text{eV}$.

field and spectrum data that shows the evolution of levels as a function of magnetic field.

4.2.2 Discrete Energy Levels and Gate Voltage Sweeps at Fixed V_{ds}

In the previous Section we presented data that showed the current, I , that passes through a small electron gas when V_{ds} is swept at fixed gate voltage, V_g . In this Section, we present additional data showing I as V_g is swept at fixed V_{ds} . (Such data corresponds to a horizontal cross section through the plot in Figure 4-6.) According to the Classical single-electron charging model discussed in Chapter 2, at successively larger V_{ds} conductance peaks broaden and possibly become skewed depending on the asymmetry of the barriers. The prediction of the charging model are shown in Figures (4-8)-(4-10) for the case of symmetric barriers, and asymmetric barriers at $T = 0$. The computer code that generated these traces is in Appendix G. Figure 4-12 shows the measured current as a function of gate-voltage for V_{ds} fixed at 0.5 mV. The trace shows broadened conductance peaks on top of which are superimposed a modulated overstructure. The spacing between peaks in the overstructure is ~ 0.2 mV. At $T \approx 250$ mK the overstructure washes out. The modulated structure corresponds to the peaks in dI/dV_{ds} versus V_{ds} at fixed V_g such as those plotted in Figure 4-5.

Figure 4-11 shows I as a function of gate voltage for V_{ds} ranging from $50 \mu\text{V}$ to $500 \mu\text{V}$ in increments of $25 \mu\text{V}$. As V_{ds} is increased, the low-bias peaks broaden and take on an asymmetric profile. In addition the broadened peaks display a modulated overstructure. This overstructure persists to $T \sim 250$ mK and is observable in both zero and finite magnetic fields. The data in Figure 4-11 is in zero-magnetic field. In Reference [52] the data in Figure 4-11 was interpreted according to a model that incorporates discrete levels into the Classical Coulomb-blockade model, just as

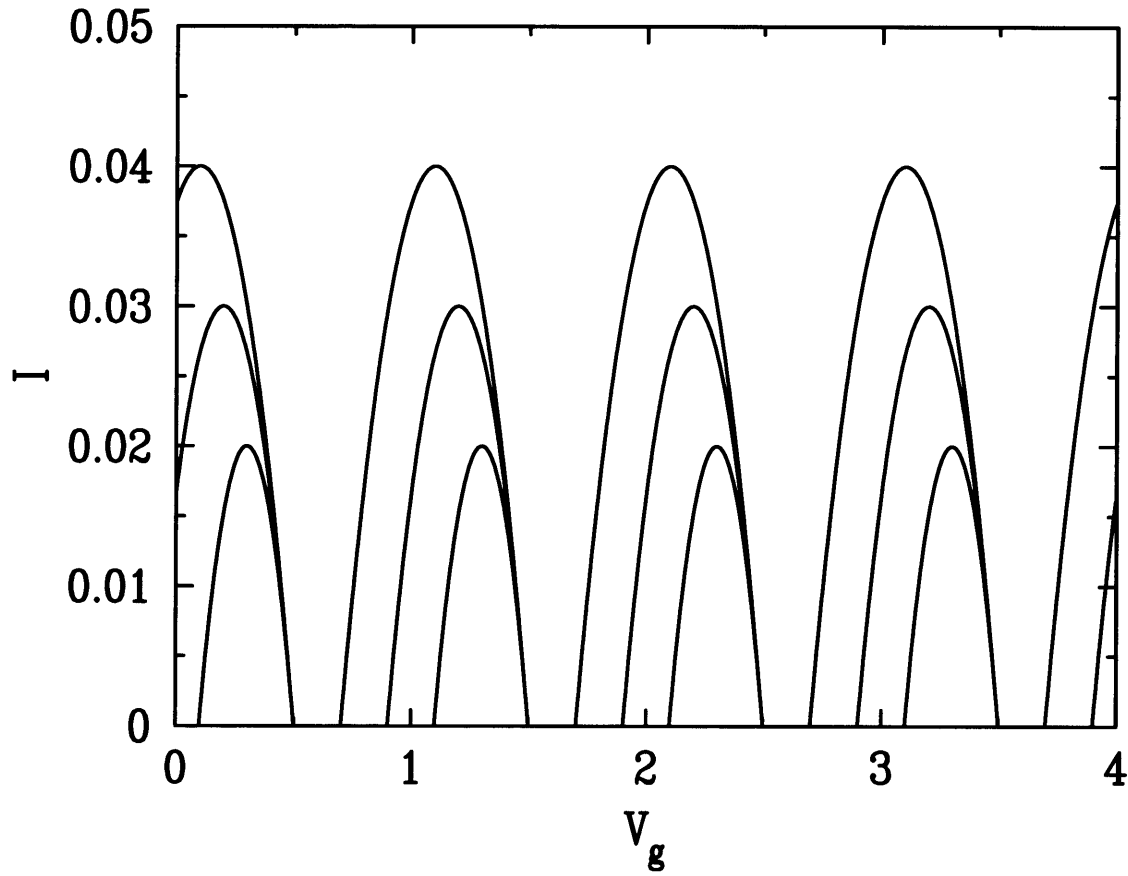


Fig. 4-8. I versus V_g for finite V_{ds} calculated in the classical model for the case of symmetric barriers. In the calculation, the resistance was the same for both the left and right barriers, $R_l = R_r \equiv 5 \Omega$ and $e/C \equiv 1$ V. The three traces correspond to $V_{ds} = 0.4$ V, 0.6 V and 0.8 V.

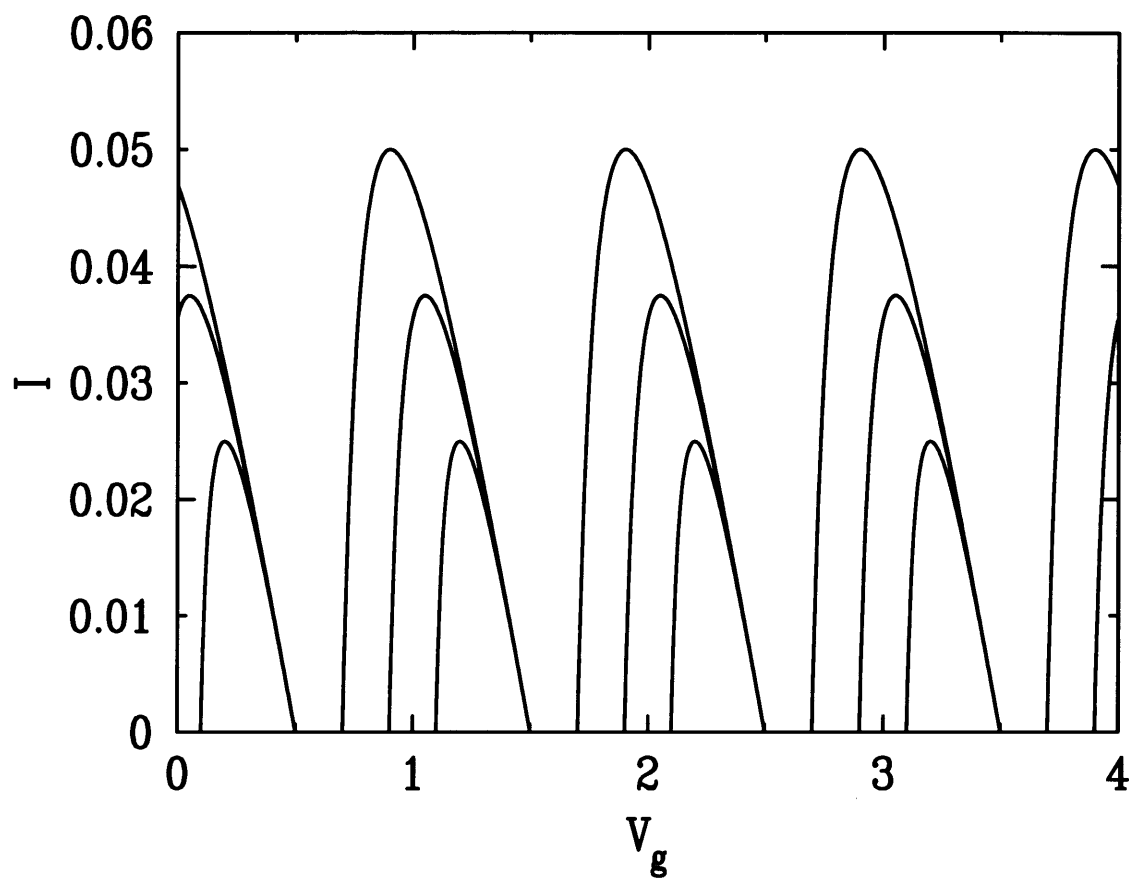


Fig. 4-9. I versus V_g for finite V_{ds} calculated in the classical model for nonsymmetric barriers, case I. In the calculation, V_{ds} raised the chemical potential on the left side of the device. $R_l \equiv 1 \Omega$, $R_r \equiv 9 \Omega$ and $e/C \equiv 1$ V. The three traces correspond to $V_{ds} = 0.4$ V, 0.6 V and 0.8 V.

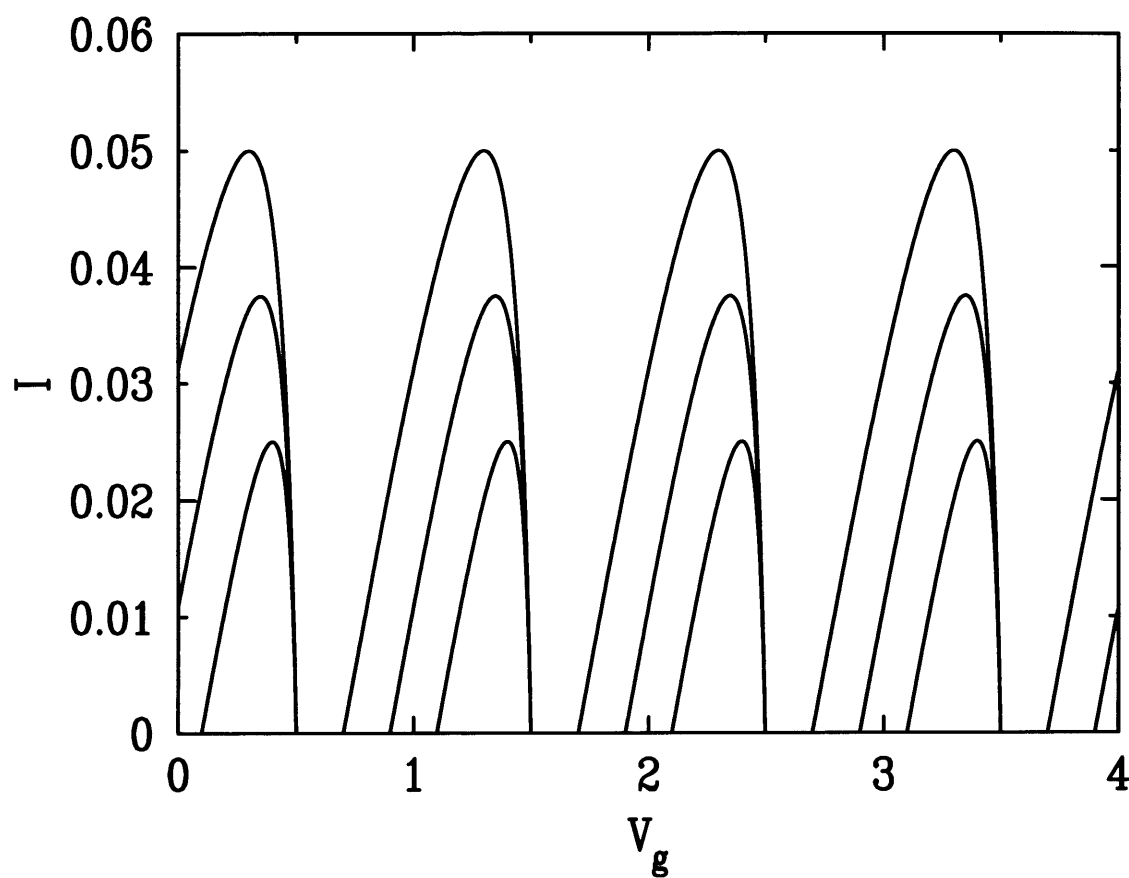


Fig. 4-10. I versus V_g for finite V_{ds} calculated in the classical model for nonsymmetric barriers, case II. In the calculation, V_{ds} raised the chemical potential on the left side of the device. $R_l \equiv 9\ \Omega$, $R_r \equiv 1\ \Omega$ and $e/C \equiv 1\ \text{V}$. The three traces correspond to $V_{ds} = 0.4\ \text{V}$, $0.6\ \text{V}$ and $0.8\ \text{V}$.

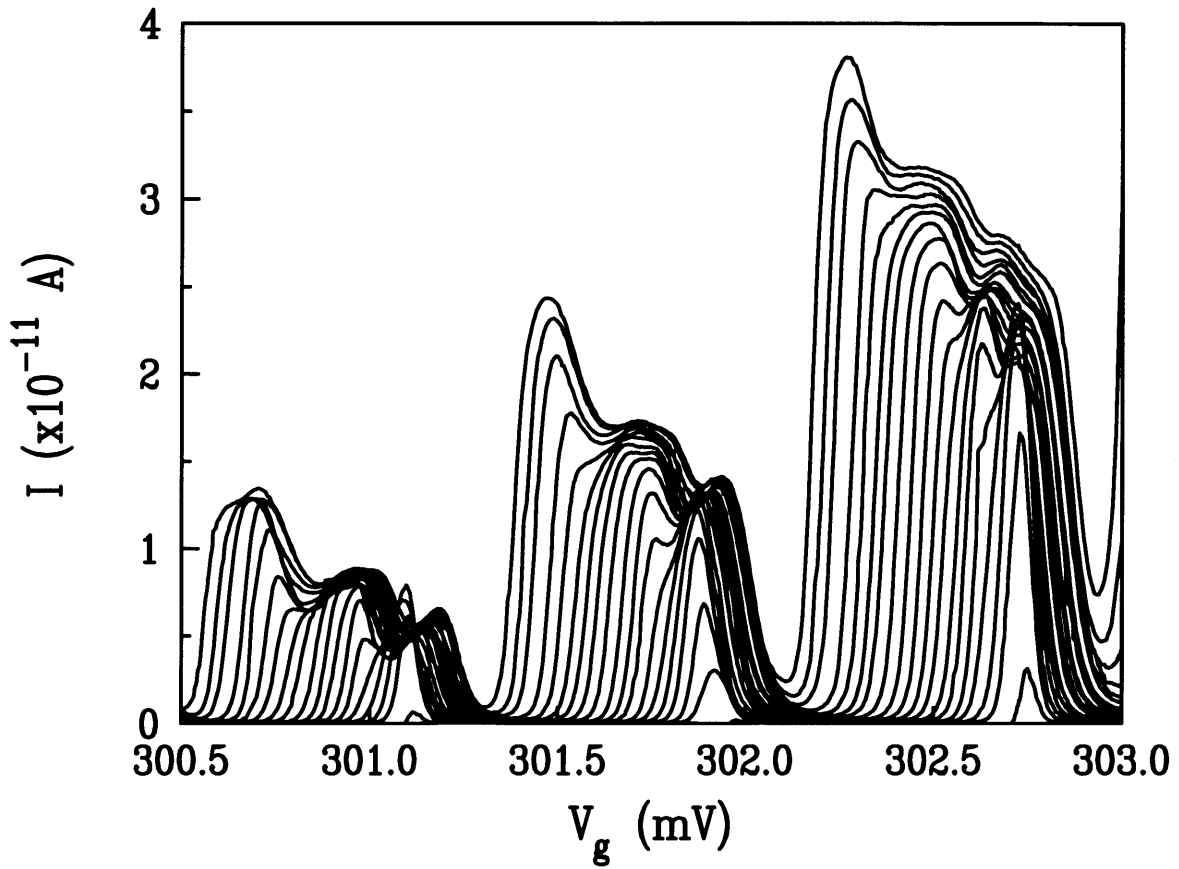


Fig. 4-11. The current, I as a function of gate voltage, V_g for drain-source biases, V_{ds} , ranging from 50 μ V to 500 μ V in increments of 25 μ V.

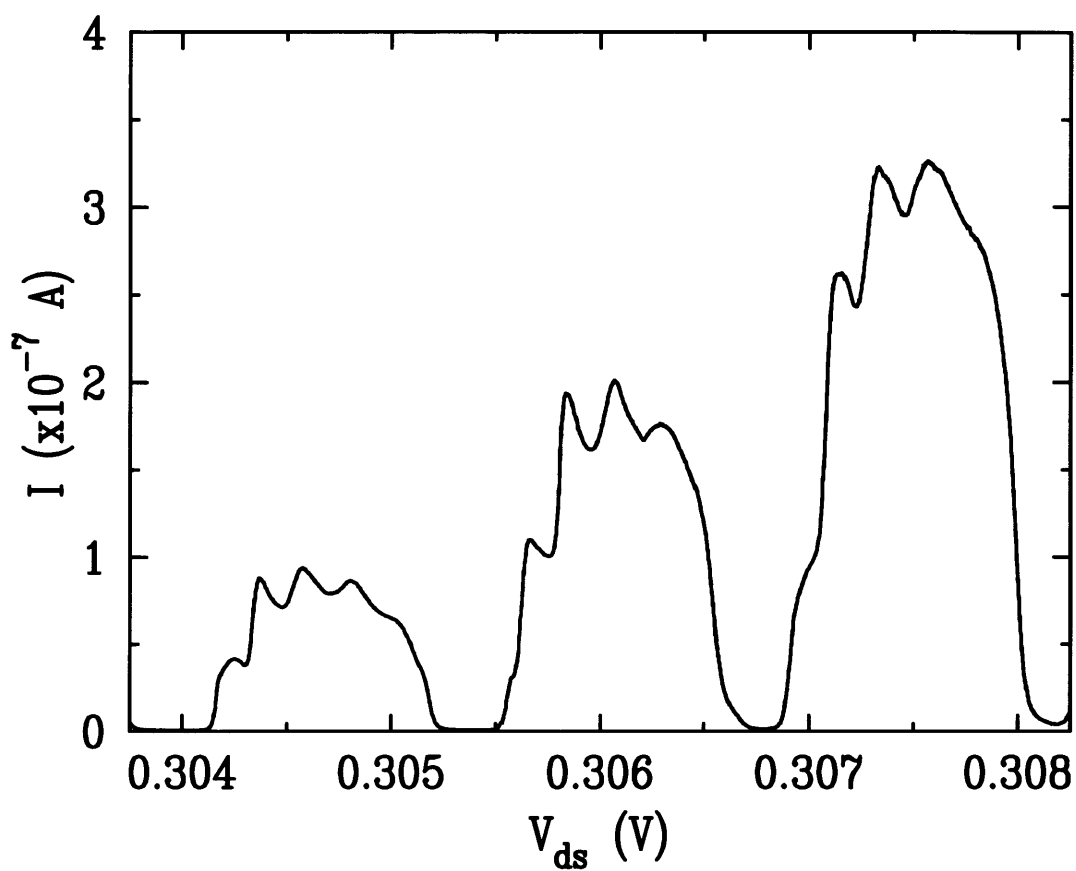


Fig. 4-12. I versus V_g for $V_{ds} = 0.5$ mV and $B = 2.53$ T.

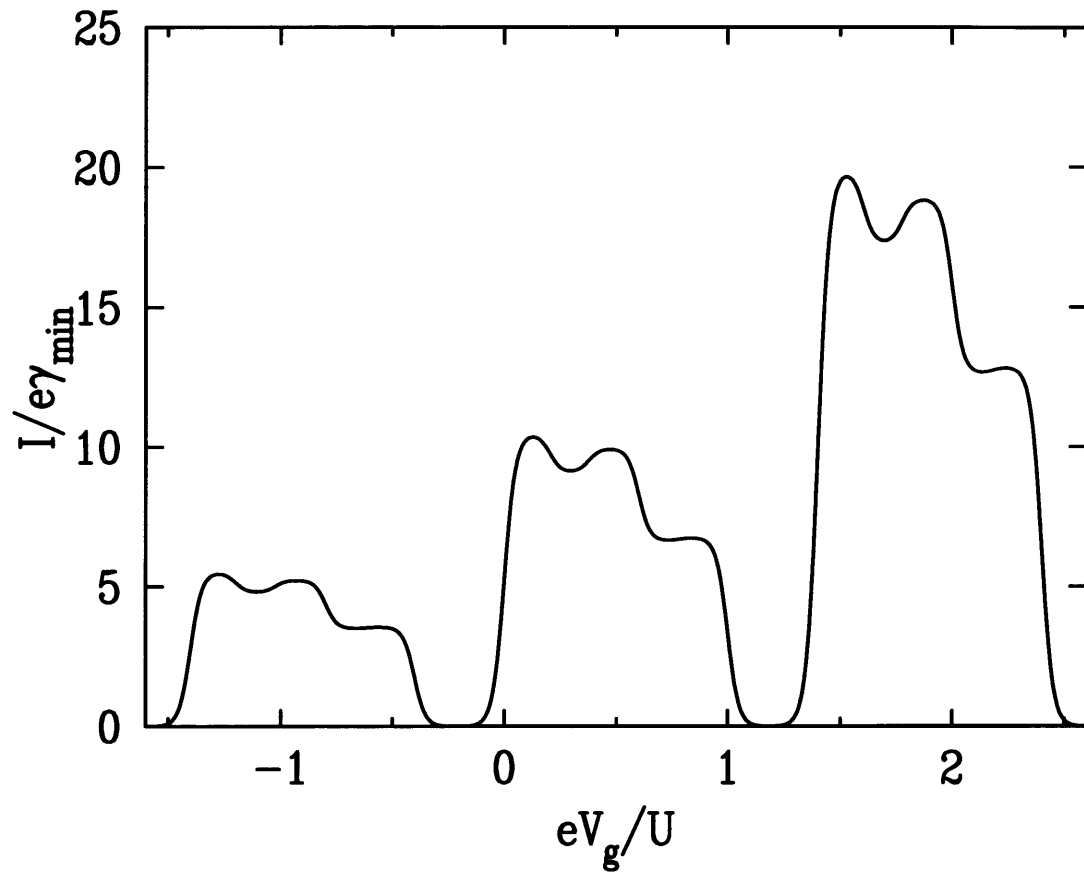


Fig. 4-13. I versus V_g at finite V_{ds} calculated in the discrete level model. The current, calculated from the model described in the text, is in units of $I/e\gamma_{min}$ where γ_{min} is the tunneling rate of the lowest active level through the right barrier[52].

we did in Figure 4-1. The data in Figure 4-11 was compared with two different calculations: one in which the electron thermalized with the system after tunneling into the small gas and one in which there was no inelastic relaxation. Comparison of these calculations with the data suggested that inelastic relaxation occurs in the small electron gas significantly faster than tunneling ($\sim 10^8 \text{sec}^{-1}$). Figure 4-13 shows the current calculated from this model. For a more detailed description of these calculation see the discussion in references [52, 67].

4.3 The Temperature Behavior of Conductance Peaks

In this Section the implications of the discrete level spectrum in a small electron gas are considered in further detail. Specifically, the interplay between single electron charging and the discrete level spectrum of a small electron gas in relation to the temperature dependence of conductance peaks is considered. This Section is divided into three parts. The first Subsection presents data showing the temperature behavior of conductance peaks. In the next Subsection, this data is compared with the predictions of a generalized theory of single-electron charging that include the effects arising from the discrete level spectrum. Finally, the third Subsection presents additional temperature data that, while not inconsistent with the generalized theory, demonstrates the wide array of temperature behavior that can be observed.

4.3.1 Conductance Peak Temperature Data

Figure 4-14 shows the temperature evolution of a series of conductance peaks at temperatures between 100 mK and 1.0 K. At 100 mK the amplitude of the peaks displays no apparent correlation with the amplitudes of adjacent peaks. As T is increased, the peak widths broaden and the amplitude of some peaks increases while

other decrease and some remain nearly unchanged. For example, the amplitude of the large peak at $V_g \cong -0.6455$ mV rapidly decreases with increasing T while the amplitude of the adjacent peak at lower V_g , decreases at first but then significantly increases by $T = 300$ mK. For reasons that will become more clear after a discussion of the theory in Section 4.3.2, it is useful to plot the reciprocal of peak amplitude against temperature. Figures 4-15 through 4-20 contain such traces for the six peaks in the gate-voltage sweeps in Figure 4-14. Notice that at low temperature a wide variety of behavior is seen, but by $T \sim 500$ mK the peak amplitudes are only weakly temperature dependent. Furthermore, as is apparent from the high temperature traces in Figure 4-14, at high temperatures the amplitudes of successive peaks in V_g increase monotonically. In fact, as shown in Figure 4-21 at $T = 1$ K the amplitude of successive peaks in V_g increases exponentially.

Compared with the behavior of peak amplitudes, there is less peak to peak variation in the temperature dependence of the full-width at half-maximum (FWHM) of a peak as a function of temperature. In Figure 4-22 the FWHM versus T of the conductance peak at $V_g \cong -0.6455$ mV is displayed. At low temperatures the trace exhibits a linear dependence between FWHM and T . At higher temperatures, $T > 600$ mK, the data continues to follow a linear relationship between FWHM and T , however, the slope of the dependence is higher by a factor of ~ 1.30 . Between $T \approx 400$ mK and $T \approx 700$ mK there seems to be a cross-over between these two relationships. Note that the integrated area under the conductance peak is not conserved as T is varied.² This is in contrast to single-particle resonant tunneling in which this quantity is conserved as a function of T [131].

Figure 4-23 shows an expanded view of a single conductance peak from Figure 4-14 on a semi-logarithmic scale. In Figure 4-23 it is seen that tails of a conductance peak fall off exponentially. The exact functional form of the lineshapes will be considered

²This is apparent since the FWHM of a peak increases with T while the peak amplitude remains nearly constant.

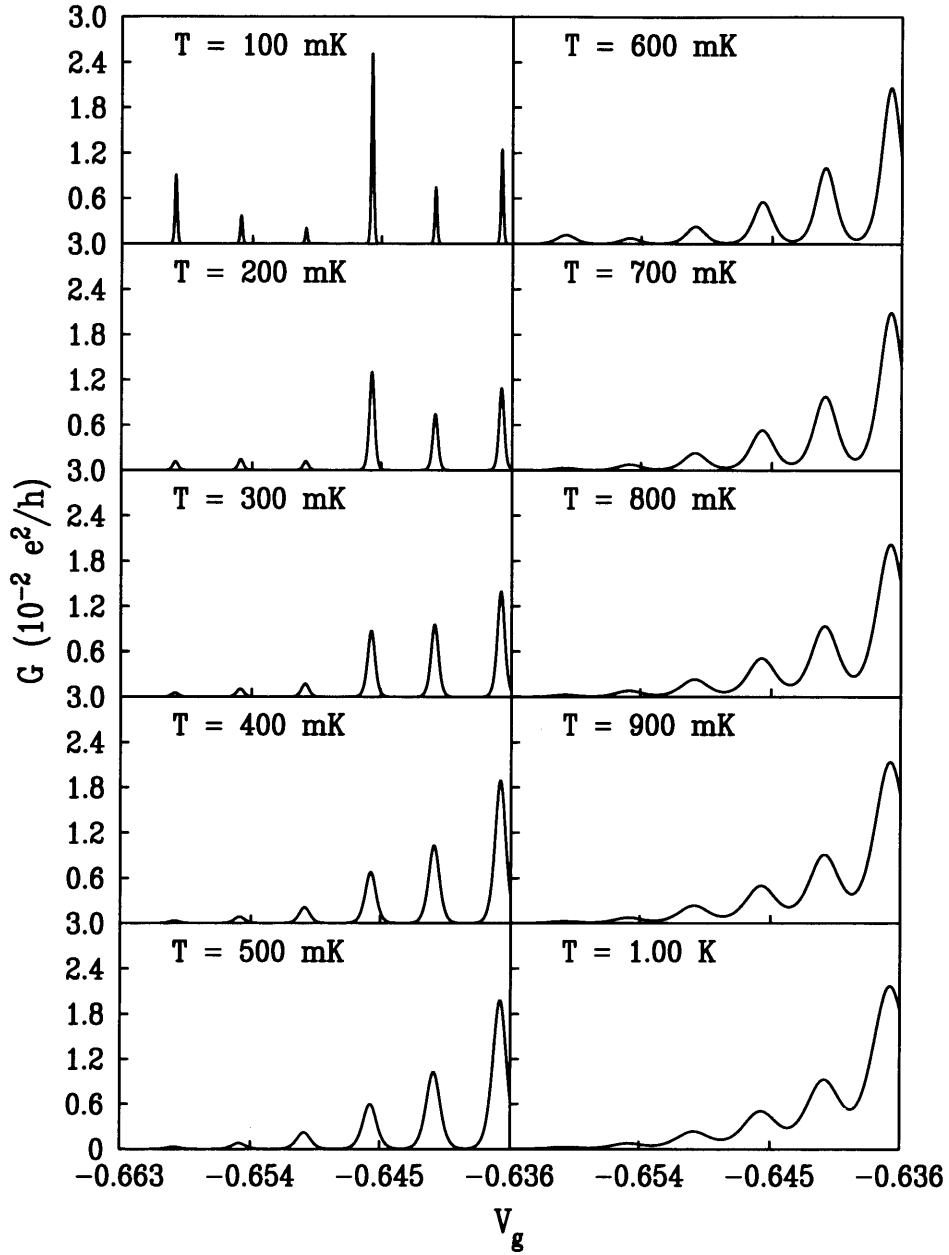


Fig. 4-14. The temperature evolution of conductance peaks. The spacing between peaks is periodic and equal to ~ 4.50 mV. As discussed in the text, C was determined from the temperature behavior of the peaks, $e^2/C = 0.68$ meV.

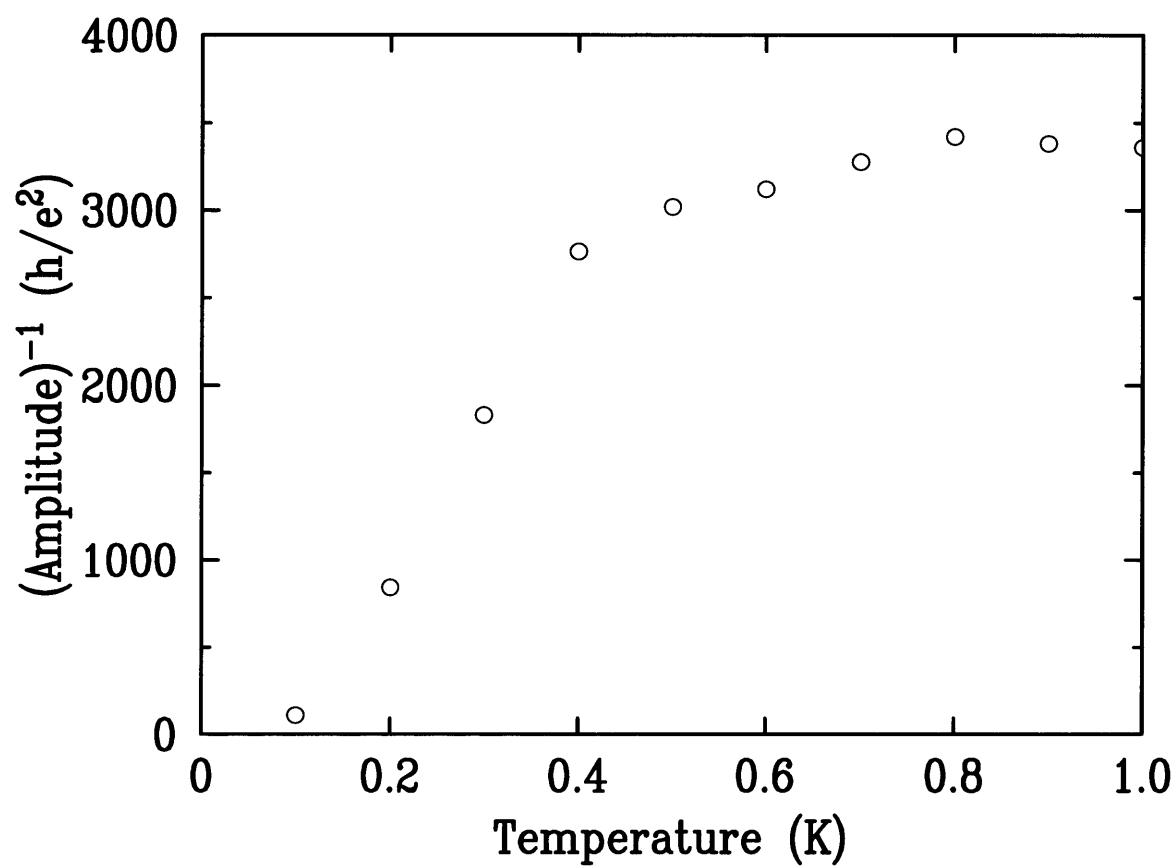


Fig. 4-15. The temperature behavior of the conductance peak at $V_g = -0.6593 \text{ mV}$ in Figure 4-14.

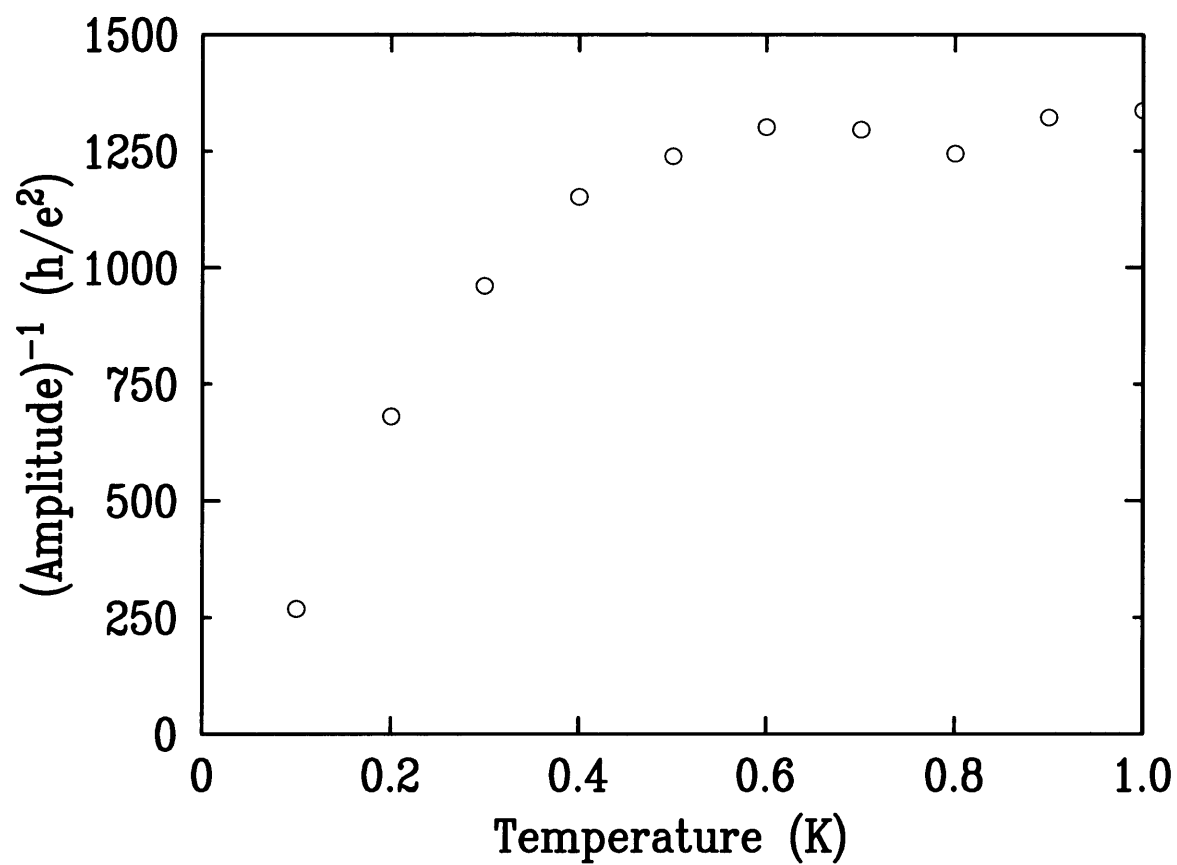


Fig. 4-16. The temperature behavior of the conductance peak at $V_g = -0.6548 \text{ mV}$ in Figure 4-14.

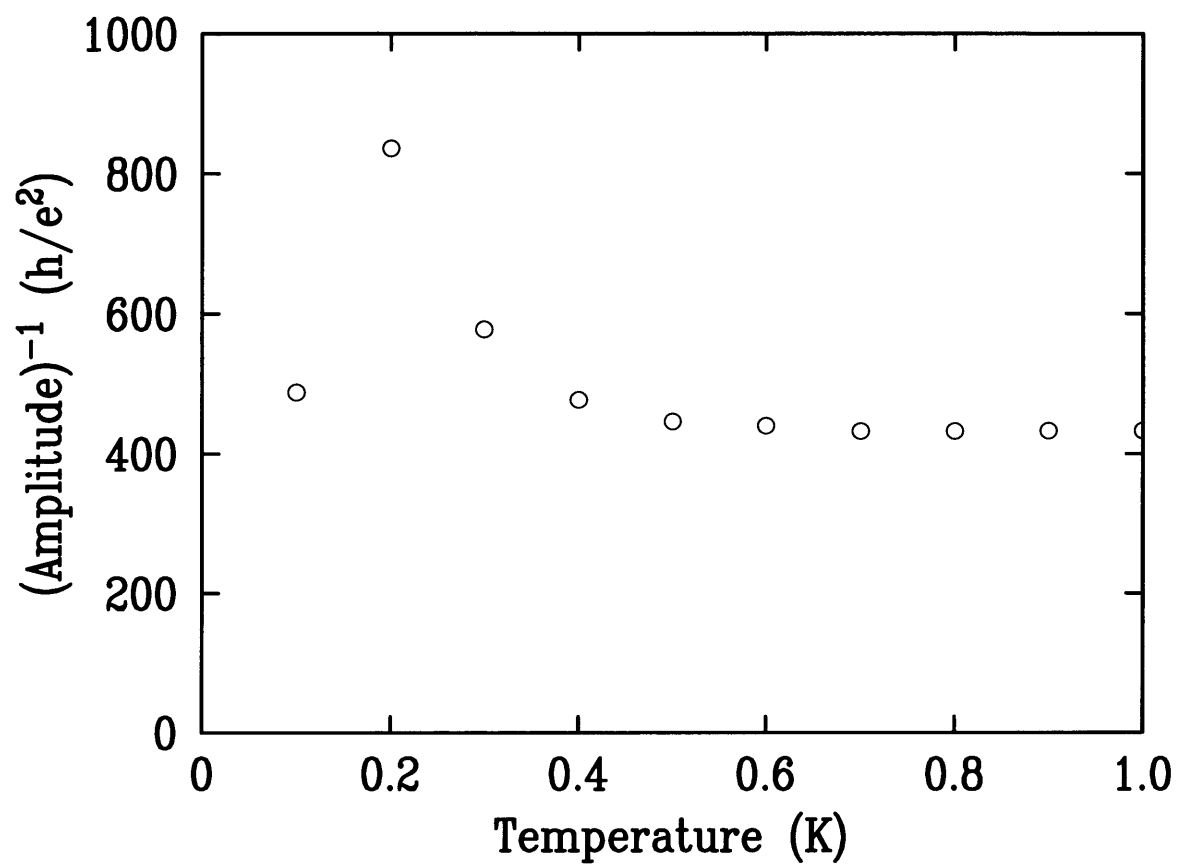


Fig. 4-17. The temperature behavior of the conductance peak at $V_g = -0.6503$ mV in Figure 4-14.

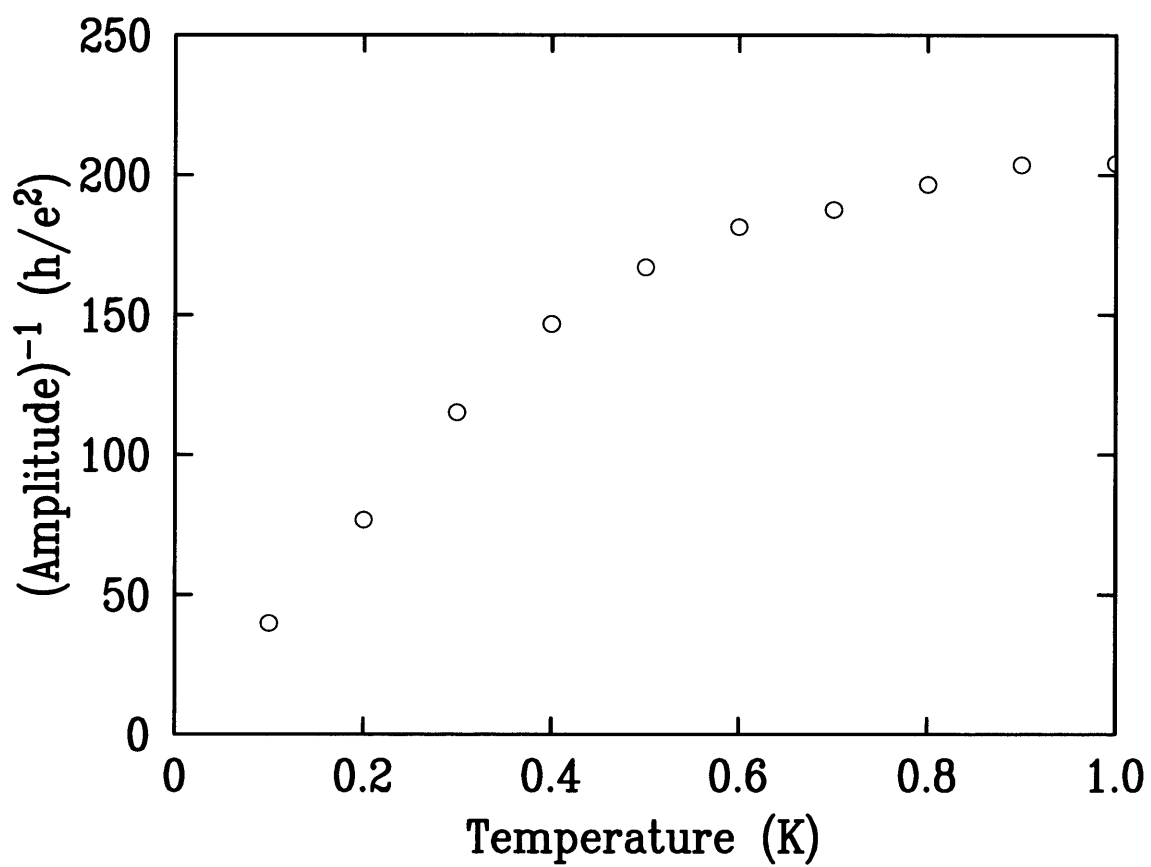


Fig. 4-18. The temperature behavior of the conductance peak at $V_g = -0.64567$ mV in Figure 4-14.

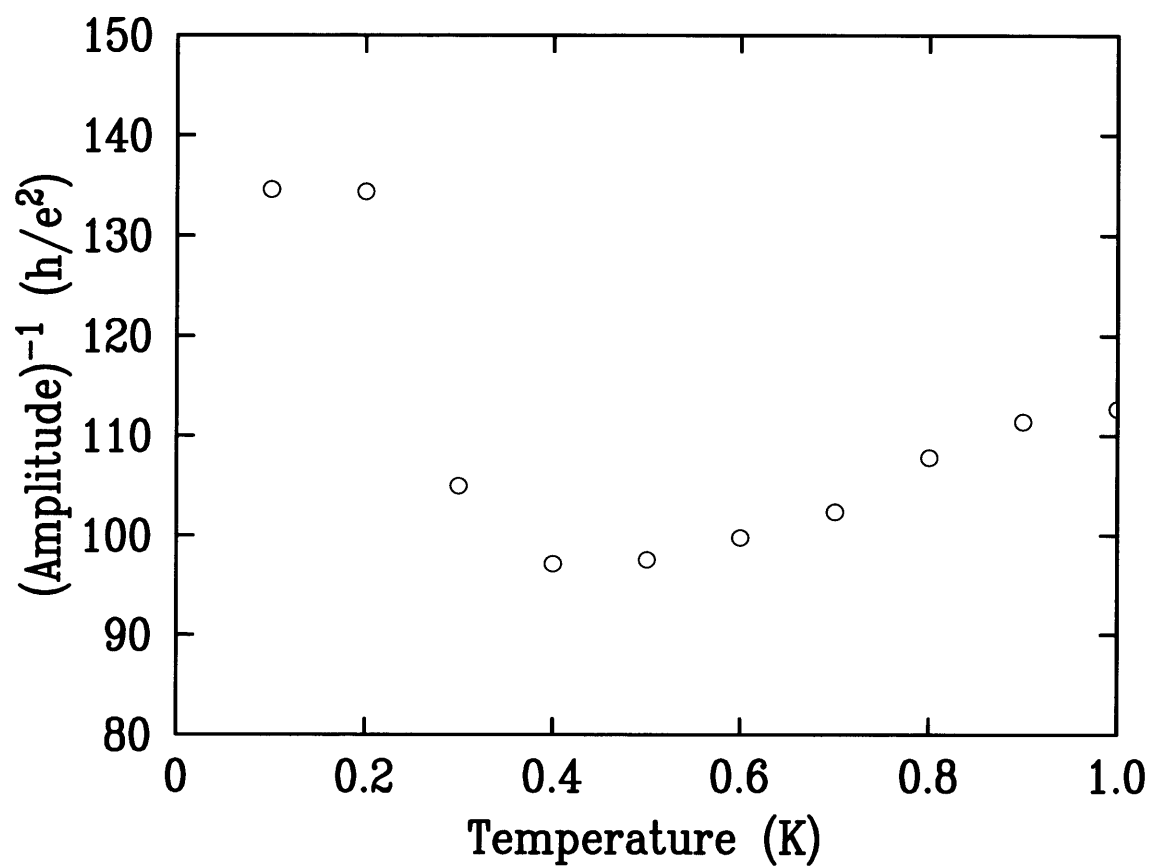


Fig. 4-19. The temperature behavior of the conductance peak at $V_g = -0.6413 \text{ mV}$ in Figure 4-14.

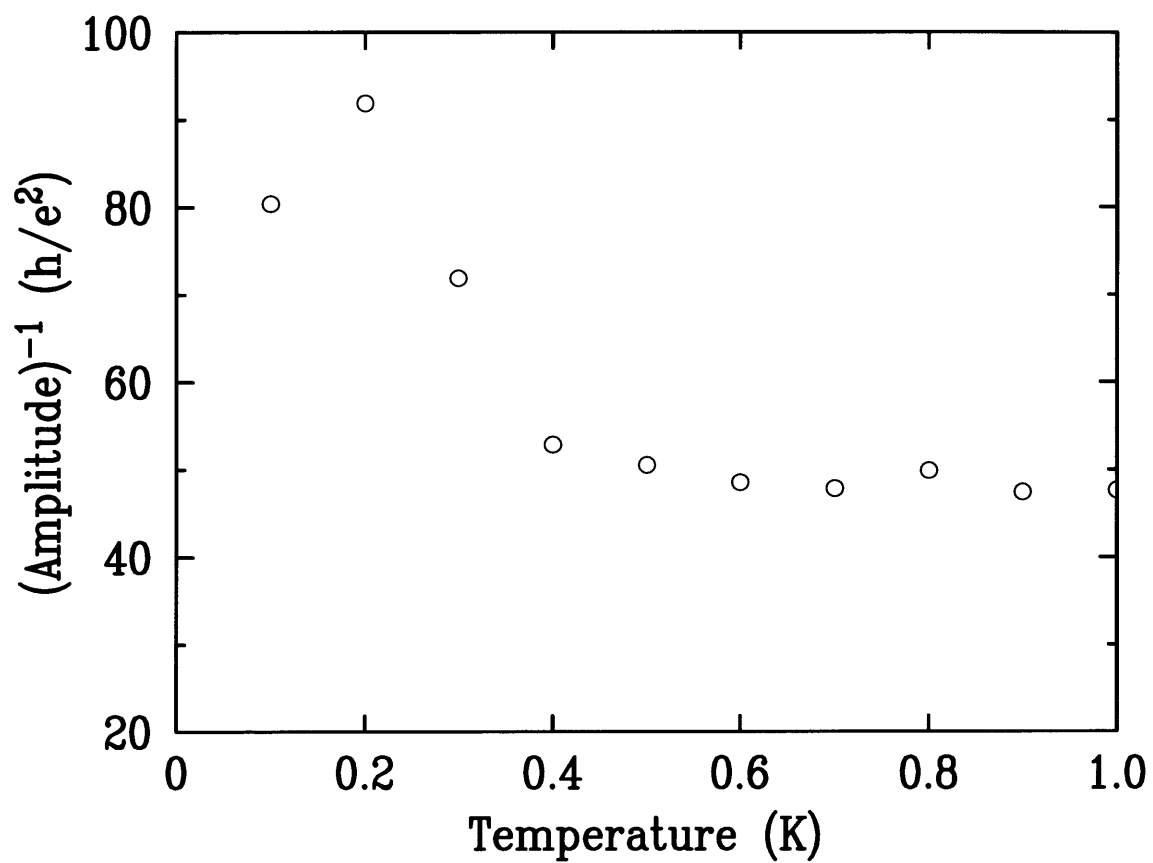


Fig. 4-20. The temperature behavior of the conductance peak at $V_g = -0.6367 \text{ mV}$ in Figure 4-14.

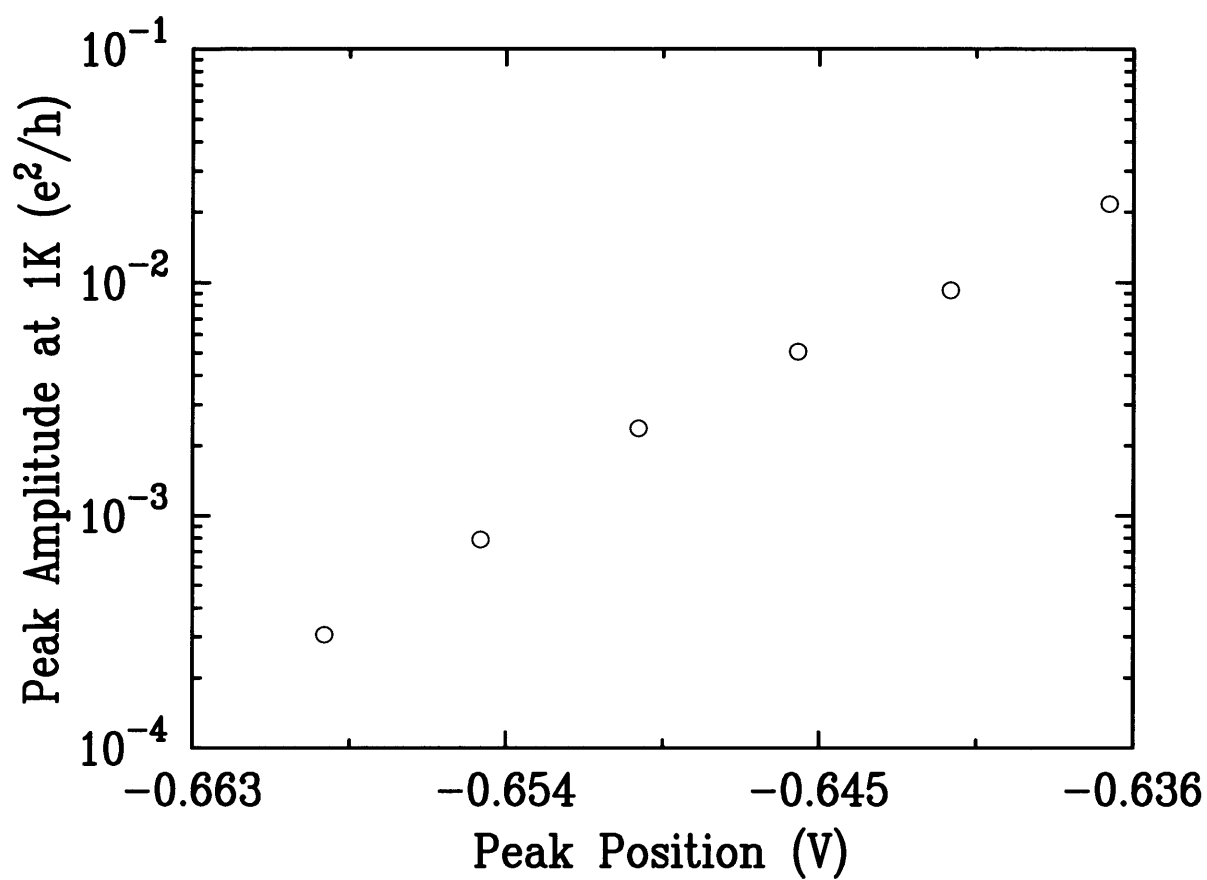


Fig. 4-21. Peak amplitude at 1 K versus peak position. This data is based on the 1 K data in Figure 4-14.

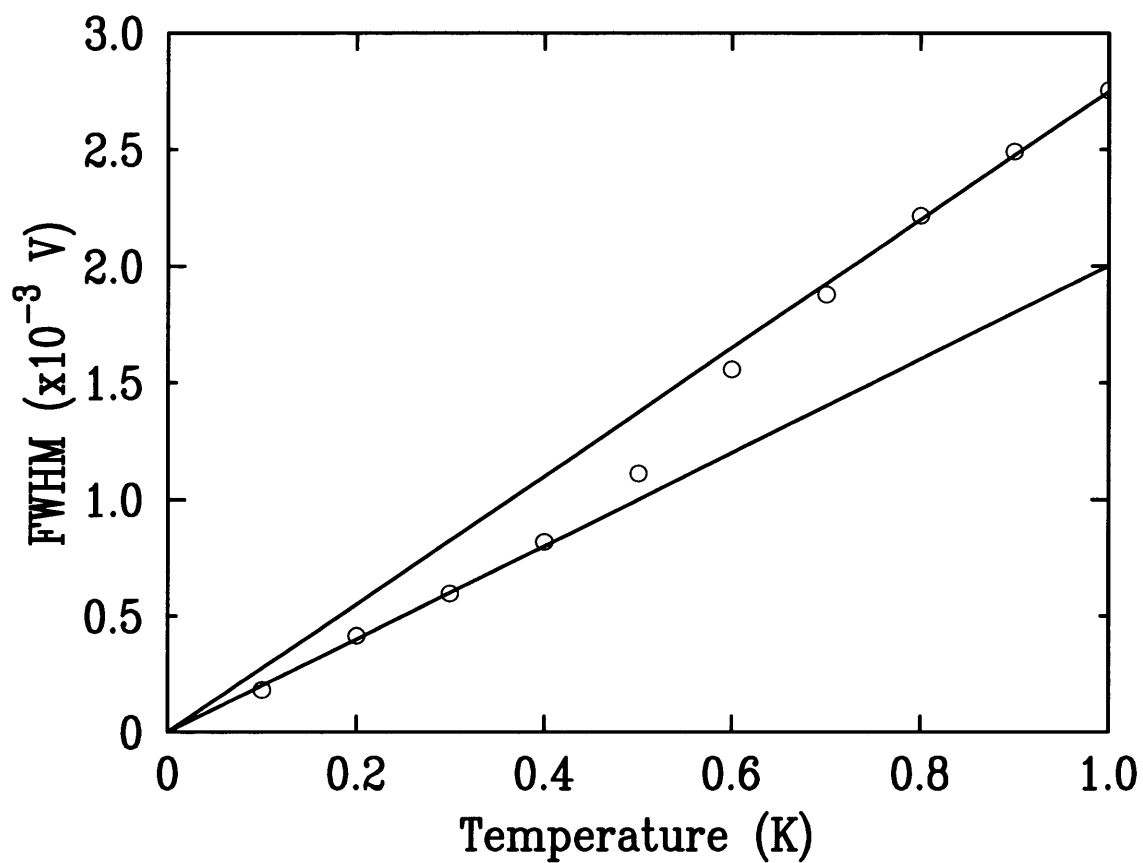


Fig. 4-22. The full-width and half-maximum of the conductance peak at $V_g = -0.6453 \text{ mV}$ from Figure 4-14 as a function of T .

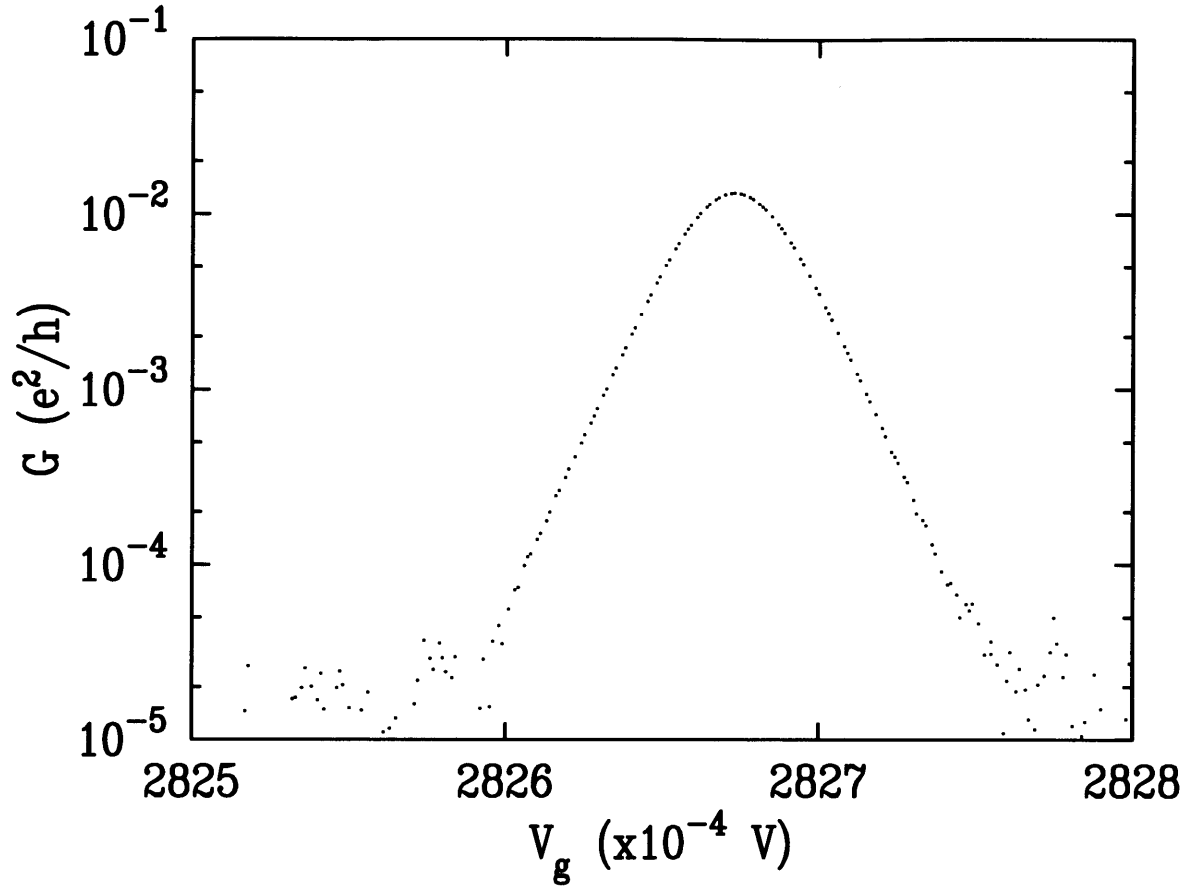


Fig. 4-23. An expanded view of a single conductance peak on a semilogarithmic scale. Note that the tails of the peak decay exponentially.

in more detail in the upcoming discussion of the theory of conductance peaks.

4.3.2 The Theory of Coulomb-blockade oscillations in the Presence of a Discrete level spectrum

This section aims to make sense of the temperature data just presented. The theory discussed here was worked out simultaneously by C.W.J. Beenakker at Phillips Research Laboratories [68] and by Yigal Meir, Ned S. Wingreen, and P.A. Lee at M.I.T.[67] who were in close contact with our group from the time that John Scott-

Thomas[60] and Udi Meirav[63] were making the initial observations of similar data in Si and GaAs structures respectively. For convenience, we refer in this thesis to the theory worked out by C.W.J. Beenakker and Yigal Meir *et al.* as the extended Coulomb-blockade theory.

In the extended model, a small electron gas is modeled exactly as we have already described in Figure 4-1 at the beginning of this Chapter. In the extended model, electron-electron interaction are assumed to be completely accounted for by classical single-electron charging. The only extension of the classical model that is made is that the continuous density of states above and below the Coulomb-gap is replaced by an *ad hoc* set of discrete levels. In the regime of linear conductance,³ ie., vanishingly small V_{ds} , the solution of this model proceeds by first calculating the occupation probability of each level, bearing in mind that the position of the Coulomb-gap in the level spectrum changes depending on the number of electrons in the gas. Since in the regime of linear conductance there is a finite bias applied across the gas, the system is not in equilibrium. Consequently, the occupation probability of the levels is not given by a Fermi-Dirac distribution. However, as will be discussed, calculating the non-equilibrium occupation probabilities is not difficult in the linear conductance regime. Once the occupation probabilities the system is fully described, its conductance, G , follows in a straight forward manner.

In order to understand the full theory, begin by considering the linear conductance in the following simple case: imagine that there is just one level above the Coulomb Gap. This condition portrayed in Figure 4-24. Notice that the level has an energy E_p relative to the chemical potential in the leads. The tunneling rates between the small electron gas and its left and right leads are respectively Γ_p^l and Γ_p^r . A small bias, $-V$ is applied to the left lead which raises the chemical potential on the left lead by eV . The stationary current through the left barrier equals that through the right barrier,

³See Section 3.1 for a definition of this term.

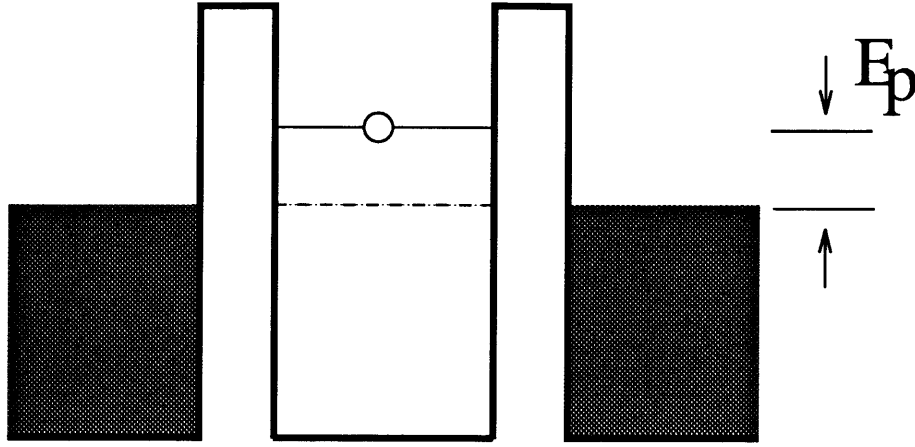


Fig. 4-24. A representation of the single level case considered in the text.

and is given by

$$I = e\Gamma_p^l [1 - F(E_p)] f(E_p - eV) - e\Gamma_p^l [F(E_p)] [1 - f(E_p - eV)], \quad (4.1)$$

where $F(E_p)$ is by definition the probability that the level will be filled and $f(x)$ is the Fermi function

$$f(x) = \frac{1}{\exp(x/kT) + 1}. \quad (4.2)$$

Furthermore, in steady state the non-equilibrium occupation probability, $F(E_p)$, is a stationary solution of the kinetic equation

$$\begin{aligned} \frac{\delta}{\delta t} F(E_p) = 0 &= [1 - F(E_p)] [\Gamma_p^r f(E_p) + \Gamma_p^l f(E_p - eV)] \\ &- [F(E_p)] [\Gamma_p^r (1 - f(E_p)) + \Gamma_p^l (1 - f(E_p - eV))]. \end{aligned} \quad (4.3)$$

Equations 4.1 and 4.3 are two equations with two unknowns whose solution yields,

$$F(E_p) = \left(\frac{1}{\Gamma_p^r + \Gamma_p^l} \right) (\Gamma_p^r f(E_p) + \Gamma_p^l f(E_p - eV)), \quad (4.4)$$

and

$$I = e \frac{\Gamma_p^l \Gamma_p^r}{\Gamma_p^l + \Gamma_p^r} \{f(E_p - eV) - f(E_p)\}. \quad (4.5)$$

which in the limit that $eV \ll kT$ reduces to

$$I = e \frac{\Gamma_p^l \Gamma_p^r}{\Gamma_p^l + \Gamma_p^r} \{f'(E_p)(-eV)\}, \quad (4.6)$$

where $f'(E_p)$ is the derivative of $f(x)$ evaluated at E_p . Evaluating $f'(E_p)$ and dividing the right side of this equation by V yields, G , the linear conductance of the system,

$$G = \frac{e^2}{4kT} \frac{\Gamma_p^l \Gamma_p^r}{\Gamma_p^l + \Gamma_p^r} \cosh^{-2}(E_p/2kT). \quad (4.7)$$

This is the linear conductance of a system composed of only one discrete level.

This discussion above was intended to illustrate a special case (*i. e.* a system with only one discrete level) of the more general theory which considers the linear conductance of a small electron gas for an arbitrary set of levels. The analysis above is easily expanded to incorporate multiple levels. The only essential difference between the calculation done above for the case of one level and the calculation of G in the multilevel case is in calculating $F(E_p)$. In the one level case, $F(E_p)$ was calculated by solving two simultaneous equations. When n levels are present, $n + 1$ simultaneous equations need to be solved. In the linear regime solving this $n + 1$ system of equation is easily done by using a trial solution for $F(E_p)$ which describe $F(E_p)$ in terms of its first order deviations from the equilibrium occupation probability of the gas at zero bias, $F_{eq}(E_p)$. The form of this trial solution is

$$F(E_p) \equiv F_{eq}(E_p) \left(1 + \frac{eV}{kT} \Psi(E_p)\right). \quad (4.8)$$

$\Psi(E_p)$ is found to be a constant, independent of temperature. Consequently, G can be expressed in terms of the equilibrium occupation probabilities. This procedure

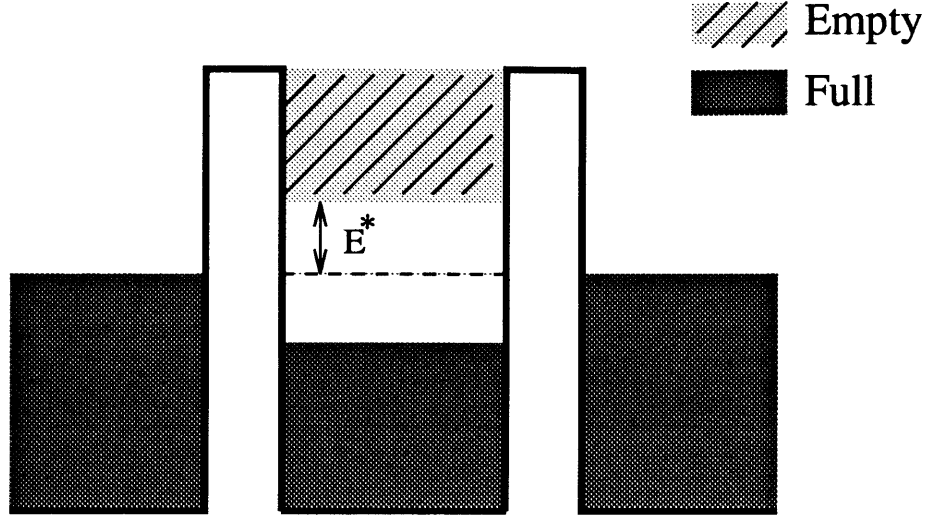


Fig. 4-25. A representation of the classical case considered in the text.

was carried out in Reference [68] by C.W.J. Beenakker where it was found that

$$G = \frac{e^2}{kT} \sum_{p=1}^{\infty} \sum_{N=1}^{\infty} \frac{\Gamma_p^l \Gamma_p^r}{\Gamma_p^l + \Gamma_p^r} P_{eq}(N) F_{eq}(E_p|N) [1 - f(E_p)], \quad (4.9)$$

where $P_{eq}(N)$ is the equilibrium probability that the small electron gas contains N electrons. Notice that when $kT \ll U$ the sum over N is reduced to a sum over only one value of N .

The single level case that was initially considered is a limiting form of Equation 4.9 in the limit that $kT \ll \Delta\epsilon \ll U$ where $\Delta\epsilon$ is the spacing between levels. It is useful to consider another limiting case of this equation, specifically, the case of a large number of equally coupled levels that are so closely spaced that they may be considered to form a band of levels. This describes exactly the classical model discussed in Chapter 3. This condition is met when the spacing between levels $\Delta\epsilon \ll kT$. Figure 4-25 which can be compared with Figure 4-24, illustrates this condition. Notice that E^* is defined through this Figure to be the minimum energy between the quasi-Fermi level in the leads and the edge of the Coulomb-blockade gap.

In this classical limit, the summation over p in Equation 4.9 reduces to an integral

of the form

$$\int_{-\infty}^{\infty} d\epsilon f(\epsilon)[1 - f(\epsilon + E^*)] = E^* (1 - e^{-E^*/kT})^{-1}. \quad (4.10)$$

When $kT \ll U$, which in our data is generally the case, the summation over N need only be evaluated at the one value of N which is closest to the corresponding equilibrium charge in the gas. In this limit, $P(N)$ can be calculated from the classical Boltzmann distribution giving

$$P_{eq}(N) \longrightarrow \frac{\int_{-E^*/kT}^{\infty} e^x dx}{1 + \int_{-E^*/kT}^{\infty} e^x dx} = \frac{e^{-E^*/kT}}{1 + e^{-E^*/kT}}. \quad (4.11)$$

The end result is that

$$G = \frac{e}{kT} \frac{\Gamma^l \Gamma^r}{\Gamma^l + \Gamma^r} \frac{e^{-E^*/kT}}{1 + e^{-E^*/kT}} \frac{E^*}{1 - e^{-E^*/kT}} = e \frac{\Gamma^l \Gamma^r}{\Gamma^l + \Gamma^r} \frac{E^*/kT}{\sinh(E^*/kT)} \quad (4.12)$$

for the classical limit. This is the temperature broadened lineshape for the classical model quoted earlier on page 78.

In summary, Equation 4.9 gives the predicted linear conductance of a small electron gas with a discrete level spectrum as a function of temperature. Two limiting forms of this equation were considered. The first applies in the regime when $kT \ll \Delta\epsilon \ll U$, which is frequently referred to as the resonant tunneling regime. Equation 4.7 gives the predicted lineshape in this regime. Its salient features are that its tails fall off exponentially, its full-width at half-maximum scales proportionally to T , $FWHM \approx 3.53 kT$, and its maximum amplitude is proportional to $1/T$. The second limiting form of Equation 4.9 corresponds to the regime when $\Delta\epsilon \ll kT \ll U$ and when the tunneling rate across the barriers is the same for all levels. The lineshape derived in this case is referred to as the classical lineshape for the reasons mentioned above. Its tails also fall out exponentially and its FWHM is also proportional to kT , however, its $FWHM \approx 4.35 kT$. Also in the classical regime the amplitude of a conductance peak is temperature independent.

4.3.3 Back to the Data

With these predictions in mind, we return the temperature data presented in Section 4.3. Begin by considering the plot of FWHM versus T in Figure 4-22 on page 123. At low temperatures, $T < 350$ mK, the FWHM scales linearly with T . At high temperatures, $T > 650$ mK, there is also a linear relationship between T and the *FWHM*, however as seen by the difference in slope between the two lines in Figure 4-22, the constant of proportionality between the high and low temperature regimes is different. The ratio of the slopes of the two lines in Figure 4-22 is equal to 1.30. If we choose to describe the low temperature data using the resonant tunneling lineshape and the high temperature data using the classical lineshape, then the expected ratio of the slopes of the lines in Figure 4-22 would be 1.23 which is in close agreement with the observed value.

The peak amplitude, A , versus temperature data in Figures 4-15–4-20 also suggest that at low temperatures the resonant tunneling lineshape is applicable and at high temperatures the classical lineshape is applicable. Notice that $1/A$ is linear with T at low temperatures for all peaks and at high temperatures A is at most only weakly temperature dependent. Furthermore, in the crossover between the resonant tunneling and classical regimes some peaks show an increase in A with T while others exhibit a decrease A with increasing T . More specifically, in the cross-over regime the amplitude of a given peaks appears to tend towards a value that reflect the average of its amplitude and the amplitude of adjacent peaks. In other words, the amplitude of big peaks that are next to small peaks decreases with increasing T , while the exact opposite behavior is seen for small peaks adjacent to large peaks. This cross-over behavior is consistent with the predictions of the discrete level model that lead to Equation 4.9. A detailed discussion of behavior in the cross-over regime has been given in Reference [67].

In Section 3.5 we mentioned that the total capacitance of the small electron gas can be determined from the temperature behavior of conductance peaks. The preceding

discussion makes it possible to illustrate how this is done. As already mentioned, in the resonant tunneling regime, G as a function of E_p is given by Equation 4.7. However, G is measured not as a function of E_p but rather as a function of V_g . As discussed in Section 3.5 changing the gate voltage by an amount δV_g changes the energy in the gas by an amount $\alpha e \delta V_g$ where $\alpha = C_g/C$. Consequently, G as a function of V_g is given from Equation 4.7 as

$$G = \frac{e^2}{4kT} \frac{\Gamma_p^l \Gamma_p^r}{\Gamma_p^l + \Gamma_p^r} \cosh^{-2} \left(\frac{\alpha e (V_g - V_o)}{2kT} \right), \quad (4.13)$$

where V_o is the gate voltage corresponding to the center of a conductance peak. In the resonant tunneling regime, peaks are fit using the lineshape of Equation 4.13 and α is determined from the fit. Figure 4-26 shows a conductance peak in the resonant tunneling regime fit with the lineshape of Equation 4.7. The total capacitance of the gas, C is determined from α using the value of C_g measured directly from, ΔV_g , the spacing between peaks, $C_g = e/\Delta V_g$. Fitting peaks from the data in Figure 4-14 gave $\alpha = 0.15$ and $e^2/C = 0.63 \text{ meV}$.

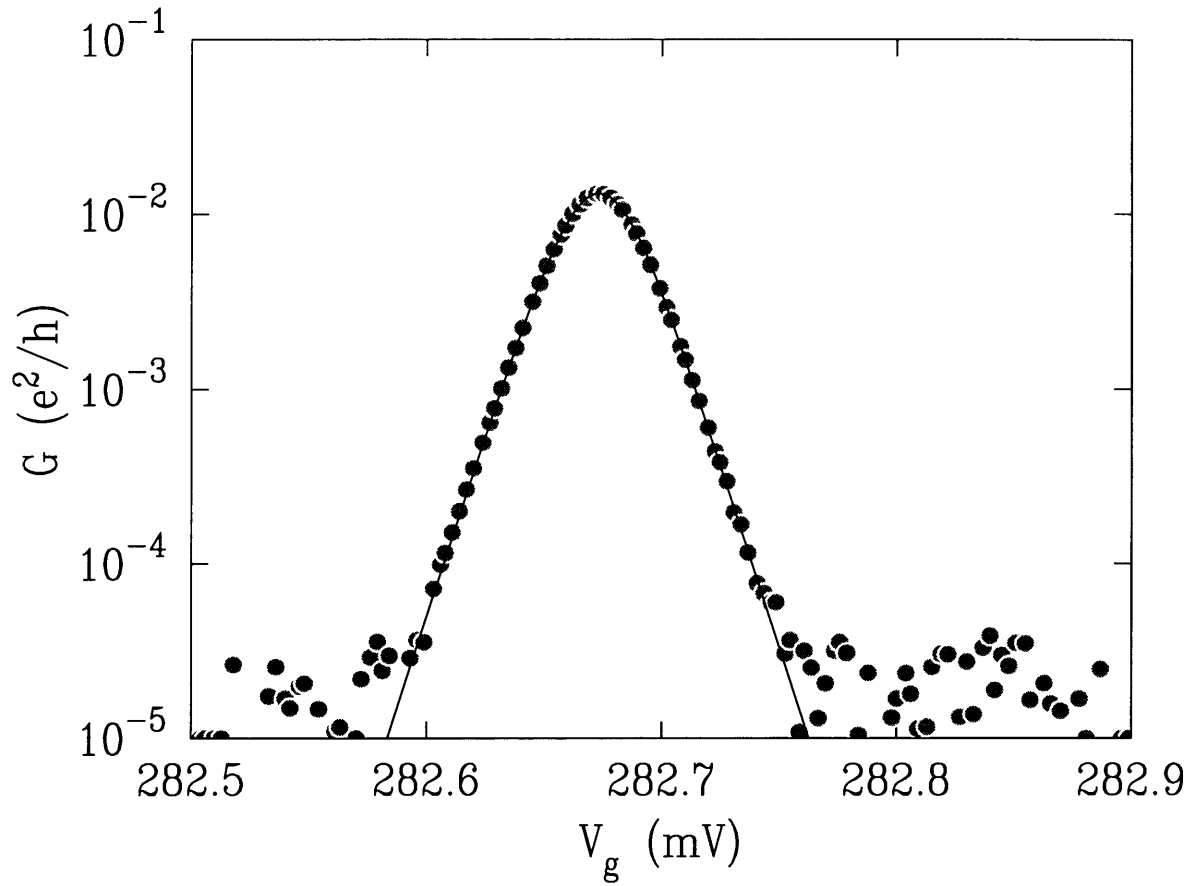


Fig. 4-26. A conductance peak fit to the resonant tunneling lineshape. The functional form of the lineshape is given by Equation 4.7.

Chapter 5

Single Electron Charging in the Quantum Hall Regime

5.1 Introduction

This chapter presents an overview of our experimental and theoretical investigation of the transport properties of a small two-dimensional electron gas in a high magnetic field (the quantum Hall regime). Section 5.2 is dedicated to presenting our experimental observations in the quantum Hall regime. As we will show, conductance peaks in this regime exhibit surprising behavior as a function of magnetic field. In Section 5.3 we present a self-consistent charging model of the electron gas system in the quantum Hall regime. Section 5.4 presents the calculated behavior of conductance peaks based on this model. This model predicts many of the features that were experimentally observed. To complement the discussion in this Chapter, Appendix H contains a brief discussion noninteracting electrons in a magnetic field and an explanation of the term “quantum Hall regime”.

5.2 Transport Measurements in the Quantum Hall Regime

In the previous chapters a number of plots were presented that showed G as a function of V_g . The salient feature in these plots was that G consists of a series of nearly periodic conductance peaks. In this Section, we present data that shows how these traces evolve as a magnetic field is applied perpendicular to the plane of the 2-DEG. Figure 5-1 shows the evolution of a series of conductance peaks with increasing magnetic field strength, B . Two effects of changing B are immediately obvious. First, the amplitude of conductance peaks fluctuates as B is increased, and second, the gate-voltage at which a conductance peak occurs has a variation on the order of 10% of the spacing between peaks. These two effects are illustrated in Figure 5-2 which plots the amplitude and gate-voltage associated with a single peak as a function of B . The magnetic field scale over which fluctuations occurs is $\Delta B \sim 750$ G which corresponds to adding one magnetic flux quantum to an area equal to $0.23 \times 0.23 \mu\text{m}^2$, roughly same area as the small electron gas. A number of researchers have been interested in interpreting such low-field behavior[132, 133, 134, 135]. In this chapter, however, our discussion will focus on the more organized behavior of conductance peaks at higher magnetic fields.

Figure 5-3 shows the magnetic field dependence of the gate-voltage and amplitude of a conductance peak for B between 1.5 T and 4.5 T¹. At roughly periodic values of B , the peak amplitude drops by as much as an order of magnitude. Commensurate with these dips, oscillations are observed in the position of the peak. This structure washes out rapidly with increasing temperature and is almost entirely destroyed by $T \sim 300$ mK. The temperature dependence of the peak amplitude and position over a narrow range in B is plotted in Figure 5-4. When the position of several successive

¹The lithographic dimensions of the small 2-DEG in this device are $0.5 \times 0.7 \mu\text{m}^2$. This device is described in detail in Reference [50]

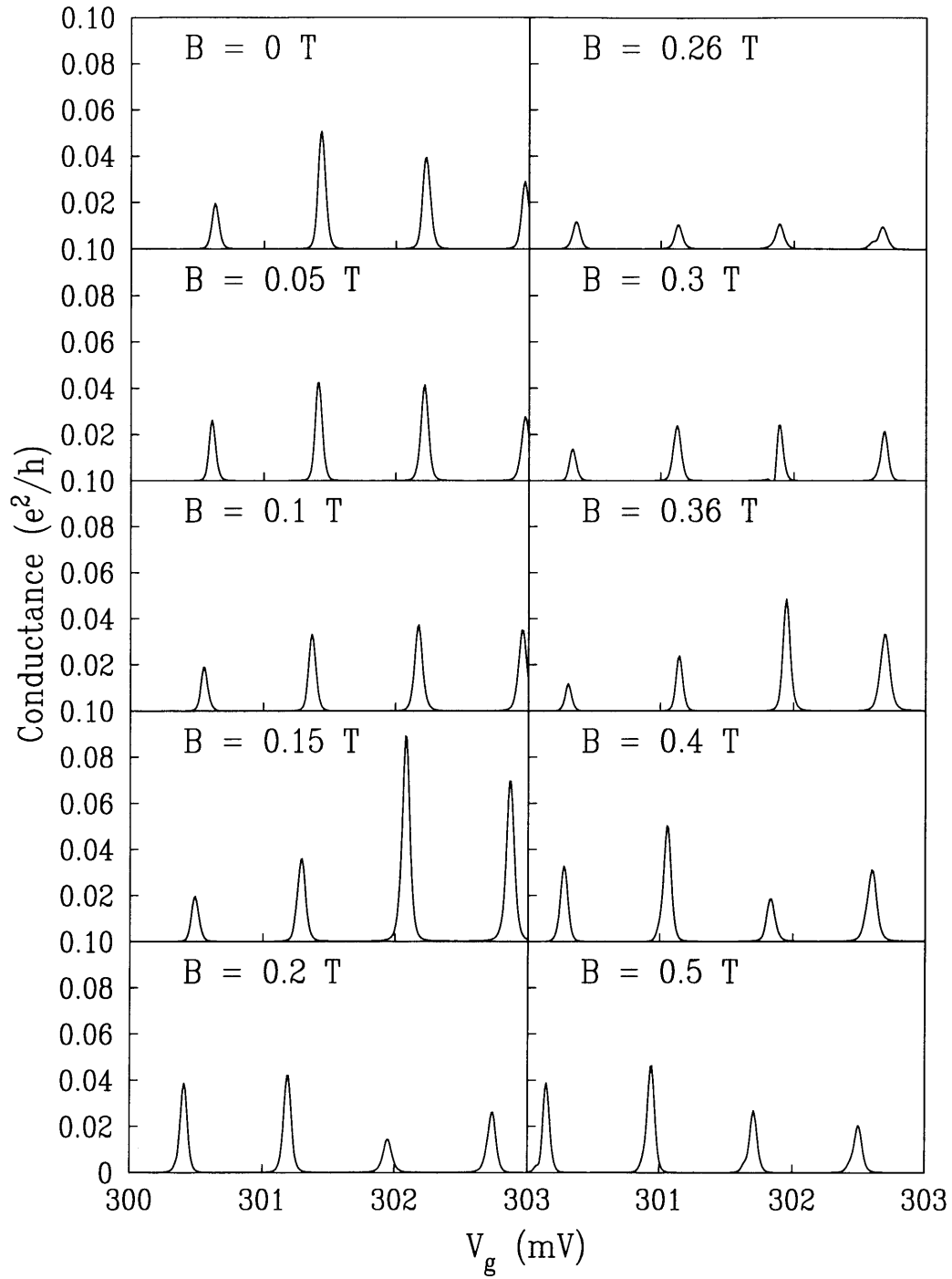


Fig. 5-1. The evolution of conductance peaks in low magnetic fields. As B is changed, the amplitude of conductance peaks fluctuates and the gate-voltage at which a peak occurs has a variation on the order of 10% of the spacing between peaks.

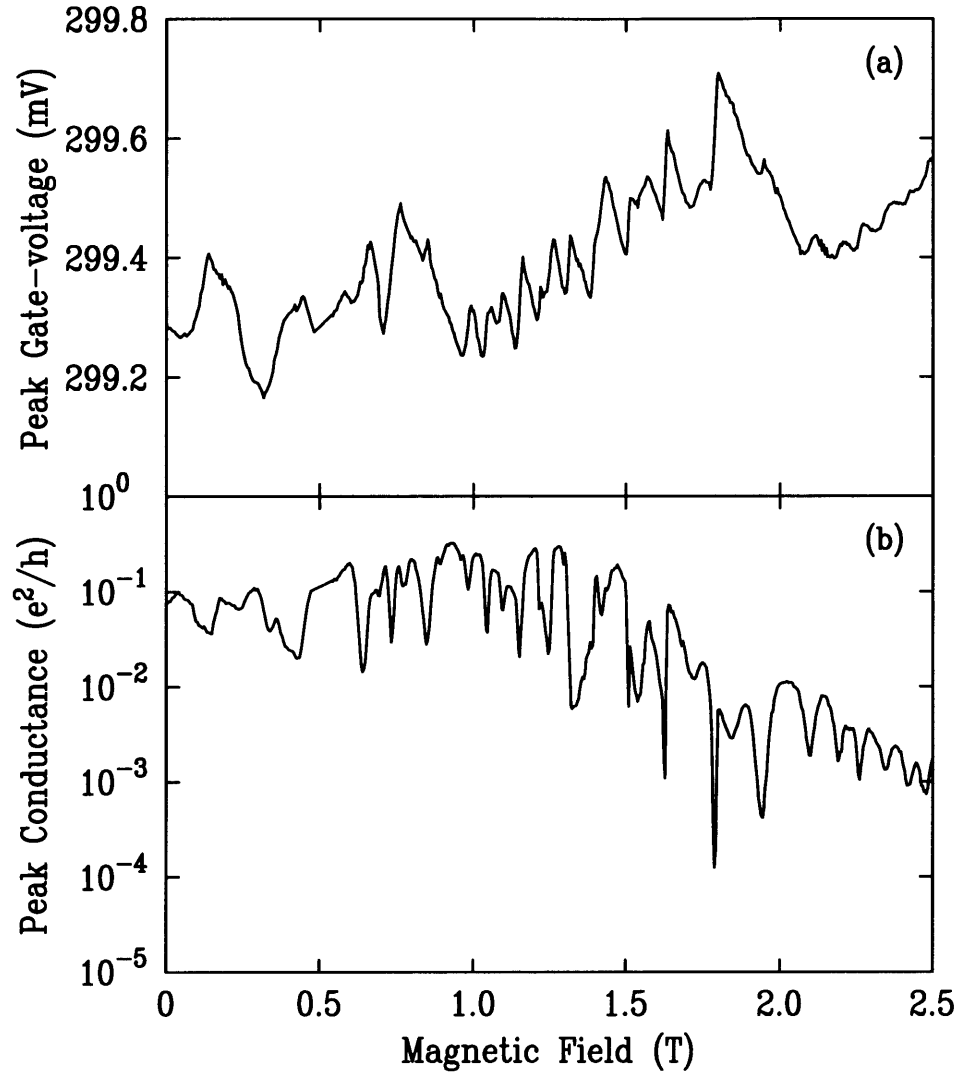


Fig. 5-2. Peak gate-voltage and amplitude as a function of B . Fluctuations occur on a field scale of ~ 750 G which corresponds to adding one flux quantum to an area of $(230 \text{ nm})^2$.

peaks in V_g is monitored as a function of B , data as in Figure 5-5(a) are obtained. We see here that successive peaks exhibit similar oscillation in their peak position. The phase of the oscillations with respect to B is different between peaks. Figure 5-5(b) shows the same data except that a constant voltage spacing (0.685 mV) has been subtracted between successive peaks². The data is plotted in this form because when these results were first seen our initial interpretation[50, 136] assumed that the spacing between peaks, ΔV_g , was due to the addition of two energies, the Coulomb blockade energy U and a single particle energy, E_N :

$$e\alpha(\Delta V_g) = U + E_N. \quad (5.1)$$

In this interpretation, E_N is simply the non-interacting, single-particle energy of a particle (ie., the electron of mass m^*) in the confining potential of the structure. So if a constant term, which is assumed to be U , is subtracted between peaks then all that remains is the single-particle energy, E_N . Despite the striking appearance of a set of curves that looks much like a non-interacting level spectrum this interpretation proved untenable. (Appendix H shows the spectrum of non-interacting levels for an electron in a harmonic confining potential.) One feature that from the outset called this view into question was the absence of Zeeman split levels. This and several other equally compelling observations[51] ruled out the simple analysis embodied in Equation 5.1. One last view of the behavior of conductance peaks in a strong magnetic field is shown in Figure 5-6. It is seen here that the amplitude of successive peaks in V_g alternates between large and small peaks[137].

²In Figure 5-5(b) after subtracting a constant ΔV_g , V_g was multiplied by $e\alpha = 0.61e$ to convert V_g to an energy as described in Section 3.5

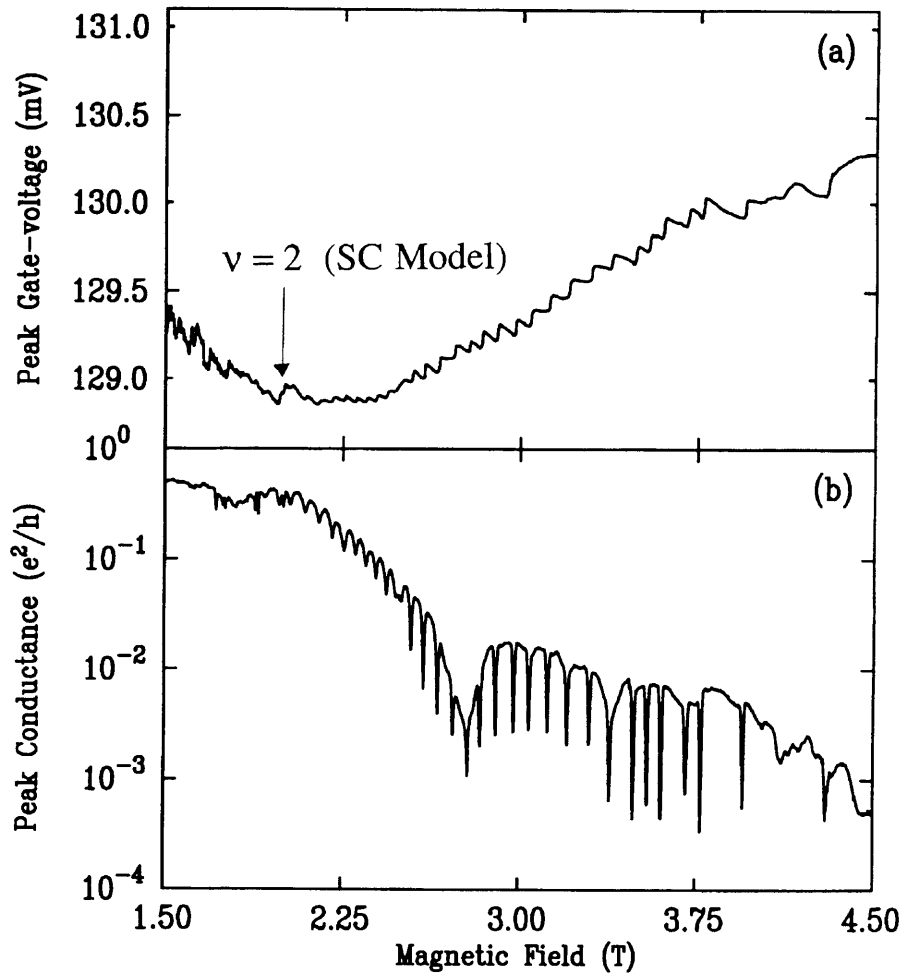


Fig. 5-3. Peak position and amplitude as a function of B in the quantum Hall regime. The filling factor $\nu = 2$ is inferred from the self-consistent (SC) model described in the text.

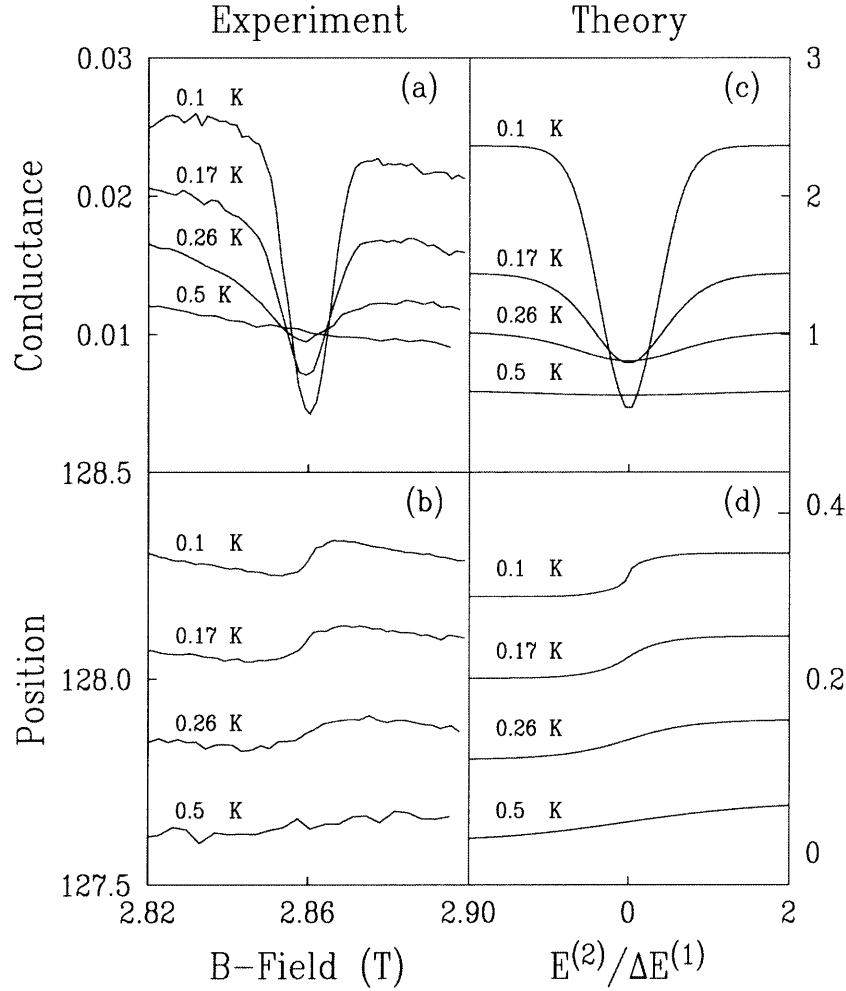


Fig. 5-4. Conductance peak temperature dependence as a function of B . The temperature dependence of (a) the peak amplitude in e^2/h and (b) the peak position in mV of a conductance peak over a narrow B range containing one dip in the peak amplitude. Also shown are the predictions of the model described in the text (page 142) for (c) the peak amplitude in units of $(e^2/h)\Gamma^{(1)}/\Delta E^{(1)}$ and (d) the peak position in meV, both for $\Delta E^{(1)} = 0.05$ meV. All except the lowest peak-position curves have been offset for clarity.

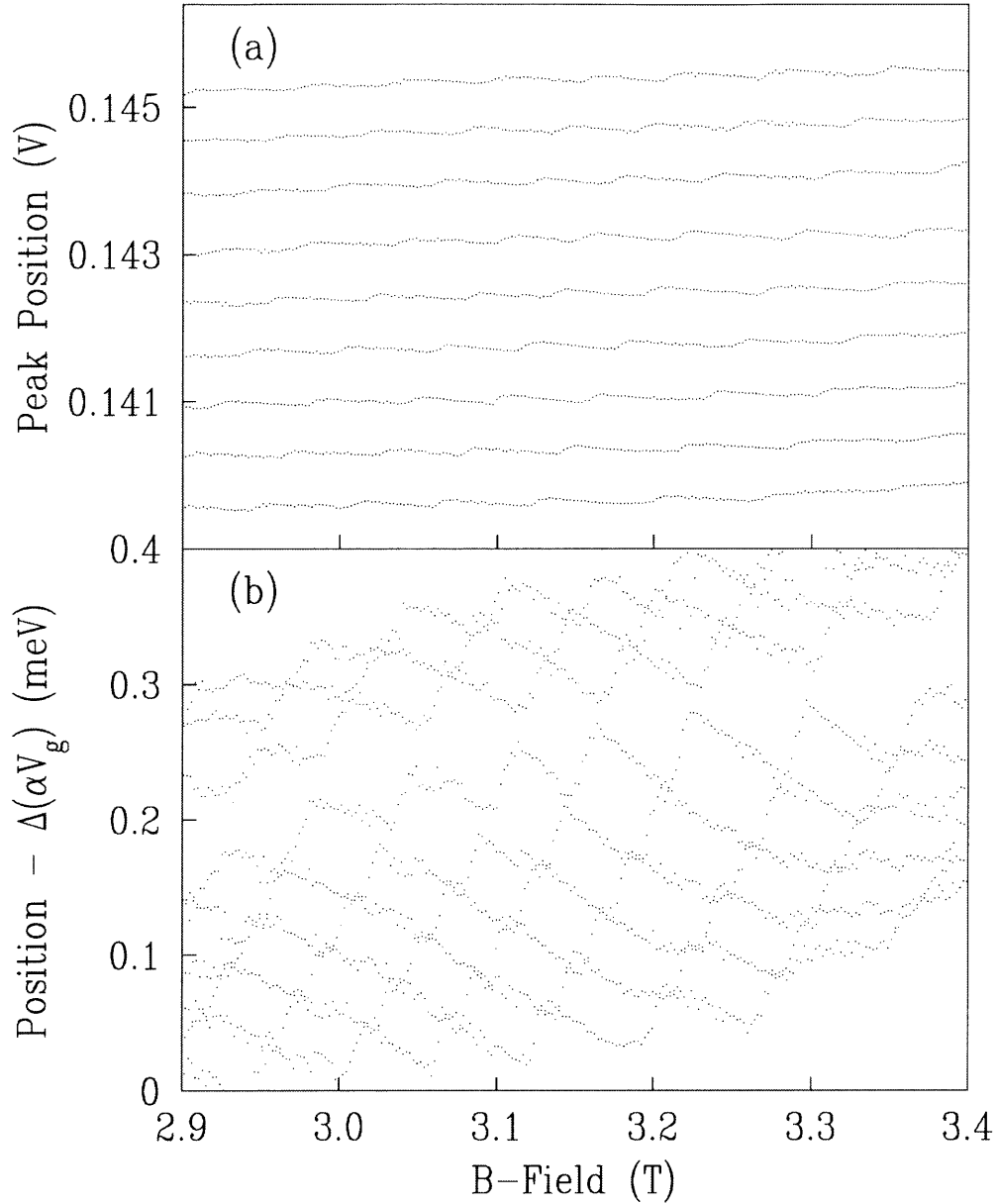


Fig. 5-5. Peak position as a function of B for consecutive conductance peaks. (a) Peak Position versus B for a series of consecutive conductance peaks. In Reference [50] the variation in the spacing between peaks (b) was interpreted as arising from the single particle energy-level spectrum in the small electron gas. The discussion in the text presents a revised interpretation of these results. See the discussion in reference to Figure 5-10 on page 153.

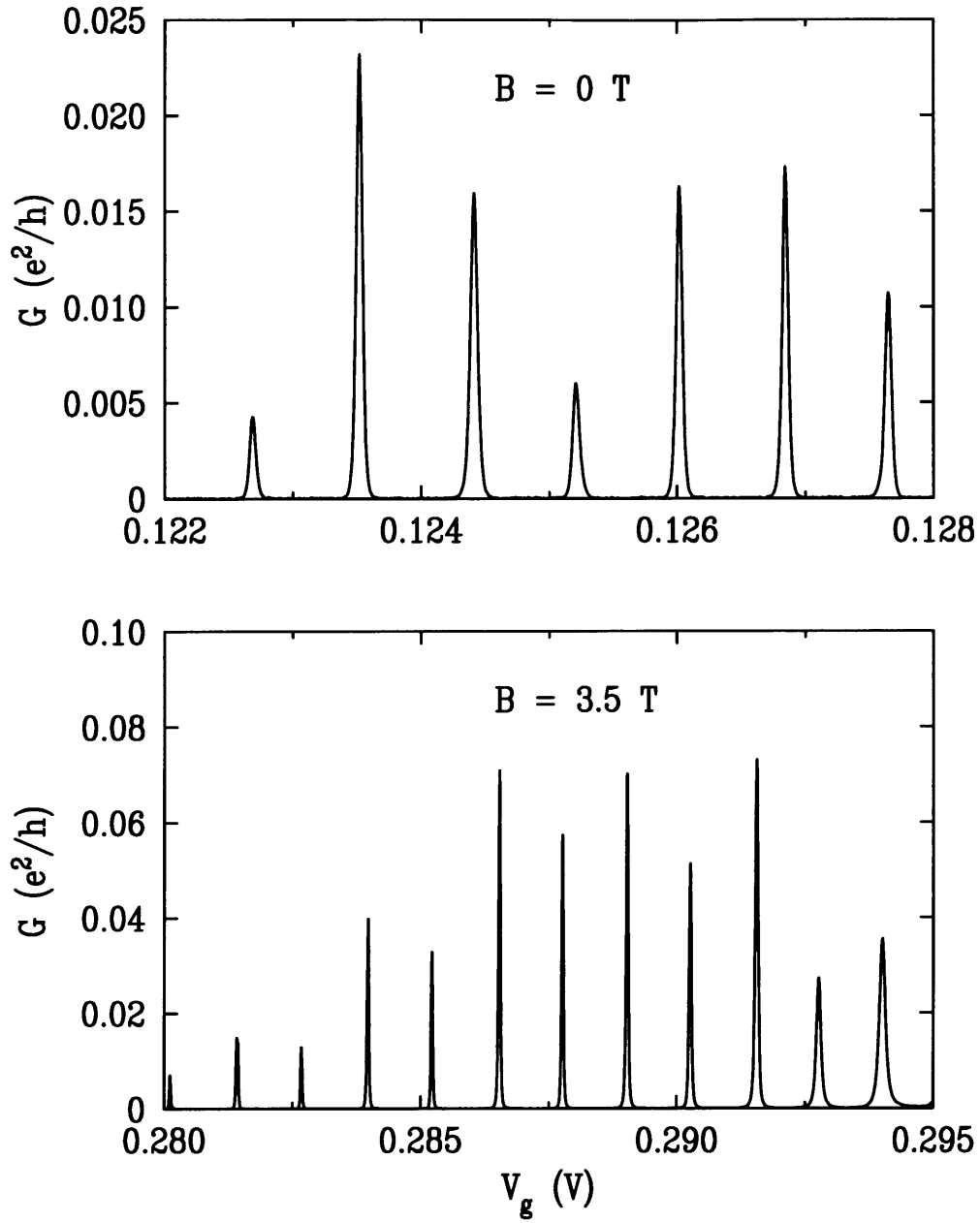


Fig. 5-6. G as a function of gate-voltage in zero and finite B . Notice the alternation of peak amplitudes in the $B = 3.5 \text{ T}$ trace which corresponds to $1 \geq \nu \geq 2$, where ν is the inferred filling factor in the small electron gas.

5.3 The Self-consistent Model of Single Electron Charging in the Quantum Hall Regime

In this Section, we present a self-consistent model of single electron charging that can in large part account for the magnetic field behavior described above[51, 138]. In the self-consistent model, the small electron gas is modeled as a system of interacting electrons confined in the external potential, V_{ext} created by the gates. For simplicity, V_{ext} is chosen to be a harmonic confining potential given by

$$V_{ext} = \frac{1}{2}m^*\omega_o^2r^2. \quad (5.2)$$

This is shown in Figure 5-7(a). Electrons placed in this bare confinement potential interact with each other via a Coulombic interaction, $V_{ee}(\mathbf{r}, \mathbf{r}')$. For the time being we use the simplest assumption for the form of the interaction, $V_{ee}(\mathbf{r}, \mathbf{r}') = 1/|\mathbf{r} - \mathbf{r}'|$. This allows for certain analytic results to be obtained from the model as will be demonstrated shortly. This expression for $V_{ee}(\mathbf{r}, \mathbf{r}')$, however, neglects the screening of electron-electron interactions by the metallic gates, as well as the finite thickness of the wave function perpendicular to the plane of the 2-DEG. Both these effects, which reduce the strength of the Coulomb interactions can be taken into account in numerical calculations[51]. (See for example, the footnote on page 149.)

Consider what happens when interacting electrons are added to the confining potential defined by Equation 5.2. If charge density is treated as a continuous quantity $\rho(r)$, then this is a problem in classical electrostatics. The electrostatic potential in the gas, ϕ , is given by:

$$\phi(r) = V_{ext}(r) + \int_A d^2r' \frac{\rho(r')}{|r - r'|} \quad (5.3)$$

The charge redistributes itself so that $\phi(r)$ is constant in the area where there is

charge. The resulting charge distribution $\rho(r)$, and electrostatic potential $\phi(r)$, and radius R of the confined electron gas of total charge eN , is found from Reference [139] to be

$$\rho(r) = \rho(0)(1 - r^2/R^2)^{1/2} \quad (5.4)$$

$$\phi(N) = [(3e^2/16\epsilon_o\epsilon_r)^2 m^* \omega_o^2]^{1/3} N^{2/3} \quad (5.5)$$

$$R = (3e^2 N / 16\epsilon_o\epsilon_r m^* \omega_o^2)^{1/3}, \quad (5.6)$$

where $\rho(0) = 3eN/2\pi R^2$ is the electron density at the center of the gas and $\epsilon_r = 13.6$ is the dielectric constant of bulk GaAs. The charge distribution is thus a hemisphere with a density and radius that grows with increasing N . This is illustrated in Figure 5-7(a) and (b).

An interesting point is that adding a single additional electron to the small electron gas increases the energy of the system by a discrete amount. This charging energy is equal to

$$\phi(N+1) - \phi(N) \approx \frac{d\phi}{dN} = \frac{e^2}{8\epsilon_o\epsilon_r R} \quad (5.7)$$

In the language of the Coulomb blockade model as depicted in Figure 5-7, the small electron gas has a self-capacitance of $C = 8\epsilon_o\epsilon_r R$. Note that C is a function of N . This implies that, within this model, the spacing between conductance peaks, $e/\alpha C$ is also a function of N . However, C is only weakly dependent on N and for reasonable values for N , (*e. g.* $N \approx 100$) and over a limited range of conductance peaks, the spacing between peaks is nearly constant.

From the data in Figure 5-3(b), which shows peak position versus B in the Quantum Hall regime, it is possible to extract values for N and $\rho(0)$. This will be done explicitly below. In that analysis we find that $\rho(0) = 9.6 \times 10^{10} \text{ cm}^{-2}$, and $N = 77$. Substituted into Equation (5.4) - (5.5), these values yield $R = 190 \text{ nm}$ and $\hbar\omega_o = 1.75 \text{ meV}$. The effective area of the small electron gas $\pi R^2 = (340 \text{ nm})^2$ compares well with estimates of the electron gas area based on simulations of

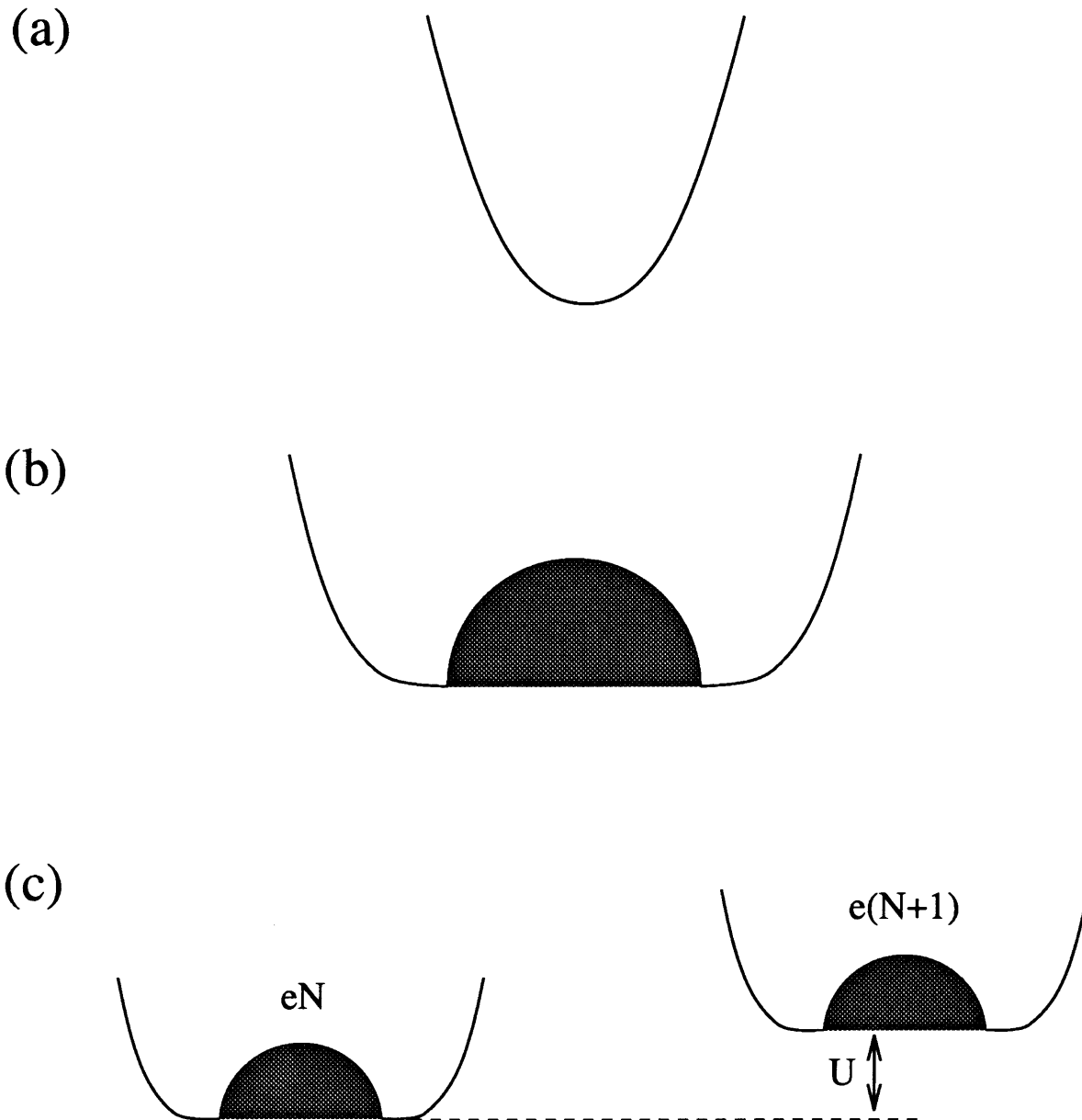


Fig. 5-7. Electrons in a harmonic confinement potential. (a) The Harmonic potential V_{ext} is produced by the gates. (b) The self-consistent charge distribution (shaded) and electrostatic potential for an small electron gas containing (b) N and (c) $N + 1$ electrons. Note the discrete shift U in the electrostatic potential associated with the addition of a single electron.

the gas ($A = (360 \text{ nm})^2$) [113], the area determined from low B conductance fluctuation ($A = (230 \text{ nm})^2$), and the area estimated from the gate capacitance of the device ($A = (310 \text{ nm})^2$). The value of $\hbar\omega_o$ is also in good agreement with values ($1 - 3 \text{ meV}$) obtained from electrostatic simulations of the structure[113]. Finally, with these parameters, the charging energy is predicted to be $U \approx 0.85 \text{ meV}$ which is in good agreement with the measured value $U = 0.65 \text{ meV}$.

Now, consider the effects of applying a high magnetic field in this model. When a large B is applied to a 2-DEG, the density of states breaks up into Landau levels. The maximum areal density of electrons in each Landau level is $1/(2\pi l_B^2)$, where $l_B = h/Be$ is the magnetic length in SI units. For a fixed electron density n_s , electrons fill the lowest $\nu = n_s/(2\pi l_B^2)$ Landau levels, where ν is called the electron gas filling factor. This describes the situation in a macroscopic 2-DEG. To first approximation, we assume that at high B electrons in the small electron gas occupy Landau levels so as to maintain the classical distribution of charge in the gas. This situation is shown in Figure 5-8(a). In this illustration, ρ and B are such that, at the center of the gas, where $\rho(r)$ has its largest value, the density of the gas is large enough that one full Landau level and part of a second Landau level are occupied. Towards the edges of the gas where $\rho(r)$ decreases, only portions of the lowest Landau level are filled.

For now, we focus on the situation in Figure 5-8(a) where only two Landau levels are brought into play. In this arrangement, the number of electrons in the first and second Landau levels, n_1^o and n_2^o respectively, are

$$n_2^o = N(1 - 1/\nu)(1 - 1/\nu^3) \quad (5.8)$$

$$n_1^o = N - n_2^o, \quad (5.9)$$

where eN is the total charge in the gas.³ Note, these equations do not constrain

³These expressions come from integrating the charge density given in Equation 5.4 in conjunction with known density of a Landau level at a given B .

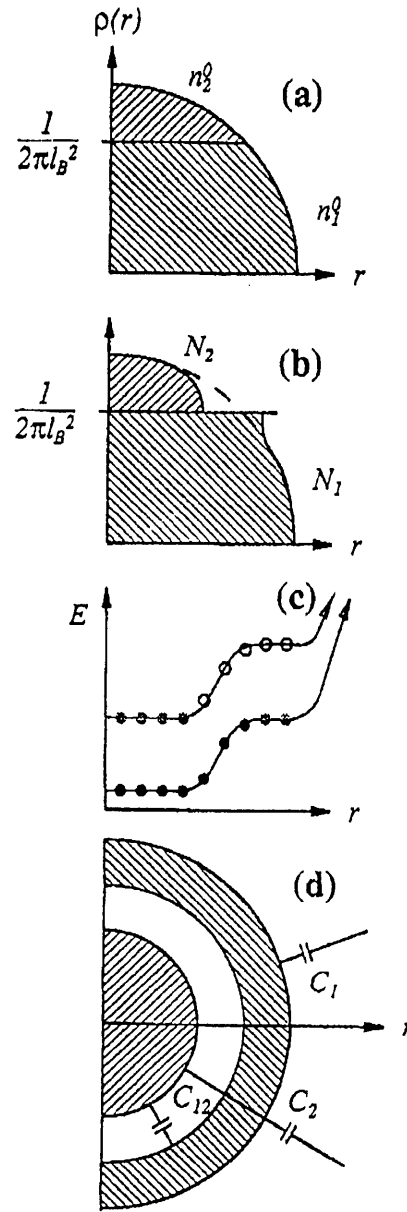


Fig. 5-8. The self-consistent model in the quantum Hall regime. (a) The filling of Landau levels that would give the classical electrostatic distribution of charge in the gas. (b) Electrons redistribute from the higher to the the lower Landau level to minimize their Landau level energy. (c) The self-consistent level diagram for the small electron gas. Solid dots: fully occupied Landau levels. Shaded dots: partially occupied Landau levels. (d) The resulting distribution of charge into compressible and incompressible regions. “Metallic regions (partially occupied Landau levels) are separated by an “insulating” region (fully occupied Landau levels). The interactions between regions can be characterized by effective capacitances, as shown in the Figure.

n_i^o to be an integer, and they will, in general, be real. As B is increased the Landau level degeneracy increases. So the line separating the first and second Landau levels in Figure 5-8 moves up as B is increased. We now take into account that electrons in different Landau levels have different energies. We will see that inclusion of these “quantum energies” associated with different Landau level leads to only small adjustments in the energy and charge distribution of the electron gas.

The kinetic and spin energy E_i , of an electron in the i^{th} Landau level is

$$E_i(l, S_z) = (l + 1/2)\hbar\omega_c \pm g\mu_B B S_z \quad (5.10)$$

where $l = 0, 1, 2, \dots$ is the orbital Landau level index, $S_z \pm 1/2$ is the spin Landau level index, and $\omega_c = eB/m^*$ is the cyclotron frequency. Referring back to Figure 5-8(a), electrons in the second (upper) Landau level have a higher spin energy than electrons in the first (lower) Landau level. So some of the electrons in the upper Landau level will move to the lower Landau level. While this process raises the electrostatic contribution to the total energy of the system, it lowers the kinetic and spin contribution. This process continues until the excess electrostatic energy associated with the redistribution of charge cancels the gain from lowering the Landau level energy. The resulting distribution of charge is shown schematically in Figure 5-8(b), and the electrostatic potential in Figure 5-8(c). In the center of the small electron gas, where the second Landau level is partially occupied, the confinement potential is screened and the self-consistent electrostatic potential is flat[140, 141]. Likewise, near the edge, where the first Landau level is partially occupied, there is screening and the potential is flat. Between these two areas is a region where exactly one Landau level is occupied. In this region the electron gas is incompressible, and no screening takes place. Consequently, $\phi(r)$ instead of being flat, rises in this region by an amount that corresponds to the energy spacing between the two Landau levels.

The resulting structure of the small electron gas is shown in Figure 5-8(d). Roughly speaking, the effect of B is to separate the gas into two metallic regions separated by an insulating strip. Each metallic region can be assigned a separate quasi-electrochemical potential given by:

$$\mu_1(N_1, N_2) = (N_1 - n_1^o)U_{11} + (N_2 - n_2^o)U_{12} + E_1 \quad (5.11)$$

$$\mu_2(N_1, N_2) = (N_2 - n_2^o)U_{22} + (N_1 - n_1^o)U_{12} + E_2 \quad (5.12)$$

where N_i is the (integer) number of electrons in the i^{th} Landau level, and U_{ij} is the shift of the electrostatic potential of the i^{th} Landau level if an electron is added to the j^{th} Landau level. A microscopic calculation is necessary to obtain numerical values of U_{ij} . Such calculations have been carried through by our group[51] and by others[142, 143, 144]. For now, however, the U_{ij} 's are simply treated as parameters. Equations 5.11 and 5.12 can be written in another useful form:

$$\mu_1(N_1, N_2) = (N - n^o)U_{12} + (N_1 - n_1^o)(U_{11} - U_{12}) + E_1 \quad (5.13)$$

$$\mu_2(N_1, N_2) = (N - n^o)U_{12} + (N_2 - n_2^o)(U_{22} - U_{12}) + E_2 \quad (5.14)$$

where $n^o = n_1^o + n_2^o$, is the total equilibrium charge in the gas if charge were continuous. Note that the first terms in Equations 5.13 and 5.14 are analogous to the charging energy in Equation 5.1 on page 137: they are proportional to the total charge on the island, and they do not depend on the Landau level index or on B . The second two terms in Equations 5.13 and 5.14 are analogous to the single-particle energy in Equation 5.1. The B dependence of the electrochemical potential is due to these terms, both the Landau energies (the terms E_1 and E_2 in Equations 5.13 and 5.14) and the self-consistent electrostatics (the terms $(N_1 - n_1^o)(U_{11} - U_{12})$ and $(N_2 - n_2^o)(U_{22} - U_{12})$ in Equations 5.13 and 5.14).

5.4 Comparison of the Self-consistent Model with Experiment

We now relate this model to the experimental data. Figure 5-9(b) shows the experimentally observed V_g of a conductance peak as a function of B . The lithographic dimensions of the electron gas in this device were slightly different ($450 \times 900 \text{ nm}^2$) than the device discussed at the beginning of this chapter but otherwise the two structures are very similar[51]. Above $B \approx 2.0 \text{ T}$ the peak position as a function of B behaves very similarly to the trace in Figure 5-3, showing regular oscillations in peak position. Figure 5-9(b) shows the calculated electrochemical potential of the 38th and 39th electrons versus B , using the self-consistent model⁴. The overall shape, as well as the scale, of the structure in μ_e is quite similar to that in the experimental data of Figure 5-9(a). In addition, the separation between successive μ_e in the calculation is in reasonable agreement with the experimentally observed peak spacing ($\alpha\Delta V_g \sim 0.48 \text{ mV}$). The density of the gas in the model is $\sim 30\%$ less than in the experiment, but uncertainties in the number of electrons and in the parameter ω_o can easily account for this difference. Most importantly, the model predicts the regular oscillation of the peak position in the $1 < \nu < 2$ regime.

Consider the following additional aspects of the self-consistent model. First, it can be used in conjunction with measurements of peak-position versus B to obtain an accurate estimate of the number of electrons in the small electron gas. For example, in the data of Figure 5-3(a) there are approximately 33 oscillations in the peak-position that occur between $\nu = 2$ and $\nu = 1$. This implies that, when the second Landau level is fully occupied just in the center of the gas, there are a total of 33 electrons in the second Landau level. According to Equations 5.8 and 5.9, the total number of

⁴ In this calculation, $\hbar\omega_o = 1.6 \text{ meV}$ and $V_{ee}(\mathbf{r}, \mathbf{r}') = e^2/\epsilon(|\mathbf{r}-\mathbf{r}'|^2+z^2)^{1/2} - e^2/\epsilon(|\mathbf{r}-\mathbf{r}'|^2+4d^2)^{1/2}$ where $z = 10 \text{ nm}$, the z -extent of the 2-DEG wave function and $d = 95 \text{ nm}$, the distance from the 2-DEG to the gates[51].

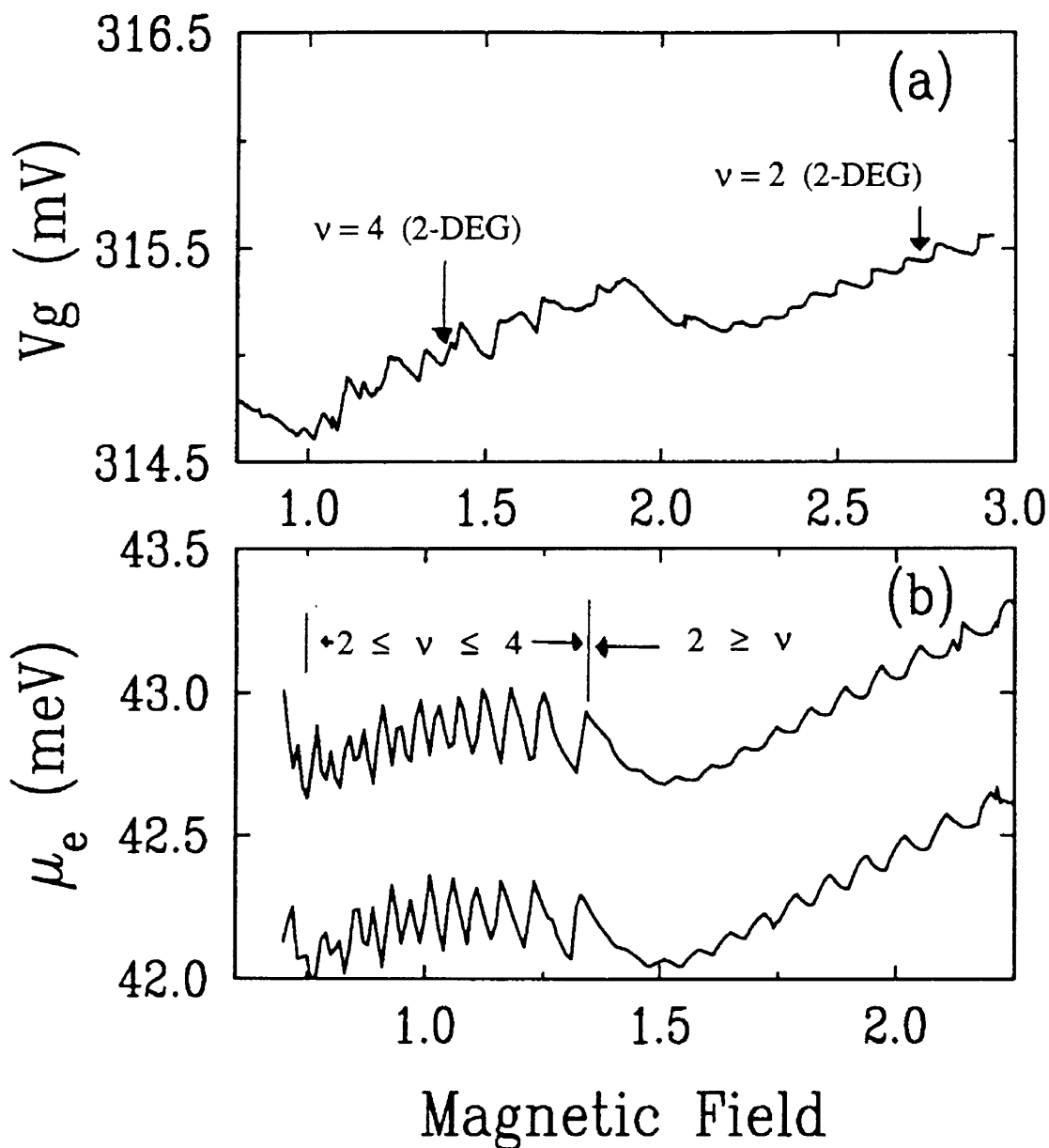


Fig. 5-9. Comparison of the self-consistent model with experiment. (a) The position in gate-voltage V_g of a conductance peak as a function of B in Tesla. The measured filling factors ν of the macroscopic 2-DEG are indicated on the plot. (b) The electrochemical potentials of the 38th and 39th electron versus B calculated using the self-consistent model described in the text.

electrons is then $N = 77$. Furthermore, if there were a total of 33 electrons in the second Landau level at $B = 2.25$ T then this implies that $\rho(0) = (33)/(2\pi l_B^2)$ which, from Equation 5.4, gives R . This is the basis from which N and R were determined in Section 5.3.

Second, note that the small electron gas can be parameterized in terms of capacitances, as is shown in Figure 5-8(d)[144]. The relation between the U_{ij} 's and C 's are given by[145]

$$U_{12} = e^2/(C_1 + C_2 + C_1 C_2 / C_{12}) \quad (5.15)$$

$$U_{11} = e^2/(1 + C_2 / C_{12}) U_{12} \quad (5.16)$$

$$U_{22} = e^2/(1 + C_1 / C_{12}) U_{12} \quad (5.17)$$

The measured values of the U 's can be used to infer these capacitances. For example, for the structure measured in Figure 5-3 in the $\nu = 2$ regime, these capacitances are found to be: $C_1 \approx 0.36$ fF, $C_2 \approx 0.18$ fF, and $C_{12} \approx 1$ fF. Of interest is the inter-Landau level capacitance C_{12} . If this value is divided by the circumference of the electron gas ($\sim 1.5 \mu\text{m}$), an order of magnitude estimate for the inter-edge capacitance between Landau levels per unit length is obtained, $C_{12}/L \sim 600$ pF/m. Third, the self-consistent model can be used to calculate the behavior of a series of conductance peaks as a function of B . Such computer calculations were carried out by J. Kinaret in Reference [51]. Figure 5-10 shows the results of those calculations where peak position versus B has been plotted with a constant spacing subtracted between peak positions. This was done for comparison with data such as that plotted in Figure 5-5(b) on page 140(b).

Finally, consider once again the oscillations in peak position with B as in Figure 5-3(b) on page 138(b). If we assume that only the lower Landau level has significant coupling across the barriers and that the upper Landau level has no coupling across the barriers then it is possible to calculate the temperature behavior of a peak as B is

varied. This is done using the model discussed in Chapter 4 and assuming a discrete level spectrum composed of well-coupled levels and levels with no coupling. As B is varied the relative position of the levels changes. This corresponds to changes in energy of electrons in the first and second Landau levels as B is varied. Whenever a weakly coupled level is aligned with the Fermi level in the leads, the peak amplitude dips. In Figure 5-4 the results of carrying through this calculation are compared with our measurements. In the Figure, $\Delta E^{(1)}$ is the relative spacing between well coupled levels, which is assumed to be constant over a limited range of B , and $E^{(2)}$ is the energy of the weakly coupled level closes to the Fermi energy in the leads[50].

In closing, bear in mind that while the self-consistent model seems to account for much of what is observed, our discussion has focused mainly on the regime $1 \leq \nu \leq 2$. Outside this regime, the B dependence of conductance peaks displays additional interesting behavior which has yet to be fully understood. Figure 5-11 shows peak position as a function of B over a wide range of B . Notice that in addition to the regular oscillatory behavior already discussed above (Figure 5-5(a)) this plot shows behavior such as the emergence of a peak between two other peaks as B is increased and “dislocations” that run vertically through several peaks.

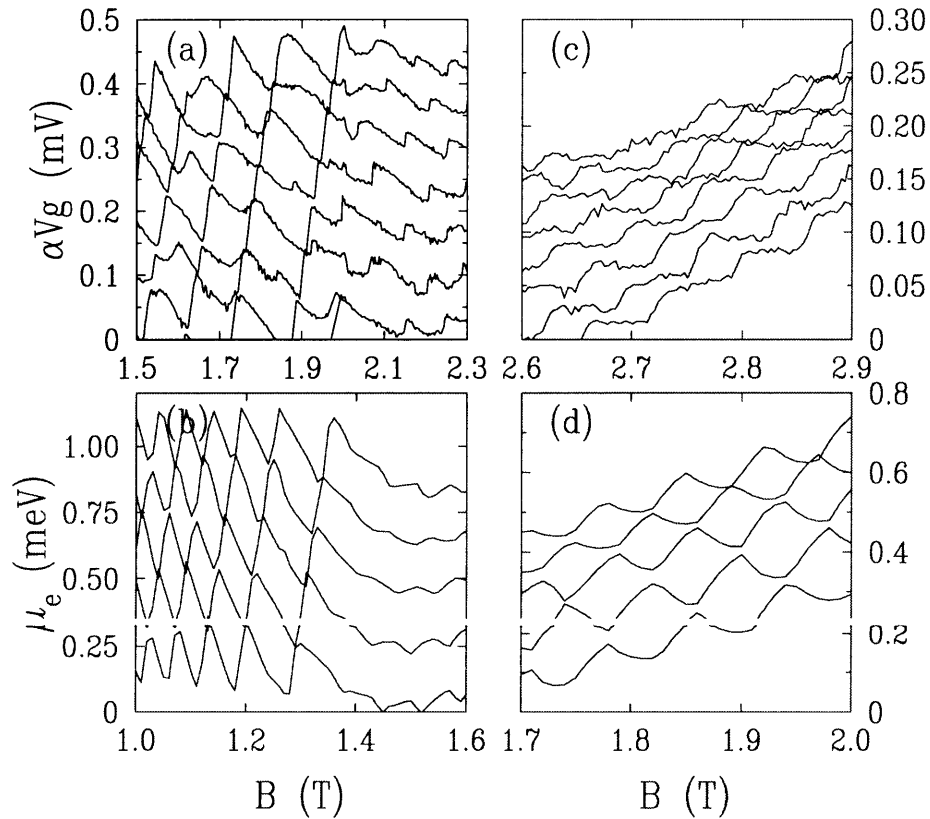


Fig. 5-10. Peak position versus B for successive peaks calculated in the self-consistent model. (a) Experimental “spectrum” (as in Fig. 5-5(b)), and (b) the calculated “spectrum” from the self-consistent model in the $3 \geq \nu \geq 2$ regime. these spectra are constructed by subtracting a constant between successive peak position traces. (c) Experimental spectrum and (d) calculated spectrum in the $\nu \leq 2$ regime, constructed by subtracting slightly larger constants than in (a) and (b). (From Reference [51]).

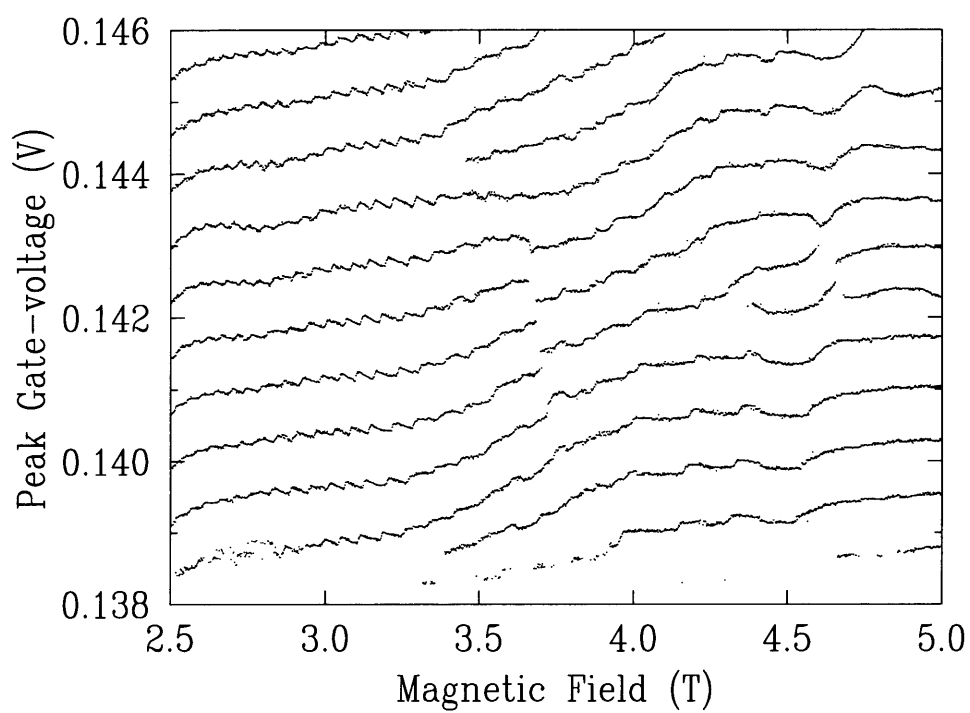


Fig. 5-11. Peak position versus B over a wide range in B .

Chapter 6

Electron Transport in Weakly Blockaded Regime

6.1 Introduction

In the previous chapters we showed that the conductance through a small electron gas as a function of gate-voltage V_g , consists of a series of nearly periodic conductance peaks. This small electron gas was created by interrupting a thin channel of 2-DEG with two tunnel barriers. The conductance of a thin channel of 2-DEG that is not interrupted by any sort of barrier is simply Ohmic. We can restate these two observations by saying that a channel with a pair of tunnel barriers is in the Coulomb blockade regime while a channel with no barriers is in the Ohmic conductance regime. It is natural to ask how the conductance of a thin 2-DEG channel evolves as it is moved from the Coulomb blockade regime to the Ohmic regime by continuously varying the strength of its tunnel barriers[146].

In this chapter we present data which address this question. Specifically, we show transport measurements of a small electron gas in the regime where the tunnel

barriers, while still strong enough to maintain the Coulomb blockade, are weak enough that the first signs of the quenching of the Coulomb blockade are observable. We refer to this conductance regime as the weakly blockaded regime.

6.2 Conductance Measurements in the Weakly Blockaded Regime

Figure 6-1(a) shows the linear conductance of through a small electron gas as a function of gate-voltage, V_g , applied to the conducting substrate of the device. (The device geometry is shown in Figure 2-10 on page 47.) At high V_g the conductance peaks in this trace broaden, the valley conductances increase and the peak to valley ratios decrease from values greater than 10^3 at low V_g to ~ 10 at higher V_g . The peaks at low V_g have tails that fall off exponentially as seen in Figure 6-1(b). Peaks at higher V_g , as in Figure 6-1(c), are broader and exhibit lineshapes having the tails do not fall off exponentially.

The conductance peak at low V_g in Figure 6-1(b) is fit well with the lineshape of Equation 4.7 on page 127 which describes the lineshape of a conductance peak when $kT \ll \Delta\epsilon \ll U$. This fit, shown as the solid line in Figure 6-1(b) yields $\alpha = 0.52$ and hence $U = 0.61$ meV. The fact the peak amplitudes in the gate-voltage trace of Figure 6-1 alternate between large and small peaks indicates that each peak corresponds to tunneling into one spin-split level, *i. e.* $kT \ll \Delta\epsilon$, and argues against fitting with the classical lineshape of Equation 4.12 on page 129 which applies in the case $\Delta\epsilon \ll kT \ll U$. Because its tails do not fall off exponentially, the conductance peak at high V_g can not be fit with either lineshape.

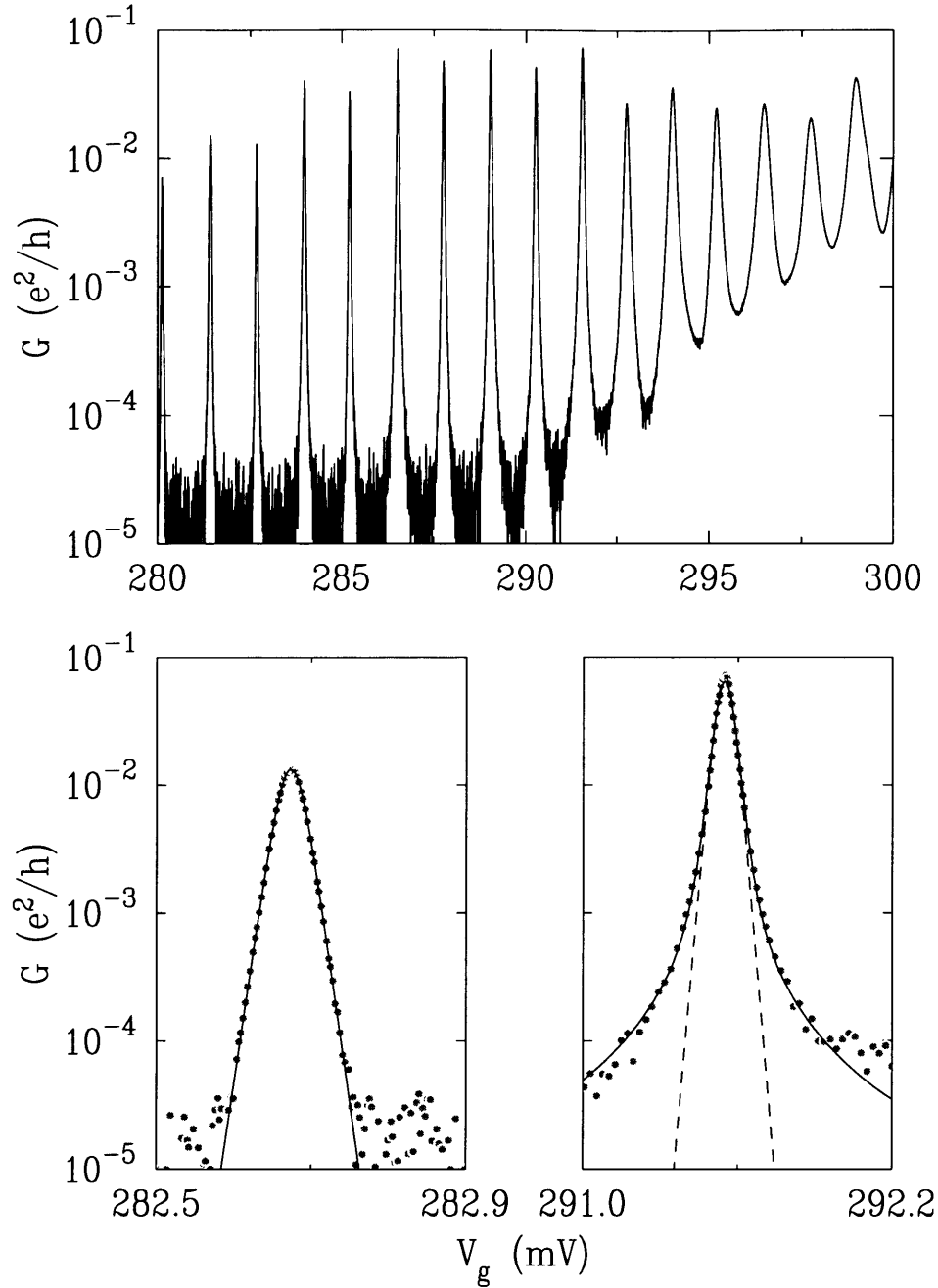


Fig. 6-1. G versus V_g showing the quenching of the Coulomb Blockade. (a) the low-bias conductance of the electron gas *vs.* V_g at $B = 2.53$ T and $T = 65$ mK. (Note the alternation of peak amplitudes which arises from the spin splitting of Landau levels as discussed in Chapter 5.) (b) A low V_g conductance peak from (a) shown fit to a thermally broadened resonance (solid line) in the limit that the intrinsic resonance width is much less than kT . (c) A conductance peak at higher V_g shown fit to a thermally broadened Lorentzian (solid line). the dashed line is the best fit using the same lineshape as in (b).

6.3 Thermally broadened Lorentzian lineshapes at high V_g

In this Section we reconsider the lineshape of the conductance peak at high V_g . We have fit the data in Figure 6-1(c) to a thermally broadened Lorentzian parameterized by a full-width at half-maximum, Γ ,

$$G = \frac{e^2}{h} \frac{1}{4kT} A \int_{-\infty}^{+\infty} \cosh^{-2}(E/2kT) \frac{(\Gamma/2)/\pi}{(\Gamma/2)^2 + [(e\alpha V_g - E_{res}) - E]^2} dE, \quad (6.1)$$

where E_{res} is the energy of the transmission resonance, and A is the integrated area of Lorentzian. The fit yields $\Gamma = 4.65 \mu\text{eV}$, $A = 1.70 \mu\text{eV}$ and $\alpha = 0.30$ giving $U = 0.35 \text{ meV}$. Equation 6.1 describes a thermally broadened transmission resonance¹ for non-interacting particles[147, 148]. Although the system that we are measuring is far from being a non-interacting system (in fact, interactions give rise to periodic conductance peaks and the magnetic field behavior discussed in Chapter 5), in the absence of any theoretical treatment, we will for the moment interpret the fit as a noninteracting transmission resonance. In this framework, the width of the resonance Γ , corresponds to the lifetime broadening of the resonance, $\Gamma \sim \hbar/\tau$, where τ is the leakage time to tunnel out of the small electron gas from a resonant state in the gas.

A and Γ are related to the leakage rates through the left and right barriers, Γ_L/h and Γ_R/h respectively, via:

$$A = 2\pi \frac{\Gamma_L \Gamma_R}{\Gamma_L + \Gamma_R} \quad (6.2)$$

$$\Gamma = \frac{1}{2}(\Gamma_L + \Gamma_R). \quad (6.3)$$

Using the values of A and Γ from above, we get $\Gamma_R = 4.35 \mu\text{eV}$ and $\Gamma_L = 2.90 \mu\text{eV}$.²

¹This is sometimes referred to as the Breit-Wigner Lineshape

²In Chapter 4 Γ_L and Γ_R denoted tunneling rates which have units of sec^{-1} .

The Fermi energy in the small 2-DEG is ~ 15 meV which implies a Fermi velocity, $v_F \sim 2.8 \times 10^{-5}$ m/s. Approximating the distance between barriers as $L = 0.5 \mu\text{m}$ then the transmission coefficient for the barriers at the Fermi level, $|t_i|^2$, is given by

$$|t_i|^2 = \frac{L}{v_F} \frac{\hbar}{\Gamma_i} \quad (6.4)$$

yielding $|t_L|^2 = 3.0 \times 10^{-4}$ and $|t_R|^2 = 2.0 \times 10^{-5}$.

Two points stand out from the above analysis. First, the Coulomb charging energy, U , for the peak at high V_g ($U = 0.35$ meV) is significantly smaller than the charging energy at associated with the low V_g peaks ($U = 0.61$ meV). We will investigate the origin of this effect below in Section 6.4. For now we only consider that the voltage width of a conductance peak, δV , scales in proportion to U ,

$$\delta V \propto \frac{kT}{\alpha} = kT \frac{C}{C_g} = kT \frac{U}{e^2 C_g} \quad (6.5)$$

where C , is the total capacitance of the small electron gas and C_g , the capacitance between the gate and the electron gas³. So the increase in U at higher V_g accounts in part for broadening of conductance peaks at large V_g . Second, lifetime broadening of the resonance, Γ also contributes to the broadening of peaks at high V_g . Roughly speaking, the full-width at half-maximum of the Lorentzian peak in Figure 6-1(c) is 80% due to thermal broadening and 20% due to Γ . So the quenching of single-electron charging effects in at high V_g is caused by both the reduction of U and the increase in Γ at large V_g .

³The gate capacitance is $C_g = e/\Delta V_g$ where ΔV_g is spacing between conductance peaks. ΔV_g is independent of V_g in Figure 6-1(a). So C_g can be treated as a constant in our analysis.

6.4 Lorentzian Fits over a range of Conductance Peaks

In order to better understand this behavior, we have fit a series of conductance peaks, shown in Figure 6-2(a), with the thermally broadened Lorentzian lineshape. From the fits, values for U and Γ were extracted from peaks at different V_g . Figure 6-2(b) shows that Γ increases exponentially with V_g , which is consistent with tunneling through a saddle point potential[107]. Figure 6-2(c) shows that U (triangle symbols) diminishes with V_g which implies that $C = e^2/U$ increases with V_g .

We test this last proposition by assuming that C is the sum of four capacitances, the capacitance between the small electron gas and the back gate, C_{gb} , the capacitance between the gas and surface gates, C_{gs} , and the gas-lead capacitances to both the left and the right leads, C_l and C_r respectively. (A schematic of this device, showing the various gates, is contained in Figure 2-10 on page 47.) C_{gb} and C_{gs} are measured directly from ΔV_g , the spacing between peaks.^{4,5} C_l and C_r are determined from the slope of the peak positions versus gate voltage, dV_{ds}/dV_g , in measurements similar to those in Figure 4-6 on page 103. (Notice that in this Figure the magnitude of the Coulomb-blockade gap visibly decreases at higher V_g , consistent with the decrease in U with V_g determined from the Lorentzian fits in Figure 6-2(c).) The Coulomb-blockade model gives:

$$\frac{dV_{ds}}{dV_g} = \frac{C_{gb}}{C - C_{bias}} \quad (6.6)$$

where C_{bias} is the capacitance across the barrier between the gas and the biased lead, either C_l or C_r .

The above procedure gives $C_{gb} = 0.124$ fF, $C_{gs} = 0.025$ fF and $C_l = 0.045$ fF \pm

⁴A small contribution to the spacing between peaks ($\sim 10\%$) is due to the single-particle energy to add an electron to the small electron gas. (See the discussion in Chapter 4 and in Reference [68].) Therefore, the minimum observed spacing between peaks is used for ΔV_g .

⁵In a different study, a similar procedure was carried out except that the equivalents of C_l and C_r were assumed to be zero. See Reference [149].

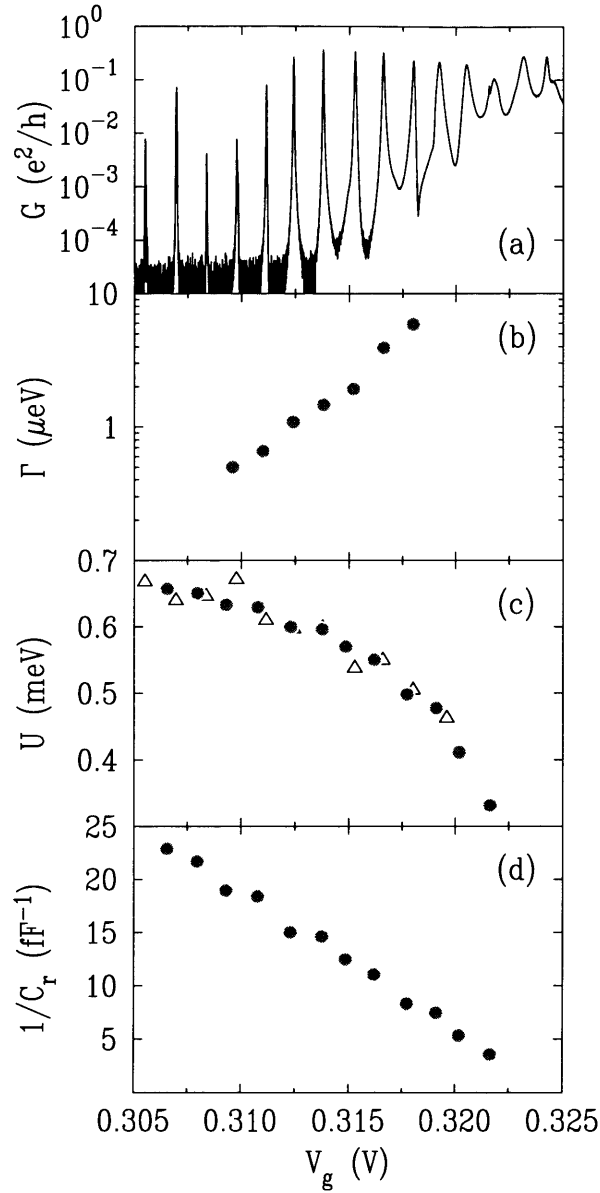


Fig. 6-2. Mechanism of the Quenching of the Coulomb Blockade. (a) Conductance versus gate voltage, V_g at $B = 3.35$ T. Each peak in (a) is fit to a thermally broadened Lorentzian yielding values for Γ , the Lorentzian full-width at half-maximum (plotted in (b)) and U , the charging energy of the small electron gas (triangular symbols in (c)). (d) The reciprocal of the capacitance across the right barrier, C_r^{-1} . U determined from the values of C_r in (d), as described in the text, is plotted as the filled circles in (c).

0.005 fF independent of V_g .⁶ Surprisingly, however, C_r increases from ~ 0.045 fF to > 0.300 fF over the range of V_g in Figure 6-2 U thus diminishes due to the increasing capacitance across the right barrier at high V_g .⁷ Figure 6-2(d) shows that C_r^{-1} goes to zero linearly in V_g . U , determined from the sum of C_{gb} , C_{gs} , C_l and C_r , is plotted as the filled circles in Figure 6-2(c). The agreement between this measurement of U and that determined from the fits confirms the accuracy of the above procedure for measuring the capacitances to the small electron gas.

6.5 Quantum Mechanical Cheating in the Coulomb Blockade

We close this chapter with a general discussion of what we refer to a quantum mechanical cheating in the Coulomb blockade. Our discussion above of the lifetime broadened peaks is an example of such “cheating”. By this we mean that electrons that would classically be confined between two barriers can quantum mechanically tunnel out through one of those barriers. Stated another way, if the time required for this electron to tunnel out of the barriers, τ , is finite then it is really not possible to say that there are N electrons in the small electron gas. Rather one can say that there are on average N electrons in the gas but, because electrons can tunnel through the barriers, there is a finite probability of measuring a number of electrons in the gas that is an integer other than N . If such measurements are done repeatedly then the average number of electron in the gas, $\langle N \rangle$ can be ascertained, where $\langle N \rangle$ is not necessarily an integer. The Coulomb blockade, which is a classical theory, assumes that the number of electrons in the small electron gas is has no such quantum mechanical fluctuations. That is, that N is a good quantum number. As the coupling

⁶1 fF = 10^{-18} F

⁷The capacitance across the barriers probably accounts for the missing stray capacitance discussed in References[63, 50].

across the tunnel barriers is increased, there will be a point beyond which this is no longer a good assumption, and the Coulomb blockade theory breaks down. We now wish to address the problem of determining where this will occur. In other words we want to determine the dividing line between the classical and quantum description of the small electron gas. This is really the same question addressed above which asked how we go between the Strongly blockaded regime and the Ohmic regime of the conducting channel.

6.5.1 Thouless' Criteria for Single-electron Charging

We review here three theoretical arguments that address this question. The first is attributable to D. J. Thouless who examined a similar question when considering the conductance of thin wires[150]. His argument, in slightly different terms, proceeds as follows: The boundary between the classical and quantum worlds is marked by the point at which the lifetime energy broadening of resonances Γ , is comparable to the average spacing between resonances ϵ . This is simply to say that one can only speak of there being N electrons in the gas when the transmission probability through the gas actually breaks up into discrete resonances. So a necessary condition implicit in models of single electron charging is that

$$\Gamma \ll \epsilon \quad (6.7)$$

We now consider the implications of this statement.

The current that passes through the gas in response to a voltage bias V , is

$$I = \frac{eV}{\epsilon} \frac{e}{\tau}. \quad (6.8)$$

τ is related to the leakage times through the left and right barriers, τ_l and τ_r respec-

tively, through

$$\tau = \tau_l + \tau_r, \quad (6.9)$$

which is an expression analogous to the total conductance of two conductors in series. This relation, with Equation 6.8, implies that the conductance through the gas, G , is given by

$$G = \frac{e^2}{\epsilon(\tau_l + \tau_r)} \quad (6.10)$$

The uncertainty principal relates the resonance lifetime and the energy broadening of the resonance, Γ :

$$\Gamma \frac{\tau_l \tau_r}{\tau_l + \tau_r} \cong h. \quad (6.11)$$

This expression combined with Equation 6.10 and Thouless' criteria, in Equation 6.7, yields

$$G \ll \frac{e^2}{h} \frac{\tau_l \tau_r}{(\tau_l + \tau_r)^2}. \quad (6.12)$$

This is an interesting relation in that it implies that the conductance of a system must be below e^2/h in order to observe single electron charging effects. This criteria is in fact met in all our observations of single electron charging.⁸ The conductance of a one-dimensional free electron gas is exactly e^2/h . Landauer[40] and Buttiker[41] have based a theory of microscopic conductance on idea that the conductance of a system can be described as the superposition of a number of one-dimensional channels or modes. In light of this approach, another way of interpreting Thouless' criteria is that single-electron charging is observable only when each of the barriers is sufficiently strong enough to block (or backscatter) all the conducting modes in the channel.

⁸Using the values of τ_l and τ_r estimated from the Lorentzian fit in Figure 6-1(c), we get $G \ll 0.06e^2/h$. However, the large uncertainties in determined τ_l and τ_r must not be overlooked.

6.5.2 Macroscopic Quantum Tunneling

For completeness we review another approach to the “quantum cheating” problem. In the classical Coulomb blockade, when V_g is biased so that the conductance of the system is between conductance peaks then at $T = 0$ no current should pass through the small electron gas. When quantum mechanical tunneling is brought into play, however, this is no longer the case. It is imaginable that current could flow under these circumstances via an electron tunneling all the way across the small electron gas, in other words by tunneling not only through the potential of the barriers but through the electrostatic potential that classically blockades current between conductance peaks. This phenomena is referred to by different authors (and sometimes the same authors) as macroscopic quantum tunneling (MQT)[116], virtual electron diffusion[119], electron tunneling in a variable electrodynamics environment[151], electrostatically modified virtual electron tunneling[118] and current-voltage characteristics in a double tunnel junction[117].

Theoretically, the approach to the problem has been to calculate the current versus voltage response when V_g is biased between conductance peaks. Since, for small biases, I versus V must be antisymmetric, a Taylor expansion of I in terms of V can contain only odd power terms in V . First order perturbation theory gives the prefactor for the linear term in V and second order perturbation gives the prefactor for the cubic term in V . The first order perturbation corresponds to an electron tunneling into an empty virtual state in the gas and then tunneling out onto the other lead. (The time in which this process occurs, ζ must satisfy $\zeta U \sim \hbar$.) The V^3 process corresponds to an electron tunneling into an empty virtual state, then relaxing into another virtual state by scattering off an electron already in the gas, and then finally tunneling onto the other lead. This first process, since there is no scattering involved, is referred to as elastic-MQT and sometimes direct-MQT whereas the second process is referred to as inelastic or indirect-MQT. In the limit that $V \ll e/2C_1, e/2C_2$ where C_i is the

capacitance across the i^{th} barriers then from Reference [117]

$$I^{(elastic)} = \frac{2\hbar\epsilon(C_1 + C_2)}{\pi e^4 R_1 R_2} V, \quad (6.13)$$

$$I^{(inelastic)} = \frac{2\hbar(C_1 + C_2)^2}{3\pi e^4 R_1 R_2} V^3 \quad (6.14)$$

Using typical values of C_i and R_i in our system, we get for the elastic process $I^{(elastic)} = 2.6 \times 10^{-11}$ V. This is in the range of what we can measure, however, it is not a measurement that we have attempted. Such measurements have been reported in semiconductor systems similar to ours[121]⁹ and in metal particles[122].

6.5.3 The Kondo Transmission Resonance

The Kondo effects refers to the scattering resonance that occurs between conduction electrons and a magnetic impurity ion. Loosely speaking, the resonance arises from an indirect exchange interaction between electrons at the Fermi surface and the magnetic moment of the ion. There is no satisfactory, intuitively straight forward explanation of this effect. One admittedly simplified explanation[152] relies on forth-order terms in the perturbation of an indirect exchange interaction known as the RKKY interaction which also plays a role in the magnetic spin order of rare-earth metals. The essential feature of this effect, though, is that a localized spin can, through collective interactions, create a resonance at the Fermi level. It has been imagined that in systems like ours, if an odd number of electrons are localized in the electron gas, then a Kondo transmission resonance might occur between the conduction electrons in the leads and the small electron gas. Predictions along these lines have been made in

⁹In Reference [121] a central part of the analysis is the discrepancy between U determined from the thermal activation and U determined from $I - V_{ds}$ measurements. Several reasons are given for this discrepancy, however, the capacitance across the tunneling barriers was neglected in this analysis. The raw data in Reference [121] suggests that this is in fact the source of the discrepancy. If this is the case than it is questionable if MQT has been observed in semiconductor systems. If so, possibly systems with large U , *e. g.* Si based devices, might prove to be good systems for investigating MQT.

References [153, 154, 155, 156, 157, 158, 159], however, as of the writing of this thesis there are only very limited experimental reports of this effect[160].

Chapter 7

Conclusion

7.1 Summary

We have conducted an experimental study of a small, two-dimensional electron gas ($\sim 0.3 \times 0.3 \mu\text{m}^2$) in a GaAs/Al_xGa_{1-x}As heterostructure. Electron transport was studied as a function of gate voltage, magnetic field, temperature, bias voltage and tunneling barrier height.

We saw that transport phenomena in these systems exhibits a rich interplay between single-electron charging and quantum effects. In Chapter 3, we showed how a simple model of classical, single electron charging accounts for some of the most striking behavior of these systems, in particular, periodic conductance peaks as a function of gate voltage and the Coulomb blockade staircase. Despite its success, however, the classical model had several noticeable shortcomings. For example, it was inconsistent with the observed temperature behavior of the conductance peaks, and it did not adequately account for the variation in peak amplitude from peak to peak.

These points were addressed in Chapter 4, where we discussed an extended model of single-electron charging that included a discrete quantum mechanical tunneling

density of states. We showed that this model accounts for the observations presented in Chapter 3. Furthermore, in Chapter 4, we presented measurements which directly mapped the discrete tunneling density of states in a small, two-dimensional electron gas as a function of both gate voltage and magnetic field. In Chapter 5, we studied in further detail the evolution of the (low-bias) tunneling density of states as a function of magnetic field. We showed that our observations can be understood through a self-consistent model of single electron charging in the quantum Hall regime. We found in this model that the magnitude of Coulomb interactions between electrons is a function of Landau-level index and magnetic field, and that Coulomb interactions strongly influence the evolution of the discrete tunneling density of states.

Finally, in Chapter 6 we reported transport measurements in the regime where the conductance across the tunnel barriers separating the small electron gas from its leads becomes of order e^2/h . We observed that in this regime single electron charging effects are quenched. We showed that this effect arises from an increased capacitance across one of the barriers and from the increased lifetime broadening of individual states in the small electron gas tunneling density of states. Appendix I contains the three reprints most relevant to the work discussed in this Thesis.

7.2 Odds and Ends

There is a quote, that I believe is attributed to the historian Barbara Tuchman[161], which states, “You never finish writing a book. You just give up on it.” The same is true of a thesis. It would be, however, unfair to the reader to end at this point without touching on some of the unanswered questions provoked by our investigation. What follows is a (perhaps random) set of ruminations revolving around some of the unanswered questions raised in the course of our work.

First, there is an implication of the self-consistent model in the Quantum hall regime that perhaps needs to be more fully thought through. Previous models[68,

50] attributed the spacing between conductance peaks to the sum of two terms: a Coulomb charging term and a non-interacting single particle term. In these pictures, electron-electron interactions were accounted for entirely in the Coulomb charging term. The self-consistent model, however, showed that in the Quantum hall regime this is not the case. Rather, electron-electron interactions give rise to the variation in peak spacing as a function of B [50]. In the previous models, this was explained incorrectly as a variation in the energy of non-interacting levels as a function of B . The implication of the self-consistent model is that, even in zero magnetic field, the discrete density of states in the small electron gas, in addition to the Coulomb gap, is strongly dependent on electron-electron interactions. If so, this should be taken into account when considering a number of experiments which interpret the $B = 0$ and low B -field variation in peak position and amplitude in terms of non-interacting level spectra[162, 163, 164], in particular experiments that attempt to differentiate between spectra in normal and chaotic geometries.

A second point concerning the self-consistent model: Recently, efforts to understand the fractional quantum Hall effect[165, 166] have focused on understanding the $\nu = 1/2$ state, since experimentally[167, 168], in the neighborhood of $\nu = 1/2$ the electron gas behaves similarly to an electron gas at $B = 0$. This behavior is shown in Figure 7-1. The 2-DEG material that we employed did not have a high enough mobility to exhibit fractional effects. (For example, fractional effects were not observed in Shubnikov de-Haas measurements.) It is intriguing to imagine repeating our experimental measurement in the fractional quantum Hall regime[169] and in particular in the neighborhood of $\nu = 1/2$.

Turning to another point, small electron gas systems similar to the one that we have studied have been used to create what are called electron pumps[170] and electron turnstile devices[171, 172]. The basic idea in each device is that the barrier heights and/or the chemical potential in the leads of a device can be cycled in a simple manner such that one electron is caused to pass through the device with each

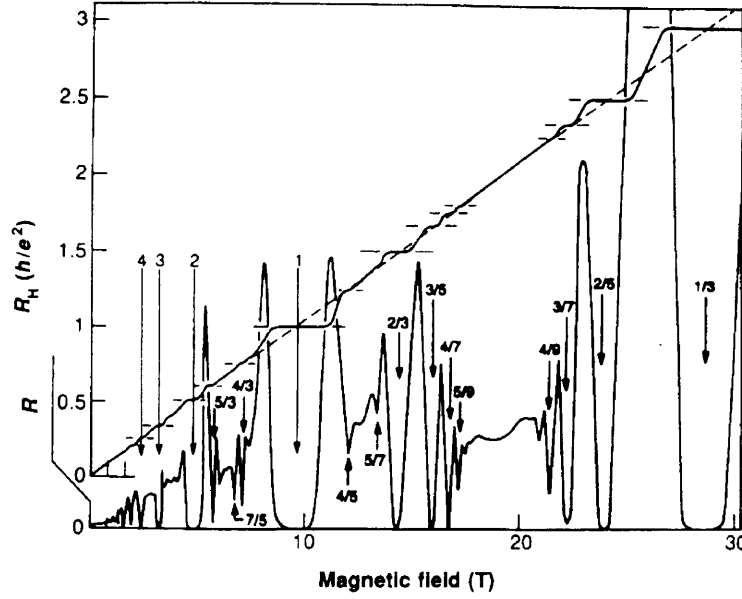


Fig. 7-1. A composite view showing the Hall resistance, R_H , and the longitudinal resistance, R , of a 2-DEG versus magnetic field from J.P. Eisenstein and H.L. Stormer in Reference [169]. Notice that the evolution of R_H from $\nu = 1/2$ to $\nu = 1/3$ is similar to the behavior of R_H from $\nu = \infty$ to $\nu = 1$.

cycle. Repeating this cycle at a frequency, f , generates a current $I = ef$. In practice, f is of order 10 MHz and the current measured is about 1% less than ef . The discrepancy is attributed to tunneling leakage through the barriers[172]. It has been pointed out[66, 173] that theoretically, even when leakage is taken into account, the error of a turnstile device is $< 0.00001\%$ of ef . To date the methods used to cycle the barriers and/or the chemical potential in the leads have employed a sine wave modulation to either the gates or the leads. It seems that a more refined cycle could greatly increase the efficiency of such devices possibly allowing them to achieve metrological importance. For example, Planck's constant h , is determined to its highest accuracy by measuring the current, I_h , that passes through a Hall bar of resistance R_H , in the $\nu = 1$ quantum Hall regime in response to a voltage, V_J generated by the a.c.

Josephson effect[174]. Planck's constant is given by

$$h = \frac{4}{f^2}(V_J^2/R_H) = \frac{4}{f^2}I_h^2R_H \quad (7.1)$$

where f is the driving frequency of the Josephson junction. The resolution of this measurement is limited by the accuracy to which I_h can be determined. It has been noted that with a turnstile device accurate to within a factor of 10 of the theoretical maximum accuracy quoted above, h could be determined to almost one and a half more digits of accuracy than is now known[175]. Furthermore, the present definition of current is the 1946 CGPM definition of an ampere based on the force between two straight parallel current carrying conductors of negligible cross section and infinite length. It has been proposed that a high efficiency turnstile device could provide a workable operational definition of current to supersede the present definition.

Another related aspect of small electron gas systems that has yet to be fully explored is the high sensitivity that these structures have for measuring small capacitances. For example, in Section 3.5 we showed that we can measure a capacitive coupling to the small electron gas of order 10^{-18} F. An example of one measurement that could possibly exploit this high sensitivity, imagine measuring the capacitance between a small electron gas and a quantum Hall or fractional quantum Hall edge state in a nearby Hall bar[142]. Also, two small electron gases in close proximity can be expected to have significant capacitive coupling. In References [176, 177] such systems have already been treated theoretically, and in fact we hope to measure capacitively coupled electron gases in the near future.

As for other experiments on the horizon, our group along with several others, is working towards performing microwave spectroscopy on small electron gas systems. In Chapter 4 we showed that the energy spacing between discrete levels in the tunneling density of states was roughly 0.1 meV. This corresponds to a frequency of 24 GHz. which, despite the constraints imposed by measuring in a dilution refriger-

ator, should be technologically accessible with coaxial cable and simple wave guide arrangements. On the more distant horizon, there are a number of biological processes that exhibit single electron (or ion) charging effects. For example, it is known that ions in aqueous solutions cannot cross the lipid bilayer membranes surrounding cells. Instead, ion transport occurs through ion channels formed by a class of membrane spanning proteins. One such class, formed by α -toxin proteins, has been studied extensively[178] with Ag-AgCl electrodes and patch clamps, which can be thought of as the biologist equivalent of ohm-meter leads that are small enough to fit into single cells. The measured current-voltage characteristics of single ion channels show a gap about zero voltage. Recently, it has been suggested that this gap arises from the Coulomb blockade due to the presence of charged species in the channel which operate analogously to the tunnel barriers in our devices[179]. (In aqueous solutions, the analogous Coulomb charging energy of single ions is enhanced by the energy to remove the hydration shell surrounding an ion before it passes through a membrane channel[180, 181].) Such systems are potentially fruitful areas of future research.

Appendix A

Additional Gate Geometries

This Appendix contains a sampling of several representative gate geometries that were fabricated but for lack of time have not yet been studied.

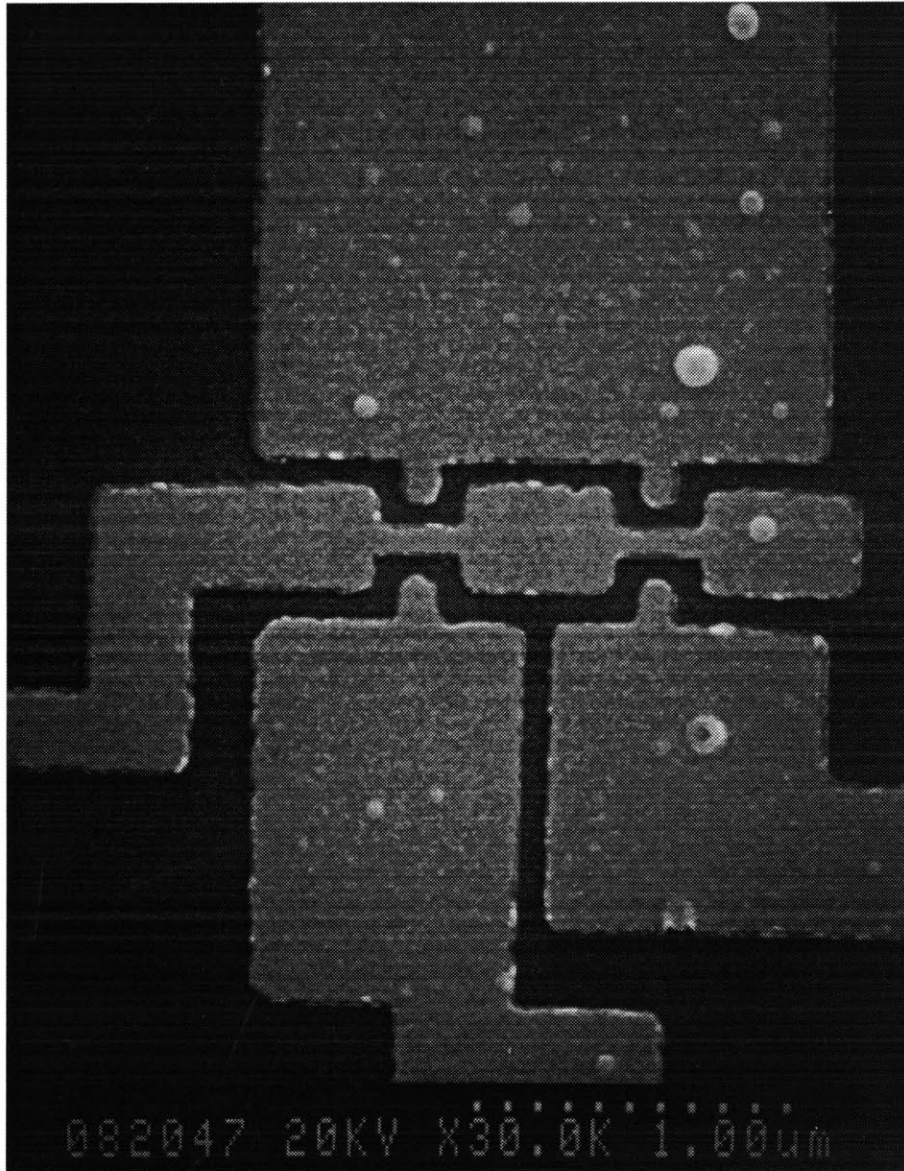


Fig. A-1. A Metallization Geometry with a Longitudinal Accumulation Gate. This gate geometry was motivated by the idea that by applying a small positive bias to the gate covering the channel and island of electron gas, electrons would be more readily accumulated in these areas than in devices such as that shown in Fig. 2-7 on page 41. Furthermore, this additional gate could also be biased negatively to serve a similar purpose as the back gate in the ISIS structure shown in Fig. 2-10 on page 47.

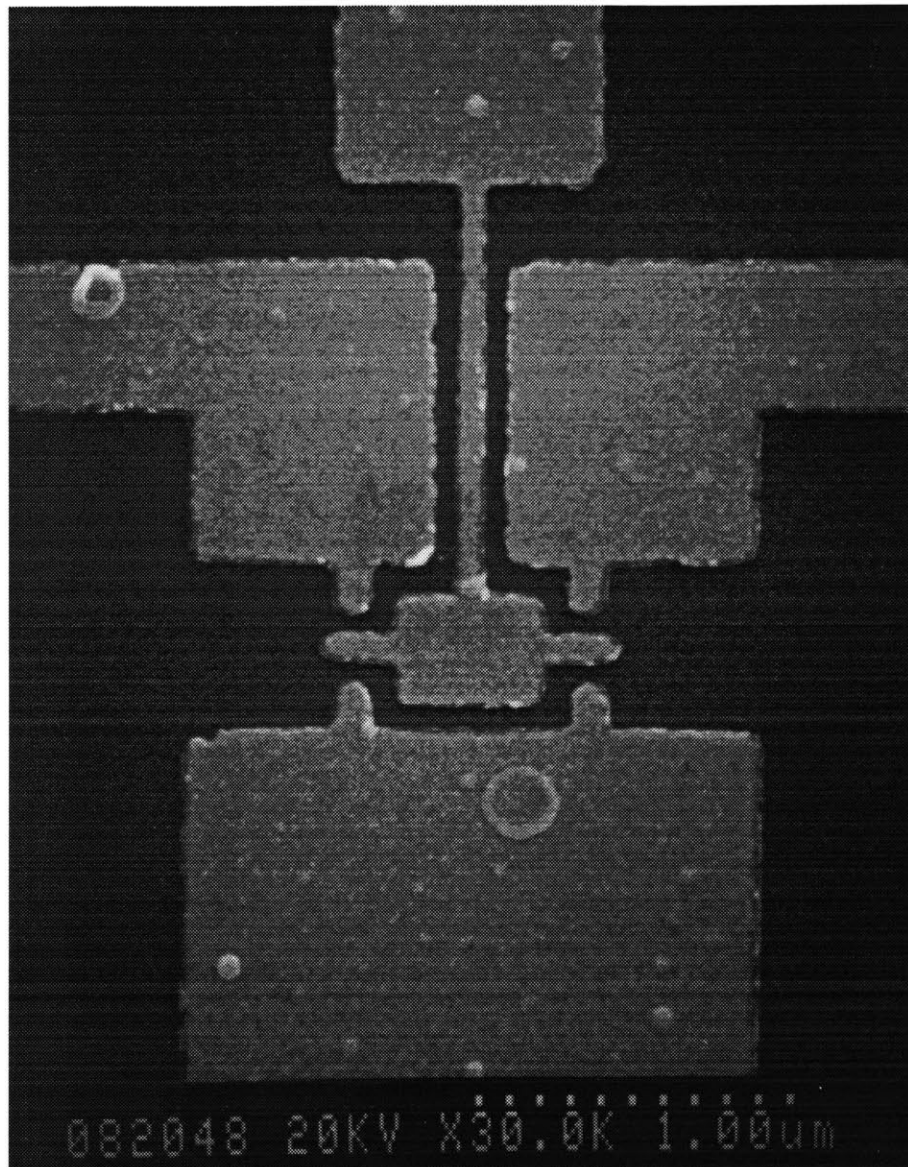


Fig. A-2. A Metallization Geometry with a Transverse Accumulation Gate. The motivation behind this geometry was similar to that in Fig. A-1, except in this case the transverse gate serves the role as the longitudinal gate in Fig. A-1. The strip leading to the “paddle” covering the area of the isolated electron gas is $0.05\ \mu\text{m}$ wide.

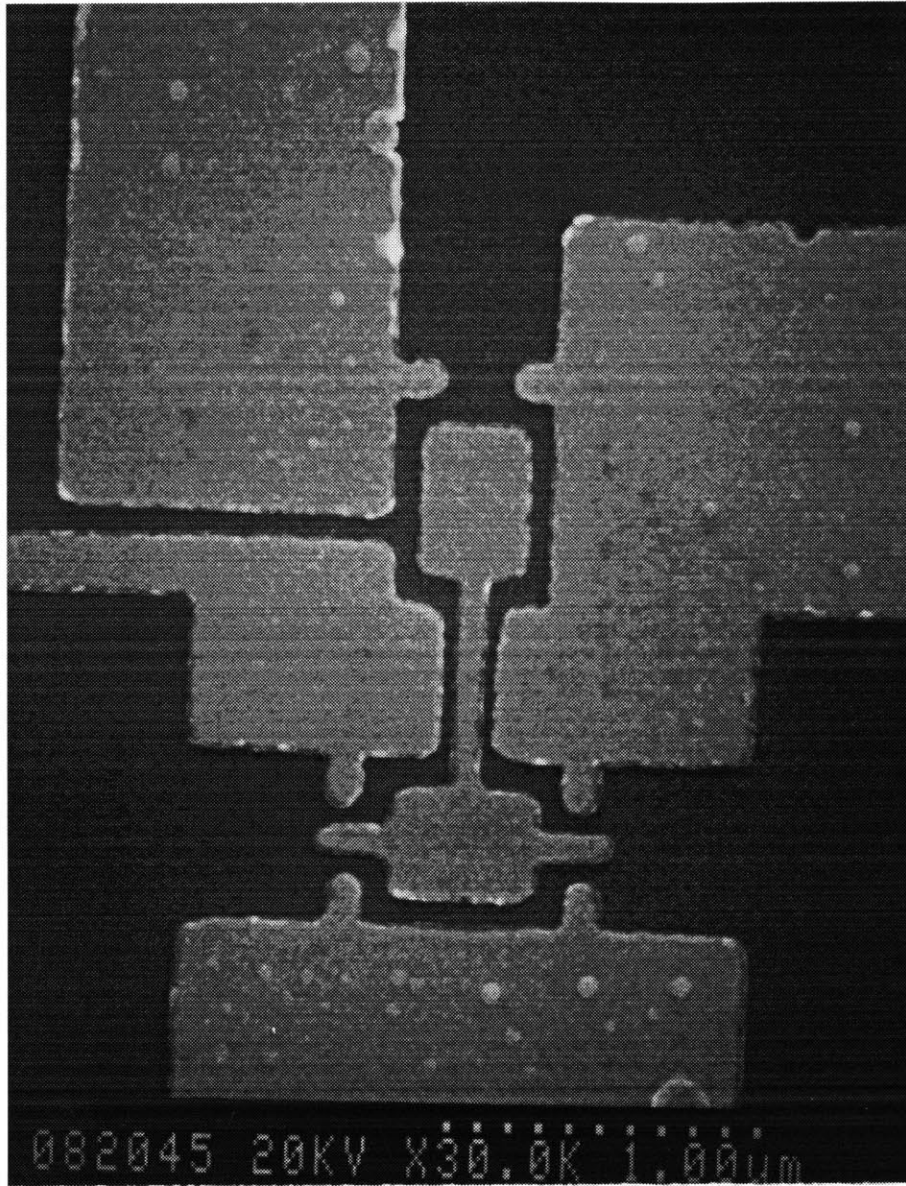


Fig. A-3. A Metallization Geometry for Coupling Between Adjacent Electron Gases Using a Floating Gate. The floating gate in this geometry was intended to capacitively couple two adjacent, small electron gases. It is unlikely that this geometry would work because the potential of the floating gate would probably not actually float since there is some finite impedance between this gate and adjacent gates. In order for this gate to be truly floating these impedances would have to be sufficiently large that even when a several mV potential difference existed between the fixed gates to the floating gate not even a single electron would be able to tunnel onto the floating gate during the time scale of a typical measurement. This corresponds to impedances of $\geq 10^{20}\Omega$.

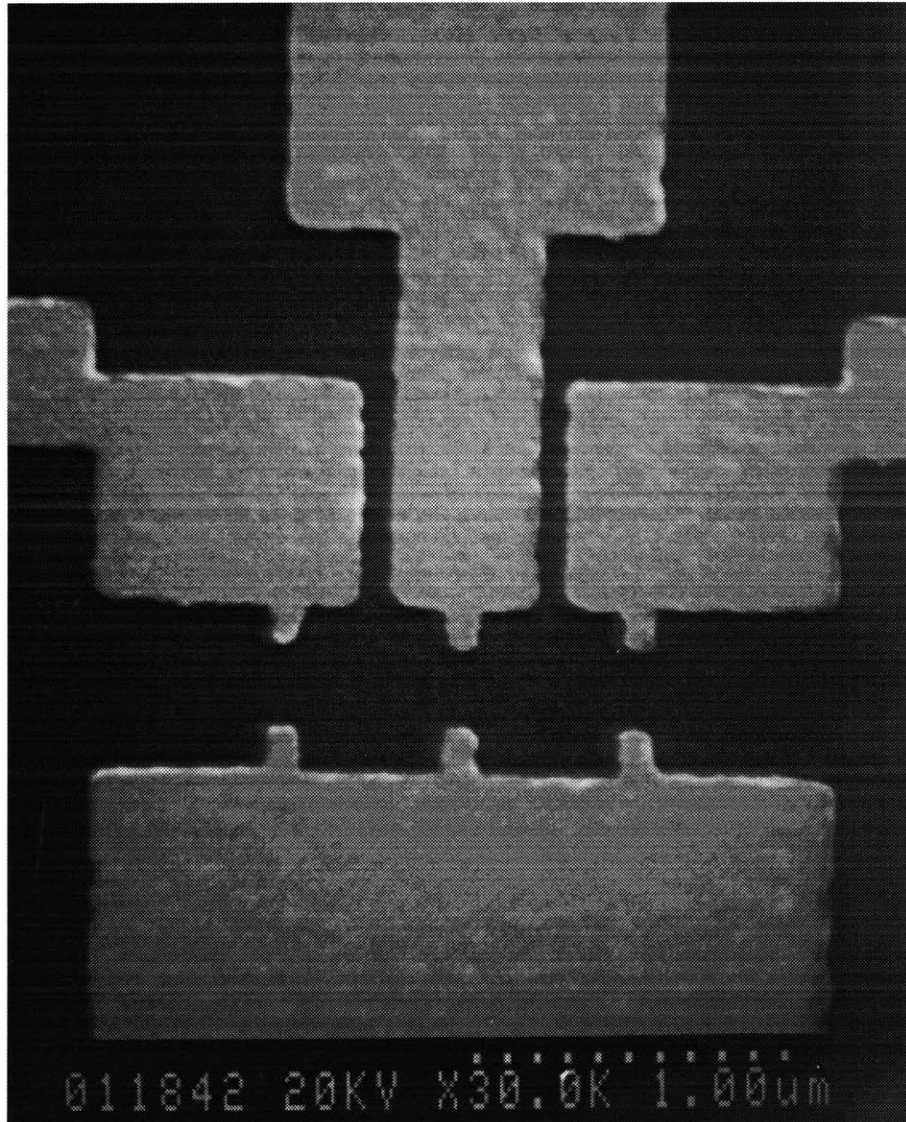


Fig. A-4. A Metallization Geometry for Small Electron Gases in Series. Notice that the tunnel barriers formed between each of the three pairs of constrictions can be controlled independently. For a theoretical discussion of such a system see Reference [176] and the accompanying note in the bibliography citation.

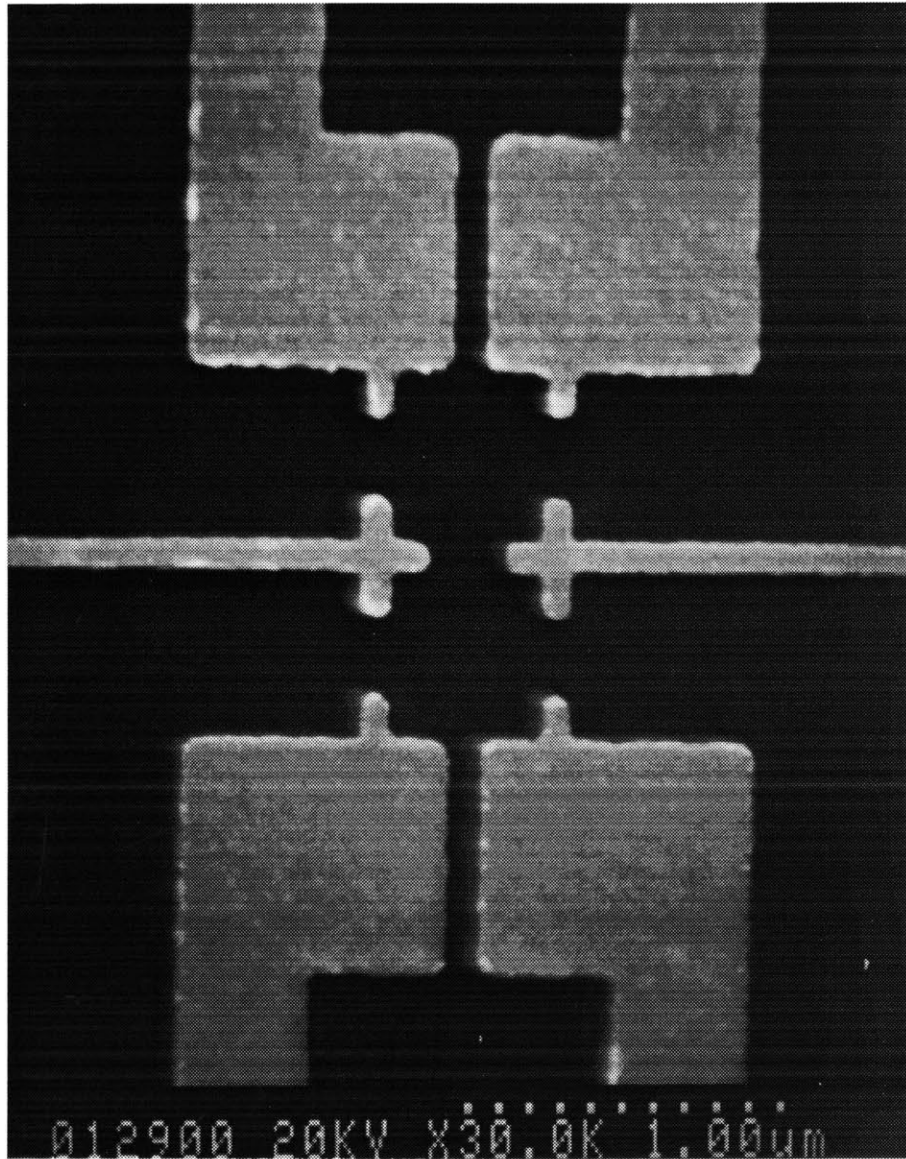


Fig. A-5. A Metallization Geometry for Small Electron Gases in Parallel. Based on the results of Section 3.5, it is reasonable to assume that in this geometry there will be a nonnegligible capacitive coupling between the small electron gases. A theoretical treatment of such a system has been given in Reference [177].

Appendix B

Heterostructure Wafers

This Appendix contains the growth structures for four of the heterostructure wafers received from Michael Melloch at Purdue University.

n-GaAs	50Å
n-Al _{0.3} Ga _{0.7} As	600Å
i-Al _{0.3} Ga _{0.7} As	200 Å
i-GaAs	1μm
Undoped GaAs Substrate 111488C	

Fig. B-1. Heterostructure #111488C. At 4.2 K $\mu = 1.4 \times 10^6 \text{ cm}^2/\text{V}\cdot\text{sec}$ and $n_s = 4 \times 10^{11} \text{ cm}^{-2}$.

n-GaAs	50Å
15 period superlattice 20 Å n-GaAs / 20 Å i-Al _{0.54} Ga _{0.46} As	600Å
4 period superlattice 20 Å i-GaAs / 20 Å i-Al _{0.54} Ga _{0.46} As	160Å
i-GaAs	1μm
Undoped GaAs Substrate 113088B	

Fig. B-2. Heterostructure #113088B. At 4.2 K $\mu = 1.0 \times 10^6 \text{ cm}^2/\text{V}\cdot\text{sec}$ and $n_s = 5 \times 10^{11} \text{ cm}^{-2}$.

Growth Temperature 600°C	n-GaAs	50 Å
	n-Al _{0.3} Ga _{0.7} As	600 Å
	i-Al _{0.3} Ga _{0.7} As	730 Å
	i-GaAs	1 μm
Growth Temperature 250°C	GaAs:As	1 μm
Growth Temperature 600°C	i-GaAs	1 μm
semi-insulating GaAs 010389B		

Fig. B-3. Heterostructure #010389B. At 4.2 K $\mu = 0.5 \times 10^6 \text{ cm}^2/\text{V}\cdot\text{sec}$ and $n_s = 1.3 \times 10^{11} \text{ cm}^{-2}$.

n-GaAs	50Å
n-Al _{0.3} Ga _{0.7} As	600Å
i-Al _{0.3} Ga _{0.7} As	200 Å
i-GaAs	1μm
Undoped GaAs Substrate 010588	

Fig. B-4. Heterostructure #010588. At 4.2 K $\mu = 1.8 \times 10^5 \text{ cm}^2/\text{V}\cdot\text{sec}$ and $n_s = 5.2 \times 10^{11} \text{ cm}^{-2}$.

Appendix C

Notes on the Fabrication Process

The following notes outline the fabrication steps for making a conventional devices such as the one described in Section 2.1. All mask levels were processed with electron beam lithography. The fabrication took place at IBM T. J. Watson Research Center. Room numbers refer to locations at this site.

Zero-Level Alignment Marks. In room 07-004 (combination 2095) Spin on 2000 Å of 2010 PMMA, bake at 180 C for 1 hr, spin on 1000 Å 2041 PMMA bake at 180 C for 1 hr. N2 blowoff and acetone and IPA (isopropal alcohol) clean before spinning on resist. N2 Blowoff between PMMA layers. After bake should be green color. *E*-beam write alignment marks. Develop to wedge #84 in 2:1 IPA:MiBk, roughly 30 sec. Do in 5 sec increments so as to not over develop. Check development visually. Evaporate 100 Å of Ge at 0.5 Å/sec followed by 800 Å of Au at 2 Å/sec. Lift-off in acetone. Keep in acetone at least 10 minutes to guarantee good lift-off. Check results.

Trench Etch. Acetone, IPA, N2 Clean two times. (Takes about 20 minutes but its worth it.) Spin on 3000 Å of 2010 PMMA. Bake 1 hr 15 min at 180 C. (Check thickness of spun on PMMA with dummy wafer. Scratch spun on layer and then measure scratch depth with DECtak.) *E*-beam expose. Develop to wedge 84 using procedure describe above. Etch trench in 40:1:1 H₂O:H₂O₂:H₃PO₄. Want 2000 Å

deep trench. Etch times are approx 2 minutes. Etch incrementally and check to avoid over etching. Remove PMMA after etch.

Ohmic Contacts Repeat cleaning procedure discussed above. Spin on 2000 Å 2010 PMMA bake at 180 C for 30 min. Spin on 1000 Å of 2041 PMMA bake for 1 hour 15 minutes at 180 C. *E*-beam expose. Develop to wedge 84 in same solution as described in the Trench etch section. Evaporate 80 Å of Ni, 300 Å of Ge, 600 Å Au, 120 Å of Ni and 1000 Å of Au. (Other, similar formulas work just as well.) Evaporate in aisle 17 top floor. Anneal in 19-106 for 20 sec at 430 °C. Ask somebody who has used the annealer recently what the best temperatures and times currently are. Measure conductances of contacts at room temperature and at 77 K to check results. See footnote on page 43.

Gate Level Metallization In this section we describe a single metallization step. The problem with this is that the bond pad metallization is just as thin a layer as the submicron metallization which potentially makes it hard to bond to the bond pads. A large feature size evaporation preceding the submicron metallization would eliminate this potential problem. For the submicron gates, clean wafer very well. Then, spin on 700 Å of 2010 bake at 180 C for 1 hour. Spin on 300 Å of 4010 bake at 180 C for 1 hour. Develop in 3:1 IPA:MiBk + 3% MeK. Do a test wafer. MeK is a strong developer. Typically 30 sec to Develop to wedge 84. MeK makes sure that the exposed areas are clean of PMMA. Evaporate 75 Å of Ti (or Pd) and then 200 to 300 Å of Au.

Dicing and Bonding. Use a well maintained dicer. Ask to find one. Make sure the chiplet array from the very first processing step is aligned with the crystal axes of the wafer. This greatly facilitates dicing. Bond using Au wires with a large loop setting and a low contact force. Recommend ultrasonic over ball bonding. Silver paint chiplets to headers. Use only fresh silver paint.

Appendix D

Notes on the Operation of the Dilution Refrigerator

These notes are intended to supplement the instruction set provided by Oxford Instruments. They were written in conjunction with Paul Belk.

Number for LN2 and LHe: x3-2215 (one day in advance). Cooling down requires 1, 240-litre can of LN2, 1, 100-litre can of LHe. Enough for cooling down, plus one day of operation, then 25 litres/day LHe and approx 240 litres LN2 for every 5 days.

Check pump oil in rotary pumps.

With insert in place:

1. Put exchange gas in IVC: (approx 15 minutes)
 - (a) pump IVC using rotary pump A. Must first rough pump IVC to 10mbar using 16, 24, 25 and watching P2
 - (b) pump IVC using diffusion pump through valves 16, 17, 23, 25 until Penning gauge goes below lowest reading on scale.
 - (c) Add exchange gas from normal helium cylinder: added via exchange gas

vent, valves 20, 19. pinch 2m segment of rubber tube and allow to be pumped into vent. repeat once.

2. Pump OVC (if necessary, e.g. if softened recently): (approx 45 minutes)

- (a) Connect hose from OVC valve on fridge to OVC valve on wall.
- (b) Pump using same procedure as for IVC.
- (c) Remove OVC tube.

3. Clean pure He line:

- (a) make sure 1K pot pump connected ONLY to port b.
- (b) open valve 11, with valves 6, 10 closed.
- (c) open pure He valve, until gauge moves. Close valve.
- (d) pump to port B through valve 10, until P3 stops moving.
- (e) repeat twice.

4. Clean mixing lines:

- (a) pressurize still lines to 800 mbar on G2 with pure He, through valves 11, 6, 7. (valve 2 closed)
- (b) close 11. Wait for pressure on condenser line (G3) to move (about 2 to 4 minutes).
- (c) Equilibrate still and condenser lines by opening valve 2.
- (d) Pump line both lines with 1K pot through valves 6, 10 until P3 on scale.
- (e) Repeat twice.

5. Evacuate 1K pot:

- (a) Reconnect 1K pot to 1K pot pump, valve 27.

(b) Make sure needle valve is closed. [Note: there are two needle valves, the upper knob is usable, the lower knob is stuck.]

(c) Pump 1K pot through 1K pot pump, valve 27, until G5 off scale

6. Fill main bath with LN2:

(a) put steel rod into main bath transfer port and screw into tube at bottom. Screw down cap.

(b) make sure recovery system venting to air.

(c) Transfer LN2 for about 1 hour, 15 minutes (objective is to fill main bath about half way).

(d) Stop transfer. Wait for main bath to reach 77K. [Note: at room temperature, thermometer is approx 2.945 Ohms. resistance will drop below room temperature and then increase again to 6.15 Ohms at 77K.] (approx 2-3 hours).

7. Transfer LN2 to outer jacket:

(a) connect tube through which LN2 was transferred to port into outer LN2 jacket.

(b) disconnect recovery system (valve 29)

(c) connect He to exchange gas vent

(d) open valves to main bath (valves 20, 30) – pressure approx 3-4 PSI

(e) stop transfer when no more liquid flows through tube.

(f) check that transfer is completed by warming tube at main bath with heat gun and removing. Verify that no LN2 coming out of main bath.

(g) Remove transfer tube from main bath port and seal main bath port.

8. Prepare Main Bath for LHe transfer:

- (a) close off valves between exchange gas vent and main bath (valves 30, 20)
- (b) Pump down main bath using 1K pot pump (valve 28) until Main bath pressure is approx 10 mbar. [Note: if there is still LN2 not transferred, it will pump only to approx 150 mbar]
- (c) Backfill main bath with He, via exchange gas port (valves 20, 30).
- (d) when pressure in main bath reached 1 ATM, open valve to recovery system (valve 29).
- (e) Flush out mixing lines using procedures 3 and 4. Repeat 4 only once to verify capillary not clogged. If clogged, go home.
- (f) Check that temperature is approx 5.4 Ohms.

9. Transfer LHe to Main Bath

- (a) Put both extensions on transfer tube, and connect tube port to He.
- (b) Turn off release valve on LHe dewar. Insert end of transfer tube with small extension slowly into dewar.
- (c) Place ring and gasket on long end of transfer tube.
- (d) When LHe flame at transfer tube insert tube into Main Bath port. – Make certain that cone at end of transfer tube mates with cup in main bath.
- (e) Maintain He pressure at approx 1.5 PSI during transfer (recovery gauge should show approx 30
- (f) Turn on recovery system when boil off observed.
- (g) Continue transfer until large boil off observed in recovery system.
- (h) Plug in level meters.
- (i) Note resistance on magnet. Should make transition from about 2.06 Ohm (cold) to ≈ 1 Ohm (Super).

(j) Continue transfer until approx 20

10. Remove Transfer tube:

- (a) Turn off recovery system.
- (b) Unscrew cap at main bath port and pull out transfer tube.
- (c) remove transfer tube from dewar.
- (d) recover and replace cap and gasket at main bath port.

11. Prepare cold traps:

- (a) Dump garbage out of cold trap dewars.
- (b) Heat cold traps with heat gun while pumping with 1K pot pump.
- (c) Pump until pressure on P3 is "low".
- (d) Place in dewar.
- (e) Open valve to LN2 about 15 degrees
- (f) Switch LN2 control switch to auto to fill with LN2.

12. Pump 1K pot:

- (a) Turn off valve to 1K pot pump (valve 27).
- (b) Open needle valve.
- (c) Verify that 1K pot level meter at 100
- (d) Close needle valve (approx 15 turns).
- (e) Open needle valve 1/8 turn.
- (f) Pump VERY CAREFULLY on 1K pot: Open valve 27 (by sound) until pump starts to work. Continue carefully opening valve until pressure below 10 mbar. Make sure 1K pot level meter still $i = 20$

192 Appendix D: Notes on the Operation of the Dilution Refrigerator

13. Prepare to circulate mixture:

- (a) Evacuate IVC with roughing pump (valves 16, 24, 25) until on scale, then pump through diffusion pump (valves 16, 17, 23, 25).
- (b) Condense mixture by introducing to fridge via still (valves 5, 7). Make sure that valve 2 is closed, valve 3 is open.
- (c) Wait for pressure on G1, G2, G3 to equilibrate (approx 45 minutes). If pressure on G3 doesn't change (time scale approx 1 minute), go home.
- (d) Make sure heater is off (on temperature controller panel).

14. Check to see if cold traps unclogged

- (a) Turn on He3 rotary pump
- (b) Make sure cold traps isolated (valves 1, 4, 8)
- (c) Open valve at bottom of cold trap (valve 8 a/b)
- (d) Check response of G4. If pressure drops approx 200 mbar, trap is OK, else repeat step 11.

15. Circulate Mixture

- (a) Wait for pressure on G1, G2, G3 to drop below 300 mbar.
- (b) Open valve at top of cold trap (valve 1).
- (c) Wait for pressure to equilibrate.
- (d) Begin circulation by opening throttle valve (speedivalve, valve 12) a small amount to bring pressure on G3 just above 300 mbar.
- (e) Continue d until throttle valve all the way open (usually 60 Ohms).
- (f) Open butterfly valve (valve 13)

Warm

16. Collect Mixture in Dump

- (a) open circulation to dump (valve 9)
- (b) close normal circulation (valve 5, 8)
- (c) open bypass to dump (valve 2)
- (d) close needle valve

17. Soften IVC

- (a) transfer 1 m He to exchange gas vent (valve 19, 20) (pressure in dump will rise quickly – full dump 800 T)

18. Turn on heater

- (a) heater switch on
- (b) load resistor at 0 Ohms

19. Isolate dump when full

- (a) Pressure in dump between 750, 820
- (b) Pressure on input of circulation pump (P1) stops dropping
- (c) turn off circulation from still (valve 12, 13)
- (d) close off dump (valve 9)
- (e) turn off rotary pump

20. Shut down diffusion pump

- (a) close valves to pump (16, 17)
- (b) turn off diffusion pump (yellow switches on front)
- (c) Allow pump to cool (20 minutes)
- (d) close valves to rotary pump (23, 25)

21. Shut off cold traps

22. Vent pot to air

Appendix E

The Low-Noise

Current-to-Voltage Amplifier

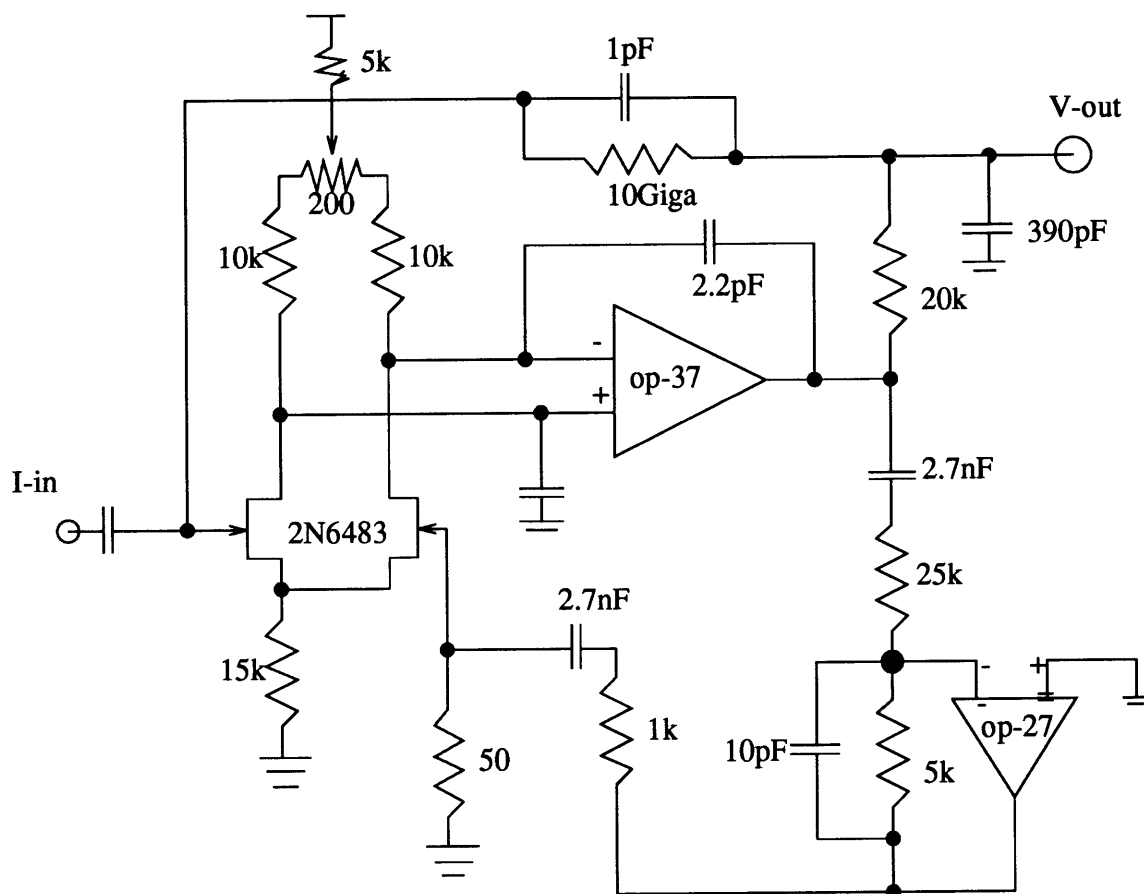


Fig. E-1. This is the schematic of the current amplifier that was used to significantly improve our signal-noise ratio to $\geq 10^4$ and noise floor to ~ 10 fA in addition to greatly reducing electron heating in the measurement samples. This design was conceived and built for us by Nathan Belk. Furthermore, all signal lines going to the device were actively filtered and attenuated with respect to analog ground common to the current amplifier. This circuitry is not shown in the above.

Appendix F

Computer Code to calculate I versus V_{ds} in the classical Coulomb blockade model

The following is “c” code used to calculate I vs. V_{ds} in the classical Coulomb blockade model as outlined in Section 3.4. This code admits to many versions of trial and error and with little effort could be greatly simplified.

```
# include <stdio.h>
# include <math.h>
# include <ctype.h>

#define pi 3.1415926

double pout(hn,hr2,hc)
int hn;
double hc,hr2;
```

```
{  
hr2=((double)hn-(1/(2*hc)))/(hr2*hc*1);  
if (hr2<0) {hr2=0;};  
return(hr2);  
}
```

```
double pin(jv,jn,jr1,jc)  
double jc,jv,jr1;  
int jn;  
{  
jv=(jv-((double)jn-(1/(2*jc)))/(1*jc))/jr1;  
if(jv<0) {jv=0;};  
return(jv);  
}
```

```
main()  
{  
double ptotal,v,c,r1,r2,vmax,itotal;  
double p[50000];  
int i,n,m,step;  
char out_name[25];  
FILE *out;
```

```
printf("input V max: ");  
scanf("%lf",&vmax);  
printf("input R1: ");  
scanf("%lf",&r1);
```

```
printf("input R2: ");
scanf("%lf",&r2);
printf("input C: ");
scanf("%lf",&c);
printf("input step: ");
scanf("%ld",&step);
printf("output file: ");
scanf("%24s",out_name);
out = fopen(out_name,"w");

for(v=0;v<=vmax;v=v+vmax/(double)step)
{

m=(int)(v*c+0.5);
p[0]=1;
p[1]=p[0]*pin(v,1,r1,c);
p[1]/=pout(1,r2,c);

for (n = 1; n <= (m-1); n=n+1)
{
p[(n+1)]=p[n]*pout(n,r2,c)+p[n]*pin(v,(n+1),r1,c);
p[(n+1)]=p[(n+1)]-p[(n-1)]*pin(v,n,r1,c);
p[(n+1)]=p[(n+1)]/pout((n+1),r2,c);
};

ptotal=0;
```

```
for (n= 0; n<= m; n=n+1)
{
ptotal=ptotal+p[n];
};
for (n= 0; n<= m; n=n+1)
{
p[n]/=ptotal;
};
itotal=0;
for (n= 1; n<= m; n=n+1)
{
itotal=itotal+p[n]*(n-0.5)/(r2*c);
};
fprintf(out,"%g %g\n",v,itotal);

};

}
```

Appendix G

Computer Code to calculate I versus V_g at finite V_{ds} in the classical Coulomb blockade model

The following is “c” code used to calculate I vs. V_g at finite V_{ds} in the classical Coulomb blockade model as outlined in Section 3.4.

```
# include <stdio.h>
# include <math.h>
# include <ctype.h>

#define pi 3.1415926

double pout(hn,hr2,hc,hadd)
int hn;
double hc,hr2,hadd;
```

```

{
hr2=((double)hn+hadd-(1/(2*hc)))/(hr2*hc*1);
if (hr2<0) {hr2=0;};
return(hr2);
}

double pin(jv,jn,jr1,jc,jadd)
double jc,jv,jr1,jadd;
int jn;
{
jv=(jv-jadd-((double)jn-(1/(2*jc)))/(1*jc))/jr1;
if(jv<0) {jv=0;};
return(jv);
}

main()
{
double ptotal,v,c,r1,r2,vmax,itotal;
double p[50000];
int i,n,m,step;
double ncont,vg,vgmax,delta,add;
char out_name[25];
FILE *out;

printf("input Vg max: ");
scanf("%lf",&vgmax);
printf("input Vds : ");

```

```
scanf("%lf",&vmax);
printf("input R1: ");
scanf("%lf",&r1);
printf("input R2: ");
scanf("%lf",&r2);
printf("input C: ");
scanf("%lf",&c);
printf("input step: ");
scanf("%ld",&step);
printf("output file: ");
scanf("%24s",out_name);
out = fopen(out_name,"w");

for (vg=0; vg <= vgmax; vg=vg+(vgmax/step)){
v=vmax;
ncont=vg*c+0.5;
ncont=(int)(ncont);
ncont=(double)(ncont);
delta=(ncont+0.5)/c-vg;
add=delta-(1/(2*c));

m=(int)(v*c+0.5-add);
p[0]=1;
p[1]=p[0]*pin(v,1,r1,c,add);
p[1]/=pout(1,r2,c,add);
```

```

for (n = 1; n <= (m-1); n=n+1)
{
p[(n+1)]=p[n]*pout(n,r2,c,add)+p[n]*pin(v,(n+1),r1,c,add);
p[(n+1)]=p[(n+1)]-p[(n-1)]*pin(v,n,r1,c,add);
p[(n+1)]/=pout((n+1),r2,c,add);
};

```

```

ptotal=0;
for (n= 0; n<= m; n=n+1)
{
ptotal=ptotal+p[n];
};
for (n= 0; n<= m; n=n+1)
{
p[n]/=ptotal;
};
itotal=0;
for (n= 1; n<= m; n=n+1)
{
itotal=itotal+p[n]*(n-0.5+add)/(r2*c);
};
fprintf(out,"%g %g\n",vg,itotal);

};

```

}

Appendix H

Electrons in a Magnetic Field

According to classical electrodynamics, a free electron with velocity v in a static, uniform magnetic field \mathbf{B} , moves in a circular orbit perpendicular to the direction of \mathbf{B} . The orbital frequency ω_c , is independent of v , is referred to as the cyclotron frequency which is given by

$$\omega_c = \frac{eB}{m_o} \quad (\text{SI}) \quad (\text{H.1})$$

where $e = 1.6 \times 10^{-19}$ Coulombs is the electron charge, B is measured in Tesla and $m_o = 9.1 \times 10^{-31}$ kg is the electron mass. The orbital radius of the electron l_c , referred to as the cyclotron radius, given by:

$$l_c = \frac{m_o v}{eB} \quad (\text{SI}) \quad (\text{H.2})$$

So free electrons in a static, uniform magnetic field move in circular orbits of radius l_c . The the angular frequency of the orbit is independent of B and l_c . The more kinetic energy that an electron has the larger is its cyclotron radius.

Now, consider the quantum mechanical treatment of a free electron in a static, uniform magnetic field in the non-relativistic limit. This problem has an exact solution and can be found in any number of elementary texts on quantum mechanics. Here we present a rough sketch of the solution of this problem based on the smemiclassical

Born-Sommerfeld rule of quantization:

$$\int \mathbf{p} \cdot d\mathbf{q} = h(n - 1/2), \quad (\text{H.3})$$

where \mathbf{p} is the canonical momentum vector $\mathbf{p} = m\mathbf{v} - e\mathbf{A}$. Substituting for \mathbf{p} in the integral gives:

$$\int m\mathbf{v} \cdot d\mathbf{q} - \int e\mathbf{A} \cdot d\mathbf{q} = h(n - 1/2). \quad (\text{H.4})$$

The first integral is just $mv(2\pi l_c)$. The second integral can be rewritten using,

$$\int \mathbf{A} \cdot d\mathbf{q} = \int_{\text{area}} (\nabla \times \mathbf{A}) \cdot d\mathbf{a} = \int_{\text{area}} \mathbf{B} \cdot d\mathbf{a} \equiv \Phi, \quad (\text{H.5})$$

where Φ is simply the magnetic flux enclosed by the semi-classical orbit of the electron. Recalling that $mv = eBl_c$, Equation H.5 gives,

$$l_c^2 = (2n - 1)l_B^2 \quad (\text{H.6})$$

where l_B is known as the magnetic length, $l_B^2 = \hbar/eB$. So the radius of the cyclotron orbits is quantized so the area of an orbit encloses a half integer number of magnetic flux quantum, $\phi = (n - 1/2)\phi_o$ where $\phi_o = h/e = 4.14 \text{ T} \cdot \text{m}^2$. The quantization of l_c also implies a quantization of the electron's energy,

$$E = \frac{(mv)^2}{2m} = (n - 1/2)\hbar\omega_c \quad (\text{H.7})$$

When spin is included in this expression,

$$E = \frac{(mv)^2}{2m} = (n - 1/2)\hbar\omega_c + g\mu_B B S_Z \quad (\text{H.8})$$

where $S_Z = \pm 1/2$ is electron spin index.

Ignoring spin for the moment, we see that in a magnetic field the energy of an

electron is a half integer quantum of the cyclotron energy, $(n - 1/2)\hbar\omega_c$. The electron is said to occupy the n^{th} Landau level¹. When the effective mass of electrons in a GaAs 2-DEG is taken into account $\hbar\omega_c = 1.6 \text{ meV/T}$. The degeneracy of a Landau level is independent of n and is equal to one electron per flux quantum. So in a gas of noninteracting electrons of areal density n_s , the number of spin-split Landau levels occupied, ν , is

$$\nu = n_s(2\pi l_B^2), \quad (\text{H.9})$$

where ν is called the filling factor.

Figure H-1 shows a plot of the longitudinal resistance R_L and the Hall resistance R_H of a GaAs 2-DEG as a function of magnetic field B from Reference [182]. At high fields, plateaus in the Hall resistance and zeros in the longitudinal resistance are observed. This phenomena is known as the quantum Hall effect. It was first observed in 1980 and its discoverers[13] received the Nobel Prize in 1984. Analysis of the plateaus in Figure H-1 reveals that R_H is quantized according to the relation,

$$R_H = \frac{1}{p} \frac{e^2}{h} \quad (\text{H.10})$$

where p is the number of completely full (spin resolved) Landau levels in the 2-DEG. In order for this effect to be observed, kT must be less than the energy spacing between Landau levels and the scattering time in the 2-DEG τ , must be long compared to the time it takes for an electron to complete a cyclotron orbit, $\omega_c\tau \gg 1$. When these conditions are met, the electron gas is said to be in the Quantum Hall regime. We will not discuss this effect in any further detail except to say that the Quantum Hall effect continues to be a subject of interest both on experimental and theoretical fronts.

In Section 5.2, in the discussion of Figure 5-5 on page 140 we mentioned that

¹When spin is taken into account, each Landau level splits into a spin up and and spin down Level. Some authors refer to these two levels as different Landau levels while others refer to them as Zeeman split levels within the same Landau level.

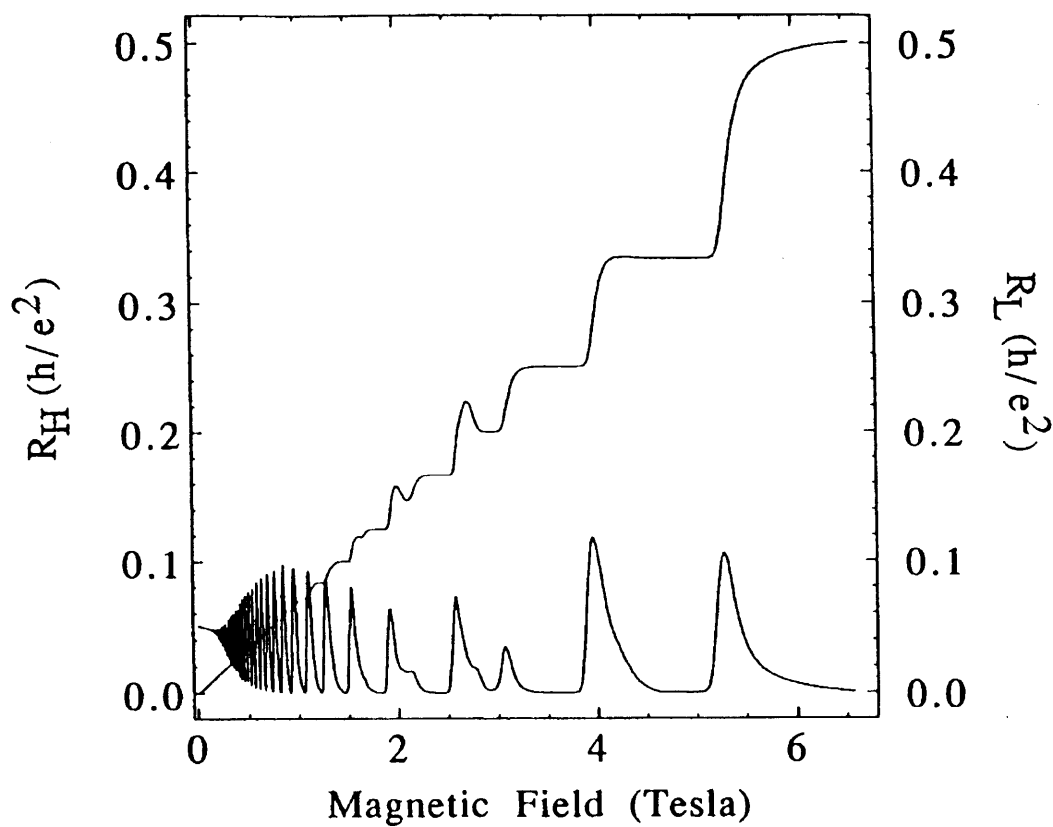


Fig. H-1. The Longitudinal and Hall Resistance of a GaAs 2-DEG from Reference [182].

part(b) of this figure was reminiscent of the single particle non-interacting level spectrum of an electron in a confining potential. To better illustrate this point we discuss briefly the level spectrum of a noninteracting electron in a two-dimensional harmonic oscillator confining potential given by

$$V(r) = \frac{1}{2}m\omega_o^2 r^2. \quad (\text{H.11})$$

This is a useful problem to consider because its solution has an exact analytic given by [183, 184, 185, 186]

$$E_{nl} = \hbar\omega \left(n + \frac{|l|}{2} + \frac{1}{2} \right) + \frac{l}{2}\hbar\omega_c \quad (\text{H.12})$$

where $\omega = \sqrt{\omega_c^2 + 4\omega_o^2}$ and ω_c is the cyclotron frequency, eB/m in SI units. Spin has been specifically neglected in this expression. Figure H-2 shows the evolution with B of the first 21 $B = 0$ nondegenerate states in a harmonic oscillator. Notice that at higher B the condensation of states into Landau levels is apparent. A portion of this plot is magnified in Figure H-3. In this Figure level crossings which look similar to the trace in Figure 5-5(b) can be seen.

In References [187, 188] similar plots have been calculated for electrons in square and cylindrical confining potentials. The calculated level spectra in these geometries are qualitatively different from the level spectrum of a harmonic oscillator. First, the level spectrum appears more chaotic than in the harmonic potential which has a higher symmetry than the square or cylindrical potentials, and second, there is a genuine condensation of states into distinct levels in the square and cylindrical potentials [189, 190]. In the harmonic potential this is not the case. For example, in Figure H-2 by $\sim 4\hbar\omega_o$ bands corresponding to individual Landau levels are apparent. However, as more states are taken into account the field at which individual Landau levels are distinguishable moves to larger values, and in the limit of an infinite number of states, there is no field at which individual Landau levels are distinguishable.

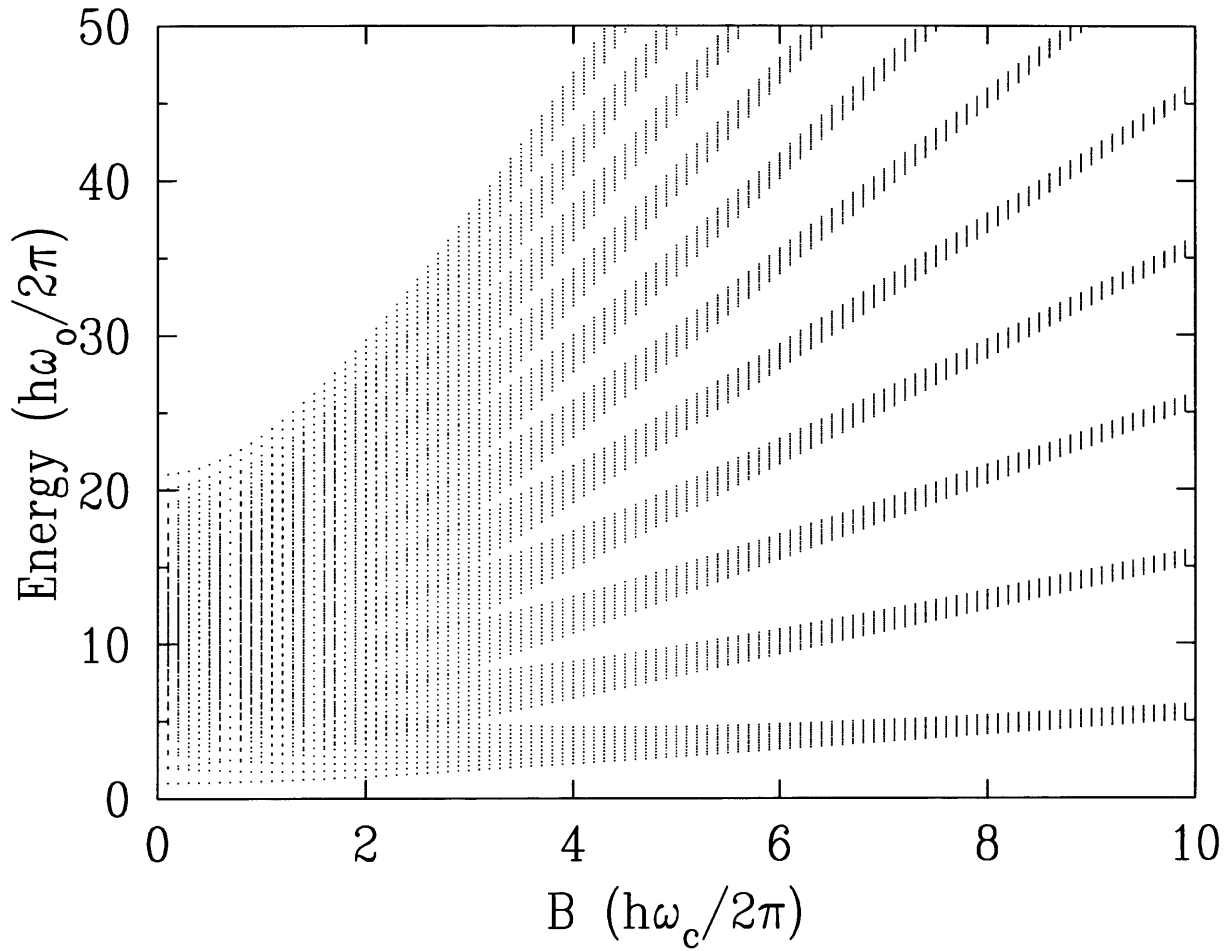


Fig. H-2. The Noninteracting Level Spectrum in a 2-D harmonic oscillator as a function of B . Only the evolution of the first 21 $B = 0$ nondegenerate states are shown. At high fields bands corresponding to individual Landau levels are apparent. ω_o is the nature frequency of the oscillator. See Equation 5.2 on page 142.

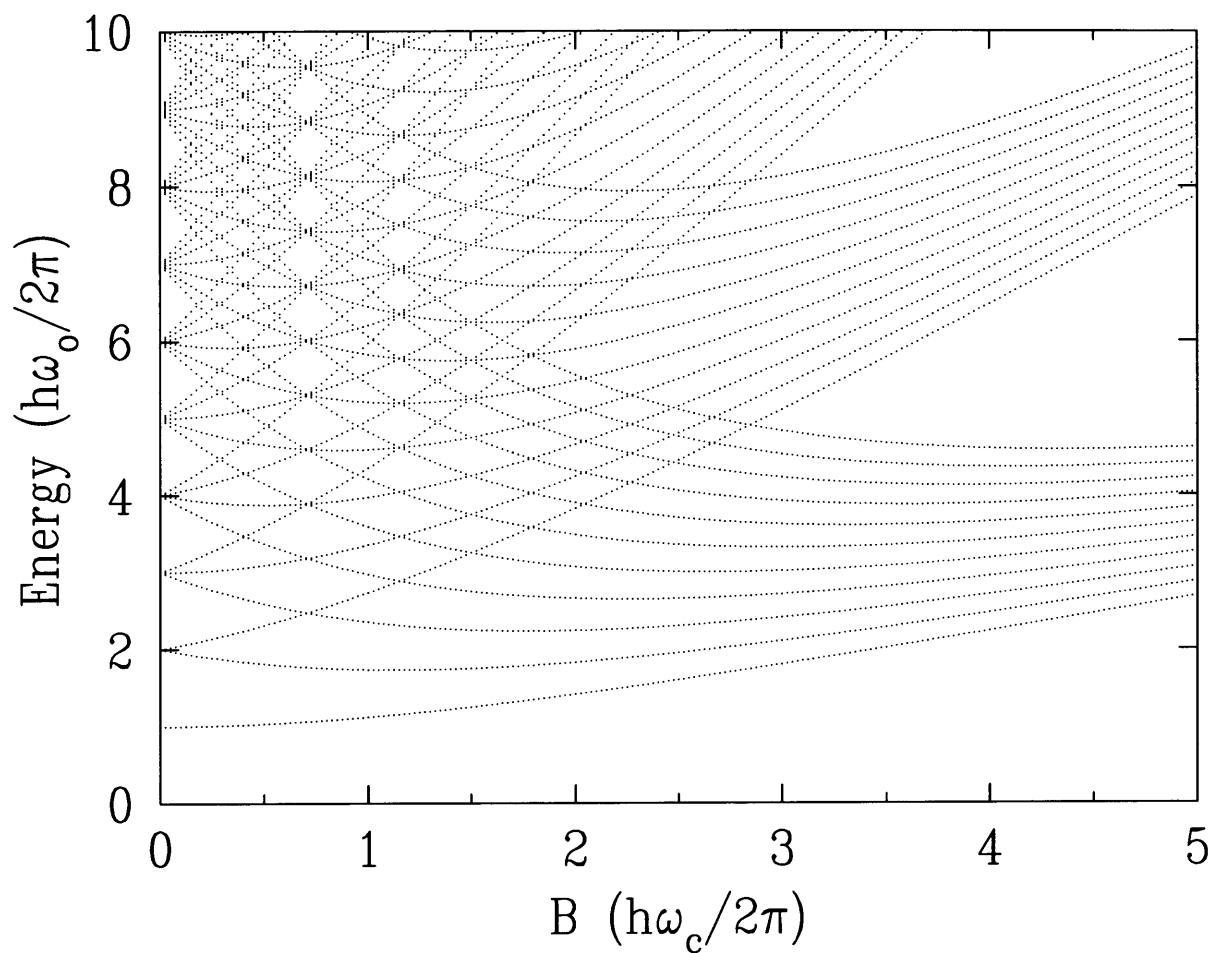


Fig. H-3. The Noninteracting Level Spectrum in a 2-D harmonic oscillator as a function of B at low fields. The level crossings apparent in this Figure are intended to be compared with the data in Figure 5-5(b).

Appendix I

Reprints

This Appendix contains reprints of three of the most relevant papers to the work described in this Thesis

Transport Spectroscopy of a Coulomb Island in the Quantum Hall Regime

P. L. McEuen, E. B. Foxman, U. Meirav,^(a) M. A. Kastner, Yigal Meir, and Ned S. Wingreen
Department of Physics, Massachusetts Institute of Technology, Cambridge, Massachusetts 02139

S. J. Wind

IBM Thomas J. Watson Research Center, Yorktown Heights, New York 10598

(Received 30 January 1991)

Transport measurements of a Coulomb island, a semiconductor dot small enough that Coulomb interactions dominate transport, are presented. At moderate magnetic fields ($B=2-4$ T) the amplitude and position of the Coulomb-regulated conductance peaks show distinct periodic structure as a function of B . This structure is shown to result from the B dependence of the quantized single-particle energy states on the island. Analysis of successive peaks is used to map out the single-particle level spectrum of the island as a function of B .

PACS numbers: 73.20.Dx, 72.20.My, 73.40.Gk

Transport through nanometer-scale electron gases such as small metal particles¹ or lithographically patterned semiconductor dots² is currently a subject of great experimental and theoretical interest. In these structures the quantization of the charge and energy of the electron gas has important implications for transport. Charge quantization is important since it means that adding an extra electron to the dot can require a finite charging energy. Transport is suppressed if this charging energy exceeds $k_B T$, creating a "Coulomb island"—a small electron gas electrically isolated from the leads by Coulomb interactions. This suppression is lifted whenever the charge fluctuations required for transport do not change the total energy of the system, and a peak in the conductance results. A semiclassical stochastic model of these devices, called the Coulomb-blockade model,¹ has been remarkably successful in explaining experiments on small metal structures. Although also capable of explaining some aspects of experiments on semiconductor dots,^{3,4} this model is inappropriate at low temperatures since it ignores the quantization of the dot's energy spectrum. The discrete spectrum of dots, which has been explored by various spectroscopic techniques,⁵⁻⁷ causes such transport effects as Aharonov-Bohm-type oscillations⁷ and resonant tunneling.^{6,7}

While charge and energy quantization effects are, taken separately, well understood, the regime in which both are important is only beginning to be explored. Recent theoretical work⁸⁻¹¹ has predicted that the properties of the Coulomb-blockade conductance peaks are affected by the single-particle electronic eigenstates of the dot. In this Letter, we present an experimental study of a semiconductor dot in the quantum Hall regime, where the properties of the single-particle states are well known.^{12,13} We find that the conductance peaks reflect the properties of the quantized energy levels of the island in surprising and dramatic ways. We further show that these measurements allow spectroscopy of *all* energy levels of the island—including levels through which negli-

ble current flows.

The geometry of the device used here is shown schematically in Fig. 1(a); a detailed description may be found in Refs. 3 and 14. Briefly, it is an inverted GaAs/AlGaAs heterostructure in which electrostatic gates are used to confine and adjust the density of a two-dimensional electron gas. A negative bias applied to a lithographically patterned split upper gate defines the island¹⁵ while a positive bias applied to a lower gate ad-

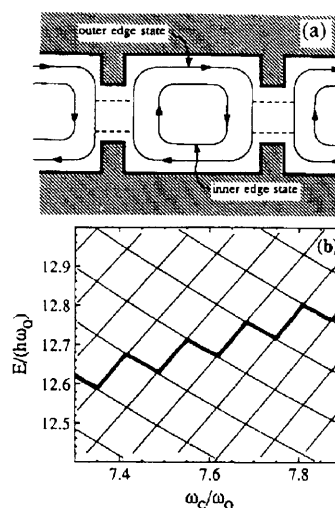


FIG. 1. (a) Schematic top view of the device, showing the path of the edge states associated with the lowest two Landau levels (LLs). The upper gate (shaded) defines a dot whose lithographic dimensions are 500 nm by 700 nm. (b) Energy levels of a dot with a parabolic confining potential $\frac{1}{2} m^* \omega_d^2 r^2$ as a function of $\omega_c = eB/m^*$ in a parameter range where two LLs are present (Ref. 12). The heavy line represents the energy of the single-particle state that is 78th lowest in energy.

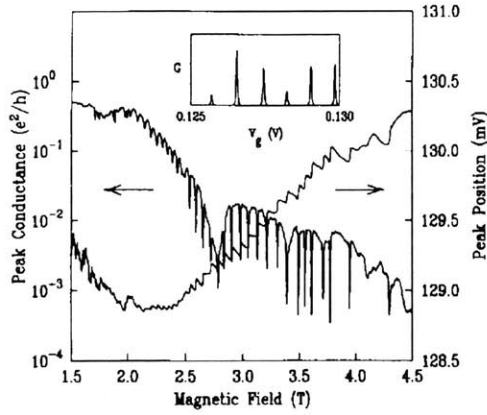


FIG. 2. Height and position of a conductance peak as a function of magnetic field at base temperature. The temperature of the electron gas is approximately 0.1 K (Ref. 3). Inset: Conductance vs V_g for the device at $B=3$ T. Full scale is $0.03e^2/h$.

justs the electron density. The conductance G versus gate voltage V_g applied to the lower gate is shown in the inset of Fig. 2. As reported previously,³ the conductance consists of a periodic series of sharp peaks.

We have studied, in detail, the dependence of the amplitude and position of these conductance peaks on magnetic field B . At low fields ($B < 1$ T), the amplitude shows strong random fluctuations with B which give way to more systematic behavior at higher magnetic fields. Figure 2 shows the position and amplitude of a particular conductance peak for $B=1.5$ – 4.5 T. At roughly periodic values of B , the peak amplitude drops by as much as an order of magnitude. Commensurate with these dips, oscillations are observed in the position of the peak. This structure washes out rapidly with increasing temperature and is almost entirely destroyed by $T \sim 0.3$ K [Figs. 3(a) and 3(b)], although the peaks in the conductance versus gate voltage remain well defined.

We now discuss the origin of this behavior. The basic periodicity of the series of conductance peaks shown in the inset of Fig. 2 can be understood within the standard Coulomb-blockade model.^{1,4} A valley corresponds to a gate voltage where an integer number of electrons minimizes the electrostatic energy of the dot. Changing the occupancy of the dot requires a finite charging energy, and transport is suppressed. A conductance peak, on the other hand, corresponds to a gate voltage where a half-integer charge $(N - \frac{1}{2})e$ on the dot would minimize the electrostatic energy. Since the actual charge on the dot is restricted to integer values of e , it fluctuates between $(N-1)e$ and Ne with no cost in charging energy, and transport can occur at $T=0$. The spacing of the peaks is determined by the gate-voltage change required to change the occupancy of the dot by one electron.

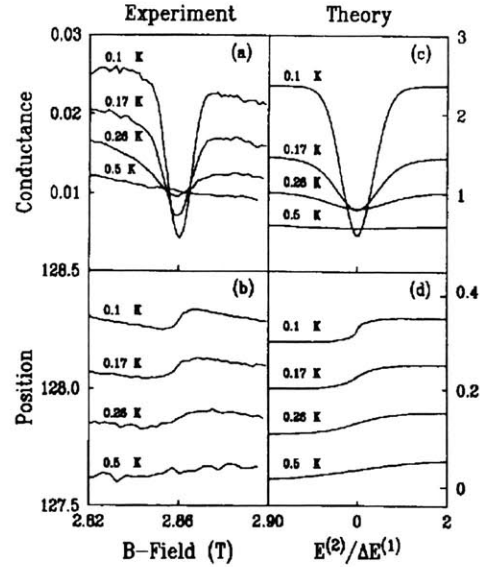


FIG. 3. Temperature dependence of (a) the peak amplitude in e^2/h and (b) the peak position in mV of a peak over a narrow B range containing one dip. Also shown are the predictions of the three-level model described in the text for (c) the peak amplitude in units of $(e^2/h)\Gamma^{(1)}/\Delta E^{(1)}$ and (d) the peak position in meV, both for $\Delta E^{(1)} = 0.05$ meV. All but the lowest peak-position curves have been offset for clarity.

If $k_B T$ is less than the single-particle level spacing, the discreteness of the energy levels of the dot must be considered, since in this case the charge fluctuation between $(N-1)e$ and Ne involves emptying and filling the N th single-particle state in the dot. The energy E_N of this single-particle state directly affects the position of the peak. For example, if E_N increases, the peak occurs at a higher V_g since, roughly speaking, the state is more difficult to fill. Elementary arguments show that, for constant Coulomb energy U , the position of the N th conductance peak at $T=0$ can be written as^{1,4,10}

$$V_g(N) = (1/ae)[(N - \frac{1}{2})U + (E_N - \mu)] + \text{const},$$

where μ is the chemical potential in the leads and a is a dimensionless constant relating changes in gate voltage to changes in the electrical potential of the dot. The constant a can be determined from the temperature dependence of the width of a conductance peak³ and is found to be 0.4 for this device.¹⁶

The position of the N th conductance peak is thus determined by a Coulomb term proportional to $(N - \frac{1}{2})U$ and by a single-particle term proportional to $E_N - \mu$. In our device, the dominant term is the Coulomb term, producing conductance peaks roughly periodic in V_g . The Coulomb energy does not vary with magnetic field, however, so the variation of the position of the peak

shown in Fig. 2 results from variations in E_N .

To understand why E_N exhibits a periodic modulation, consider Fig. 1(b), a plot of the single-particle energy-level spectrum of a dot in a high magnetic field. In the parameter range shown, the spectrum consists of two Landau levels (LLs), which, in turn, are composed of discrete nondegenerate states because of the confinement potential^{12,13} (spin is suppressed for clarity). States in the first LL fall in energy with increasing B while those in the second LL rise. The thick line in Fig. 1(b) shows the behavior of E_N , the state occupied by the N th electron on the dot, as a function of B . This electron alternately occupies a state in the first LL and a state in the second LL as the magnetic field is increased. Consequently, the position of the N th peak oscillates, as is evident in the data of Fig. 2.

These oscillations will be clear if there are two Landau levels occupied. With many more than two, the simple oscillations give way to complicated fluctuations, while with less than two there are no oscillations because all the electrons are in the lowest LL.¹⁰ In Fig. 2, the oscillations become clear around $B=2$ T, and then die out around $B=4$ T. We thus attribute these field values to filling factors of $\nu=4$ and $\nu=2$, respectively. In addition, the oscillations change character above a B value (2.5 T) that roughly corresponds to $\nu=3$. In this regime, the second LL is likely spin polarized due to the enhancement of the g factor.¹⁷ We note that each oscillation in Fig. 2 represents the transfer of one electron from the second LL to the first LL. We are thus watching the magnetic depopulation of the second LL, *one electron at a time*.

We now consider the behavior of the amplitude of a conductance peak. The behavior evident in Figs. 2 and 3 follows if (a) only two LLs are occupied, and (b) the states of the second LL do not couple to the leads.^{7,18} These assumptions are schematically illustrated in Fig. 1(a). At a particular B , if the N th single-particle state is in the first LL [the outer-edge state shown in Fig. 1(a)], it couples well to the leads and transport can occur by resonant tunneling through this state. If the N th state is in the second LL [the inner-edge state in Fig. 1(a)], however, the peak amplitude is suppressed since the coupling to this state is minimal. A dip in amplitude is thus expected whenever the N th state is in the second LL, i.e., when the position of the peak is moving up in energy.¹⁹ This is indeed what is observed in Fig. 2. The dip in conductance disappears when $k_B T$ becomes comparable to the single-particle level spacing in the first LL, since transport can then occur by thermal activation to the nearest energy state in the first LL.

The arguments above can be made quantitative using the theory of Meir, Wingreen, and Lee.¹¹ This theory gives an explicit expression for the conductance in terms of the interaction energy U , the single-particle energies E_i , and the single-particle elastic-tunneling widths Γ_i . The main features of the experimental data can be ac-

counted for by a simple three-level model: two states (representing states in the first LL) with energy separation $\Delta E^{(1)}$ and equal elastic widths $\Gamma^{(1)}$ and a single state (representing a state in the second LL) with an energy $E^{(2)}$ that increases with B and has negligible coupling to the leads ($\Gamma^{(2)}=0$). In Fig. 3, the temperature dependence of the height and position of a particular conductance peak are compared with the theoretical predictions for the three-level system. The agreement between theory and experiment is excellent,²⁰ considering that the only free parameter determining the shape of the theoretical curves is the energy-level spacing in the first LL, $\Delta E^{(1)}$. This spacing is found to be 0.05 meV for this peak at this magnetic-field value. Further, the elastic width can be obtained from the height of the conductance peak and is found to be $\Gamma^{(1)}=0.0006$ meV, assuming symmetric barriers. The theory also predicts a significant broadening of the width of the conductance peak at the dip in amplitude, which is also observed (not shown).

Having understood the behavior of a single conductance peak, we now turn our attention to the behavior of successive peaks, as shown in Fig. 4(a). As indicated by the arrows, a single-particle level within a given LL moves continuously through successive conductance peaks, allowing it to be tracked over a wide range of magnetic field.¹⁹ The Coulomb portion U/ae of the peak separation in Fig. 4(a) is approximately constant and

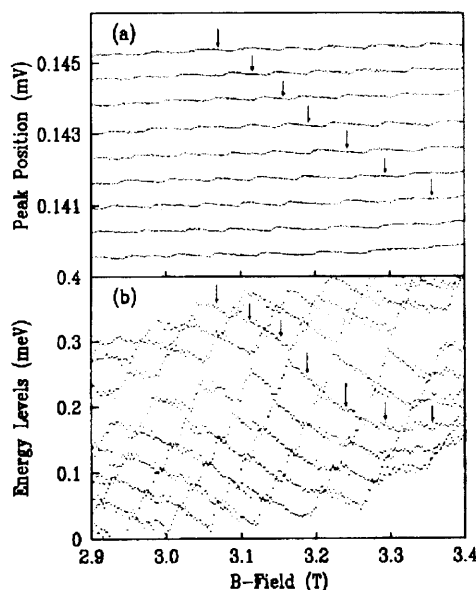


FIG. 4. (a) Peak position vs B for a series of consecutive conductance peaks. The arrow follows a particular state in the first LL as it moves through successive peaks. (b) Single-particle energy-level spectrum inferred from (a) as described in the text. The zero of the energy scale is arbitrary.

can be removed by subtracting a constant gate-voltage spacing (chosen to be 0.685 mV) between successive peaks. Furthermore, the resulting peak positions in V_g can be converted to energies using the factor $\alpha=0.4$ determined from the temperature dependence of the width of a conductance peak.³ Doing this, we obtain the results shown in Fig. 4(b). This plot represents the single-particle energy-level spectrum of the island as a function of B .

The level spectrum of Fig. 4(b) is qualitatively very similar to the theoretical spectrum shown in Fig. 1(b). The curves moving to higher (lower) energy with B are states in the second (first) LL.¹⁹ The parts of the curves inferred from different conductance peaks match up well, indicating that the assumption of a constant Coulomb term is a reasonably good one. There are deviations, however, such as the discontinuity in the inferred single-particle states starting near 0.2 meV. Other regions of magnetic field show even more unusual behavior. These deviations indicate the importance of interaction effects beyond the scope of the constant-Coulomb-energy model and will be explored in future experiments.

The quantitative aspects of Fig. 4(b) are also in excellent agreement with expectations. For example, the increase in energy of the states in the second LL relative to those in the first LL with increasing B is approximately 3.6 meV/T. This value compares favorably with theoretical predictions for parabolic confinement¹² ($\sim 2\hbar\omega_c/B = 3.2$ meV/T) or hard-wall confinement¹³ ($\sim 3\hbar\omega_c/B = 4.8$ meV/T) when the second LL is nearly depopulated. The single-particle energy-level spacings within a LL can be found directly from Fig. 4(b); they are $\Delta E^{(1)} = 0.05$ meV and $\Delta E^{(2)} = 0.1$ meV. The level splitting $\Delta E^{(1)}$ inferred in this way agrees with the value of $\Delta E^{(1)} = 0.05$ meV obtained earlier from the temperature dependence of a peak dip.

The level splitting in the second LL is about twice that in the first LL, again suggesting that the second LL is spin resolved at this field value (and hence has half as many states per unit energy). The periodic spacing of the states in the first LL is somewhat unexpected, since spin splitting would in general group the states into twos. We note, however, that the anticipated bare spin splitting $g\mu_B H = 0.06$ meV at 3 T, and so the observation of a single energy spacing may simply be because the spin splitting is approximately half the spin-resolved level spacing.

In conclusion, we have shown that the B dependence of the conductance peaks of a Coulomb island in the quantum Hall regime are determined by the B dependence of the single-particle energy levels. The amplitude of the N th peak reflects the coupling of the N th single-particle state to the leads. The position of the N th conductance peak reflects the energy of the N th state. The Coulomb part of the energy spacing between peaks can be subtracted to obtain the single-particle energy spectrum. These measurements show the importance of the

single-particle energy states to transport in Coulomb islands and also demonstrate a powerful new tool for probing the quantized energy levels of these structures.

We wish to thank P. A. Lee, K. K. Likharev, and R. G. Wheeler for useful discussions. In addition, we thank N. R. Belk for help with the instrumentation. This work was supported by NSF Grant No. ECS-8813250 and by the U.S. Joint Services Electronics Program under Contract No. DAAL03-89-C-001. One of us (Y.M.) acknowledges the support of a Weizmann Fellowship.

^(a)Present address: Department of Nuclear Physics, Weizmann Institute of Science, Rehovot 76100, Israel.

¹For a review of Coulomb-blockade phenomena in metals, see D. V. Averin and K. K. Likharev, in *Mesoscopic Phenomena in Solids*, edited by B. L. Altshuler, P. A. Lee, and R. A. Webb (Elsevier, Amsterdam, 1991).

²For a review of quantum transport in semiconductor nanostructures, see C. W. J. Beenakker and H. van Houten, *Solid State Phys.* **44**, 1 (1991).

³U. Meirav, M. A. Kastner, and S. J. Wind, *Phys. Rev. Lett.* **65**, 771 (1990).

⁴L. I. Glazman and R. I. Shekhter, *J. Phys. Condens. Matter* **1**, 5811 (1989); H. van Houten and C. W. J. Beenakker, *Phys. Rev. Lett.* **63**, 1893 (1989).

⁵T. P. Smith, III, *et al.*, *Phys. Rev. B* **38**, 2172 (1988); W. Hansen *et al.*, *Phys. Rev. Lett.* **62**, 2168 (1989); Ch. Sikorski and U. Merkt, *Phys. Rev. Lett.* **62**, 2164 (1989).

⁶M. A. Reed *et al.*, *Phys. Rev. Lett.* **60**, 535 (1988); C. G. Smith *et al.*, *J. Phys. C* **21**, L893 (1988).

⁷B. J. van Wees *et al.*, *Phys. Rev. Lett.* **62**, 2523 (1989).

⁸L. I. Glazman and K. A. Matveev, *Pis'ma Zh. Eksp. Teor. Phys.* **51**, 425 (1990) [*JETP Lett.* **51**, 484 (1990)].

⁹D. V. Averin and Yu. V. Nazarov, *Phys. Rev. Lett.* **65**, 2446 (1990).

¹⁰C. W. J. Beenakker, H. van Houten, and A. A. M. Staring (to be published); C. W. J. Beenakker (to be published).

¹¹Y. Meir, N. S. Wingreen, and P. A. Lee (to be published).

¹²V. Fock, *Z. Phys.* **47**, 446 (1928); C. G. Darwin, *Proc. Cambridge Philos. Soc.* **27**, 86 (1930); R. B. Dingle, *Proc. Roy. Soc. London A* **216**, 118 (1953); **219**, 463 (1953).

¹³U. Sivan and Y. Imry, *Phys. Rev. Lett.* **61**, 1001 (1988).

¹⁴U. Meirav, M. Heiblum, and Frank Stern, *Appl. Phys. Lett.* **52**, 1268 (1988).

¹⁵In all of the experiments reported here, the voltage on the upper gate is held fixed at -0.3 V.

¹⁶The inferred value of α is smaller than expected from the known upper-gate and lower-gate capacitances (see Ref. 3). The origin of this discrepancy is not known.

¹⁷See, e.g., T. Ando, A. B. Fowler, and F. Stern, *Rev. Mod. Phys.* **54**, 437 (1982).

¹⁸B. J. van Wees *et al.*, *Phys. Rev. Lett.* **62**, 1181 (1989).

¹⁹At finite temperatures the energy of a state in the second LL is only indirectly related to the position of the peak since conduction is mostly by thermal activation to states in the first LL [see Fig. 3(d)].

²⁰The remaining minor discrepancies with experiment in Fig. 3 can be accounted for within the theory by including additional single-particle states and small variations in the elastic widths.

Self-consistent addition spectrum of a Coulomb island in the quantum Hall regime

P. L. McEuen,* E. B. Foxman, Jari Kinaret, U. Meirav,[†] and M. A. Kastner

Department of Physics, Massachusetts Institute of Technology, Cambridge, Massachusetts 02139

Ned S. Wingreen

NEC Research Institute, 4 Independence Way, Princeton, New Jersey 08540

S. J. Wind

IBM Thomas J. Watson Research Center, Yorktown Heights, New York 10598

(Received 11 March 1992)

Coulomb interactions are shown to influence the addition spectrum of a small electron gas in the quantum Hall regime in ways that cannot be described by a classical charging energy. The interaction energy between electrons is observed to depend upon Landau-level index, and the evolution of the addition spectrum with magnetic field is found to depend strongly on Coulomb interactions. A self-consistent model of the island is introduced that can account for these results.

The energy-level spectrum of a two-dimensional island of electrons in a high magnetic field is a subject of considerable recent interest.¹⁻¹¹ For noninteracting electrons residing in a circularly symmetric external confinement potential $V_{\text{ext}}(r)$, the behavior is well known. In the limit where $V_{\text{ext}}(r)$ varies slowly on the scale of the magnetic length $l_B = (\hbar/eB)^{1/2}$, the kinetic and spin energies of the electrons are quantized into Landau levels (LL's), and the single-particle energies are given by

$$E(n, m, S_z) \approx [(n + \frac{1}{2})\hbar\omega_c + g\mu_B B S_z] + V_{\text{ext}}(r_m), \quad (1)$$

where $\omega_c = eB/m^*$ is the cyclotron frequency, $n=0, 1, 2, \dots$ is the orbital Landau-level index, $S_z = \pm \frac{1}{2}$ (denoted \uparrow and \downarrow) is the spin LL index, and $r_m = (2m\hbar/eB)^{1/2}$ is the radius of the drifting cyclotron orbit that encloses m flux quanta. The behavior of these single-particle energies, calculated for $V_{\text{ext}}(r) = (\frac{1}{2})m^*\omega_c^2 r^2$, is shown in Fig. 1(a). A rich spectrum of level crossings is observed with increasing B as the LL degeneracy (given by $1/2\pi l_B^2$) increases, and the number of occupied LL's (given by $\nu = 2\pi l_B^2 n_s$, where n_s is the sheet electron density) decreases.

Coulomb interactions are expected to strongly alter this picture, however, as studies of both microscopic³⁻⁷ and phenomenological^{1,2} models have shown. In the microscopic models, Coulomb repulsion causes electrons to spread out and partially occupy higher r_m orbitals,⁴ and correlations lead to the formation of fractional quantum Hall states.⁶ These microscopic models have been solved, however, only for small numbers of electrons³⁻⁶ or for oversimplified forms for the interaction,^{6,7} making comparison to experiment difficult. Because of this, a phenomenological model, which we call the constant-interaction (CI) model,^{1,2} has typically been employed to interpret experiments.^{1,8,9} In this CI model, the electrochemical potential, i.e., the energy required to add the N th electron to the island, is given by (Ref. 1)

$$\mu_c(N) = (N - \frac{1}{2})U + E_N, \quad (2)$$

where U is the Coulomb interaction energy between elec-

trons on the island and E_N is the N th quantized single-particle energy state of the island. U is assumed to be a constant, independent of both magnetic field and particle number, and E_N is calculated for a noninteracting system [cf. Fig. 1(a)].

Despite its simplicity, the CI model has been quite suc-

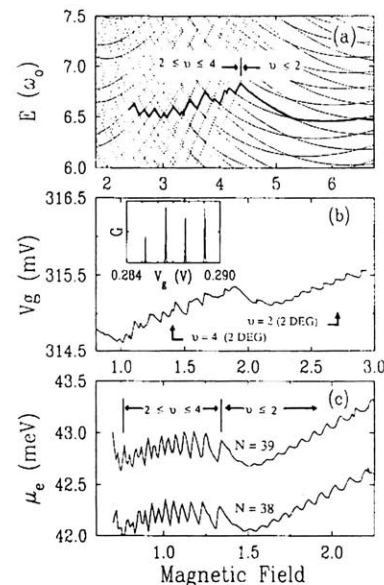


FIG. 1. (a) Dots: Calculated noninteracting level spectrum of an island vs B (in units of ω_c/ω_0). Thick solid line: Energy of the 39th electron. The filling factor ν of the island is as indicated. (b) Position in back-gate voltage V_g of a conductance peak as a function of B (in T) at $T \approx 30$ mK. The measured filling factors ν of the 2DEG are also shown. Inset: Conductance vs V_g at $B = 2.5$ T. (c) Electrochemical potential of the 38th and 39th electron vs B (in T) calculated using the self-consistent (SC) model described in the text.

cessful in describing a variety of transport experiments by our group⁸ and others.¹ In this Rapid Communication, however, we present new experimental results that are inconsistent with the CI model. These experiments lead us to reinterpret our previous results⁸ and to develop a different *self-consistent* (SC) model of the island. This SC model, whose predictions are in good agreement with experiment, gives an interesting picture of a small electron gas in the quantum Hall regime.

We begin with some experimental observations. The device, which has been discussed in detail previously,^{8,10} consists of a two-dimensional electron gas (2DEG) in an inverted GaAs/Al_xGa_{1-x}As heterostructure with electrostatic gates above and below it. A negative bias applied to the upper depletion gate defines an island of 2DEG (lithographic dimensions, 450 × 900 nm²) containing fewer than 100 electrons. The island is probed by weakly coupling it to two large 2DEG regions and measuring the conductance as a function of the voltage V_g applied to the lower (n^+ -type GaAs) gate. The positions in V_g of the observed conductance peaks [Fig. 1(b) inset] are a direct measurement of the energies for adding additional electrons to the island:¹ $V_g(N) = \mu_c(N)/ea$, where a [≈ 0.4 (Ref. 8)] is a constant. Figure 1(b) shows the position of a particular conductance peak as a function of magnetic field. Also shown are the filling factors ν of the 2DEG adjacent to the island, as determined by Shubnikov-de Haas measurements.

In Ref. 8, we presented similar results from a different device. Based on the predictions of the CI model, the structure in $V_g(N)$ in the region above 1.9 T was attributed to level crossings between states in the lowest two *orbital* Landau levels. In that interpretation, $B = 1.9$ T in Fig. 1(b) would correspond to a filling factor of $\nu = 4$ in the island. Comparison with the filling factors in the 2DEG, however, show that this interpretation is unreasonable. It would require the filling factor (and density) of the island to be *larger* than that of the 2DEG, while other experiments^{1,9} (and common sense) indicate that it should be *smaller*. We are thus led to a different interpretation than the one given in Ref. 8; namely, that 1.9 T corresponds to $\nu = 2$, and the region above 1.9 T to $\nu \leq 2$. The structure in the peak position above 1.9 T thus represents crossings between states in the two lowest *spin-split* LL's. This interpretation presents a dilemma, however. The experimental data does *not* resemble the predictions of the constant-interaction model. The CI model predicts very *infrequent* level crossings in the $\nu \leq 2$ regime [Fig. 1(a)] since, in GaAs, the spin-splitting $g\mu_B B$ is small. In the experiment, however, *frequent* level crossings are observed [Fig. 1(b)].

Motivated by this discrepancy, we have developed an alternative self-consistent (SC) model of the island, which we now discuss in detail. In this model, the total energy of the island, $E_{\text{tot}}(N)$, is given by

$$E_{\text{tot}}(N) = \left[\sum_n \sum_s \left[(n + \frac{1}{2}) \hbar \omega_c + g \mu_B B S_z \right] \int d^2r \rho_{ns}(r) \right] + \int d^2r \rho(r) \left[V_{\text{ext}}(r) + \frac{1}{2} \int d^2r' \rho(r') V_{ee}(r, r') \right], \quad (3)$$

where $\rho_{ns}(r)$ is the electron density in the n , S_z spin-polarized Landau level, $\rho(r)$ is the total electron density, $V_{\text{ext}}(r)$ is the bare (unscreened) confining potential created by the upper gates, and $V_{ee}(r, r')$ is the electron-electron interaction. The electron density in each LL is limited by the Landau-level degeneracy:

$$\rho_{ns}(r) \leq 1/2\pi l_B^2. \quad (4a)$$

We further assume that the *charge in each Landau level is quantized*, i.e.,

$$\int d^2r \rho_{ns}(r) = N_{ns}, \quad \sum_n \sum_s N_{ns} = N, \quad (4b)$$

and N_{ns} is an integer. This is expected to be a valid approximation if the coupling between states in different Landau levels is small. According to simulations of our device by Kumar,¹¹ V_{ext} is roughly parabolic with oscillator frequencies given by $\hbar \omega_c = 3.5$ meV, and $\hbar \omega_v = 0.8$ meV. For computational simplicity, we will assume radial symmetry: $V_{\text{ext}}(r) = (\frac{1}{2}) m^* \omega_0^2 r^2$ and use a single parameter, $\hbar \omega_0 = [(\hbar \omega_c)(\hbar \omega_v)]^{1/2} = 1.6$ meV, to characterize the potential. Electrons added to this bare confinement potential interact with each other and screen the potential. This interaction $V_{ee}(r, r')$ is cut off at short distances by the finite z -extent δz of the 2DEG wave function (~ 10 nm) and is screened at long distances by the image charges associated with the nearby metallic n^+ region. We use the following form for the interaction to ac-

count for these effects:

$$V_{ee}(r, r') = e^2/\epsilon(|r - r'|^2 + \delta z^2)^{1/2} - e^2/\epsilon(|r - r'|^2 + 4d^2)^{1/2}, \quad (5)$$

where d is the distance from the 2DEG to the gate (100 nm) and $\epsilon = 13.6$ is the dielectric constant of GaAs. Finally, we will use the bare g factor of GaAs $g = -0.44$ to describe the spin splitting, although the exchange enhancement of the g factor¹² can be included in a straightforward manner. As we will see, the size of the spin splitting does not qualitatively affect the predictions.

We now discuss the results of the SC model, obtained by numerically minimizing (3) subject to the constraints (4), and by using the definition of the electrochemical potential:

$$\mu_c(N) \equiv E_{\text{tot}}(N) - E_{\text{tot}}(N - 1). \quad (6)$$

Figure 2(c) shows the calculated $\mu_c(N)$ for $N = 38$ and 39 as a function of magnetic field. The overall shape, as well as the scale, of the structure in μ_c is quite similar to that in the experimental data of Fig. 1(b). In addition, the separation between successive μ_c curves in the SC model [~ 0.6 meV between $\mu_c(N = 38)$ and $\mu_c(N = 39)$] is in reasonable agreement with the experimentally observed peak spacing ($\alpha \Delta V_g \sim 0.48$ mV). The density of the island in the model is $\sim 30\%$ less than in the experiment, but uncertainties in the number of electrons and in the pa-

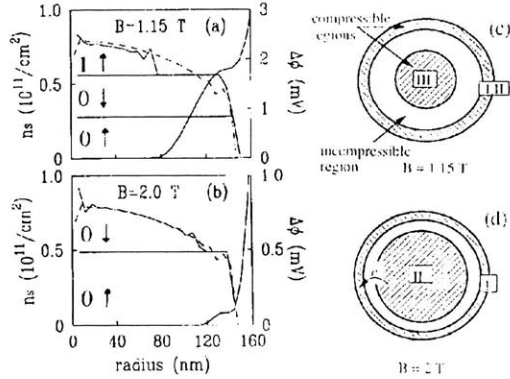


FIG. 2. Charge density and electrostatic potential in the self-consistent model for 39 electrons and (a) $B = 1.15$ T and (b) 2.0 T. The dashed line is the classical electrostatic solution. Partially filled (compressible) LL's screen the confining potential, while full (incompressible) LL's do not. (c), (d) Schematic top views of the island showing the compressible regions of the $0\uparrow$ LL (region I), the $0\downarrow$ LL (region II), and the $1\uparrow$ LL (region III).

parameter ω_0 can easily account for this difference. Most importantly, there are frequent level crossings in the $\nu \leq 2$ regime; the SC model can thus account for the level crossings observed in the experiment [Fig. 1(b)].

To understand the physics underlying this behavior, we first note that in the SC model the shape of the charge distribution closely approximates the classical electrostatic solution.¹³ This can be seen in Figs. 2(a) and 2(b), where the SC charge density $\rho(r)$ (solid lines) is given at two very different magnetic fields and compared to the classical result (dashed line). While electrons can lower their kinetic and spin energies by shifting to lower LL's, these quantum effects are only a small perturbation. We can now immediately understand the origin of frequent level crossings in the $\nu \leq 2$ regime. An electron transfers from the upper to the lower LL roughly whenever a flux quantum h/e is added to the area of the island and an additional electron can be accommodated in the lower LL. The frequency of these level crossings is governed by classical electrostatics and LL degeneracies, and *not* by the spin-splitting energy between LL's.

To understand the oscillations in greater detail, we first note that the readjustment of charge to minimize kinetic and spin energy leaves the island in a configuration, as shown in Figs. 2(c) and 2(d), where compressible regions (partially filled LL's) are separated by incompressible regions (full LL's). The compressible regions can be thought of as metallic regions that screen the external potential,¹⁴ leaving the self-consistent electrostatic potential flat [see Figs. 2(a) and 2(b)]. The incompressible regions, on the other hand, can be thought of as insulators that do not screen the external potential. Now consider adding an additional electron to the island, e.g., in the $\nu \leq 2$ regime shown in Fig. 2(d). The electron may be added to either compressible region I or II, and the behavior of $\mu_e(N)$ with B depends upon where it is added. To see this, note

that when the magnetic field is increased slightly, the degeneracy of the LL's increases. The charge density in the lower LL then increases in the center of the island and thus decreases near the edges, thereby increasing the electrostatic potential in region II and decreasing it in region I. The rising (falling) portions of the $\mu_e(N)$ vs B curves in Fig. 1(c) thus correspond to the N th electron being added to region II (region I). As the magnetic field is further increased the electrostatic potential disparity between regions II and I becomes large and discrete charge e will move from the upper to the lower LL, as shown in Fig. 2(d). These electron transfers show up as crossovers between the rising and falling parts of the μ_e traces. The oscillations of μ_e with B are thus due to the periodic buildup and release of electrostatic frustration in the island that occurs because the charge must distribute itself among the LL's in multiples of e .

Another important result from the SC model is that the magnitude of the interaction between electrons depends upon the shape of the charge distributions and upon the width of the incompressible region separating them. This can be seen by constructing "level spectra"^{8,15} in different magnetic-field regimes, as is done in Fig. 3. These spectra are made by subtracting a constant between successive μ_e curves in the model, or between peak position curves in the experiment. Physically, this constant represents the interaction energy U between an electron in one metallic region and an electron in another. In particular, it is the U between electrons whose electrochemical potentials are crossing with increasing B . Figures 3(a) and 3(b) are level spectra in the $3 \geq \nu \geq 2$ regime. The amount subtracted ($U_{0,1} = 0.45$ meV in the model, $\Delta V_{0,1} = 1.175$ mV in the data) is the Coulomb interaction between an electron in the $n=0$ LL and an electron in the $n=1$ LL. A

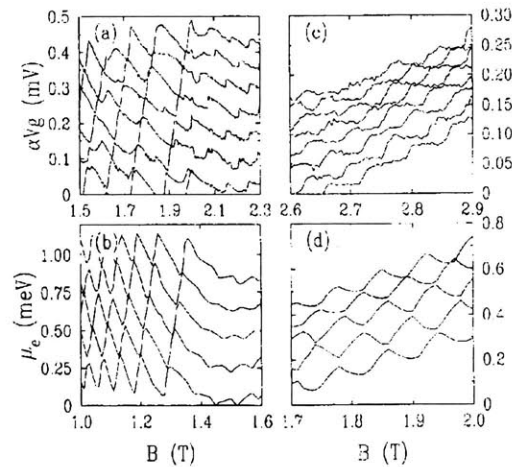


FIG. 3. (a) Experimental spectrum and (b) SC model spectrum in the $3 \geq \nu \geq 2$ regime. These spectra are constructed by subtracting a constant between successive peak position traces. (c) Experimental spectrum and (d) SC model spectrum in the $\nu \leq 2$ regime, constructed by subtracting slightly larger constants than in (a) and (b).

in the $n=1$ LL. A different, larger constant must be subtracted to construct a level spectrum in the $\nu \leq 2$ regime. This is done in Figs. 3(c) and 3(d), where the amounts subtracted are $U_{01,01}=0.55$ meV in the model, and $\Delta V_{g01,01}=1.35$ mV in the experiment. The Coulomb interaction U thus depends upon LL index. In addition, U depends on the magnetic field, since the level spectra in general line up only over a limited range of B .⁷ These variations in U again illustrate the limitations of the constant-interaction model and the necessity of a self-consistent approach.

In conclusion, we have studied the addition spectrum of a small electron gas in the quantum Hall regime. We find that the magnitude of the Coulomb interaction between electrons is a function of the Landau-level index and mag-

netic field, and that Coulomb interactions strongly influence the evolution of the addition spectrum with B . The experimental results are in good agreement with a self-consistent model of the island.

We thank Yigal Meir, Patrick Lee, and Xiao-Gang Wen for useful discussions. We also thank Arvind Kumar for his expert simulations, and Nathan Belk and Paul Belk for their help with the instrumentation. The work at MIT was supported by the NSF under Grant No. ECS-8813250 and by the U.S. Joint Services Electronics Program under Contract No. DAAL03-89-C-001. One of us (J.K.) acknowledges the support of the Academy of Finland.

*Present address: Department of Physics, University of California at Berkeley, Berkeley, CA 94720.

[†]Present address: Department of Nuclear Physics, Weizmann Institute of Science, Rehovot 76 100, Israel.

[‡]For a review, see C. W. J. Beenakker and H. van Houten, in *Single Charge Tunneling*, edited by H. Grabert, J. M. Martinis, and M. H. Devoret (Plenum, New York, 1991).

²C. W. J. Beenakker, H. van Houten, and A. A. M. Staring, *Phys. Rev. B* **44**, 1657 (1991).

³Garnett W. Bryant, *Phys. Rev. Lett.* **59**, 1140 (1987).

⁴P. A. Maksym and Tapash Chakraborty, *Phys. Rev. Lett.* **65**, 108 (1990).

⁵Arvind Kumar, Steven E. Laux, and Frank Stern, *Phys. Rev. B* **42**, 5166 (1990).

⁶Jari M. Kinaret, Yigal Meir, Ned S. Wingreen, Patrick Lee, and Xiao-Gang Wen, *Phys. Rev. B* (to be published).

⁷N. F. Johnson and M. C. Payne, *Phys. Rev. Lett.* **67**, 1157

(1991); N. F. Johnson and M. C. Payne (unpublished).

⁸P. L. McEuen *et al.*, *Phys. Rev. Lett.* **66**, 1926 (1991).

⁹A. A. M. Staring, H. van Houten, C. W. J. Beenakker, and C. T. Foxon (unpublished).

¹⁰U. Meirav, M. A. Kastner, and S. J. Wind, *Phys. Rev. Lett.* **65**, 771 (1990).

¹¹Arvind Kumar, in *Proceedings of Electronic Properties of Two-Dimensional Solids-9* [Surf. Sci. (to be published)].

¹²See, e.g., T. Ando, A. B. Fowler, and F. Stern, *Rev. Mod. Phys.* **54**, 437 (1982).

¹³V. Shikin, S. Nazin, D. Heitmann, and T. Demel, *Phys. Rev. B* **43**, 11903 (1991).

¹⁴A. M. Chang, *Solid State Commun.* **74**, 271 (1990).

¹⁵Note that these are addition spectra, *not* excitation spectra. Nonlinear measurements must be used to explore the excitation spectrum.

Effects of quantum levels on transport through a Coulomb island

E. B. Foxman, P. L. McEuen,* U. Meirav,[†] Ned S. Wingreen,[‡] Yigal Meir,[§] Paul A. Belk, N. R. Belk, and M. A. Kastner

Department of Physics, Massachusetts Institute of Technology, Cambridge, Massachusetts 02139

S. J. Wind

IBM Thomas J. Watson Research Center, Yorktown Heights, New York 10598

(Received 16 December 1992)

Transport measurements are used to study the quantized energy levels in a small electron gas, referred to as a Coulomb island. First, large-bias measurements reveal the excitation spectrum of the island. Second, small-bias measurements probe the intrinsic line shape of energy levels. Line shapes are generally fit well by thermally broadened Lorentzians. In addition, a decrease in the charging energy of the island is observed as the coupling to its leads is increased. This effect is shown to be consistent with a dramatic increase in one of the island-lead capacitances.

Conductance studies have demonstrated that transport through a small electron gas is strongly regulated by Coulomb interactions.¹ Initially, much of this behavior was interpreted through the theory of the Coulomb blockade,² a classical theory in which the discreteness of the energy spectrum of the electron gas is ignored. In metals, where the separation between energy levels is generally negligible, this has proven to be an excellent approximation. In submicrometer semiconductor systems, however, the spacing between energy levels can be orders of magnitude larger and must be taken into account. Consequently, several models have recently been introduced which extend the Coulomb-blockade model to include the effects of quantized energy levels in the limit that kT is much greater than the intrinsic energy width of the levels.³⁻⁶ Some of the predictions of these models have been verified by experiments in small, two-dimensional electron gases (2DEG), which we refer to as Coulomb islands, when the Coulomb energy is larger than the level spacing.⁷⁻⁹

In this paper we report effects of quantized energy levels on transport through a Coulomb island. First, large-bias measurements are employed to map the discrete excitation spectrum of a Coulomb island. Specifically, this is the spectrum of excited states of the island when the number of charges on the island is constant. This is in contrast to previous experiments which measured the spectrum of states for adding additional charge to the island.⁸ Second, low-bias measurements are used to probe the intrinsic line shape of transmission resonances through the island; the line shapes are in general fit well by thermally broadened Lorentzians. Last, we observe a vanishing of the Coulomb charging energy as the coupling through one of the tunnel barriers is increased. This behavior is shown to be consistent with a dramatic increase in the measured value of the capacitance between the island and one of its leads.

The device studied is shown schematically in the inset to Fig. 1(a) and has been discussed in detail elsewhere.¹⁰ Briefly, the density of the 2DEG in an inverted GaAs/Al_xGa_{1-x}As heterostructure is varied by a volt-

age V_g on the substrate of the device. The density of the 2DEG is $\sim 2 \times 10^{15} \text{ m}^{-2}$ and varying V_g by 1 mV changes the density by $\sim 1 \times 10^{13} \text{ m}^{-2}$. A negative bias V_c applied to an electrode on the top of the device

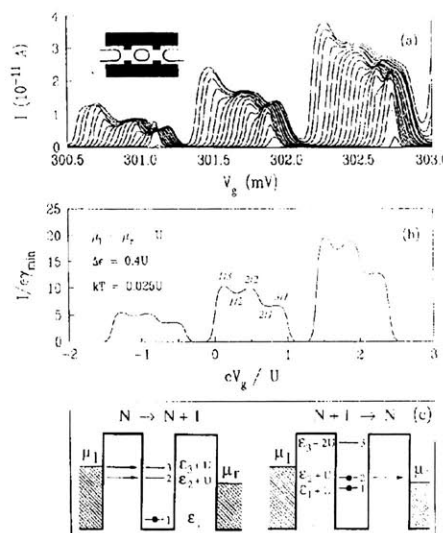


FIG. 1. (a) The current as a function of gate voltage V_g for drain-source biases V_{ds} ranging from 50 to 500 μV in increments of 25 μV . Inset: A schematic top view of the device (not to scale) showing e-beam patterned gates (opaque) and 2DEG (shaded). (b) The current, calculated from the model described in the text, in units of I/I_{\min} where I_{\min} is the tunneling rate of the lowest active level through the right barrier. The notation n/m labeling the extrema in the overstructure denotes that electrons can tunnel into n single-particle levels in the island and out from m levels. (c) A schematic of the "2/1" tunneling processes. Only the levels active in transport are shown. Increasing V_g lowers the energy of levels relative to μ_L , ultimately changing the set of active levels.

confines electrons to the island geometry with lithographic dimensions $450 \times 500 \text{ nm}^2$. In this configuration the island is separated from its leads by tunnel barriers. The current I , which flows through the island in response to a bias between the right and left leads V_{ds} , is typically measured, with a high-precision, low-noise current amplifier. The output of the current amplifier was measured by a lock-in amplifier, which also provided the ac drain bias. The device is cooled in a 12-mK base-temperature dilution refrigerator. Due to residual electron heating, the resulting electron temperature, as determined from the temperature evolution of conductance peaks, is 60 mK at low bias.¹¹

We begin by discussing large-bias transport measurements which reveal the discrete excitation spectrum of the island. The current as a function of gate voltage is plotted in Fig. 1(a), for V_{ds} ranging from 50 to 500 μV in increments of 25 μV in zero magnetic field. The periodic spacing of the current peaks at low V_{ds} reflects the quantization of charge on the island.¹⁰ As V_{ds} is increased, the low-bias peaks broaden, take on an asymmetric profile, and exhibit a modulated overstructure. This overstructure persists to $T \sim 250 \text{ mK}$ and is observable in both zero and finite magnetic fields.¹²

Figure 1(b) shows the current versus gate voltage calculated from a generalized Coulomb-blockade model in which quantized levels have been included.^{3,13} The levels are spaced by $\Delta\epsilon = 0.4U$, where U is the Coulomb-blockade charging energy required to increase the charge of the island by e . To reflect the reduction of the tunnel barrier heights with increasing level energy, the tunneling rates across the barriers are increased in the calculation by a factor of 1.2 for each higher level. As shown in Fig. 1(c), the current rises (falls) when a level is pulled below the higher (lower) chemical potential and becomes accessible (inaccessible) for tunneling. This simple model is clearly consistent with the observed modulations of the current in Fig. 1(a). We therefore interpret the modulations in the data as arising from a discrete set of well-coupled, single-particle levels in the island. Furthermore, we point out that unlike previous experiments,⁸ these data probe the quantized levels of the island in zero magnetic field. To match the experimental results, it is necessary to assume that for each level the tunneling rate through the barrier on the left is larger than that on the right by a factor of 10.

The excitation spectrum of the well-coupled, single-particle levels of the island is also manifest in I versus V_{ds} measurements at fixed V_g . The inset to Fig. 2(a) shows $|I|$ versus V_{ds} for $V_g = 304.06 \text{ mV}$ and $B = 3.35 \text{ T}$. The suppression of current in the neighborhood of $V_{ds} = 0$ is due to the Coulomb blockade and the large rise in current at $V_{ds} \approx 1.1 \text{ mV}$ is a manifestation of the Coulomb staircase.² Additional fine structure, seen most clearly in the plot of dI/dV_{ds} in Fig. 2(a), arises from the discrete excitation level spectrum. A peak in dI/dV_{ds} occurs each time a level in the island is aligned with the Fermi level in the biased lead.¹⁴ Similar observations have been reported in vertical quantum-dot structures.⁷ The V_{ds} of peaks in dI/dV_{ds} , multiplied by a factor $e\beta$, are plotted as a function of V_g in Fig. 2(b). The factor

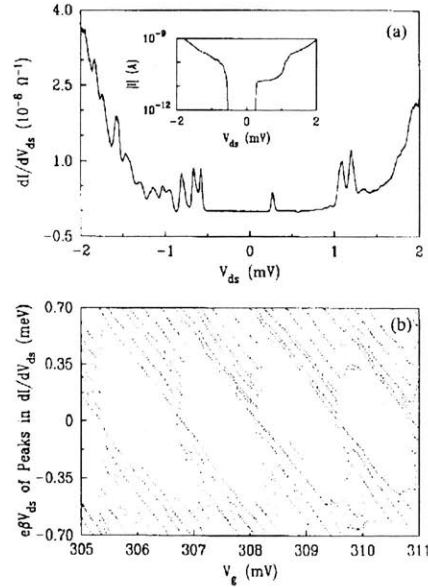


FIG. 2. (a) dI/dV_{ds} as a function of V_{ds} for $V_g = 304.06 \text{ mV}$ and $B = 3.35 \text{ T}$. Inset: $|I|$ vs V_{ds} for the data in (a). (b) The energy of peaks in dI/dV_{ds} as a function of V_g . The V_{ds} of a peak is converted to an energy via the factor β described in the text. The lines represent the single-particle excitation spectrum of the island as a function of V_g . Note that the Coulomb gap decreases with V_g .

$\beta = -0.80$ relates V_{ds} to the actual change in the Fermi energy of the biased lead relative to the island.¹⁵ The lines in Fig. 2(b) show the single-particle excitation spectrum of the island as a function of V_g .¹⁶ The Coulomb-blockade gap in the tunneling density of states and the downward shift in energy of excitation levels with increasing V_g are clearly visible. The typical level spacing is seen to be $\Delta\epsilon \approx 0.1 \text{ meV}$. Also evident is the realignment of the Coulomb gap when the charge state of the island increases by e and levels shift by U .

We now discuss measurements which probe the intrinsic line shapes of transmission resonances of the island. Figure 3(a) shows the low-bias ($V_{ds} = 2.5 \mu\text{V}$) conductance of the island as a function of V_g at $B = 2.53 \text{ T}$. At high V_g the peaks broaden, the valley conductances increase, and the peak to valley ratios decrease from values greater than 10^3 at low V_g to ~ 10 at higher V_g . Figure 3(b) is an expanded view of a low V_g conductance peak from Fig. 3(a), for which the coupling to the island is still relatively small and hence so too is its intrinsic width. This peak is fit well with the line shape of a purely thermally broadened resonance¹⁰ in the limit that the resonance width is much less than kT ,

$$G = (e^2/h) (1/4kT) A \cosh^{-2}[(e\alpha V_g - E_{\text{res}})/2kT], \quad (1)$$

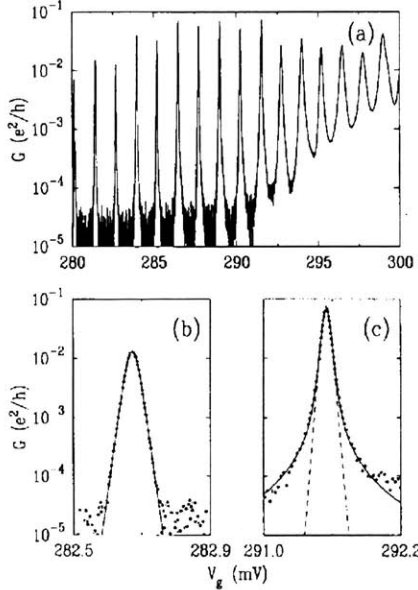


FIG. 3. (a) The low-bias conductance of the island vs V_g at $B = 2.53$ T. [Note the alternation of peak amplitudes which arises from the spin splitting of levels (Ref. 17).] (b) A low V_g conductance peak from (a) shown fit to a thermally broadened resonance (solid line) in the limit that the intrinsic resonance width is much less than kT . (c) A conductance peak at higher V_g shown fit to a thermally broadened Lorentzian (solid line). The dashed line is the best fit using the same line shape as in (b).

where E_{res} is the energy of the transmission resonance and A is the temperature-independent energy-integrated strength of the resonance. The factor α , in Eq. (1), relates a change in V_g to a shift in the energy of the island; $\alpha = U/e\Delta V_g$ where ΔV_g is the spacing between peaks.¹⁸ From the fit we obtain $\alpha = 0.52$ and hence $U = 0.61$ meV. Figure 3(c) shows a peak at higher V_g , at which the island is more strongly coupled to its leads. A striking feature of this peak is that its tails do not fall off exponentially. Clearly, this line shape cannot be fit by the expression in Eq. (1); the intrinsic line shape of the resonance is influencing the conductance peak profile. We have fit the data in Fig. 3(c) to a thermally broadened Lorentzian parametrized by a full width at half-maximum Γ ,

$$G = \frac{e^2}{h} \frac{1}{4kT} A \int_{-\infty}^{\infty} \cosh^{-2}(E/2kT) \times \frac{(\Gamma/2)\pi}{(\Gamma/2)^2 + [(e\alpha V_g - E_{\text{res}}) - E]^2} dE, \quad (2)$$

which describes resonant tunneling in noninteracting systems. The fit yields $\Gamma = 5.0$ μeV and $\alpha = 0.30$ giving $U = 0.35$ meV. As seen in Fig. 4(a) peaks often exhibit asymmetries and other features which underscore the

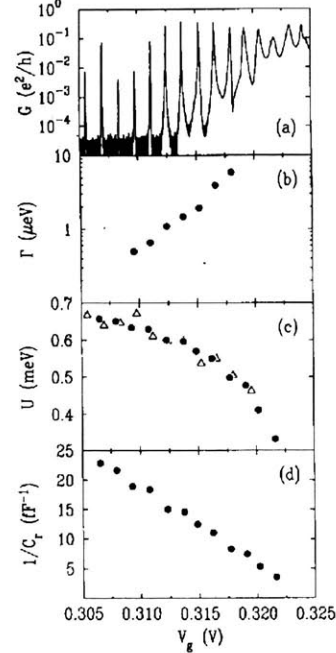


FIG. 4. (a) The low-bias conductance of the island vs V_g at $B = 3.35$ T. Each peak in (a) is fit to a thermally broadened Lorentzian yielding values for Γ , the Lorentzian full width at half-maximum [plotted in (b)] and U , the charging energy of the island [open triangles in (c)]. (d) The reciprocal of the island-lead capacitance C_r^{-1} across the right barrier. U determined from the values of C_r in (d), as described in the text, is plotted as the filled circles in (c).

limitations of broadly applying the Lorentzian line shape.¹¹ Nevertheless, reasonable fits can be made with this line shape for many of the peaks observed. The success of the fit in Fig. 3(c) strongly indicates that transmission resonances in a Coulomb island have Lorentzian intrinsic line shapes despite the presence of interactions. In zero magnetic field, similar results are seen, though in general a larger percentage of peaks show deviations from the Lorentzian line shape.

As a final consideration, notice the different values of U determined from the fits in Figs. 3(b) and 3(c), 0.61 and 0.35 meV, respectively. In order to understand this behavior we have fit a series of peaks, shown in Fig. 4(a), with the line shape of Eq. (2) and have extracted values of U and Γ . Figure 4(b) shows that Γ increases exponentially with V_g , consistent with tunneling through a saddle-point potential in a magnetic field.¹⁹ Figure 4(c) shows that U (open triangles) diminishes with V_g . Within the context of the Coulomb-blockade model this implies that the total capacitance of the island, $C = e^2/U$, increases with V_g . We test this proposition by assuming that C is the sum of four capacitances, the island-gate capacitance C_g , the island-electrode capacitance C_e , and the island-lead capacitances to both the left and right leads C_l and

C_r , respectively. C_g and C_e are measured directly from ΔV_g , the spacing between low-bias peaks.^{18,20} C_l and C_r are determined from the slope of the peak positions versus gate voltage, dV_{ds}/dV_g in measurements similar to those in Fig. 2(b). The Coulomb-blockade model gives

$$dV_{ds}/dV_g = C_g / (C - C_{\text{bias}}), \quad (3)$$

where C_{bias} is the capacitance of the island to the biased lead.¹

The above procedure gives $C_g = 0.124$ fF, $C_e = 0.025$ fF, and $C_l = 0.045 \pm 0.005$ fF independent of V_g . Surprisingly, however, C_r increases from ~ 0.045 to > 0.300 fF over the range of V_g in Fig. 4. U thus diminishes due to the increasing island-lead capacitance.²¹ Figure 4(d) shows that C_r^{-1} goes to zero linearly in V_g . U , determined from the sum of C_g , C_e , C_l , and C_r , is plotted as the filled circles in Fig. 4(c). The agreement between this measure of U and that determined from the fits confirms the accuracy of the above procedure for measuring the

capacitances to the island.

In summary, the effects of quantized energy levels on transport through a Coulomb island have been characterized. Large-bias measurements reveal the quantized excitation spectrum of these levels, and low-bias measurements probe their intrinsic line shapes. In addition, a decrease in the charging energy of the island at larger island-lead couplings is consistent with an observed increase in the island-lead capacitance.

We recently received a copy of work by A. T. Johnson *et al.* of the Delft University of Technology which reports measurements similar to our results in Figs. 1(a) and 2(a).

We wish to thank A. Kumar, D. Chklovskii, L. I. Glazman, and P. A. Lee for useful discussions. This work was supported by NSF Grant No. ECS-8813250 and by the U.S. Joint Services Electronics Program under Contract No. DAALL03-89-C-001.

*Present address: Department of Physics, University of California at Berkeley, Berkeley, CA 94720.

†Present address: Department of Nuclear Physics, Weizmann Institute of Science, Rehovot 76100, Israel.

‡Present address: NEC Research Institute, 4 Independence Way, Princeton, NJ 08540.

§Present address: Department of Physics, University of California at Santa Barbara, Santa Barbara, CA 93106.

¹For a review, see C. W. J. Beenakker and H. van Houten, in *Single Charge Tunneling*, edited by H. Grabert, J. M. Martinis, and M. H. Devoret (Plenum, New York, 1991).

²For a review, see D. V. Averin and K. K. Likharev, in *Mesoscopic Phenomena in Solids*, edited by B. Altshuler, P. A. Lee, and R. A. Webb (Elsevier, Amsterdam, 1990).

³D. V. Averin and A. N. Korotkov, Zh. Eksp. Teor. Fiz. **97**, 1661 (1990) [Sov. Phys. JETP **70**, 937 (1990)].

⁴Yigal Meir, Ned S. Wingreen, and P. A. Lee, Phys. Rev. Lett. **66**, 3048 (1991).

⁵C. W. J. Beenakker, Phys. Rev. B **44**, 1646 (1991).

⁶S.-R. Eric Yang and G. C. Aers (unpublished).

⁷Bo Su, V. J. Goldman, and J. E. Cunningham, Science **255**, 313 (1992).

⁸P. L. McEuen *et al.*, Phys. Rev. Lett. **66**, 1926 (1991).

⁹P. Guéret *et al.*, Phys. Rev. Lett. **68**, 1896 (1992); R. C. Ashoori *et al.*, *ibid.* **68**, 3088 (1992).

¹⁰U. Meirav, M. A. Kastner, and S. J. Wind, Phys. Rev. Lett. **65**, 771 (1990).

¹¹E. B. Foxman *et al.* (unpublished).

¹²In the device discussed here the modulated overstructure was not observed for fields $B \geq 4$ T. It is not yet known if this is a general feature of these systems.

¹³The division of the energy scales into separate Coulomb and single-particle pieces is an oversimplification. (See Ref. 17.) Nevertheless, the division is very illustrative and will be used exclusively in our discussion.

¹⁴In principle, peaks may also result from levels being brought into alignment with the unbiased lead due to the finite island-to-biased-lead capacitance. However, given the relatively small size of this capacitance such peaks occur rarely in Fig. 3.

¹⁵According to the Coulomb-blockade model $\beta = -(1 - C_{\text{bias}}/C)$, where C_{bias} and C are as defined later in the text.

¹⁶The results shown in Figs. 1 and 2 are from measurements on two different devices. This accounts for the different values of U and ΔE in Figs. 1 and 2.

¹⁷P. L. McEuen *et al.*, Phys. Rev. B **45**, 11 419 (1992).

¹⁸A small contribution to the spacing between peaks ($\sim 10\%$) is due to the single-particle energy to add an electron to the island. (See Ref. 5.) Therefore, the minimum observed spacing between peaks is used for ΔV_g .

¹⁹H. A. Fertig and B. I. Halperin, Phys. Rev. B **36**, 7969 (1987).

²⁰In a different study, a similar procedure was carried out except that the equivalents of C_l and C_r were assumed to be zero [L. P. Kouwenhoven *et al.*, Z. Phys. B **85**, 367 (1991)].

²¹The island-lead capacitances probably account for the missing stray capacitance discussed in Refs. 8 and 10.

Bibliography

- [1] For a review see: *Phys. Today*, **43**, 22 (1990).
- [2] C. W. J. Beenakker and H. van Houten, “Quantum Transport in Semiconductor Nanostructures,” in Solid State Physics 44, eds. Henry Ehrenreich and David Turnbull, (Academic Press, Inc., Boston, 1991).
- [3] M.A. Reed, ed., “Nanostructures Systems.” Academic Press, New York, to be published.
- [4] P.A. Lee, R. A. Webb and B. L. Al’tshuler, eds., “Mesoscopic Phenomena in Solids.” Elsevier, Amsterdam, to be published.
- [5] B. L. Al’tshuler, R. A. Webb, and R. B. Laibowitz, eds., *IBM J. Res. Dev.* **32**, 304-437, 439-579 (1988).
- [6] “Proceedings of the International Conference on Electronic Properties of Two-Dimensional Systems,” IV-VIII, *Surf. Sci.* **113** (1982); **142** (1984); **170** (1986); **196** (1988); **229** (1990).
- [7] M. J. Kelly and C. Weisbuch, eds., “The Physics and Fabrication of Microstructures and Microdevices.” Proc. Winter School Les Houches, 1986, Springer, Berlin, 1986.
- [8] H. Heinrich, G. Bauer, and F. Kuchar, eds., “Physics and Technology of Sub-micron Structures.: Springer, Berlin, 1988.

-
- [9] M. Reed and W. P. Kirk, eds., "Nanostructures Physics and Fabrication." Academic Press, New York, 1989.
- [10] S. P. Beaumont and C. M. Sotomayor-Torres, eds., "Science and Engineering of 1- and 0-Dimensional Semiconductors." (Plenum, London, 1990).
- [11] H. L. Stormer, R. Dingle, A. C. Gossard, and W. Wiegman, "Proc. 14th ICPS," p. 6 (B. L. H. Wilson, ed.). Institute of Physics, London, 1978; R. Dingle, H. L. Stormer, A. C. Gossard, and W. Wiegman, *Appl. Phys. Lett.* **7**, 665 (1978).
- [12] C. W. J. Beenakker and H. van Houten, *Solid State Physics*, **44**, 1 (1991).
- [13] K. von Klitzing, G. Dorda, and M. Pepper, *Phys. Rev. Lett.* **45**, 494 (1980).
- [14] D. C. Tsui, H. L. Stormer, and A. C. Gossard, *Phys. Rev. Lett.* **48**, 1559 (1982).
- [15] E. Abrahams, P. W. Anderson, D. C. Licciardello, and T. V. Ramakrishnan, *Phys. Rev. Lett.* **42**, 673 (1979).
- [16] P. W. Anderson, E. Abrahams, and T. V. Ramakrishnan, *Phys. Rev. Lett.* **43**, 718 (1979).
- [17] L. P. Gorkov, A. I. Larkin, and D. E. Khmel'nitskii, *Pis'ma Zh. Eksp. Teor. Fiz.* **30**, 248 (1979) [*JETP Lett.*] **30**, 228 (1979).
- [18] B. L. Al'tshuler, D. Khmelnitskii, A. I. Larkin, and P. A. Lee, *Phys. Rev. B* **22**, 5142 (1980).
- [19] P. A. Lee and T. V. Ramakrishnan, *Rev. Mod. Phys.* **57**, 287 (1985).
- [20] B. L. Al'tshuler, *Pis'ma Zh. Eksp. Teor. Fiz.* **41**, 530 (1985) [*JETP Lett.* **41**, 648 (1985)].
- [21] P. A. Lee and A. D. Stone, *Phys. Rev. Lett.* **55**, 1622 (1985).

- [22] P. A. Lee, *Physical* **140A**, 169 (1986).
- [23] Y. Aharonov and D. Bohm, *Phys. Rev.* **115**, 485 (1959).
- [24] B. L. Al'tshuler, A. G. Aronov, and B. Z. Spizak, *Pis'ma Zh. Teor. Fiz.* **33**, 101 (1981) [*JETP Lett.* **33**, 94 (1981)].
- [25] B. L. Al'tshuler, A. G. Aronov, B. Z. Spivak, D. Yu Sharvin, and Yu. V. Sharvin, *Pis'ma Zh. Teor. Fiz.* **35**, 476 (1981) [*JETP Lett.* **35**, 588 (1981)].
- [26] Yu. V. Sharvin, *Physica B*, **126**, 288 (1984).
- [27] M. Gijs, C. van Haesendonck, and Y. Bruynseraede, *Phys. Rev. Lett.* **52**, 2069 (1984).
- [28] H. Sakaki, K. Wagatsuma, J. Hamasaki, and S. Saito, *Thin Solid films* **36**, 497 (1976).
- [29] R. T. Bate, *Bull. Am. Phys. Soc.* **22**, 407 (1977).
- [30] P. f. Bagwell and T. P. Orlando, *Phys. Rev. B* **40**, 3735 (1989).
- [31] K. Ismail, W. Chu, D. A. Antoniadis, and H. I. Smith, *Appl. Phys. Lett.* **52**, 1071 (1988).
- [32] A. C. Warren, D. A. Antoniadis, H. I. Smith, and J. Melngailis, *IEEE Electron Device Letts*, **EDL-6**, 294 (1985).
- [33] D. Weiss, K. von Klitzing, K. Ploog, and G. Weimann, *Europhys. Lett.* **8**, 179 (1989).
- [34] D. Weiss, C. Zhang, R.R. Gerhardt, K. von Klitzing, and G. Weimann, *Phys. Rev. B* **39**, 13020 (1989).
- [35] S. Komiyama, H. Hirai, S. Sasa, and S. Hiyamizu, *Phys. Rev. Lett* **62**, 1181 (1989).

-
- [36] B.J. van Wees, E.M.M. Williams, L.P. Kouwenhoven, C.J.P.M. Harmans, J.G. Williamson, C.T. Foxon, and J.J. Harris, *Phys. Rev. B* **39**, 8066 (1989).
- [37] B.W. Alphenaar, P.L. McEuen, R.G. Wheeler, and R.N. Sacks, *Phys. Rev. Letts.* **64**, 677 (1990).
- [38] B.J. van Wees, H. van Houten, C.W.J. Beenakker, J.G. Williamson, L.P. Kouwenhoven, D. van der Marel, and C.T. Foxon, *Phys. Rev. Letts.* **60**, 848 (1988).
- [39] D.A. Wharam, T.J. Thornton, R. Newbury, M. Pepper, H. Ahmed, J.E.F. Frost, D.G. Hasko, D.C. Peacock, D.A. Ritchie, and G.A.C. Jones, *J. Phys. C* **21**, L209 (1988).
- [40] Landauer, R., *IBM J. Res. Dev.* **1**, 223 (1957).
- [41] Büttiker, M., *IBM J. Res. Dev.* **32**, 63 (1988).
- [42] M. Büttiker, *Phys. Rev. Lett.* **57**, 1761 (1986).
- [43] H. van Houten, B.J. van Wees, J.E. Mooji, C.W.J. Beenakker, J.G. Williamson, and C.T. Foxon, *Europhys. Lett.* **5**, 721 (1988).
- [44] J. Spector, H.L. Stormer, K.W. Baldwin, L.N. Pfeiffer, and K.W. West, *Surf. Sci.* **228**, 283 (1990).
- [45] M.L. Roukes, A. Scherer, S.J. Allen, Jr., H.G. Craighead, R.M. Ruthen, E.D. Beebe, and J. P. Harbison, *Phys. Rev. Lett.* **58**, 2814 (1987).
- [46] G. Timp, H.U. Baranger, P. deVegvar, J.E. Cunningham, R.E. Howard, R. Bhringer, and P. M. Mankiewich, *Phys. Rev. Lett.* **60**, 2081 (1988).
- [47] U. Sivan, M. Heiblum, and C.P. Umbach, and H. Shtrikman, *Phys. Rev. Lett.* **41**, 7937 (1990).

- [48] J. Spector, H.L. Stormer, K.W. Baldwin, L.N. Pfeiffer and K.W. West, *Appl. Phys. Lett.* **56**, 1290 (1990).
- [49] H. van Houten *et al.*, *Phys. Rev. B* **39**, 8556 (1989).
- [50] McEuen, P.L., Foxman, E.B., Meirav, U., Kastner, M.A., Meir, Yigal, Wingreen, Ned S., Wind, S.J., *Phys. Rev. Lett.* **66**, 1926 (1991).
- [51] McEuen, P.L., Foxman, E.B., Kinaret, Jari, Meirav, U., Kastner, M.A., Wingreen, Ned S., and Wind, S.J., *Phys. Rev. Lett.* **45**, 11419 (1993).
- [52] Foxman, E.B., McEuen, P.L., Meirav, U., Wingreen, Ned S., Meir, Yigal, Belk, Paul A., Belk, N.R., Kastner, M.A. and Wind, S.J, *Phys. Rev. B* **47**, 10020 (1993).
- [53] J.P. Kirtley, Z. Schlesinger, T. N. Theis, F. P. Milliken, s. L. Wright, and L. F. Palmateer, *Phys. Rev. B* **34**, 5414 (1986).
- [54] L. Blik, E. Braun, G. Hein, V. Kose, J. Niemeyer, G. Weimann, and W. Schlapp, *Semicond. Sci. Technol.* **1**, 110 (1986).
- [55] A. Schere and M. L. Roukes, *Appl. Phys. Lett.* **55**, 377 (1989).
- [56] G. Timp, A. M. Chang, P. Mankiewich, R. Behringer, J. E. Cunningham, T. Y. Chang, and R. E. Howard, *Phys. Rev. Lett* **58**, 732 (1987).
- [57] A. M. Chang, G. Timp, T. Y. Chang, J. E. Cunningham, P. M. Mankiewich, R. E. Behringer, and R. E. Howard, *Solid State Comm.* **67**, 769 (1988).
- [58] T. J. Thornton, M. Pepper, H. Ahmed, D. Andrews, and G. J. Davies, *Phys. Rev. Letts.* **56**, 1198 (1986).
- [59] H. Z. Zheng, H. P. Wei, D. C. Tsui, and G. Weimann, *Phys. Rev. B* **34**, 5635 (1986).

-
- [60] Scott-Thomas, J.H.F., Field, S.B., Kastner, M.A., Smith, H.I., and Antoniadis, D.A., *Phys. Rev. Lett.* **62**, 583 (1989).
- [61] Staring, A.A.M., van Houten, H., Beenakker, C.W.J., and Foxon, C.T., in *High Magnetic Fields in Semiconductor Physics III*, edited by G. Landwehr, Springer, Berlin (1991).
- [62] Meirav, U., Kastner, M.A., Heiblum, M., and Wind, S.J., *Phys. Rev. B* **40**, 5871 (1990).
- [63] Meirav, U., Kastner, M.A., and Wind, S.J., *Phys. Rev. Lett.* **65**, 771 (1990).
- [64] van Houten, H., and Beenakker, C.W.J., *Phys. Rev. Lett.* **63**, 1893 (1989).
- [65] Kulik, I.O., Shekhter, R.I., *Zh. Eksp. Teor. Fiz.* **63**, 1410 (1972) [*Sov. Phys. JETP* **36**, 747 (1973)].
- [66] For a review, see: Averin, D.V., and Likharev, K.K., in *Quantum Effects in Small Disordered systems*, eds. B. Altshuler, P.A. Lee, and R.A. Webb (Elsevier, Amsterdam, 1990).
- [67] Meir, Yigal, Wingreen, Ned S., and Lee P.A., *Phys. Rev. Lett.* **66**, 3048 (1991).
- [68] Beenakker, C.W.J., *Phys. Rev. B* **44**, 1646 (1991).
- [69] P. Gueret, N. Blanc, R. Germann, and H. Rothuizen, *Phys. Rev. Lett.* **68**, 1896 (1992).
- [70] A. T. Johnson, L. P. Kouwenhoven, W. de Jong, N. C. van der Vaart, C. J. P. M. Harmans, C. T. Foxon, *Phys. Rev. Lett.* **69**, 1592 (1992).
- [71] T. Demel, D. Heitmann, P. Grambow, and K. Ploog, *Phys. Rev. Letts.* **64**, 788 (1990).
- [72] B. Meurer, D. Heitmann, and K. Ploog, *Phys. Rev. Lett.* **68**, 1371 (1992).

- [73] W. Hanse, T. P. Smith, III, K. Y. Lee, J. A. Brum, C. M. Knoedler, J. M. Hong, and D. P. Kern, *Phys. Rev. Lett.* **62** 2168 (1989).
- [74] R. C. Ashoori, H. L. Stormer, J. S. Weiner, L. N. Pfeiffer, S. J. Pearton, K. Baldwin, K. W. West, *Phys. Rev. Lett.* **68**, 3088 (1992).
- [75] M. A. Kastner, *Rev. Mod. Phys.* **64**, 849 (1992).
- [76] M. A. Kastner, *Phys. Today*. **46**, 24 (1993).
- [77] *The New York Times* (New York Times Publishing, New York, 1991). Tech notes.
- [78] *The Economist*, Feb. 27, 1993, p. 85.
- [79] *Science*, “The Single Electron Transistor Explained”, April 12, 1991, p. 215.
- [80] K. K. Likharev and T. Claeson, *Sci. Am.* **262**, June, 1992 p. 80.
- [81] Udi Meirav and Mordehai Heiblum, *The World & I*, June, 1990 p. 294.
- [82] The Cleveland Plain Dealer, Dec. 12, 1991 p. B4.
- [83] Leo Kouwenhoven to possibly appear in Encyclopedia Britannica, from Paul McEuen, private communication.
- [84] S. J. Wind, *Byte*, **17** Feb. 1992, p. 140.
- [85] *Time*, Aug 12, 1991 p.23.
- [86] R. Landauer, *Phys. Today* **42**, 119, (1989).
- [87] R. T. Bate, *Sci. Am.* **258**, 78 (1988).
- [88] Adachi, Sadao, *J. Appl. Phys.* **58**, R1 (1985).
- [89] Blakemore, J.S., *J. Appl. Phys.* **53**, R123 (1982).

-
- [90] Chang, L.L., Esaki, L., *Surface Science* **98**, 70 (1980).
- [91] See related articles in special section in *Physics Today* Feb. 1990 in particular Chang, Leroy L., and Esaki, Leo on p. 40.
- [92] P. M. Mooney in Burns, Gerald Solid State Physics, Academic Press, Orlando p. 746 (1985).
- [93] Dohler, G. H., *Japanese J. of Appl. Phys.* **22**, 21 (1983).
- [94] Foxman, E.B., Ikarashi, N. and Hirose, K., *Appl. Phys. Lett.* **59**, 2403 (1991).
- [95] Lanoo, M., and Bourgoin, J., *Point Defects in Semiconductors Vol. I and II* Springer-Verlag, New York (1981).
- [96] Pantelides, S.T. eds. *Deep Centers in Semiconductors* Gordon and Breach, New York (1986).
- [97] Theis, T.N. and Mooney, P.M. *Comments Cond. Mat. Phys.* **16** No. 3, pp. 167-190 (1992).
- [98] Monch, W., *Phys. Rev. Lett.* **58**, 1260 (1987).
- [99] Uri Sivan, private communication.
- [100] Pruisken, A.M.M. in The Quantum Hall Effect, ed. by R.E. Prange and S. M. Girvin, Springer-Verlag, Berlin (1987).
- [101] Meirav, U. in Doctoral Thesis, "Single Electron Charging and Periodic Conductance Oscillations in Gallium Arsenide Nanostructures", The Massachusetts Institute of Technology, Department of Physics, May 1990.
- [102] Meirav, U., Heiblum, M. and Stern, Frank *Appl. Phys. Lett.* **52**, 1268 (1989).
- [103] C. W. J. Beenakker and H. van Houten, *Solid State Physics*, **44**, pp. 25-6 (1991).

- [104] Millo, O., Klepper, S.J., Keller, M.W., Prober, D.E., Xiong, S., and Stone, D.A. *Phys. Rev. Lett.* **65**, 1494 (1990).
- [105] See, e.g., Ando, T., Fowler, A.B., and Stern, F. *Rev. Mod. Phys.* **54**, 437 (1982).
- [106] Van Houten, H., van Wees, B.J., and Beenakker, C.W.J. in Physics and Technology of Submicron Structures Springer, Berlin (1988).
- [107] Fertig, H.A., and Halperin, B.I., *Phys. Rev. B* **36**, 7969 (1987).
- [108] Kumar, Arvind, Laux, Steven E., and Stern, Frank *Appl. Phys. Lett.* **54**, 1270 (1988).
- [109] Kumar, A. in *Proceedings of Electronic Properties of Two-Dimensional Solids-9* [Surf. Sci. (to be published)].
- [110] Chklovskii, D.B., Shklovskii, B.I. and Glazman, L.I. *Phys. Rev. B* **46**, 4026 (1992); **46**, 15505 (E) (1992).
- [111] Madelung, O., *Introduction to Solid-State Theory* (Springer-Verlag, Berlin, 1981) chap. 1.
- [112] For a review see, Betts, D.S. *Contemporary Physics* **9**, 97 (1968); Kittel, Charles and Kroemer, Herbert Thermal Physics second edition, W. H. Freeman and Company, New York p. 341 (1980).
- [113] Arvind Kumar, in *Proceedings of Electronic Properties of Two-Dimensional Solids-9* [Surf. Sci. (to be published)].
- [114] Kulik, I.O., Shekhter, R.I., *Zh. Eksp. Teor. Fiz.* **68**, 623 (1975) [*Sov. Phys. JETP* **41**, 308 (1975)].
- [115] Gorter, C.J., *Physica* **17**, 777 (1951).
- [116] Averin, D.V, and Odintsov, A.A., *Phys. Letts. A* **140**, 251; (1989).

-
- [117] Laikhtman, B., *Phys. Rev. B* **43**, 2731 (1991).
- [118] Nazarov, Yu. V., *Phys. Rev. B* **43**, 6220 (1991).
- [119] Averin, D.V., and Nazarov, Yu. V., *Phys. Rev. Letts* **34**, 2446 (1990).
- [120] Matveev, K.A., *Zh. Eksp. Teor. Fiz.* **99**, 1598 (1991) [*Sov. Phys. JETP* **72**, 5 (1991).].
- [121] Geerligs, L.J., Averin, D.V., and Mooji, J.E. *Phys. Rev. Lett.* **65**, 3037 (1990).
- [122] Hanna, A., Tuominen, M.T., and Tinkham, M., *Phys. Rev. Lett.* **68**, 3228 (1992).
- [123] Glazman, L.I., and Shekhter, R.I., *J. Phys.: Condens. Matter* **1**, 5811 (1989).
- [124] Landau, I.D., Lifshitz, E.M., and Pitaevskii, Electrodynamics of Continuous Media, (Pergamon Press, Oxford 1982), p. 3.
- [125] Stopa, M., preprint titled "Coulomb oscillation amplitudes and semiconductor quantum dot self-consistent level structure".
- [126] Jackson, J.D., Classical Electrodynamics, (John Wiley & Sons, New York, 1975).
- [127] Schönenberger, C., van Houten H., and Donkersloot, H.C., *Europhys. Lett.* **20** 249 (1992).
- [128] Su, B., Goldman, V.J., and Cunningham, J.E., *Science* **255**, 313 (1992).
- [129] Su, Bo., Goldman, V.J., and Cunningham, J.E., *Phys. Rev. B* **46**, 7644 (1992).
- [130] Johnson, A.T., Kouwenhoven, L.P., de Jong W., van der Vaart, N.C., and Harmans, C.J.P.M., *Phys. Rev. Lett.* **69**, 1592 (1992).

- [131] Kopley, T.E., McEuen, P.L., and Wheeler, R.G., *Phys. Rev. Lett.* **61**, 1654 (1988).
- [132] Jalabert, Rodolfo A., Baranger, Harold U., and Stone, Douglas A., *Phys. Rev. Lett.* **65**, 2442 (1990).
- [133] Stone, A. Douglas, and Jalabert, Rodolof A., in Proceedings of the 14th Taniguchi symposium on Mesoscopic Physics, Kashikojima, Japan, 1991.
- [134] Jalabert, Rodolfo A., Stone, A. Douglas, and Alhassid, Y., *Phys. Rev. Lett* **68**, 3468 (1992).
- [135] Marcus, C.M., Rimberg, A.J., Westervelt, R.M., Hopkins, P.F., and Gossard, A.C., *Phys. Rev. Lett* **69**, 506 (1992).
- [136] Meirav, U., McEuen, P.L., Kastner, M.A., Foxman, E.B., Kumar, A., and Wind, S.J., *Z. Phys. B. - Condensed Matter* **85**, 357 (1991).
- [137] Similar observations have been reported by Staring, A.A.M, Alphenaar, B.W., van Houten, H., Molenkamp, L.W., Buyk, O.J.A., Mabesoone, M.A.A, and Foxon, C.T., *Phys. Rev. B* **46**, 12869 (1992).
- [138] P.L. McEuen, Ned S. Wingreen, E.B. Foxman, Jari Kinaret, U. Meirav, M.A. Kastner, Yigal Meir, and S.J. Wind, *Physica - B* **189**, 70 (1993).
- [139] Shikin, V., Nazin, S., Heitmann, D., and Demel, T., *Phys. Rev. B* **43**, 11903 (1991).
- [140] Chang, A.M., *Solid State Commun.* **74** , 271 (1990).
- [141] Beenakker, C.W.J., *Phys. Rev. Lett.* **64**, 216 (1990).
- [142] Chklovskii, D.B., Shklovskii, B.I., and Glazman, L.I., *Phys. Rev. B* **46**, 4026 (1992).

-
- [143] Marmorkos, I.K., and Beenakker, C.W.J., preprint.
- [144] Glazman, L.I., private communication.
- [145] McEuen, P.L., private communication.
- [146] Pasquier, C., Meirav, U., Williams, F.I.B., and Glattli, D.C., *Phys. Rev. Letts* **70**, 69 (1993).
- [147] Breit, G., and Wigner, E., *Phys. Rev.* **49**, 519 (1936).
- [148] McEuen, P.L., Alphenaar, B.W., and Wheeler, R.G., *Surf. Sci.* **229** 312 (1990).
- [149] Kouwenhoven, L.W., van der Varrrt, N.C., Johnson, A.T., Kool, W., Marmans, C.J.P.M., Williamson, J.G., and Staring, A.A.M., *Z. Phys. B.* **85**, 367 (1991).
- [150] Thouless, D.J., *Phys. Rev. Lett* **39**, 1167 (1977).
- [151] Nazarov, Yu.V., *Solid State Comm.* **75**, 669 (1990).
- [152] Kondo, J., *Solid State Phys.* **23** 248 (1969).
- [153] Ng, Tai Kai, and Lee, Patrick A., *Phys. Rev. Lett.* **61**, 1768 (1988).
- [154] Glazman, L.I., and Raïkh, M. É., *Pis'ma Zh. Eksp. Teor. Fiz.* **47**, 378 (1988)
[JETP Lett. **47**, 452 (1988)].
- [155] Lane, A.M., and Thomas, R.G., *Rev. Mod. Phys.* **30**, 257 (1958).
- [156] Gergmann, Gerd, *Phys. Rev. Lett.* **67**, 2545 (1991).
- [157] Hershfield, Selman, Davies, John H., and Wilkins, John W., *Phys. Rev. Letts.* **67** 3720 (1991).
- [158] Sigrist, Manfred, Tsunetsugu, Hirokazu and Ueda, Kazue, *Phys. Rev. Letts.* **67** 2211 (1991).

-
- [159] Meir, Yigal, Wingreen, Ned S., and Lee, Patrick A., preprint titled “Low Temperature Transport through a Quantum Dot: The Anderson Model out of Equilibrium”.
- [160] Gregory, Stephen, *Phys. Rev. Letts.* **68** 2070 (1992).
- [161] Tuchman, Barbara Wertheim, “The Guns of August” (Dell Publishing Co., New York 1971), preface.
- [162] Rodolfo A. Jalabert, Harold U. Baranger, and A. Douglas Stone, *Phys. Rev. Lett.* **65**, 2442 (1990).
- [163] C.M. Marcus, A.J. Rimberg, R.M. Westervelt, P.F. Hopkins, and A.C. Gossard, *Phys. Rev. Lett.* **69**, 506 (1992).
- [164] Rodolfo A. Jalabert, A. Douglas Stone, and Y. Alhassid, *Phys. Rev. Lett.* **68**, 3468 (1992).
- [165] Goldman, V.J., Jain, J.K., and Shayegan, M., *Phys. Rev. Lett.* **65**, 907 (1990).
- [166] Jain, J.K., Kivelson, S.A., and Trivedi, Nandini, preprint titled “Scaling Theory of the Fractional Quantum Hall Effect”.
- [167] T. Sajoto, Y.W. Suen, L.W. Engel, M.B. Santos, and M. Shayegan, *Phys. Rev. B* **41**, 8449 (1990).
- [168] J.K. Wang and V.J. Goldman, *Phys. Rev. B* **45**, 13479 (1992).
- [169] J.P. Eisenstein and H.L. Stormer, *Science* **248**, 1510 (1990).
- [170] Pothier, H., Lafarge, P., Orfila, P.F., Urbina, C., Esteve, D., Devoret, M.H., *Physica B* **169**, 573 (1991).
- [171] Kouwenhoven, L.P., Johnson, A.T., Vaart, N.C. van der, Harmans, C.J.P.M., Foxon, C.T., *Phys. Rev. Lett.* **67**, 1626 (1991).

-
- [172] Kouwenhoven, L.P., Johnson, A.T., Vaart, N.C. vander, Enden, A. van der, Harmans, C.J.P.M., and Foxon, C.T., *Z. Phys. B – Condensed Matter* **85**, 381 (1991).
- [173] Geerligs, L.J., Anderegg, V.F., Holweg, P.A.M., Mooij, J.E., Pothier, H., Esteve, D., Urbina, C., Devoret, M.H., *Phys. Rev. Lett.* **64**, 2691 (1990).
- [174] B.W. Petley, *Metrologia* **29**, 95-112 (1992).
- [175] Barry N. Taylor, NIST Special Publication 330, “The International System of Units”, National Institute of Standards and Technology, Gaithersburg, MD., Aug. 1991.
- [176] Ruzin, I.M., Chandrasekhar, V., Levin, E.I., and Glazman, L.I. *Phys. Rev. B* **45**, 13469 (1992). Note: I believe that the first plus sign in the second expression of equ. 6 should be a negative sign. This is not simply a typographical error. Rather it effect the outcome of the paper’s calculations. Notice that equ. 9 and equ. 10 do not recover the independent dot formulas for U when the coupling between dots is removed. I spoke with I.M. Ruzin about this.
- [177] Averin, D.V., Korotkov, A.N., and Nazarov, Yu. V. *Phys. Rev. Lett.* **66**, 2818 (1991).
- [178] G. Menestrina, *J Membrane Biol.* **90**, 177 (1986).
- [179] Michael Land and E.B. Foxman, private communication.
- [180] P.M. Campbell, E.S. Snow, W. J. Moore, O.J. Glembocki, and S. W. Kirchoefer, *Phys. Rev. Lett.* **67**, 1330 (1991).
- [181] Holde, K.E. van, and Mathews, Christopher, K., Biochemistry, (The Benjamin/Cummings Publishing Company, Inc., Redwood City, 1990), p. 39.

-
- [182] Paul L. McEuen, Ph.D. thesis from Yale University, Department of Physics, 1991, "Transport in One Dimensional Systems," p. 88.
- [183] Fock V., *Z. Phys.* **47**, 446 (1928).
- [184] Darwin, C.G., *Proc. Cambridge Philos. Soc.* **27**, 86 (1930).
- [185] Dingle, R.B., *Proc. Roy. Soc. London A* **216**, 118 (1953).
- [186] Geerinckx, F., Peeters, F.M., and Devreese, J.T., *J. Appl. Phys* **68**, 3435 (1990).
- [187] Kumar, Arvind, Laux, Steven E., Stern, Frank, *Phys. Rev. B* **42**, 5166 (1990).
- [188] Lent, Craig S., *Phys. Rev. B* **43**, 4179 (1991).
- [189] Dempsey, Jeb, and Halperin, B.I., *Phys. Rev. Letts.* **45**, 1719 (1992).
- [190] Merkt, U., Huser, J., and Wagner, M., *Phys. Rev. B* **43**, 7320 (1991).

Biographical Sketch of the Author

Ethan Bradley Foxman was born May 31, 1966 in Cleveland, Ohio to Jean and David Foxman. He has a sister, Susan, who is three years his junior. He graduated from Shaker Heights Public High School in June, 1984, and attended college at the Massachusetts Institute of Technology, graduating in May, 1988, with a bachelor of science in physics and minors in Japanese language and American history. During college, the author traveled to Europe and China on a cultural exchange program and worked two summers in an x-ray scattering laboratory at M.I.T.. After graduating college, he worked at the Nippon Electric Company Fundamental Research Laboratories in Kawasaki and Tsukuba, Japan where he participated in semiconductor device research. In September, 1989, the author returned to M.I.T. to begin the doctoral program in the Department of Physics. Three months later, he began research with Professor Marc Kastner, with whom he completed his doctoral work in experimental, solid-state physics.